



NAVAL POSTGRADUATE SCHOOL

MONTEREY, CALIFORNIA

DISSERTATION

**PROCESSING, MICROSTRUCTURE, AND MATERIAL
PROPERTY RELATIONSHIPS FOLLOWING FRICTION
STIR WELDING OF OXIDE DISPERSION
STRENGTHENED STEELS**

by

Bradford Baker

September 2013

Dissertation Supervisor:

Luke Brewer

Approved for public release; distribution is unlimited

THIS PAGE INTENTIONALLY LEFT BLANK

REPORT DOCUMENTATION PAGE			<i>Form Approved OMB No. 0704-0188</i>	
Public reporting burden for this collection of information is estimated to average 1 hour per response, including the time for reviewing instruction, searching existing data sources, gathering and maintaining the data needed, and completing and reviewing the collection of information. Send comments regarding this burden estimate or any other aspect of this collection of information, including suggestions for reducing this burden, to Washington headquarters Services, Directorate for Information Operations and Reports, 1215 Jefferson Davis Highway, Suite 1204, Arlington, VA 22202-4302, and to the Office of Management and Budget, Paperwork Reduction Project (0704-0188) Washington DC 20503.				
1. AGENCY USE ONLY (Leave blank)		2. REPORT DATE September 2013	3. REPORT TYPE AND DATES COVERED Dissertation	
4. TITLE AND SUBTITLE PROCESSING, MICROSTRUCTURE, AND MATERIAL PROPERTY RELATIONSHIPS FOLLOWING FRICTION STIR WELDING OF OXIDE DISPERSION STRENGTHENED STEELS			5. FUNDING NUMBERS	
6. AUTHOR(S) Bradford W. Baker				
7. PERFORMING ORGANIZATION NAME(S) AND ADDRESS(ES) Naval Postgraduate School Monterey, CA 93943-5000			8. PERFORMING ORGANIZATION REPORT NUMBER	
9. SPONSORING /MONITORING AGENCY NAME(S) AND ADDRESS(ES) N/A			10. SPONSORING/MONITORING AGENCY REPORT NUMBER	
11. SUPPLEMENTARY NOTES The views expressed in this thesis are those of the author and do not reflect the official policy or position of the Department of Defense or the U.S. Government. IRB Protocol number ____N/A ____.				
12a. DISTRIBUTION / AVAILABILITY STATEMENT Approved for public release; distribution is unlimited			12b. DISTRIBUTION CODE A	
13. ABSTRACT (maximum 200 words) A comprehensive set of processing, microstructure, and material property relationships is presented for friction stir welded oxide dispersion strengthened MA956 steel. Eight rotational and traverse speed combinations were used to produce friction stir welds on MA956 plates using a polycrystalline cubic boron nitride tool. Weld parameters with high thermal input produced defect-free, full penetration welds. Microstructural analysis showed a significant increase in grain size, a persistent body centered cubic torsional texture in the stir zone, a sharp transition in grain size from the thermo-mechanically affected zone into the stir zone, and an asymmetric reduction in hardness across the weld, all of which were sensitive to weld parameters. Oxide particles were significantly coarsened by friction stir welding resulting in a complete loss of particle strengthening. Base metal MA956 mechanical properties were determined up to 600°C and the effect of friction stir welding on these properties was directly correlated to the evolved microstructure. Grain refinement is a dominant strengthening mechanism in the base metal and for all friction stir welding conditions, as the welding process removed essentially all dislocation and dispersion strengthening contributions. Friction stir welded MA956 retains a majority of its high temperature strength, making the alloy and joining method a suitable candidate for a structural material in advanced nuclear reactor designs.				
14. SUBJECT TERMS Oxide Dispersion Strengthened Steel; MA956; Friction Stir Welding			15. NUMBER OF PAGES 319	
			16. PRICE CODE	
17. SECURITY CLASSIFICATION OF REPORT Unclassified	18. SECURITY CLASSIFICATION OF THIS PAGE Unclassified	19. SECURITY CLASSIFICATION OF ABSTRACT Unclassified	20. LIMITATION OF ABSTRACT UU	

THIS PAGE INTENTIONALLY LEFT BLANK

Approved for public release; distribution is unlimited

**PROCESSING, MICROSTRUCTURE, AND MATERIAL PROPERTY
RELATIONSHIPS FOLLOWING FRICTION STIR WELDING OF OXIDE
DISPERSION STRENGTHENED STEELS**

Bradford W. Baker
Commander, United States Navy
B.S., United States Naval Academy, 1994
M.S., National Defense University, 2007

Submitted in partial fulfillment of the
requirements for the degree of

DOCTOR OF PHILOSOPHY IN MECHANICAL ENGINEERING

from the

**NAVAL POSTGRADUATE SCHOOL
September 2013**

Approved by:

Luke Brewer
Associate Professor
Mech. and Aero. Engineering
Dissertation Supervisor

Garth Hobson
Professor
Mech. and Aero. Engineering
Dissertation Committee Chair

Terry McNelley
Distinguished Professor Emeritus
Mech. and Aero. Engineering

Joseph Hooper
Assistant Professor
Physics

Joseph Farmer
Visiting Professor
Mech. and Aero. Engineering

Bassem El-Dasher
Structural Materials Engineer
Lawrence Livermore National
Laboratory

Approved by:

Knox Millsaps, Chair, Department of Mech. and Aero. Engineering

Approved by:

Douglas Hensler, Provost

THIS PAGE INTENTIONALLY LEFT BLANK

ABSTRACT

A comprehensive set of processing, microstructure, and material property relationships is presented for friction stir welded oxide dispersion strengthened MA956 steel. Eight rotational and traverse speed combinations were used to produce friction stir welds on MA956 plates using a polycrystalline cubic boron nitride tool. Weld parameters with high thermal input produced defect-free, full penetration welds.

Microstructural analysis showed a significant increase in grain size, a persistent body centered cubic torsional texture in the stir zone, a sharp transition in grain size from the thermo-mechanically affected zone into the stir zone, and an asymmetric reduction in hardness across the weld, all of which were sensitive to weld parameters. Oxide particles were significantly coarsened by friction stir welding resulting in a complete loss of particle strengthening.

Base metal MA956 mechanical properties were determined up to 600°C and the effect of friction stir welding on these properties was directly correlated to the evolved microstructure. Grain refinement is a dominant strengthening mechanism in the base metal and for all friction stir welding conditions, as the welding process removed essentially all dislocation and dispersion strengthening contributions. Friction stir welded MA956 retains a majority of its high temperature strength, making the alloy and joining method a suitable candidate for a structural material in advanced nuclear reactor designs.

THIS PAGE INTENTIONALLY LEFT BLANK

TABLE OF CONTENTS

I.	INTRODUCTION.....	1
A.	MOTIVATION: THE IMPORTANCE AND REQUIREMENTS OF STRUCTURAL MATERIALS FOR NUCLEAR POWER	1
1.	Historical Perspective of Materials in Nuclear Reactors	3
2.	Material Requirements for Nuclear Energy Applications	6
B.	CANDIDATE ALLOYS FOR FUTURE REACTOR DESIGNS	12
C.	REVIEW OF OXIDE DISPERSION STRENGTHENED STEELS	14
1.	Manufacturing Review	14
2.	Examples of Oxide Dispersion Strengthened Steels	16
3.	Oxide Dispersion Strengthened Steel MA956	20
a.	<i>History</i>	<i>20</i>
b.	<i>MA956 Used in this Research</i>	<i>22</i>
D.	JOINING OF OXIDE DISPERSION STRENGTHENED STEELS.....	23
1.	Traditional Fusion Welding Techniques	23
2.	Non-traditional Joining Techniques.....	24
3.	Friction Stir Welding, a Solid-State Joining Technique	25
a.	<i>Background</i>	<i>25</i>
b.	<i>Modeling.....</i>	<i>29</i>
c.	<i>Friction Stir Welding on Oxide Dispersion Strengthened Steels</i>	<i>37</i>
d.	<i>Friction Stir Welding Techniques Used in this Research</i>	<i>38</i>
E.	RESEARCH TASKS AND HYPOTHESES	40
F.	CHAPTER OUTLINES	44
II.	PROCESSING-MICROSTRUCTURE RELATIONSHIPS FOLLOWING FRICTION STIR WELDING	47
A.	INTRODUCTION.....	47
B.	EXPERIMENTAL PROCEDURE.....	48
C.	RESULTS	56
1.	Base Metal Microstructure	56
2.	Weld Consolidation.....	58
3.	Stir Zone Microstructure	62
4.	Thermo-Mechanically Affected Zone	71
D.	DISCUSSION	73
1.	Weld Consolidation.....	73
2.	Grain Growth in the Stir Zone	74
3.	Texture Development in the Stir Zone.....	76
4.	Hardness Analysis.....	77
E.	CONCLUSIONS	81
III.	OXIDE PARTICLE COARSENING DURING FRICTION STIR WELDING.....	83
A.	INTRODUCTION.....	83

B.	EXPERIMENTAL PROCEDURE.....	86
1.	Microscopy techniques	87
2.	X-ray Energy dispersive spectroscopy techniques.....	90
C.	RESULTS	95
1.	Base Metal Particle Distribution	95
2.	Stir Zone Particle Distribution	98
3.	Thermo-Mechanically Affected Zone Distribution.....	104
4.	Oxide Particle Phase Determination	105
D.	DISCUSSION	116
1.	Oxide Particle Coarsening	116
2.	Titanium Particle Effects	119
3.	Proposed Coarsening Mechanisms.....	119
E.	CONCLUSIONS	128
IV.	MATERIAL PROPERTIES AND STRENGTHENING MECHANISMS FOLLOWING FRICTION STIR WELDING.....	129
A.	INTRODUCTION.....	129
B.	EXPERIMENTAL PROCEDURE.....	130
1.	Tensile Specimen Design	132
2.	Finite Element Verification of Design	136
3.	Initial Tensile Testing Setup	149
4.	Experimental Verification of Design.....	161
5.	Final Tensile Setup.....	162
6.	Fractography	164
C.	RESULTS	165
1.	Base Metal Tensile Behavior.....	165
2.	Tensile Behavior of the Stir Zone in Friction Stir Welded Material.....	169
3.	Thermo-Mechanically Affected Zone	174
D.	DISCUSSION	175
1.	Temperature Effects	178
2.	Friction Stir Welding Effects	178
3.	Strengthening Mechanisms	181
4.	Relationship to Hardness	185
E.	CONCLUSIONS	189
V.	LIQUID METAL EMBRITTLEMENT OF MA956.....	191
A.	INTRODUCTION.....	191
B.	EXPERIMENTAL PROCEDURE.....	197
C.	RESULTS	208
1.	U-bend Results	208
2.	Slow Strain Rate Testing Results.....	210
a.	1018 Steel Results.....	212
b.	SS316 Results	215
c.	MA956 Results	219
D.	DISCUSSION	224
E.	CONCLUSIONS	227

VI.	CONCLUSIONS AND RELEVANCE OF THIS RESEARCH	229
A.	CONCLUSIONS	229
B.	RELEVANCE	231
C.	RECOMMENDATIONS FOR FUTURE WORK.....	235
APPENDIX A		237
APPENDIX B		245
APPENDIX C		253
APPENDIX D		259
APPENDIX E		263
LIST OF REFERENCES		267
INITIAL DISTRIBUTION LIST		287

THIS PAGE INTENTIONALLY LEFT BLANK

LIST OF FIGURES

Figure 1.1	Maximum alloy use temperature development over time showing a consistent increase in material property performance from Zinkle [from 1]. T22, T9, T91, E911, NF12, NF616, and SAVE12 are all Ferritic or Martensitic steels with variations in alloy concentrations and manufacturing techniques. Similarly HCM12 and HCM12A are High Chromium Martensitic steels.	2
Figure 1.2	Operating temperature windows for refractory alloys, oxide dispersion strengthened steels, ferritic martensitic steels, SiC composites, annealed and aged CuNiBe, and traditional stainless steels alloys from Zinkle [from 11].	2
Figure 1.3	Yield strength as a function of temperature for candidate structural materials in the Laser Inertial Fusion Energy program from Farmer [from 18].	7
Figure 1.4	Overview of operating temperatures and displacement damage dose regimes for structural materials in current and future fission and fusion reactors from Zinkle [from 1]. The six fission based systems are: Very High Temperature Reactor (VHTR), Super Critical Water Reactor (SCWR), Lead Fast Reactor (LFR), Gas Fast Reactor (GFR), Sodium Fast Reactor (SFR), and Molten Salt Reactor (MSR).	10
Figure 1.5	Scanning electron micrographs of (a) pre-alloyed powders and (b) as milled powders for a nominal oxide dispersion strengthened steel from Zhou [from 51].	15
Figure 1.6	Simplified block diagram of a typical mechanical alloying process.	16
Figure 1.7	Comparison plot of yield strength as a function of test temperature for five oxide dispersion strengthened steels from Klueh [from 55].	20
Figure 1.8	Schematic drawing of friction stir welding from Mishra [from 121].	27
Figure 1.9	Typical macrograph of friction stir weld from Mishra [from 121]. The alloy shown is AA7075.	28
Figure 1.10	Different stir zone shapes from Mishra [from 121] showing: (a) basin shaped SZ and (b) elliptical shaped stir zone. The alloy in both images is AA356 and the only difference between the two is differences in welding rotational and traverse speeds.	28
Figure 1.11	Tool torque versus weld pitch during friction stir welding of aluminum [from 148].	32
Figure 1.12	Effect of tool rotation rate/traverse speed ratio (defined as heat index in this research) on peak temperature for three different aluminum alloys from Hashimoto [from 140].	34
Figure 1.13	Typical heating and cooling rates during friction stir welding from [from 149] during friction stir welding of NiAl bronze plates with embedded thermocouples (TC).	35

Figure 1.14	Friction stir welding tool used in this research. The tool is fabricated using a MS80 grade polycrystalline cubic boron nitride and includes a convex scroll shoulder and step spiral pin.	39
Figure 1.15	Example of a MA956 friction stir welded plate used in this research. Due to limited availability of MA956, single bead-on-plate runs with varying welding conditions were performed on individual plates.	39
Figure 1.16	Weld orientation.....	40
Figure 1.17	Flowchart breakdown of tasks and hypotheses for this research.	42
Figure 1.18	Block diagram outline of chapters in this dissertation.....	45
Figure 2.1	Initial MA956 plate used for friction stir welding consolidation analysis. The white annotations in this image indicate the welding parameters used in English Engineering units of revolutions per minute and inches per minute. The purple outlines indicate areas of optical microscopy samples used in other figures of this chapter.	49
Figure 2.2	Subsequent MA956 plate used for friction stir welding analysis. Annotations in this image indicate the welding parameters used in English Engineering units. The transverse sections for optical microscopy specimens are visible from three different welding conditions. This friction stir welded plate of MA956 is the basis for data in Chapters II, III, and IV of this dissertation.	50
Figure 2.3	MA956 plate used from previous collaborative research. This friction stir welded plate utilized the low heat input conditions of 275 RPM and 100 MMPM and was only used for microstructural analysis and hardness determination of that condition in this chapter.	50
Figure 2.4	(a) HVS-1000 microhardness tester used in this research, (b) specimens from Figure 2.2 used for micro-indentation, and (c) a typical indentation as seen through the indenter.....	53
Figure 2.5	Optical micrograph of the thermo-mechanically affected zone for the 500 RPM/25 MMPM condition showing the vertical and horizontal spacing used for indentation. The inset area corresponds to Figure 2.6.	55
Figure 2.6	Optical micrograph taken through the HVS-1000 microhardness tester showing the large vertical and horizontal gradients in hardness in the vicinity of the thermo-mechanically affected zone. This area correlates to the inset area on Figure 2.5.	55
Figure 2.7	Micro-indentation test area used to verify that the proximity of indentations did not adversely affect indentation accuracy. The left most, right most, and center indentations in the lines A, B, and C all had hardness values within the accuracy of the indenter.....	56
Figure 2.8	Inverse pole figure map for base metal MA956 showing sub-micron grains oriented in the rolling direction of the plate.....	57
Figure 2.9	Pole figures for base metal MA956 corresponding to rolled texture for a body centered cubic structure.	57
Figure 2.10	Friction stir welding parameter map illustrating weld parameters for defect-free welds. The dotted line is illustrative of an estimated minimum process parameters achieve weld consolidation. Green triangles represent	

	typical high heat input conditions used during friction stir welding of similar oxide dispersion strengthened steels in the current literature.	60
Figure 2.11	Optical macrographs of transverse metallographic cross-sections for (a) 400 RPM/100 MMPM and (b) 500 RPM/25 MMPM weld parameter combinations showing full penetration defect-free welds and (c) 300 RPM/100 MMPM and (d) 300 RPM/150 MMPM combinations showing tunnel defects.	61
Figure 2.12	Inverse pole figure maps for (a) 275 RPM/100 MMPM (HI=2.75), (b) 400 RPM/100 MMPM (HI=4), (c) 300 RPM/50 MMPM (HI=6), and (d) 500 RPM/25 MMPM (HI=10) showing increase in grain size as HI is increased during friction stir welding.	63
Figure 2.13	Stir zone grain size distribution for different friction stir welding parameters.	63
Figure 2.14	Average grain diameter for 500 RPM/25 MMPM weld parameter condition along the mid-plane of the weld.	64
Figure 2.15	Stir zone grain size maps for (a) 275 RPM/100 MMPM, (b) 300 RPM/50 MMPM, (c) 400 RPM/100 MMPM, and (d) 500 RPM/25 MMPM combinations. Bold/red lines indicate low angle grain boundaries ($1 < \theta < 10$ degrees). Black lines indicate high angle grain boundaries ($\theta > 10$ degrees). ...	65
Figure 2.16	Hardness profile across the stir zone for varying friction stir welding parameters.	66
Figure 2.17	Inverse pole figure map and correlated micro-hardness indentation image showing large gradients in hardness in the thermo-mechanically affected zone.	67
Figure 2.18	Hardness profile as a function of depth along each vertical line in the weld for 500 RPM/25 MMPM weld parameters for the retreating side (blue), stir zone (red), and advancing side (green).	68
Figure 2.19	Hardness profile as a function of depth along each vertical line in the weld for 300 RPM/50 MMPM weld parameters for the retreating side (blue), stir zone (red), and advancing side (green).	69
Figure 2.20	Hardness profile as a function of depth along each vertical line in the weld for 400 RPM/100 MMPM weld parameters for the retreating side (blue), stir zone (red), and advancing side (green).	70
Figure 2.21	Pole figures for (a) 275 RPM/100 MMPM, (b) 300 RPM/50 MMPM, (c) 400 RPM/100 MMPM, and (d) 500 RPM/25 MMPM welding conditions showing a persistent BCC torsional texture following friction stir welding. ..	71
Figure 2.22	Stir zone to thermo-mechanically affected zone interfaces on the advancing side of the weld for (a) 400 RPM/100 MMPM, (b) 300 RPM/50 MMPM, and (c) 500 RPM/25 MMPM conditions showing the increase in microstructural gradient as a function of HI.	72
Figure 2.23	Representation of inverse pole figure maps across the weld nugget for 500 RPM/25 MMPM. The same 100 micron scale bar applies to all maps.	73
Figure 2.24	Stir zone texture shown with overlaid ideal BCC torsional texture from Baczynski [after 165]. Annotations from Baczynski: $D1-[1\ 1\ \bar{2}]<111>$	

	(triangles), $D2-\overline{[1\ 1\ 2]}<111>$ (squares), $E1-[0\ 1\ \overline{1}]<111>$ (inverted triangles), and $E2-[0\ \overline{1}\ 1]<111>$ (circles). The orientation of this pole figure corresponds to the shear plane between the friction stir welding tool and the workpiece.	77
Figure 2.25	(a) Horizontal and (b) vertical gradients in hardness at the advancing side thermo-mechanically affected zone for the 500 RPM/25 MPM welding combination.....	78
Figure 2.26	Application of the Hall-Petch equation using hardness and grain size following friction stir welding. The base metal condition (red) does not correlate with the Hall-Petch line. The y-axis is broken to show the base metal condition without vertical compression of the remaining data.	80
Figure 3.1	(a) Secondary electron microscopy image showing Y-Al-O particles distributed homogenously in MA956 following friction stir welding and (b) subsequent image created by Woertz's MATLAB code for optical counting techniques [after 176].	88
Figure 3.2	Energy spectrum typical of the base matrix for MA956.....	91
Figure 3.3	Energy spectrum typical of a complex Y-Al-O particle (white on inset) within MA956 following FSW.	91
Figure 3.4	Energy spectrum typical of a TiCN particle (black on inset) within MA956.	92
Figure 3.5	Phase diagram of the alumina-rich portion of the Al_2O_3 - Y_2O_3 system from Caslavsky [from 179].....	94
Figure 3.6	Scanning electron microscopy imagery of base metal MA956 with energy dispersive x-ray spectroscopy spectra showing (a) Al-O particles (white) and (b) TiCN particles (dark) uniformly distributed in the base metal.....	96
Figure 3.7	Scanning transmission electron microscopy image of base metal MA956 showing fine grains, nano-scale particles (small dark particles), and large dislocation densities in the base metal.	97
Figure 3.8	Small angle x-ray scattering data for base metal MA956.....	98
Figure 3.9	Scanning electron microscopy imagery of the stir zone for 500 RPM/25 MPM friction stir welding combination with energy dispersive x-ray spectroscopy spectra showing (a) coarsened Y-Al-O particles (white) and (b) similar sized TiCN particles (dark) uniformly distributed in the base metal.....	99
Figure 3.10	Scanning transmission electron microscopy imagery of the stir zone for 300 RPM/50 MPM friction stir welding combination showing grain growth, oxide particle coarsening, and reduction in dislocation density following friction stir welding.	100
Figure 3.11	Scanning electron microscopy image comparison of (a) BM, (b) 400 RPM/100 MPM, (c) 300 RPM/50 MPM, and (d) 500 RPM/25 MPM showing oxide particle coarsening following friction stir welding..	101
Figure 3.12	Scanning electron microscopy imagery and energy dispersive x-ray spectroscopy spectral maps for yttrium (left side-yellow), aluminum (center-blue), and titanium (right side-purple) for (a) base metal, (b) 400	

	RPM/100 MPPM (low heat input), and (c) 500 RPM/25 MPPM (high heat input) showing increasing oxide particle coarsening as heat input was increased during friction stir welding.	102
Figure 3.13	Small angle x-ray scattering data from the stir zone material for friction stir welding conditions.	103
Figure 3.14	Gradients in (a) oxide particle size, (b) grain size, and (c) hardness at the advancing side thermo-mechanically affected zone (top left) for the 500 RPM/25 MPPM parameter combination. Dotted lines on (a) and (b) are illustrative of the separation that exists at the thermo-mechanically affected zone. The annotation on the hardness graph (c) indicates the approximate area for the images in (a) and (b).	104
Figure 3.15	(a) Oxide particle size, (b) grain size, and (c) hardness at the retreating side thermo-mechanically affected zone (bottom right) for the 500 RPM/25 MPPM parameter combination. The annotation on the hardness graph (c) indicates the approximate area for the images in (a) and (b).	105
Figure 3.16	Scanning electron microscopy image of the stir zone from the high heat input condition (500 RPM/25 MPPM) showing particles analyzed by energy dispersive x-ray spectroscopy. Particle numbering refers to Table 3.3.	106
Figure 3.17	Energy dispersive line scan across an yttrium aluminum garnet particle in the stir zone of the high heat input condition. The inset area corresponds to Figure 3.16 and depicts the orientation of the scan.	108
Figure 3.18	Energy dispersive line scan across an yttrium aluminum monoclinic particle in the stir zone of the high heat input condition. The inset area corresponds to Figure 3.16 and depicts the orientation of the scan.	109
Figure 3.19	Energy spectrum for a yttrium aluminum garnet particle from experimental data from the EDAX Genesis software and theoretical simulations using DTSA-II.	110
Figure 3.20	Energy spectrum for a yttrium aluminum monoclinic particle from experimental data from the EDAX Genesis software and theoretical simulations using DTSA-II.	111
Figure 3.21	Scanning electron microscopy image of the stir zone from the low heat input condition (400 RPM/100 MPPM) showing particles analyzed by energy dispersive x-ray spectroscopy. Particle numbering refers to Table 3.4.	112
Figure 3.22	Energy dispersive line scan across a yttrium aluminum garnet particle in the stir zone of the low heat input condition. The inset area corresponds to Figure 3.21 and depicts the orientation of the scan.	114
Figure 3.23	Energy dispersive line scan across an indeterminate particle in the stir zone of the low heat input condition. The inset area corresponds to Figure 3.21 and depicts the orientation of the scan.	115
Figure 3.24	Energy dispersive line scan across an indeterminate particle in the stir zone of the low heat input condition. The inset area corresponds to Figure 3.22 and depicts the orientation of the scan.	116

Figure 3.25	Visualization of (a) oxide particle distribution in the base metal, (b) theoretical oxide particle coarsening predicted by Ostwald ripening alone, and (c) experimental oxide particle coarsening seen in this research. Grain and oxide particle sizes are not to scale and are meant to be an approximation of data previously reported.	124
Figure 3.26	Summary of oxide particle coarsening observed in this research.	127
Figure 4.1	Summary of materials and geometries used in this research with corresponding description of use discussed in Table 4.1.	132
Figure 4.2	(a) Miniature tensile specimen geometry used for all MA956 tensile test data in this research and (b) SolidWorks image to scale of the same geometry overlaid with a machinable new geometry with an increased radius of curvature and narrower gage section.	135
Figure 4.3	Tensile specimens fractured from the original miniature tensile geometry (left) and increased radius of curvature tensile geometry (right) all showing proper fracture in the gage section. Based on these results, the increased radius of curvature sample (right) was deemed not required.	135
Figure 4.4	ANSYS modeling results showing stress distribution in a tensile specimen with no fillet between grip and gage sections.	138
Figure 4.5	ANSYS modeling results showing high stress concentration at the intersection between the grip and gage section.	139
Figure 4.6	ANSYS modeling results of a miniature rectangular tensile specimen used to evaluate nanostructured metals and alloys [after 189] showing a low stress concentration due to the fillet between the grip and gage section.	141
Figure 4.7	ANSYS modeling results for the AA5052 sample used in this research (Figure 4.1d).	142
Figure 4.8	ANSYS modeling results for the standard miniature tensile sample used throughout this research (Figure 4.1b).	143
Figure 4.9	ANSYS modeling results for the new increased radius of curvature miniature tensile sample analyzed in this research (Figure 4.1a).	144
Figure 4.10	(a) Cutaway SolidWorks model showing bolt restraint and seating restraint and (b) photograph of a tensile specimen fully assembled in its grips showing grip compression restraint.	146
Figure 4.11	ANSYS finite element models showing non-uniform stress distribution in the gage section when using bolt restraint alone.	147
Figure 4.12	ANSYS finite element models showing uniform stress distribution in the gage section when using both bolt and seating restraint.	148
Figure 4.13	(a) Standard tensile testing setup used for miniature tensile specimens and (b) close up view of the specimen area.	150
Figure 4.14	Tensile testing setup used for AA1100 and AA5052 specimens.	150
Figure 4.15	(a) Standard miniature tensile setup, (b) upper section grip slippage locations (red circles), and (c) lower section grip slippage locations (red circles).	151
Figure 4.16	Raw MA956 data showing (a) load drops due to grip slippage in the elastic region and (b) smooth elastic region for the sample alloy and geometry with preload applied to prevent grip slippage.	151

Figure 4.17	AA5052 specimen instrumented with a strain gage to measure strain vice using crosshead speed.	153
Figure 4.18	(a) Front and (b) side views of a SS316 specimen instrumented with a strain gage to measure strain vice using crosshead speed.....	154
Figure 4.19	Data from AA5052 tensile test showing the improved response in the elastic region when using a strain gage. The strain gage fell of the sample shortly after the yield point due to specimen elongation. The difference in the slopes of these two lines is due to machine compliance.	154
Figure 4.20	Comparison plots of AA5052 yield strength calculation using (a) a strain gage to measure strain and (b) crosshead speed to measure strain that show a negligible difference in measured yield strength.	155
Figure 4.21	Use of a strain gage to calculate and adjust for machine compliance that includes: (a) simple modeling as a two spring system, (b) calculation of machine modulus from experimentally measured data, and (c) adjustment of stress strain curves removing machine compliance.....	156
Figure 4.22	Data from SS316 tensile test showing the improved response in the elastic region when using a strain gage. The strain gage fell of the sample shortly after the yield point due to specimen elongation. The difference in the slopes of these two lines is due to machine compliance.	157
Figure 4.23	Comparison plots of SS316 yield strength calculation using (a) a strain gage to measure strain and (b) crosshead speed to measure strain that show a negligible difference in measured yield strength.	158
Figure 4.24	Typical raw data from a MA956 tensile test using the experimental methods developed.....	159
Figure 4.25	Summary of data reduction steps for all SS316 and MA956 tensile tests in this chapter. These steps included: (a) recording of raw data, (b) determination of the slope of the elastic region (note: this is the equivalent response), (c) application of a foot correction and elimination of data beyond fracture, (d) calculation of the 0.2% offset yield strength, and finally (e) removal of machine compliance in the elastic region. All vertical axis shown are Engineering Stress in MPa and all horizontal axis are Engineering Strain in mm/mm.....	160
Figure 4.26	Stress strain curves for five identically tested SS316 specimens showing limited variation in experimental results.....	162
Figure 4.27	Tensile specimen geometry (gage section measurements: length=12.7 mm, width=5.08 mm, and thickness=1.09 mm) shown with corresponding location with respect to welded MA956 plate.	163
Figure 4.28	Engineering stress-strain curves for base metal MA956 at various temperatures.....	165
Figure 4.29	Fractography of (a) base metal MA956 and (b) SS316 at room temperatures showing the brittle behavior of MA956 at room temperature..	166
Figure 4.30	Fractography of base metal MA956 at (a) 400C and (b) 600C showing the change in fracture mode from brittle to ductile of MA956 at elevated temperatures compared to the brittle fracture at room temperature in Figure 4.29.	167

Figure 4.31	True stress-strain curves for base metal MA956 at various temperatures. True stress-strain values were calculated from the engineering stress-strain values (Figure 4.28) to the onset of necking allowing for calculation of strain hardening exponent (n).	168
Figure 4.32	Strain hardening exponent (n) and strain hardening coefficient (k) as a function of temperature for base metal MA956 using the Holloman equation (Equation 4.1).....	169
Figure 4.33	Room temperature engineering stress-strain curves for base metal MA956 and friction stir welded MA956 showing a reduction in strength and increase in ductility following friction stir welding.....	170
Figure 4.34	Engineering stress strain curves of friction stir welded MA956 at 600°C. ...	171
Figure 4.35	Fractography of MA956 at room temperature for (a) base metal, (b) low heat input condition (400 RPM/100 MPM) and (c) high heat input condition (500 RPM/25 MPM).	173
Figure 4.36	Fractography of MA956 friction stir welded with high heat input conditions (500 RPM/25 MPM) fractured in tension at 600C showing the largest amount of ductility corresponding to the highest test temperature and highest heat input condition.	174
Figure 4.37	(a) Failure in the stir zone for the high heat input condition (500 RPM/25 MPM) as opposed to failure at the advancing side as hypothesized in Chapter II with (b) corresponding inverse pole figure maps at each location from Chapter II for reference.	175
Figure 4.38	MA956 tensile specimens after fracture showing qualitative changes in ductility for different conditions.	176
Figure 4.39	Yield and ultimate strengths of fine grain unrecrystallized MA956 with comparison to manufacture's specifications for coarse grain recrystallized MA956 [after 93] (error bars show 5% variation based on SS316 test results).....	177
Figure 4.40	Percent elongation of fine grain unrecrystallized MA956 with comparison Special Metals manufacture specifications of coarse grain recrystallized MA956 [after 93] (error bars show 5% variation based on SS316 test results).....	177
Figure 4.41	Yield strength versus temperature for consolidated friction stir welded conditions. The softening effect of FSW is less evident at high temperature.	179
Figure 4.42	Scanning electron microscopy backscatter images of (a) base metal MA956 and (b) friction stir welded MA956 with high heat input (500 RPM/25 MPM) showing grain and oxide particle coarsening following friction stir welding.	180
Figure 4.43	Scanning transmission electron microscopy images of (a) base metal MA956 and (b) friction stir welded MA956 with low heat input (300 RPM/50 MPM) showing a qualitative increase in grain size and reduction in dislocation density following friction stir welding.	181
Figure 4.44	Hall Petch plot of MA956 with varying grain size achieved by friction stir welding. The difference in strength of the base metal compared to the	

	Hall Petch line is attributed to changes in particle and dislocation strengthening mechanisms.....	183
Figure 4.45	Comparison of hardness Hall-Petch data from Chapter II (Figure 2.26) and yield strength Hall-Petch data from Chapter IV (Figure 4.44).	186
Figure 5.1	Oxygen concentration effect on corrosion of steels in molten lead from Zhang [from 193].	192
Figure 5.2	Typical ductility trough for a liquid metal embrittlement couple from Nicholas [from 155]. T_E is defined as the temperature corresponding to the onset of the reduction in ductility and T_R is defined as the temperature corresponding to the recovery of ductility.	194
Figure 5.3	Ductility trough observed during liquid metal embrittlement of a silicon enriched steel in lead-bismuth eutectic from Van den Bosch [from 202]. Full black symbols represent results in lead-bismuth eutectic. Empty white symbols represent results in inert gas (Argon). Triangles represent uniform strain. Diamonds represent total strain.....	196
Figure 5.4	MA956 U-bend specimens in (a) unloaded condition and (b) fully loaded condition.	198
Figure 5.5	Equivalent stress distribution in U-bend specimens.	199
Figure 5.6	(a) Melting pot used for liquid lead exposure of U-bend specimens and (b) top view of melting pot showing thin layer of lead oxide (brown) on top of pure molten lead (silver). In (b) the lead oxide has been manually moved to reveal the pure molten layer beneath.	200
Figure 5.7	Oxygen solubility in lead, LBE, and bismuth from Zhang [from 195].	201
Figure 5.8	(a) Photograph of lead containment apparatus for standard miniature geometry (Figure 4.1b), (b) Photograph of lead containment apparatus for long miniature geometry (Figure 4.1c), and (c) cutaway SolidWorks model of the lead containment apparatus.....	205
Figure 5.9	SolidWorks images showing assembly of the lead containment apparatus....	205
Figure 5.10	Liquid metal embrittlement tensile testing setup (a) at room temperature with solid form embrittler (lead as shown) and (b) at operating temperature (328°C) with molten embrittler (lead with lead oxide layer as shown).....	207
Figure 5.11	Photographs of MA956 U-bend specimens (a) loaded prior to lead exposure, and (b), (c) after exposure to lead at 350°C for 300 hours. The lead (silver) and lead oxide (red) was allowed to solidify on the specimen after exposure but readily spalled off the sample.	209
Figure 5.12	Energy dispersive spectroscopy analysis of oxide layers on the outer surface of the MA956 U-bend specimens after exposure to molten lead. The line scan correlates to measurement across the cross section of the specimen at the apex of curvature of the specimen as shown.....	210
Figure 5.13	Blue brittleness of SS316 for the geometries used in this chapter. Both samples were fractured under identical conditions in air except: (a) 328°C and (b) room temperature.....	211
Figure 5.14	Engineering stress-strain curves for 1018 steel in air and molten lead both at 328°C showing similar tensile behavior.	212

Figure 5.15	Fractography of 1018 steel fractured in (a) air at 328°C and (b) molten lead at 328°C showing similar failure.....	213
Figure 5.16	Engineering stress-strain curves for 1018 steel in air and molten LBE both at 150°C showing similar tensile behavior.	214
Figure 5.17	Fractography of 1018 steel fractured in (a) air at 150°C and (b) molten lead-bismuth eutectic at 150°C showing similar failure.	215
Figure 5.18	Engineering stress-strain curves for SS316 in air and molten lead both at 328°C showing similar tensile behavior.	216
Figure 5.19	Fractography of SS316 fractured in (a) air at 328°C and (b) molten lead at 328°C showing similar failure.	217
Figure 5.20	Engineering stress-strain curves for SS316 in air and molten LBE both at 150°C showing similar tensile behavior.	218
Figure 5.21	Fractography of SS316 fractured in (a) air at 150°C and (b) molten LBE at 150°C showing similar failure.	219
Figure 5.22	Engineering stress-strain curves for MA956 in air and molten lead both at 328°C showing similar tensile behavior.	220
Figure 5.23	Fractography of MA956 fractured in (a) air at 328°C and (b) molten lead at 328°C showing similar failure.	221
Figure 5.24	Engineering stress-strain curves for MA956 in air and molten LBE both at 150°C showing similar tensile behavior.	222
Figure 5.25	Fractography of MA956 fractured in (a) air at 150°C and (b) molten lead-bismuth eutectic at 150°C showing similar failure.	223
Figure 6.1	Simplified summary of microstructural effects of FSW on MA956 with a fine grain starting microstructure.	233
Figure 6.2	Simplified summary of material properties and microstructure for a composite MA956 weld structure.	234
Figure A.1	MA956 Plate-1.....	237
Figure A.2	MA956 Plate-2.....	238
Figure A.3	MA956 Plate-3.....	239
Figure A.4	MA956 Plate-4.....	240
Figure A.5	MA956 Plate-5.....	241
Figure A.6	MA956 Plate-6.....	242
Figure A.7	MA956 Plate-7.....	243
Figure B.1	Optical macrograph for 200 RPM/50 MPM.....	245
Figure B.2	Optical macrograph for 300 RPM/50 MPM.....	246
Figure B.3	Optical macrograph for 300 RPM/100 MPM.....	247
Figure B.4	Optical macrograph for 300 RPM/150 MPM.....	248
Figure B.5	Optical macrograph for 400 RPM/50 MPM.....	249
Figure B.6	Optical macrograph for 400 RPM/100 MPM.....	250
Figure B.7	Optical macrograph for 400 RPM/175 MPM.....	251
Figure B.8	Optical macrograph for 500 RPM/25 MPM.....	252
Figure C.1	Engineering drawing for miniature tensile specimen (standard).	253
Figure C.2	Engineering drawing for miniature tensile specimen (narrow).	254
Figure C.3	Engineering drawing for miniature tensile specimen (long).....	255
Figure C.4	Engineering drawing for AA5052 specimen.	256

Figure C.5	Engineering drawing for AA1100 specimen.	257
Figure D.1	ANSYS meshing used for AA5052 specimen.	259
Figure D.2	ANSYS application of restraints and forces for AA5052 specimen.....	259
Figure D.3	ANSYS meshing used for miniature tensile specimen geometry (standard).260	
Figure D.4	ANSYS application of restraints and forces for miniature tensile specimen geometry (standard).	260
Figure D.5	ANSYS meshing used for miniature tensile specimen geometry (narrow)...261	
Figure D.6	ANSYS application of restraints and forces for miniature tensile specimen geometry (narrow).	261
Figure D.7	ANSYS application of restraints and forces for U-bend specimen.	262
Figure E.1	Engineering drawing for large containment apparatus.	263
Figure E.2	Engineering drawing for small containment apparatus.	264
Figure E.3	Engineering drawing for gasket used in containment apparatus.	265

THIS PAGE INTENTIONALLY LEFT BLANK

LIST OF TABLES

Table 1.1	Power reactors by type worldwide as of December 2011 [after 12].....	4
Table 1.2	Reactor environments and materials for fission and advanced fission reactor concepts from Zinkle [after 13].	5
Table 1.3	Comparison of ODS and non-ODS steels used in high temperature energy applications. All alloys shown have a remaining balance of Fe.	17
Table 1.4	Chemical Composition of MA956 (wt%) used in this research.	23
Table 2.1	Friction stir welding parameter summary. Shaded entries indicate defect-free consolidated welds.....	59
Table 2.2	Stir zone hardness and stir zone grain size diameter for friction stir welding parameter conditions.	66
Table 3.1	Proposed oxide formation reactions from Hsiung [after 37].	85
Table 3.2	Parameters used for DTSA-II simulation	94
Table 3.3	Theoretical yttrium to aluminum intensity ratio ($IR_{Y/Al}$) and yttrium to aluminum atom ratio ($AR_{Y/Al}$) values for Yttrium Aluminum Monoclinic (YAM), Yttrium Aluminum Perovskite (YAP), and Yttrium Aluminum Garnet (YAG) as determined by DTSA-II software and stoichiometric relationships respectively.....	95
Table 3.4	Parameters used to identify phase of complex Y-Al-O particles in friction stir welds with high heat input parameters.	107
Table 3.5	Parameters used to identify phase of complex Y-Al-O particles in friction stir welds with low heat input parameters.....	113
Table 3.6	Oxide particle density (N), average particle diameter (d_{avg}), and inter-particle spacing (S) for different friction stir welding conditions for the same sample area.	118
Table 3.7	Evaluation of Ostwald ripening by comparison of oxide particle parameters for base metal and stir zone of high heat input condition.	123
Table 3.8	Evaluation of Ostwald ripening by comparison of oxide particle parameters for stir zones of low heat input and high heat input conditions. .	123
Table 4.1	Summary of materials and geometries of tensile specimens used in this research.	133
Table 4.2	Variability of SS316 tensile testing at room temperature showing less than 5% variation in tensile parameters for the given experimental setup.	162
Table 4.3	Summary of processing, microstructure, and material property relationships of MA956 at room temperature following friction stir welding with varying process parameters.....	181
Table 4.4	Theoretical strengthening contributions used by other authors for MA956 prior to FSW (σ_O -Peierls-Nabarro stress, σ_{SS} -strengthening contribution from solid solution strengthening, σ_P -strengthening contribution from particle strengthening, and σ_D - strengthening contribution from dislocation strengthening). Contribution from grain boundary strengthening (σ_{GB}) was calculated by each author using an assumed value of $0.5 \text{ MPam}^{1/2}$ for the Hall-Petch constant, k and varied depending on the grain size.	185

Table 5.1	Summary of conditions used for liquid metal embrittlement experiments....	203
Table 5.2	Summary of conclusions with regard to liquid metal embrittlement susceptibility of alloys tested in this research.....	226

LIST OF ACRONYMS AND ABBREVIATIONS

ANL	Argonne National Laboratory
ASM	American Society for Metals
APPM	Atom Parts Per Million
APT	Atom Probe Tomography
BCC	Body Centered Cubic
BM	Base Metal
BWR	Boiling Water Reactor
CERT	Constant Extension Rate Test
CG	Coarse Grain (grain size $>10\text{ }\mu\text{m}$)
DPA	Displacements Per Atom
DBTT	Ductile-Brittle Transition Temperature
EAC	Environmentally Assisted Corrosion
EBSD	Electron Backscatter Diffraction
EBW	Electron Beam Welding
EDM	Electrical Discharge Machining
ESD	Electro-Spark Deposition
EDS	Energy Dispersive x-ray Spectroscopy
FG	Fine Grain (grain size $\leq 10\text{ }\mu\text{m}$)
FM	Ferritic-Martensitic
FSP	Friction Stir Processing
FSW	Friction Stir Welding
GFR	Gas Fast Reactor
GMA	Gas Metal Arc
GTA	Gas Tungsten Arc
HAGB	High Angle Grain Boundary (misorientation angle $>10^\circ$)
HAZ	Heat Affected Zone
HI	Heat Index
HIP	Hot Isostatic Pressing
HRTEM	High Resolution Transmission Electron Microscopy

HSLA	High-Strength Low-Alloy
HTHX	High Temperature Heat Exchanger
IFMIF	International Fusion Materials Irradiation Facility
INL	Idaho National Laboratory
IPF	Inverse Pole Figure
IPM	Inches Per Minute
LAGB	Low Angle Grain Boundary (misorientation angle $\leq 10^\circ$)
LANL	Los Alamos National Laboratory
LBE	Lead-bismuth Eutectic
LBW	Laser Beam Welding
LFR	Lead Fast Reactor
LIFE	Laser Inertial Fusion Energy
LLNL	Lawrence Livermore National Laboratory
LME	Liquid Metal Embrittlement
MA	Mechanical Alloying
MMPM	Millimeters Per Minute
MSR	Molten Salt Reactor
ND	Normal Direction
NPS	Naval Postgraduate School
NFA	Nanostructured Ferritic Alloy
NIST	National Institute of Standards and Technology
NNPP	Naval Nuclear Propulsion Program
ODS	Oxide Dispersion Strengthened
OIM	Orientation Imaging Microscopy
ORNL	Oak Ridge National Laboratory
PCBN	Polycrystalline Cubic Boron Nitride
PNNL	Pacific Northwest National Laboratory
PM	Powder Metallurgy
PWR	Pressurized Water Reactor
RAFM	Reduced Activation Ferritic/Martensitic
RD	Rolling Direction
RPM	Revolutions Per Minute

SANS	Small Angle Neutron Scattering
SAXS	Small Angle X-ray Scattering
SCC	Stress Corrosion Cracking
SCW	Super Critical Water
SCWR	Super Critical Water Reactor
SEM	Scanning Electron Microscopy
SFR	Sodium Fast Reactor
SSRT	Slow Strain Rate Testing
STEM	Scanning Transmission Electron Microscopy
SZ	Stir Zone
TD	Transverse Direction
TEM	Transmission Electron Microscopy
TLP	Transient Liquid Phase
TMAZ	Thermo-mechanically Affected Zone
TWI	The Welding Institute
UCSB	University of California Santa Barbara
VHTR	Very High Temperature Reactor
WD	Welding Direction
WP	Weld Pitch
YAG	Yttrium Aluminum Garnet
YAH	Yttrium Aluminum Hexagonal
YAM	Yttrium Aluminum Monoclinic
YAP	Yttrium Aluminum Perovskite
YAT	Yttrium Aluminate

THIS PAGE INTENTIONALLY LEFT BLANK

ACKNOWLEDGMENTS

I am very thankful for the guidance, help, and contributions of all my committee members: Professor Garth Hobson, Professor Luke Brewer, Professor Terry McNelley, Professor Joe Hooper, Professor Joe Farmer, and Dr. Bassem El-Dasher. In particular, I would like to specifically thank my advisor, Professor Luke Brewer for his exceptional mentorship over the last three years. The time we have spent together has made me a better student, researcher, and teacher, and for that I am eternally grateful.

I would also like to thank Lawrence Livermore National Laboratory specifically Dr. Mike Dunne, Professor Joe Farmer, and Dr. Bassem El-Dasher for their sponsorship of this research as well as MegaStir and Murray Mahoney for their help on friction stir welding. Having an end goal and practical application is always helpful in keeping work and research on track.

I would also like to thank several staff members of Naval Postgraduate School for their contributions and assistance specifically Professor Sarath Menon for his unparalleled expertise in all areas of microscopy and material preparation, Dr. Chanman Park for his tireless support of all laboratory facilities, and Doug Seivwright for his assistance with instrumentation. I would also like to thank all my fellow Doctoral students past and present. Often our simple discussions lead to the best understanding and most innovative ideas.

Finally, and without equal, I would like to thank my three favorite girls Clarissa, Eva, and Brooke. Without your unending support, patience, and selfless love none of this would have been possible or worthwhile. After over twenty years spanning all corners of the country, it is finally time to go back where it all began.

THIS PAGE INTENTIONALLY LEFT BLANK

I. INTRODUCTION

A. MOTIVATION: THE IMPORTANCE AND REQUIREMENTS OF STRUCTURAL MATERIALS FOR NUCLEAR POWER

One of the most fundamental principles of any energy production process is that the theoretical maximum cyclic efficiency is a function of the highest temperature achievable in the process, typically expressed as the Carnot efficiency (Equation 1.1). This simple theoretical relationship states that for a given sink temperature (T_L) the maximum efficiency of a cyclic process (η_{th}) increases as the source temperature (T_H) is increased. When coupled with the typically observed reduction in strength and overall degradation of thermo-mechanical properties of most structural materials as a function of increasing temperature, this relationship drives the search of alloys, ceramics, or composites that have sufficient material properties to withstand the continuous increase in temperatures desired in advanced thermal energy cycles. Zinkle at Oak Ridge National Laboratory (ORNL) has reviewed the materials challenges in nuclear energy and operating temperatures of nuclear reactor designs covering decades of material development and has shown a steady 2.5°C/year increase of maximum use temperature over time for alloys used in reactor plant designs (Figure 1.1) [1]. The observed trend in increasing maximum operating temperatures of structural materials in Figure 1.1 is a direct result of the desire to increase cyclic efficiencies via the relationship in Equation 1.1. Following a similar perspective Zinkle has developed a widely used operating temperature plot that depicts a variety of traditional and new developmental alloys used or designed for use across a wide range of operating temperatures (Figure 1.2). Despite improvements already made in structural alloy design and manufacture, material development remains one of the key pacing elements for fusion, fission, space based, or other advanced energy production processes [2–10].

$$\eta_{th} = 1 - \frac{T_L}{T_H} \quad \text{Equation 1.1}$$

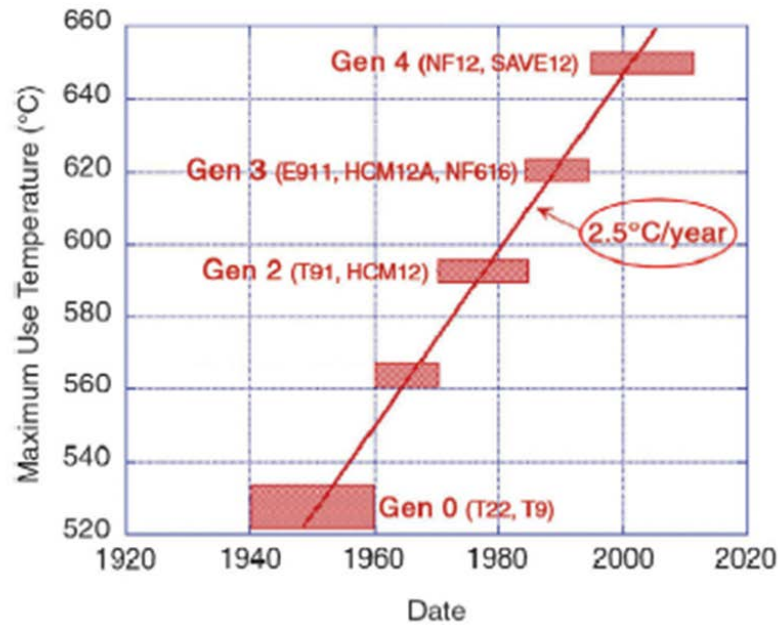


Figure 1.1 Maximum alloy use temperature development over time showing a consistent increase in material property performance from Zinkle [from 1]. T22, T9, T91, E911, NF12, NF616, and SAVE12 are all Ferritic or Martensitic steels with variations in alloy concentrations and manufacturing techniques. Similarly HCM12 and HCM12A are High Chromium Martensitic steels.

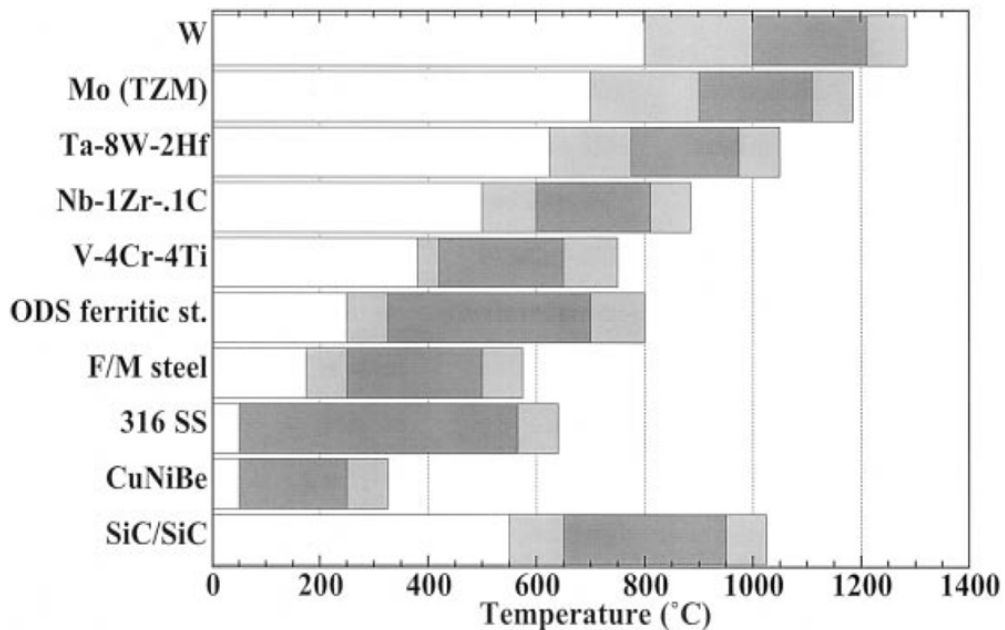


Figure 1.2 Operating temperature windows for refractory alloys, oxide dispersion strengthened steels, ferritic martensitic steels, SiC composites, annealed and aged CuNiBe, and traditional stainless steels alloys from Zinkle [from 11].

1. Historical Perspective of Materials in Nuclear Reactors

As of 2011 nuclear power provides approximately 13% of the electrical power worldwide and has emerged as a reliable source of electricity following over forty years of fission based nuclear plant operation [12]. The United States is the largest producer of power from nuclear energy with 104 reactors operating at 65 sites, producing over 100 GW_e of electricity. These reactors provide approximately 20% of the nation's total electrical energy and account for more than 30% of the worldwide nuclear energy generating capacity [12, 13]. These numbers also do not include the 145 reactors operating on 119 ships in the Naval Nuclear Propulsion Program (NNPP) which have safely steamed over 100,000,000 miles as of 1994 [14].¹ A current summary of reactor types, numbers operating or forthcoming, and net energy production is shown in Table 1.1 [12]. This summary shows the significant preponderance of pressurized water reactors (PWR) in operation but also shows the evolution of advance fission based reactors that include alternate coolants such as superheated gases or liquid metals. Additionally, although no current operational fusion reactor exists, Lawrence Livermore National Laboratory (LLNL) continues to make progress towards achieving a self-sustaining burn wave of fusion fuel producing a net energy gain, a milestone event called ignition, which will help pioneer the next fusion based energy revolution [15].

¹ The number of reactors quoted on ships operating in the NNPP is not intended to be an up-to-date summary at the time of this research, but rather a snapshot summary of reactors and ships operating at the time of the landmark 100,000,000 miles steamed document by the NNPP. Contrastingly, the number of commercial reactors and energy production statistics quoted from *Nuclear News* is intended to be an accurate and current estimate of the commercial impact of fission based nuclear energy.

Table 1.1 Power reactors by type worldwide as of December 2011 [after 12].

Reactor Type	# Units (operating)	Net MW _e	# Units (forthcoming)	Net MW _e	# Units (total)	Net MW _e
Pressurized light-water reactors	267	247,000	89	93,000	356	340,000
Boiling light-water reactors	84	78,300	6	8,000	90	86,300
Gas-cooled reactors	17	8,700	1	200	18	8,900
Heavy-water reactors	51	25,600	8	5,100	59	30,700
Graphite-moderated reactors	15	10,200	0	0	15	10,200
Liquid-metal cooled reactors	1	600	4	1,000	5	1,600
Totals	435	370,000	108	108,000	543	478,000

Common to all operational reactor types listed in Table 1.1 as well as future designs, including fusion reactors, is the extreme environment that structural alloys in these designs are exposed to, including high temperatures, intense neutron radiation spectra, and varied coolant conditions that have necessitated decades of material design. Additionally in several systems the material requirements for first-wall or cladding materials, generally those materials in direct contact with fuel and unshielded from any radiation, differ from requirements for in-core structural material such as pressure vessels, piping systems, or other components generally not in direct contact with fuel. Table 1.2 is a summary of current reactor system designs, their coolants, maximum operating temperature, neutron spectrum including estimated end-of-life radiation damage levels, and structural materials divided into cladding and in-core structural materials [13].

Table 1.2 Reactor environments and materials for fission and advanced fission reactor concepts from Zinkle [after 13].

System	Coolant	Max Temperature (C)	Neutron spectrum, maximum dose (dpa)	Cladding material	In-core structural materials
Pressurized water reactor	Water	320	Thermal, ~80	Zirconium alloys	Stainless steels and nickel alloys
Boiling water reactor	Water	288	Thermal, ~7	Zirconium alloys	Stainless steels and nickel based alloys
Supercritical water cooled reactor	Supercritical water	600	Thermal, ~30 or fast, ~70	Ferritic-martensitic steels, ODS alloys, advanced nickel alloys	Same as cladding
Very high temperature reactor	Helium	1000	Thermal, <20	Silicon or zirconium carbides	Graphites and ferritic-martensitic steels
Gas fast reactor	Helium, supercritical CO ₂	850	Fast, 80	Ceramics	ODS alloys, ceramics, or refractory metals
Sodium fast reactor	Sodium	550	Fast, 200	Ferritic-martensitic steels, ODS alloys	Stainless steels
Lead fast reactor	Lead or lead-bismuth	800	Fast, 150	Ferritic-martensitic steels, ODS alloys, or silicon alloys	Ceramics, refractory alloys, or silicon alloys
Molten salt reactor	Molten salts	1000	Thermal, 200	Not applicable	Nickel based alloys

In addition to listing specifications of different reactor systems and coolant compatibility, Table 1.2 gives insight into the history of nuclear material development as reactor systems have evolved. Zirconium alloys were selected in the early 1950s as part of the NNPP for fuel cladding predominantly because of their very low neutron absorption rate compared to traditional steels despite their higher cost and generally less favorably thermo-mechanical performance compared to iron or nickel based alloys. In early fission reactors, traditional stainless steels, such as 316 stainless steel (SS316), were sufficient for in-core structural materials. Although initially designed for turbine propulsion applications, significant improvements were made in the corrosion resistance of in-core structural materials with advancements in nickel based alloys such as Inconel 600 through Inconel 690 currently produced by Special Metals.² However, the increased maximum temperature range achievable by advanced reactor systems such as super critical water reactors (SCWR), very high temperature reactors (VHTR), and gas fast reactors (GFR) have necessitated improvements in high temperature thermo-mechanical properties of alloys both for cladding and in-core structural materials. Finally, although nickel based alloys have been proven to be effective in current PWRs and boiling water reactors (BWR) for corrosion resistance, nickel based alloys are highly susceptible to radiation swelling and reduction in ductility during high temperature (greater than 400°C) radiation exposure thus making nickel based alloys undesirable in some advanced reactor systems [16, 17].

2. Material Requirements for Nuclear Energy Applications

The most fundamental requirements for any structural material in an application is that the material have sufficient yield strength to avoid deformation to a degree that renders the component no longer serviceable and to avoid yielding or eventual catastrophic fracture. For high temperature applications this requirement is heightened by the reduction in strength of materials at elevated temperatures. Therefore it can be anticipated that as the maximum use temperature of an alloy is increased (Figure 1.1), its

² Inconel 600 and its follow on alloys were originally manufactured by Inco Alloys International Inc. (hence the name Inconel), but in 1998 Inco Alloys International Inc. was acquired by Special Metals, and thus Special Metals is currently the producer of Inconel and its derivatives.

yield strength will be decreased, and either the alloy will have to be subjected to lower values of stress (such as lowering the internal pressure for pressure vessel applications) or the alloy must be designed to a higher yield strength by a variety of strengthening mechanisms. Following similar logic as the Zinkle operating temperature plot of Figure 1.2, Farmer at LLNL has summarized several steel based alloys and projected a target high temperature yield strength curve for structural materials proposed for use in the Laser Inertial Fusion Energy (LIFE) program (Figure 1.3) [18]. This approach sets a baseline yield strength standard required for an intended application and allows for material development to meet that standard. Figure 1.3 shows yield strength as a function of temperature for an improved stainless steel alloy (316FR), a ferritic steel (non-ODS ferritic), and three Oxide Dispersion Strengthened (ODS) steels (PM2000, 9Cr-ODS, and 12YWT).

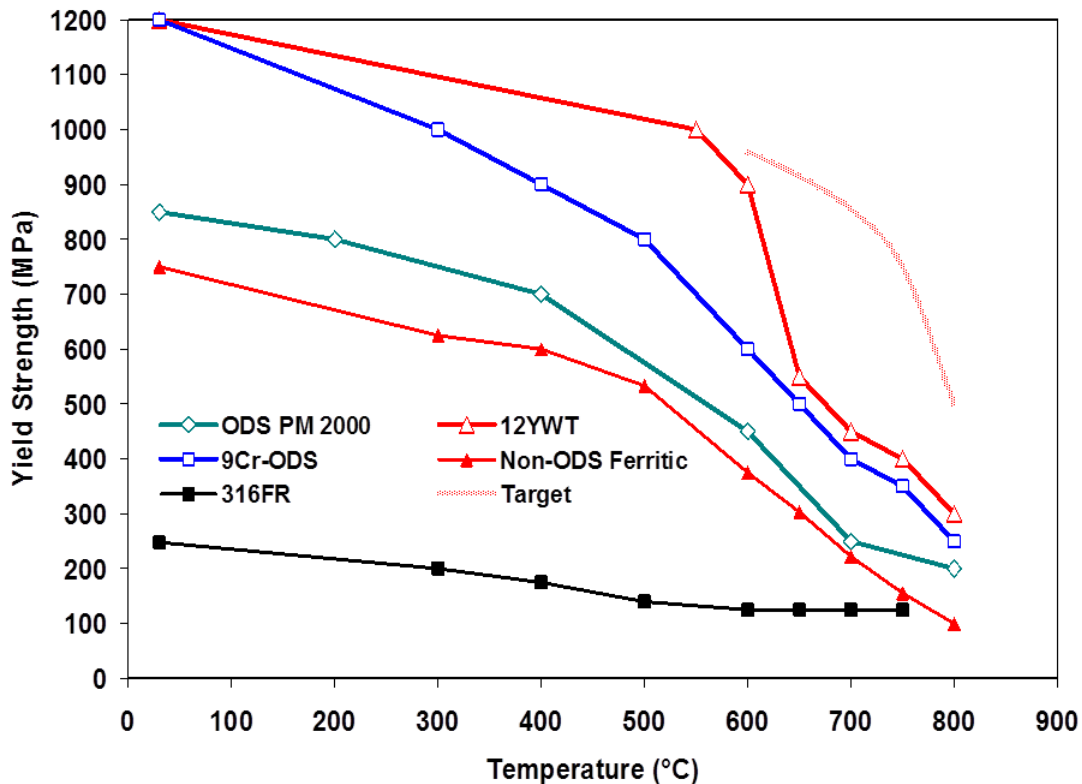


Figure 1.3 Yield strength as a function of temperature for candidate structural materials in the Laser Inertial Fusion Energy program from Farmer [from 18].

In addition to the steady increase in operating temperatures of energy production designs shown in Figure 1.1, there has been a continual development in coolants used in these designs from pressurized water, boiling water, supercritical water, and a variety of gas and superheated gas cycles as well as the development of advanced alternate coolants such as molten salts and liquid metals. This development in coolants has been predicated on numerous requirements including the improved heat transfer and thermal performance of some of the coolants, fuel or cycle compatibility such as neutron moderation, or other required functionality such as tritium production for fusion designs; however, these changes in coolant selection introduce new significant corrosion concerns including both general corrosion and environmentally assisted corrosion (EAC). Currently there are numerous methods in use to compensate for general corrosion including coolant chemistry control or selection of alloys with passive protective layers achieved either through design or initial system preconditioning. EAC can be more difficult to both predict and control and failure mechanisms such as Stress Corrosion Cracking (SCC) or Liquid Metal Embrittlement (LME) often need to be prevented by material and coolant selection based on compatibility. Additionally this compatibility between structural materials and exposed environments is often an empirically determined relationship.

Structural materials used in nuclear energy applications are also subjected to extreme radiation environments, most notably a wide variety of neutron spectra that have a severe effect on material performance. Radiation effects on materials, in general, are discussed in a variety of textbooks [19, 20], and developments in irradiation resistant steels are summarized in a recent review by Odette at the University of California Santa Barbara (UCSB) [17]. In this review, Odette summarizes the major effects of radiation damage as follows: (1) hardening at lower temperatures, (2) enhanced softening and recovery at higher temperatures, (3) degradation of fracture toughness, (4) loss of uniform strain ductility, (5) void swelling, (6) low temperature irradiation creep, and (7) enhanced EAC. In particular for fusion reactors, the production of large amounts of hydrogen and helium can be expected to cause swelling and embrittlement significantly

greater than that seen in current fission reactors unless structural material design allows for the accumulation of their atoms within the alloy matrix.

Radiation damage to structural materials is traditionally quantified in terms of displacements per atom (dpa) referring to the displacement of atoms from their lattice position in the unit cell due to neutron bombardment. Displacement damage also occurs from complex reactions of hydrogen and helium transmutation product gases which is quantified in terms of atom parts per million (appm) and can be significantly greater than damage from neutrons alone, in particular for fusion reactors. Similar to the continual increase in operating temperatures for advanced reactor designs, estimates of end of life damage in dpa have increased over time as new reactor designs have evolved. Combining the operating temperature goals and end of life radiation damage expectations, Zinkle has developed an aggregate plot of temperature versus displacement damage showing the evolution of reactor plant designs (Figure 1.4) [1]. This plot is very informative as it shows the large material development hurdles both in temperature and damage resistance that are required from current generation reactors to potential advanced fission and fusion reactors.

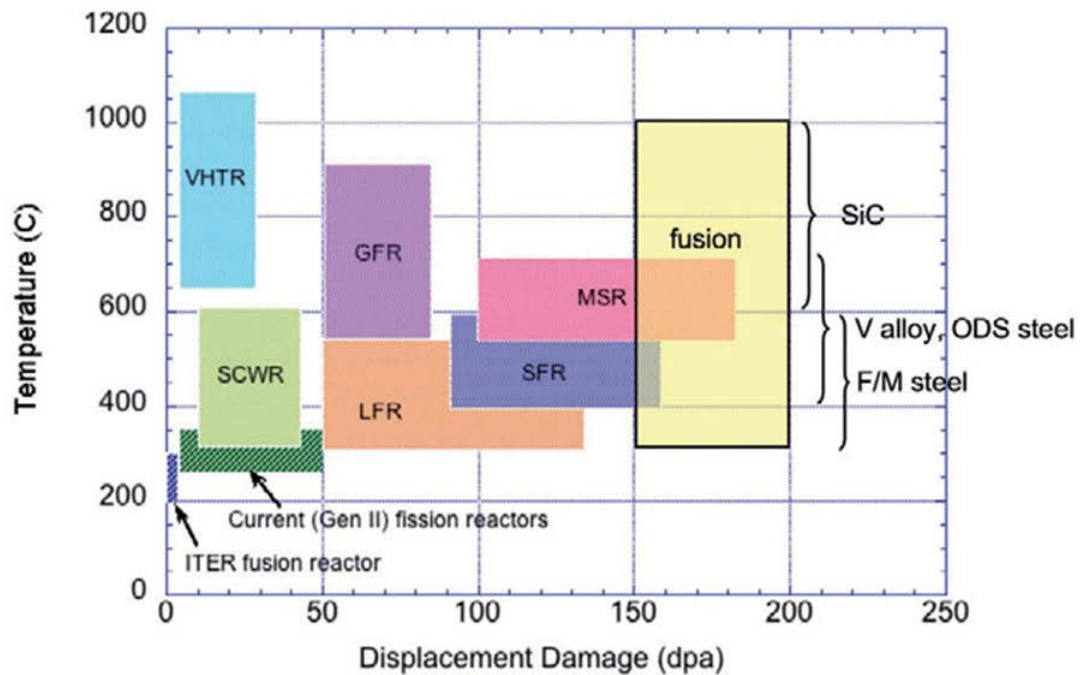


Figure 1.4 Overview of operating temperatures and displacement damage dose regimes for structural materials in current and future fission and fusion reactors from Zinkle [from 1]. The six fission based systems are: Very High Temperature Reactor (VHTR), Super Critical Water Reactor (SCWR), Lead Fast Reactor (LFR), Gas Fast Reactor (GFR), Sodium Fast Reactor (SFR), and Molten Salt Reactor (MSR).

In addition to radiation damage from lattice displacement, neutron radiation from both fission and fusion reactors causes activation of certain elemental isotopes which subsequently undergo various forms of radioactive decay resulting in the emission of gamma or x-ray radiation which, although often not detrimental to structural materials, are hazardous to personnel or potentially electronic equipment. Prevention of activation in structural materials is achieved by radiation shielding or by selection of alloys that do not contain isotopes with high absorption rates of neutrons. The steady elimination of cobalt in structural components of Naval nuclear reactor designs is an example of material selection done to eliminate the activation of structural materials. In particular, Co^{60} is an isotope of concern due its long radioactive half-life and high-energy gamma emission when activated by neutron absorption of Co^{59} . The reduction of cobalt in structural components of nuclear reactors has steadily decreased after shutdown radiation

levels and the exposure of maintenance personnel in those reactors. Similarly, the high neutron absorption rate of molybdenum has led to the reduction of use of molybdenum in certain structural materials. For current reactor designs, materials selected to reduce their neutron absorption and activation are denoted as reduced activation materials and an example of this class of materials is Reduced Activation Ferritic/Martensitic (RAFM) steels that are potential candidates for structural materials in advanced reactor designs.

In addition to requiring high strength to avoid deformation or catastrophic fracture, structural materials for advanced reactor designs require high fracture toughness to be able to resist fracture. This is most critical in pressure vessel applications with thick walls that may contain cracks or crack-like defects despite rigorous quality assurance and inspections during manufacture. Additionally, as previously identified by Odette, neutron irradiation degrades the fracture toughness of steels and is one of the primary considerations for pressure vessel lifetime calculations [17]. Fracture toughness of ODS steels or RAFM steels is not well known, but has been research by Miao and Byun on 14YWT [21, 22] and Splichal on the non-ODS variant of EUROFER-97 [23]. While evaluating the fracture toughness of 14YWT, Miao concluded that the coarse grains in 14YWT (one to several tens of μm) caused the low fracture toughness and that processing paths that produce finer grains could lead to improved fracture toughness. Simulating the radiation damage from a fusion reactor by hydrogen charging of EUROFER-97, Splichal concluded that EUROFER-97 was susceptible to brittle fracture due to degradation of fracture toughness following hydrogen charging. Taken together these two conclusions show that fracture toughness will be an important material property for structural materials, in particular for fusion designs, and that ODS alloys produced with fine grains may have sufficient fracture toughness for this application.

The final material consideration for high temperature energy applications is resistance to creep, the slow plastic deformation of material over time at a stress below the alloy's nominal yield strength while held at a temperature which is a significant fraction of its melting point. In gas or steam turbine applications for propulsion or power production, creep resistance is usually achieved by increasing the grain size of the alloy, even to the point of producing single-crystal turbine blades. For structural materials such

as those for fission or fusion reactors, this approach is not viable as it reduces the low temperature strength of the alloy to an unacceptably low level and also removes grain boundaries as sinks for radiation-induced defects, thereby also reducing the material's resistance to radiation damage. Additionally, as cited previously by Odette [17], radiation can accelerate creep. Keeping creep to a minimal level is critical to both fission and fusion reactor designs so that structural materials can meet the operational life time requirements of reactor design (on the order of tens of years) which is significantly greater than the operational life time requirements of traditional propulsion or power turbine designs (typically thousands of hours).

With the above stated framework, the initial objective of material design for high temperature energy applications is clear. Structural materials for these applications must be developed that have: (1) low and high temperature strength, (2) corrosion resistance in a variety of extreme environmental conditions, (3) radiation damage resistance for nuclear applications, (4) sufficient fracture toughness, and (5) creep resistance. Achieving this objective is a daunting task that requires alloy development which achieves high temperature strength and stability. Additionally improved material certification capability is required such as *in situ* material testing in extreme coolant conditions such as those proposed at the Lead Coolant Test Facility at Idaho National Laboratory (INL) [24], extensive radiation exposure and damage analysis such as those proposed at the International Fusion Material Irradiation Facility (IFMIF) [25] and various triple-beam irradiation facilities such as those at ORNL [26] and France [27, 28], and finally extended creep analysis to ensure material can endure the prolonged exposure to high temperature and radiation spectra expected of the intended applications.

B. CANDIDATE ALLOYS FOR FUTURE REACTOR DESIGNS

Using the previous material requirements for nuclear energy applications, the initial step in material development is the identification of candidate alloys for use in advanced reactor designs. Results by several research organizations have shown that the leading contenders based initially on high temperature strength are refractory metals such as vanadium alloys, SiC composites, RAFM steels, and ODS steels [2–5, 7, 9, 11, 18, 29–

32]. Vanadium alloys have several inherent properties that make them attractive candidates including good thermo-mechanical properties (most notably high thermal conductivity and low thermal expansion) and a low absorption cross section for thermal neutrons. The most prominent advantage of vanadium alloys is their compatibility with lithium making them an excellent selection for liquid lithium coolant/breeder blankets. However, the research and operational experience with these alloys is far less mature than traditional steels and requires additional research, including analysis of radiation effects on vanadium alloys and specifically on reactions with helium, as well as on the importance of interstitial impurities such as oxygen, carbon, and nitrogen [2, 3]. Initially designed for propulsion and power gas turbine applications, SiC composites are attractive candidates because of their low neutron activation and retained yield strength at very high temperatures (up to 1,000°C). In addition to the relative operational unfamiliarity with SiC in radiation environments, current manufacturing capacity and joining technologies are insufficient to meet expected requirements for large scale energy production designs [2, 3]. Because of these shortfalls, most current materials research and development for advanced reactor designs is on RAFM and ODS steels.

In many ways RAFM and ODS steels are similar, and in several cases ODS steels such as EUROFER97-ODS and 9/12 Cr-ODS are designed from an RAFM counterpart. This addition of an ODS component to a base RAFM material design is predicated on the observed low strength at high temperatures of several RAFM steels, as can be seen in Figure 1.3. The process of adding uniformly dispersed Y_2O_3 particles in the metal matrix has been shown to significantly increase the strength of the alloy [30, 32] and improve radiation damage resistance [17, 33]. For these reasons, materials research at several national laboratories, including LLNL [18, 34–37], ORNL [1–4, 11, 13], Pacific Northwest National Laboratory (PNNL) [7], and Los Alamos National Laboratory (LANL) [38], universities such as UCSB [17, 21, 33, 39] and University of California Berkeley [40] as well as international nuclear research agencies [5, 7, 29, 30, 41, 42] includes a significant focus on ODS alloys.

C. REVIEW OF OXIDE DISPERSION STRENGTHENED STEELS

1. Manufacturing Review

The development of metal matrix composites started in the 1960s and was one of the primary material improvements allowing for significant advancements in a wide variety of areas due to improved material performance of manufactured alloys. Two generic methods for composite manufacture are powder metallurgy (PM) and methods involving molten metal. These methods are discussed in detail in review papers by Lloyd [43] and Kaczmar [44], and it has been shown that incorporating ceramic particles into metallic melts has had limited success because most metals do not wet ceramic particles. PM overcomes this limitation by mixing elemental or pre-alloyed powders of both ceramic particles and the base metal matrix via ball milling. Because of this advantage, PM has emerged as a prominent alloy manufacturing approach for structural materials in fission and fusion based reactor designs [21, 45–48].

Mechanical alloying (MA) is a specific PM process where dry powders in either equilibrium or metastable phases are mixed in a high-energy ball mill. The repeated collision of the milling balls and powder particles produces intense plastic deformation of the powders resulting in a very fine final mixture. This mixture is subsequently consolidated into stock shapes or near-net shapes by various techniques. A brief history of MA as well as techniques, advantages, and problems are discussed in detail separately by Benjamin [49] and Suryanarayana [50] with major points summarized here. MA was initially developed to form nickel based superalloys for gas turbine applications and its primary advantage is its ability to synthesize new alloys of normally immiscible materials. Because MA is a completely solid-state technique, it is not affected by the limitations of manufacturing techniques that include melting, and the associated pitfalls of non-homogenous distribution, porosity, or other problems associated with such manufacturing approaches; however, powder contamination is a significant concern and the small particle size, large exposed surface area, and formation of new surfaces during ball milling all contribute to powder contamination. The primary methods to prevent powder contamination are the use of high-purity powders, use of a high-purity

atmosphere (usually argon), the use of milling containers of similar material to the milled material, and the minimization of milling time.

Although PM and MA have been utilized for many years, the techniques are based largely on empirical research. The controllable variables associated with MA include powder particle size, whether the powders are elemental (e.g. Fe) or pre-alloyed (e.g. Fe-Cr-Al), milling conditions (time, speed, atmosphere, ball size, etc.), use of process control agents, consolidation method, and final machining. Typical micrographs taken from Zhou of (a) pre-alloyed powders and (b) as milled powders are shown in Figure 1.5 for a typical ODS steel [51]. A simplified block diagram of the MA process is shown in Figure 1.6. In this diagram elemental powders of iron and other elements (typically chromium, titanium, and aluminum) are mixed with pre-alloyed powders of Y_2O_3 in a planetary ball mill and subsequently consolidated before final processing into the desired form. For most of the alloys discussed in this research, alloys are consolidated via hot isostatic pressing (HIP) and then hot extruded into the required form.

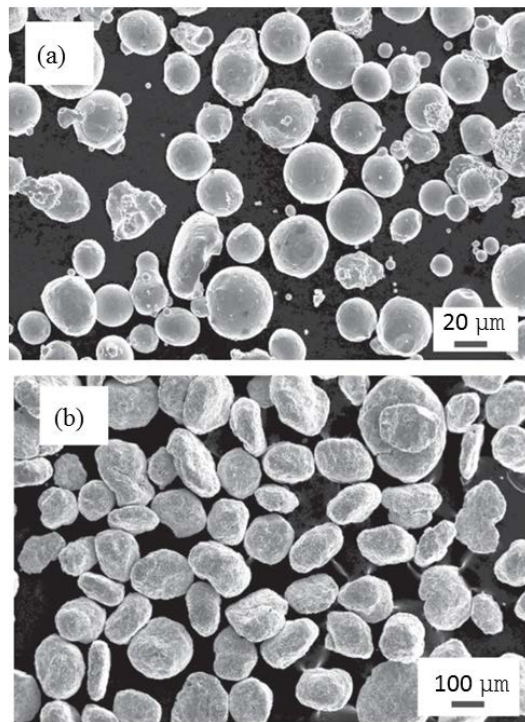


Figure 1.5 Scanning electron micrographs of (a) pre-alloyed powders and (b) as milled powders for a nominal oxide dispersion strengthened steel from Zhou [from 51].

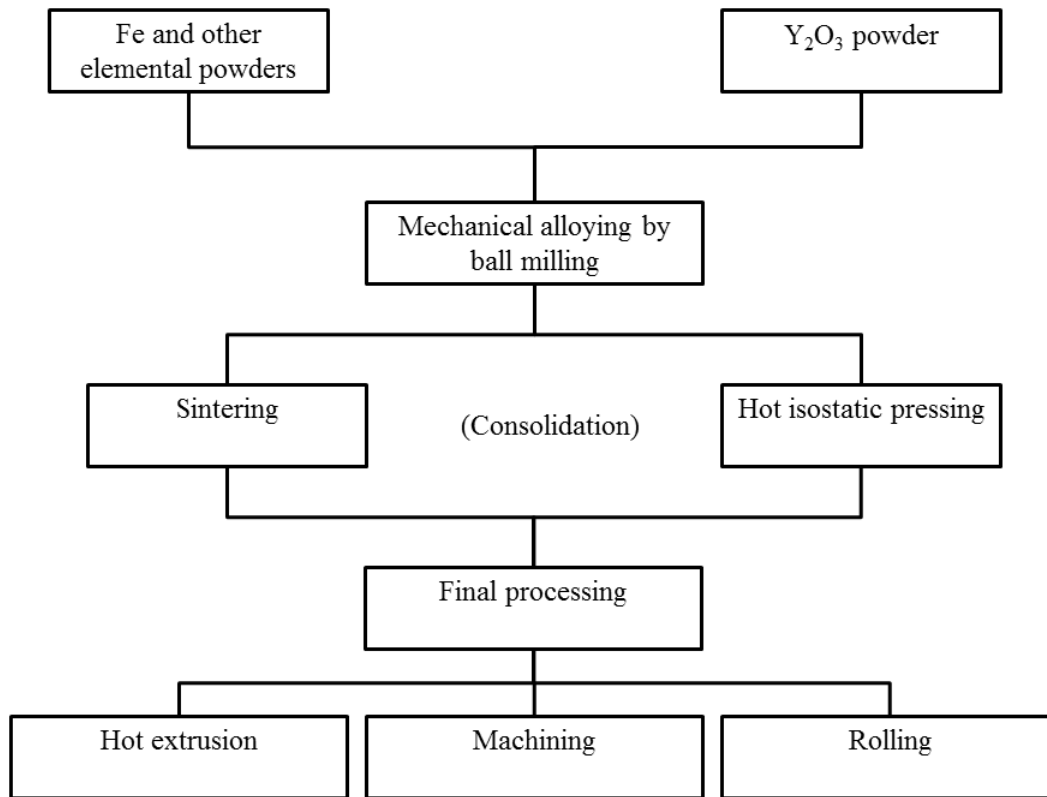


Figure 1.6 Simplified block diagram of a typical mechanical alloying process.

2. Examples of Oxide Dispersion Strengthened Steels

What becomes readily apparent following an understanding of the PM and MA processes is that there are few limitations on the types of alloys that can be created from MA, and that alloys can be specifically tailored to meet varying material requirements albeit with some higher experimental and manufacturing cost. This potential variance is exactly what is seen in the literature of ODS steels. Table 1.3 is a selected summary of eighteen different ODS steels with six traditional ferritic-martensitic (FM) steels for comparison. Table 1.3 shows the elemental breakdown of major constituent elements (with Y_2O_3 considered a single element since in each case Y_2O_3 is added as a pre-alloyed powder) with each alloy having a remaining and major component of iron. Because of the poor radiation performance of nickel, all of the alloys listed in Table 1.3 are iron based alloys, and the remainder of this research will

focus only on iron-based alloys; however, for non-radiation environments a comparable number of nickel based alloys exists and could be used.

Table 1.3 Comparison of ODS and non-ODS steels used in high temperature energy applications. All alloys shown have a remaining balance of Fe.

Alloy	Material Composition (wt%)						Literature Source
	Cr	Al	Y ₂ O ₃	C	W	Ti	
ODS Steels							
MA956	18-21.7	4.5-5.8	0.5	0.018-0.06	-	0.32-0.4	[from 34, 52-57]
MA957	13.7-14	-	0.5	<0.03	-	0.9-0.98	[from 53, 55, 58]
PM2000	19.2-20	5.5-5.7	0.5	0.01-0.013	-	<0.5	[from 52, 53, 59-61]
PM1000	20	0.3	0.6	0.05	-	0.5	[from 62]
12YWT	12	-	0.25	0.05	0.8	0.4	[from 53, 63]
14YWT	14	-	0.25	0.05	0.6	0.3	[from 53, 64-68]
9Cr-ODS	8.6-9.01	-	0.36	0.13-0.14	1.95-2	0.21	[from 69-74]
12Cr-ODS	11.95	-	0.24	0.024	2.01	0.3	[from 70, 71, 74]
K1	18.37	<0.01	0.368	0.05	0.29	0.28	[from 75]
K2	13.64	4.12	0.381	0.04	1.65	0.28	[from 75]
K3	16	4.59	0.368	0.08	1.82	0.28	[from 34, 75]
K4	18.85	4.61	0.368	0.09	1.83	0.28	[from 75]
K5	22.05	4.55	0.356	0.1	1.8	0.27	[from 34, 75, 76]
K6	19.02	4.6	0.368	0.1	1.85	0.28	[from 34, 75]
EUROFER97-ODS	9.1	-	0.3	-	1	-	[from 77]
J27	14	-	0.3	-	1	0.3	[from 78]
EFPL-E	14	-	0.3	-	2	0.3	[from 79]
SS316-ODS	16	-	0.3	-	-	0.3	[from 80]
FM Steels							
F82H	7.46-8	-	-	0.09-0.093	1.96-2	<0.004	[from 29, 81]
JLF-1	8.85-9.04	<0.003	-	0.097-0.1	1.97-1.99	<0.001	[from 29, 82-84]
EUROFER97	8.82-8.96	-	-	0.12	1.15	-	[from 8, 23, 31, 81]
HT-9	11.63	0.01	-	0.2	-	-	[from 85-88]
T91	9	0.02	-	0.1	0.4	0.01	[from 54]
EP-823	11.71	-	-	0.16	0.58	-	[from 89]

Table 1.3 shows some important similarities and differences in composition between ODS steels, and some common themes become apparent. As mentioned previously, all of the ODS steels listed in Table 1.3 are iron based for the metal matrix. Carbon is intentionally maintained at a much lower concentration than typical steels since other elements act as solid solution strengtheners. The minimization of carbon also prevents the formation of martensite which is undesirable in most applications. As such all of the ODS steels listed, with the exception of SS316-ODS, are ferritic in nature vice FM although the specific annotation of ferritic is frequently not mentioned in most literature.³ The other FM steels listed in Table 1.3 are all advanced materials also being considered in advanced fission and fusion reactor designs and all include a significantly higher concentration of carbon. Titanium is added to most ODS steels as a nitride former to scavenge nitrogen and also provides some solid solution strengthening. Titanium's more prominent role occurs in ODS steels that do not contain aluminum since in the absence of aluminum, yttrium will react with titanium and oxygen to form complex Y-Ti-O particles. Examples of this include MA957, 12/14YWT, and 9/12Cr-ODS. Aluminum plays an important role in ODS steels because if aluminum is present, complex Y-Al-O particles form that become the basis for improved dispersion strengthening. Aluminum also promotes a protective aluminum oxide layer on the surface of the steel which minimizes corrosion and oxidation. These reactions are one of the principle differences between major subsets of ODS steels and will be discussed in more detail in subsequent chapters. All of the ODS steels in Table 1.3 have relatively high concentrations of chromium compared to other FM steels. Chromium is intentionally added to improve the general corrosion and oxidation resistance of the alloy, and the amount of chromium is another major differentiator between the various ODS steels. Many of the ODS steels contain tungsten as a solid solution strengthening agent. Impurity elements such as phosphorous, sulfur, and silicon are present in ODS steels at a much lower concentration (generally <0.01 wt% or less) and are maintained at a low level to prevent material

³ The SS316-ODS steel listed in Table 1.3 is an austenitic stainless steel alloyed with similar Y₂O₃ powder as seen in the other alloys. Austenitic ODS alloys are far less prevalent in the literature but are provided here as a reference.

degradation due to these elements, and as such these elements are not included in Table 1.3.

All of the ODS steels listed in Table 1.3 include Y_2O_3 powders which are blended with the remaining constituents of the steel during the PM process, and all have similar concentrations of Y_2O_3 . During manufacture and potentially during post-manufacture processing, the Y_2O_3 powder reacts with aluminum (preferentially if present) or titanium (in the absence of aluminum) to form complex Y-Al/Ti-O particles. It is these particles that give ODS steels their high strength due to the Orowan particle dispersion strengthening mechanism. Additionally these particles improve radiation performance as discussed previously. Because of the significance of this difference, ODS steels can and should be appropriately subdivided into aluminum-containing ODS steels (MA956, PM2000, and K2-K6) and those that do not contain aluminum (MA957, 12/14YWT, and 9/12Cr-ODS).

The ODS steels listed in Table 1.3 also show the general evolution paths used by many research organizations. As mentioned previously the PM and MA processes allows for customization of alloy concentrations free from many of the typical manufacturing limitations. One of the most clear evolutionary chains is the development of ODS steels done by Kimura at Kyoto University where several iterations of ODS steels designated as “K” alloys have been developed and tested for use in advance fission and fusion based applications. At the first iteration (i.e., the development of K2), aluminum was added and subsequent iterations included refinement on aluminum concentrations and progressive changes in chromium concentration. A similar development path was followed by Plansee, Inc., in the manufacturing of PM1000 and PM2000. The major alternate path is refinement of titanium and chromium concentrations with the absence of aluminum as has been done at ORNL with 12/14YWT and the Japan Nuclear Cycle Development Institute with 9/12Cr-ODS. Of note, the developmental stages of all of the ODS steels listed in Table 1.3 includes refinement in manufacturing processes; however, they all used similar techniques as summarized in the block diagram of Figure 1.6.

Research to date suggests that ODS steels have the material properties required for structural applications in advanced reactor designs. The yield strengths as a function

of temperature for five different ODS alloys are shown in Figure 1.7 from Klueh [55]. The corrosion resistance of ODS alloys in different extreme coolant conditions such as lead-bismuth eutectic (LBE) [52, 53, 90, 91] and molten salts [34-36] has been evaluated and shows that ODS alloys are promising candidates in these environments. The improved radiation damage resistance of ODS steels, achieved primarily by the dispersed particles, has also been established [17, 33].

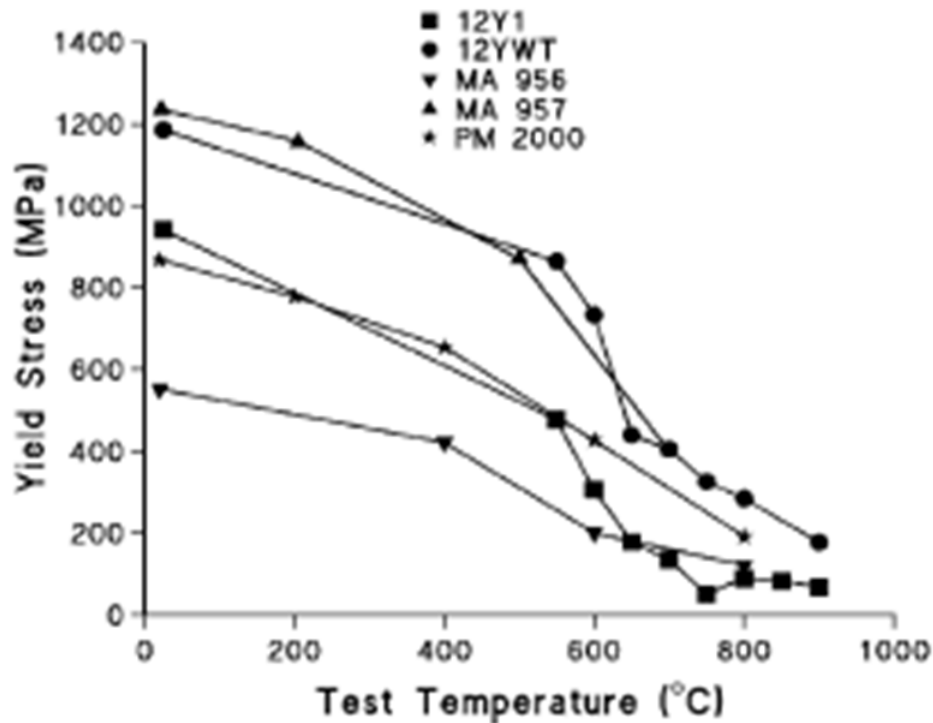


Figure 1.7 Comparison plot of yield strength as a function of test temperature for five oxide dispersion strengthened steels from Klueh [from 55].

3. Oxide Dispersion Strengthened Steel MA956

a. History

MA956 is a ferritic ODS steel that was originally designed by Special Metals for use in the gas turbine engines designs of the F-22 Raptor aircraft in 1985 [92, 93]. MA956 is produced by a MA process (the “MA” in MA956 stands for mechanical alloying) similar to that shown in Figure 1.6 with consolidation via HIP prior to final machining. Similar in many ways to PM2000 and several K alloys (most notable K4-

K6), MA956 contains approximately 4.5 wt% aluminum, primarily for corrosion and oxidation resistance. Initial MA956 material design was based on a combination of the commercial alloy Kanthal (a Fe-Cr-Al steel) and the ODS nickel based alloy MA-754 in efforts to combine the hot corrosion resistance and excellent creep strength of the two separate alloys. Upon manufacture, however, the ductile-brittle transition temperature (DBTT) of MA956 was unexpectedly found to be near ambient temperature (0-100°C from [93]) thus making it unsuitable for its original intended application and ending the majority of the production line for MA956.

Because of creep concerns in fine grain (FG) alloys, MA956 was originally designed to be manufactured in a coarse grain (CG) form for gas turbine applications including potential single crystal turbine blade designs; however, other research on MA956 has shown that the creep behavior of FG MA956 may be sufficiently close to CG MA956 to allow for its use in high temperature applications while capitalizing on the improved strength and radiation damage resistance of the FG design [94, 95]. Specifically, Wilshire showed that MA956 with fine elongated grains had minimum creep rates that were comparable to MA956 with coarse elongated grains. This creep evaluation of FG alloys is consistent with research on other FG ODS alloys such as 12YWT that show promising creep performance when compared to traditional ferritic-martensitic steels [55, 63]. The significance of starting grain size is significant both in the base mechanical properties and the evolved material properties following joining. For the purposes of this research, MA956 with an average grain size of less than 10 μm is denoted as FG, unrecrystallized material; whereas MA956 with an average grain size of greater than 10 μm is denoted as CG recrystallized material. Although no absolute standard exists, this nomenclature is consistent with other literature and both FG and CG versions of MA956 are available depending on the intended application, although most research is based on CG materials (normally grain sizes of 100s of μm or more) including Special Metals published data [56, 92, 93, 96-99]. Little has been published on the microstructure-mechanical property relationships for FG MA956 although some theoretical and experimental comparison data exists which emphasizes the significance of grain size on base material performance [95, 100-102]. The line between FG and CG

material is intended to be broad division that is based on the desired application and is achieved by an intentional post-manufacture heat treatment.

Although potentially not suitable for room temperature applications due to its low DBTT, research on potential use of MA956 in a variety of other applications continues including: fusion based energy designs [34-36], advance fission based energy designs [103-106], conventional high temperature designs including use in a High Temperature Heat Exchanger (HTHX) [107-109], space-based energy applications [10], and biomaterial applications [98, 110-112]. Research on MA956 has established the excellent corrosion resistance in various environments [52, 53, 90, 91] as well as low creep rates of MA956 at high temperatures [94, 95, 113]. Based on these findings, this research will focus on MA956 as a candidate material for use in high temperature energy applications such as advanced fission and fusion based reactor systems.

b. MA956 Used in this Research

The material used in this study was MA956 steel plate. Compositional data for MA956 used here is shown in Table 1.4 and was determined using inductively coupled plasma mass spectrometry and LECO analysis by Anamet Inc. MA956 was canned and extruded at 1100°C (2025°F) and subsequently hot-rolled in three passes at 1100°C (2025°F) over 4 hours with reheating to 1100°C (2025°F) for 30 minutes before and after each rolling pass before final machining into 4 mm (0.157 inch) thick plate. As will be demonstrated in this research, this manufacturing process produced a FG unrecrystallized MA956 base alloy. Manufacturing processes for most other MA956 research and applications includes a post-manufacture heat treatment that produces a CG recrystallized MA956 base material. A total of 7 different plates of MA956 were used in this research although all came from the same base MA956 acquired by LLNL for this and related research. A summary of each plate of MA956 used in this research is contained in Appendix A.

Table 1.4 Chemical Composition of MA956 (wt%) used in this research.

C	Cr	Al	Ti	Y ₂ O ₃	Mo	Mn	Ni	S	Si	P	Fe
0.023	19.93	4.75	0.39	0.51	0.02	0.09	0.04	0.008	0.08	0.006	Bal.

D. JOINING OF OXIDE DISPERSION STRENGTHENED STEELS

As appealing as MA956 and other ODS steels are for nuclear applications, joining structural components comprised of ODS alloys is a key technology challenge limiting their use [4, 7, 9, 13, 33]. Retention of strength in welded joints and prevention of agglomeration of oxide particles in ODS steels resulting in degraded material performance in depleted areas are key problems that need to be addressed for joining of ODS steels. Overcoming the obstacles in joining of ODS steels would further promote their utility in advanced fission and fusion based energy applications. A variety of research has addressed these issues with combinations of traditional fusion welding and non-traditional joining techniques.

1. Traditional Fusion Welding Techniques

Traditional fusion welding techniques use heat input from a variety of sources (plasma arc, laser, electron beam, etc.) to melt two materials which subsequently become joined upon cooling and solidification. Fusion welding can be performed with or without a filler material. In general, traditional fusion welding techniques create heat affected zones (HAZ) dependent on the parameters used that often have inferior strength and degraded material properties. A wide array of fusion joining techniques for ODS steels has been researched including traditional fusion welding using gas tungsten arc (GTA) or gas metal arc (GMA) processes [114], electron beam welding (EBW) [115], laser beam welding (LBW) [62], and electro-spark deposition (ESD) welding [39] with varying degrees of success and practicality. Both GTA and GMA fusion welding were shown to cause melting which disrupted both the oxide distribution and grain structure in the material. Additionally the dispersed oxides rapidly agglomerated and rose to the top of

the molten pool producing a non-homogenous distribution of particles resulting in degraded performance in depleted areas [114]. Using EBW on an ODS variant of EUROFER, Lindau concluded that EBW lead to weak weld seams, and deterioration of mechanical properties was related to the evolved microstructure in the weld zone. Thus, EBW was not suitable as a joining technique for ODS alloys for highly loaded applications [115]. Similarly for LBW, the high temperatures developed lead to melting which caused clustering of the oxide particles in PM1000 leading to a reduction of strength in the weld [62]. Using ESD welding on MA957 (an aluminum-free ODS alloy), Miao demonstrated that ESD produced significant porosity in the weld region and the particles (Y-Ti-O particles vice Y-Al-O particles) were coarsened substantially leading to a significant degradation of strength in the weld region [39].

2. Non-traditional Joining Techniques

Chosen primarily to prevent agglomeration of oxide particles, alternate joining techniques that do not produce melting, such as Transient Liquid Phase (TLP) bonding, solid-state diffusion bonding, and friction welding have been attempted on ODS steels with varying degrees of success. TLP bonding was studied by Krishnardula, and although TLP bonding was demonstrated on ODS steels such as MA956 and PM2000, the boron vapor interlayer required as a deposit between the joined materials may not be practical in all applications [116]. In another attempt to prevent melting of the substrates in ODS materials, Krishnardula used solid-state diffusion bonding to join MA956 and PM2000 producing a bond strength of 70% of the base materials [117]. Unfortunately both of these methods may not be practical for all applications including pipe welding. Ambroziak used conventional friction welding to join MA956 pipe. Although the friction welding had little effect on the oxide particle distribution, the outward flow of material produced by the upset of weld metal produced transverse grain boundaries in the joined component. This grain boundary reorientation reduced the creep resistance of the joints to that of traditional fusion welded assemblies [114, 118, 119].

3. Friction Stir Welding, a Solid-State Joining Technique

a. Background

Friction stir welding (FSW) was invented at TWI (formerly The Welding Institute, UK) in 1991 as a solid state joining technique [120]. A detailed review of process parameters, process modeling, microstructure evolution, material properties, and specific material issues for FSW has been completed by Mishra and has become the fundamental reference on FSW [121]. This review focuses primarily, although not exclusively, on aluminum alloys. Due to early limitations on tool materials, FSW was initially constrained to aluminum and other lower melting point alloys. However, improvements in FSW tool materials, such as polycrystalline cubic boron nitride (PCBN) and W-Re, have expanded the use of FSW to more refractory alloys such as steels. Expanding the use of FSW to steels and polymers, Nandan provides a comprehensive review of heat generation, heat transfer and plastic flow, tool design, defect formation, and material properties for FSW applications [122]. Correspondingly, over the last few years the amount of research on FSW of steels has increased dramatically [123-128].

The work by Mishra and Nandan has formed the basis for the vast majority of research on FSW and key points will be briefly summarized here. Mishra summarized the major advantages of FSW as: low distortion of the workpiece, good dimensional stability and repeatability, no loss of alloying elements, excellent material properties in the joint area, refinement of microstructure⁴, and absence of solidification and hot cracking [121]. The basis for the majority of these advantages arises from the fact that FSW is a solid-state joining process and does not cause melting of the workpiece such as that seen in the majority of other joining processes. Elimination of melting and phase transformations preserves the majority of the workpiece's original material properties and leads to better joint efficiency.

⁴ Refinement of microstructure is a typical response during FSW; however, grain morphology is highly dependent on initial microstructure, and it will be demonstrated that in this research FSW causes significant grain coarsening. This result is not considered to be in opposition to the general grain refinement benefit mentioned by Mishra.

Because of the advantageous material properties produced in alloys following FSW, the same process is often used on single piece alloys and is often referred to as Friction Stir Processing (FSP). The FSW and FSP processes are identical except for the primary objective of the work. In FSW the primary objective is joining of two materials while in FSP the primary objective is surface processing of an alloy. In many research studies, including this one, the process of FSW is actually performed as a bead-on-plate weld on a single sheet or tube of material. For the sake of convenience and consistency, the term FSW will be used throughout this research although the terms FSW and FSP are considered synonymous.

A schematic representation of FSW from Mishra is shown in Figure 1.8 and depicts a typical FSW tool producing a bead-on-plate weld through a workpiece. The FSW tool is comprised of a tool shoulder and a tool pin. The tool shoulder maintains contact with the planar surface of the workpiece at a small tilt angle (often zero) with a downward force referred to as the plunge force which forces the tool pin into the workpiece. The tool pin is immersed in the alloy (z-direction on Figure 1.8 corresponding to the normal direction (ND) of the weld) and traverses longitudinally along the workpiece in the direction of the desired weld (x-direction of Figure 1.8 corresponding to the welding direction (WD) of the plate). The transverse direction (TD) to the weld (y-direction of Figure 1.8) along with the z-direction defines a plane upon a weld nugget or stir zone (SZ) may be observed. The edges of the SZ are referred to as the advancing side (AS), corresponding to the side where the rotation of the pin increases the relative motion between the tool pin and the workpiece, and the retreating side (RS), corresponding to the side where the rotation of the pin reduces the relative motion between the tool pin and the workpiece. The SZ material has experienced severe plastic deformation. Immediately adjacent to the SZ is a region that has experienced only small deformation as well as a welding thermal cycle. This region is referred to as the thermo-mechanically affected zone (TMAZ) although the appearance of this region is often indistinguishable from the base metal (BM).

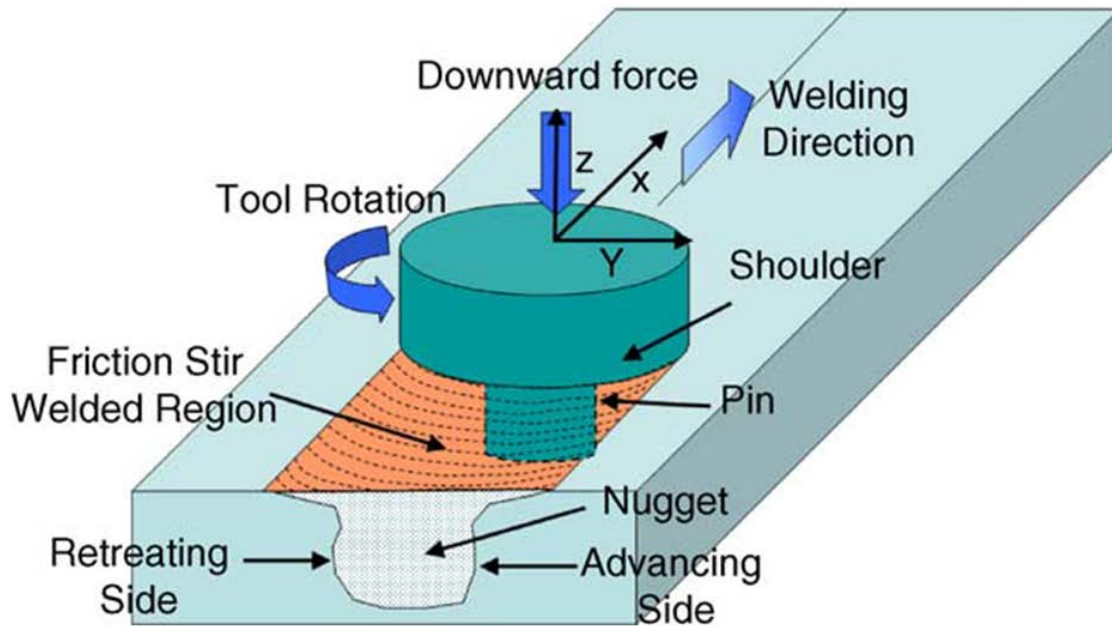


Figure 1.8 Schematic drawing of friction stir welding from Mishra [from 121].

Together, the SZ, AS, RS, and BM represent the critical elements of the welded structure. The SZ is essentially the center of the weld, and its size is determined primarily by the size and shape of the FSW tool but also the welding rotational speed and traverse speed to a lesser extent. Microstructural and material properties in the SZ are generally homogenous and often differ significantly from the BM. The AS and RS are areas of separation between the SZ and BM and correspond to the TMAZ of the weld. The HAZ for FSW is similar to the HAZ for fusion welding joining, but starts outside of the TMAZ where the deformation due to tool rotation is no longer felt. The differences in the AS and RS are known to produce asymmetric material properties, in particular hardness. A typical macrograph of a friction stir weld from Mishra is presented in Figure 1.9 showing the major areas of the weld. The shape of the SZ is dependent on several welding parameters including tool geometry, thermal conductivity of the workpiece, and both welding rotational and traverse speeds. Two major SZ shapes are prevalent in most materials, a basin shaped SZ that widens near the upper surface of the weld (Figure 1.10a) and an elliptical shaped SZ often referred to as an onion ring structure (Figure 1.10b).

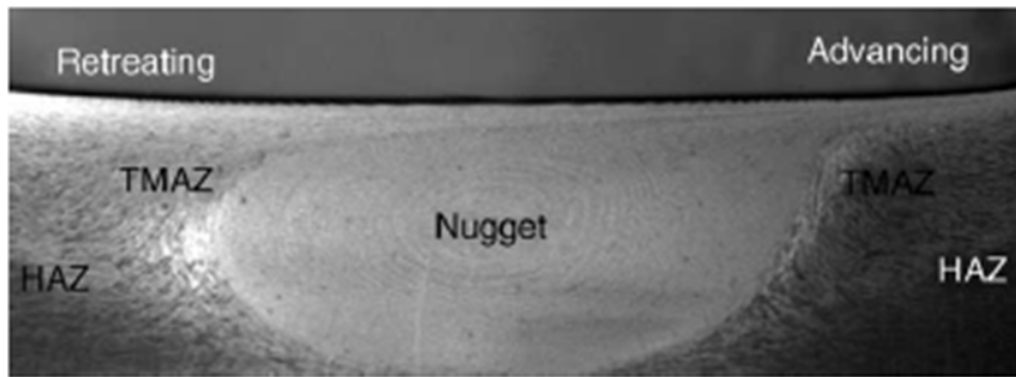


Figure 1.9 Typical macrograph of friction stir weld from Mishra [from 121]. The alloy shown is AA7075.

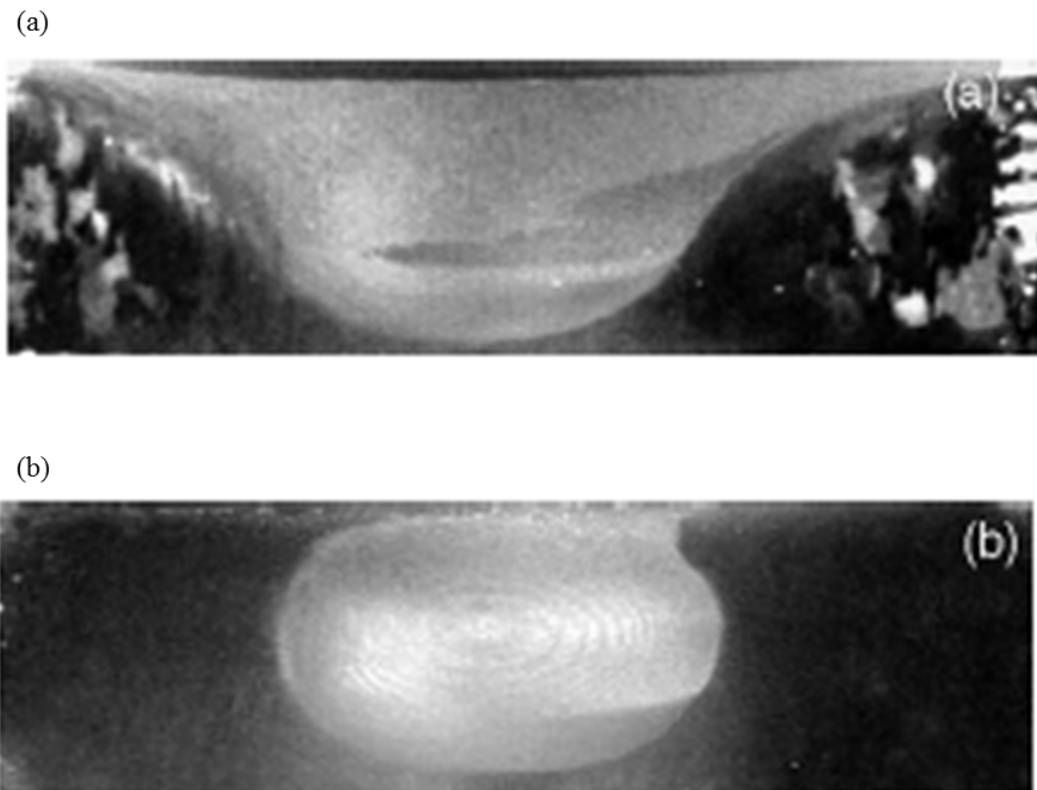


Figure 1.10 Different stir zone shapes from Mishra [from 121] showing: (a) basin shaped SZ and (b) elliptical shaped stir zone. The alloy in both images is AA356 and the only difference between the two is differences in welding rotational and traverse speeds.

The temperature distribution during FSW is difficult to measure or predict although it has been shown that peak temperatures occur in the SZ and decrease moving outward from the SZ in both the AS and RS directions. By embedding thermocouples in an AA7075 workpiece, Mahoney measured the temperature profile across the entire weld nugget and concluded that FSW did maintain temperatures below the melting temperature of AA7075 with peak temperatures being in the SZ [129]. This conclusion matches closely with thermal modeling results by Nandan which show a maximum temperature in the SZ decreasing outward to the BM [122, 130]. Although no exact value has been determined and conditions vary depending on the materials used, the maximum temperature in friction stir welds is generally thought to be approximately 80-90% of the alloy's melting temperature [121, 131]. Both experimental and theoretical work by Mishra and Nandan has shown that workpiece temperature is dependent primarily on the tool rotational speed, tool traverse speed, and plunge force.

Although the majority of research on FSW focuses on or assumes defect-free weld conditions, defects such as porosity, surface defects, and lack of consolidation can occur during FSW primarily due to insufficient flow of material around the pin. Wormhole or tunnel defects have been observed near the bottom (root) of the weld at the outer edge of the tool pin at high rotational speeds [122]. These defects normally occur on the RS of the weld. Similarly, lack of consolidation defects have been observed when the heat input due to FSW is insufficient to fully consolidate the weld [132]. These results suggest that a balance of welding parameters specifically tool rotational speed, tool traverse speed, and plunge force is required to provide sufficient heat input to consolidate the weld while preventing wormhole defects due to excessive rotational speeds.

b. Modeling

Modeling of FSW is a complex process that requires analysis of heat generation, heat transfer, and plastic flow, and must include numerous variables such as welding parameters, tool shape, and material composition for both the tool and workpiece. Modeling of FSW has been attempted by numerous authors including

Mishra, Nandan, and several others, and continues to be a very active research topic for general FSW [121, 130, 131] as well as FSW on specific alloys such as aluminum [133-136], steels [123, 124, 137], and copper [138]. For simplicity, tool design is predicated primarily on the nature of the workpiece. FSW on high strength alloys such as steels requires high strength, refractory tools such as tools with PCBN or W-Re pins. Selection of tool geometry is often an empirical process and the high cost and limited lifetime of FSW tools does not readily support multiple tool geometries. For these reasons, tool selection is considered a variable dependent on the specific application. Tool tilt angle and plunge force are also dependent on the strength and orientation of the workpiece and are similarly considered a constant in most applications since most FSW processes operate under a constant load condition. This simplified approach leaves the major welding parameters of tool rotational speed and tool traverse speed as the major variables. Intuitive reasoning suggests that the heat input during FSW (in terms of energy per unit length with units of kJ/mm) will increase as the tool rotational speed increases due to the increased friction between the tool and workpiece and that the heat input during FSW will decrease as the tool traverse speed is increased due to movement of the pin through the workpiece. This intuitive hypothesis is supported by most research on FSW although the exact dependence on each term varies [121, 122, 133, 137, 139, 140].

The heat input during FSW is proportional to the tool rotational speed and inversely proportional to the tool traverse speed. The microstructure and mechanical properties of the research herein support the hypotheses that peak temperature is dependent primarily on tool rotational speed and that overall heat input is proportional to the ratio of tool rotational speed to tool traverse speed. For the purposes of the research reported herein, the ratio of tool rotational speed (ω), in revolutions per minute (RPM), to tool traverse speed (v), in millimeters per minute (MMPM), is denoted as the heat index (HI) with units of revolutions per mm (Equation 1.2). Although several methods exist to evaluate the heat input or temperature distribution in friction stir welds, the denotation of HI in Equation 1.2 is similar to work by Chimbli who researched the lack of consolidation in friction stir welded aluminum alloys by varying process parameters and

subsequent destructive evaluation [132]. Chimbli determined that the ratio of tool rotation rate to tool traverse rate was a good measure of the ability to form defect-free consolidated welds. For comparison other research studies on FSW of ODS steels have used HI values ranging from 8 to 16 to achieve successful weld conditions [41, 141-146] with the exception of research by Etienne who used a very low heat input combination to analyze the redistribution of oxide particles following FSW without addressing weld consolidation [147]. This approach is also very similar to recent research by Biswas in a review of FSW parameters on an aluminum alloy [133]. Biswas concluded that the overall mechanical response of the welded alloy depended on the ratio of tool rotational speed to tool traverse speed similar to that proposed in this research. For the aluminum alloy and tool material used, the suitable value of this ratio was between 15 to 16 revolutions per mm. In recent FSW research on high-strength low-alloy (HSLA) steels, Wei and Nelson demonstrated that heat input (also annotated HI) calculated from tool power (P) with units of kJ/mm (Equation 1.3) provided the best correlation with post-friction stir weld microstructures and exhibited a linear relationship with ferrite grain size [137]. Wei and Nelson measured tool torque (τ) and tool rotational speed (ω) to calculate HI from tool power (Equation 1.4). In the research herein, the value of tool torque was not recorded but was assumed constant with constant tool rotational speeds, and thus for a constant value of torque, Wei and Nelson's approach (Equations 1.3 and 1.4) reduces to the simplified approach presented in Equation 1.2.

$$HI = \frac{\omega}{v} \left(\frac{\text{revolutions}}{\text{mm}} \right) \quad \text{Equation 1.2}$$

$$HI = \frac{P}{v} \left(\frac{\text{kJ}}{\text{mm}} \right) \quad \text{Equation 1.3}$$

$$P = \frac{(2\pi)\omega\tau}{60} \left(\frac{\text{kJ}}{\text{min}} \right) \quad \text{Equation 1.4}$$

The assumption that torque was constant was based on research by Peel and Nandan that showed that tool torque was primarily a function of tool rotational speed and that for constant tool rotational speeds, the tool torque was relatively constant [122,

148]. Tool torque as a function of weld pitch (WP), which is the inverse of the heat index term presented here in Equation 1.2, is shown in Figure 1.11 from [148] and shows for constant rotational speeds (dotted lines) tool torque is relatively constant. Similarly, Figure 1.11 shows that for constant tool traverse speeds (solid lines) tool torque is nearly linear with increasing WP corresponding to a near linear correlation with tool rotational speed. The observations by Peel and Nandan support the intuitive assumption that for quasi-steady state conditions, i.e. steady tool rotational and traverse speeds, the tool torque will be constant allowing the simplification of heat input discussed previously.

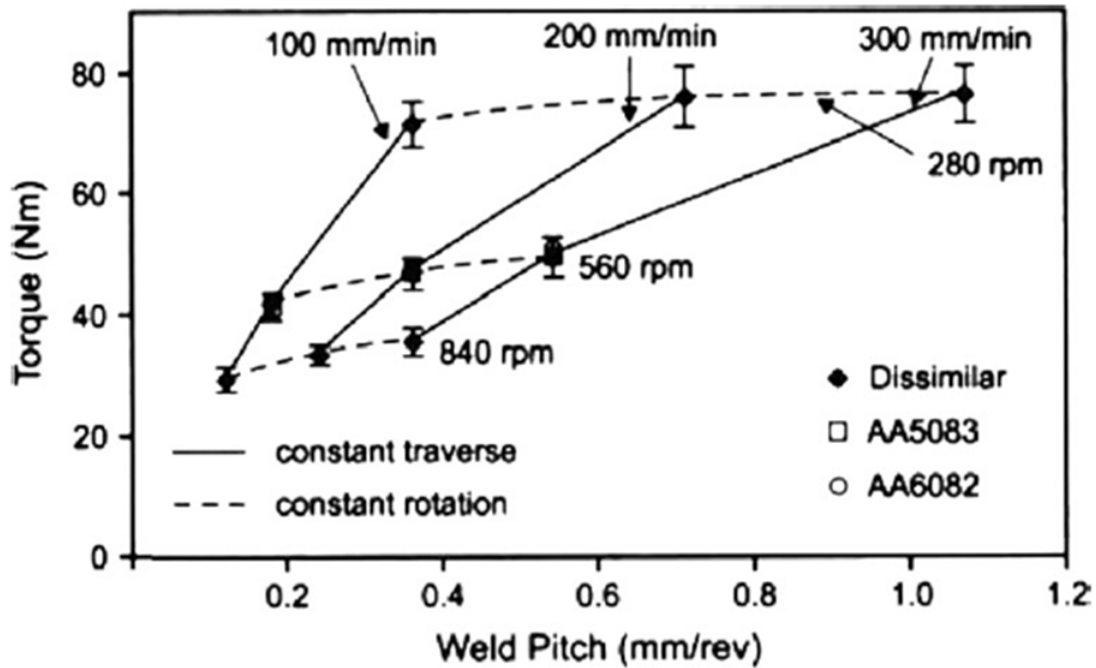


Figure 1.11 Tool torque versus weld pitch during friction stir welding of aluminum [from 148].

The term presented here has been changed from heat input (Wei and Nelson) in units of kJ/mm to heat index in unites of revolutions/mm to indicate that it is not a quantitative calculation of heat input into the workpiece, but rather is a term that is illustrative of the heat input into the workpiece while preserving the relationships established by Wei and Nelson. The term heat index is proposed vice heat input because the variables in the heat index term are fundamental processing parameters that are

normally and easily measured during FSW while preserving the fundamental relationships established by Wei and Nelson. The units of defined terms are intentionally displayed in Equations 1.2-1.4, but for the remainder of this research the heat index term, denoted as HI, in units of revolutions/mm will be utilized. Collectively, results suggest that the value of HI calculated by Equation 1.2 may be a suitable parameter to determine weld consolidation and other microstructural effects following FSW, and that a minimum value of HI may be required to achieve weld consolidation.

The HI term used in this research has been proven to be related to maximum temperature in the weld nugget for typical tool rotational and traverse speeds [121] and has been related to the formation of defects in the weld as well as grain growth in the SZ [122]. In many cases, maximum temperature is monotonically related to HI, but some cases have shown a non-monotonic relationship [140]. Researching FSW with varying process parameters on three different aluminum alloys, Hashimoto found only two conditions where temperature did not monotonically increase with the ratio of increasing tool rotation rate to tool traverse speed (Figure 1.12). Hashimoto used embedded thermocouples to directly measure temperature in various portions of the weld nugget using typical values of tool rotational speed and tool traverse speed for aluminum alloys. The representation of tool rotational rate to tool traverse speed used by Hashimoto is identical to that presented here in Equation 1.2 although Hashimoto did qualify the collective terms as a single variable.

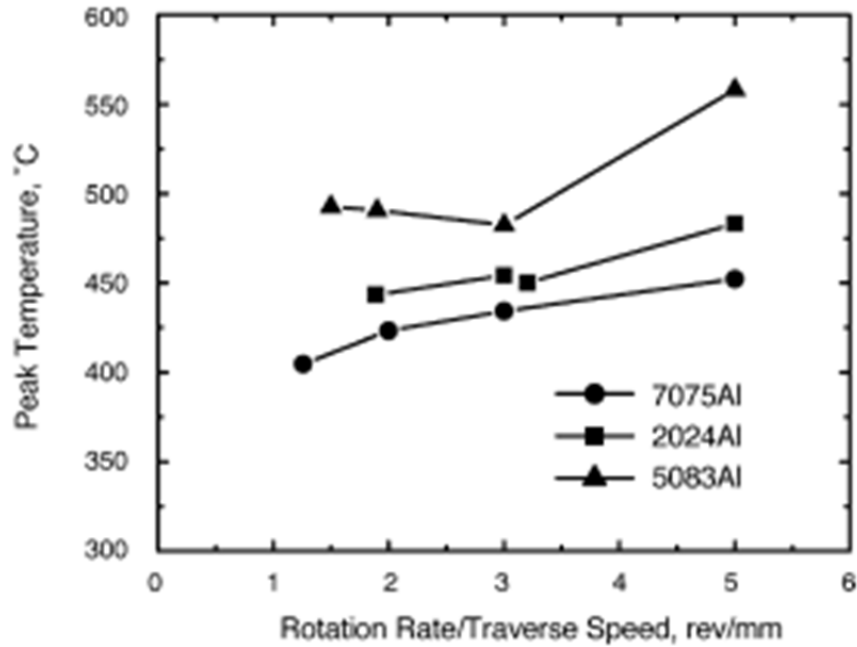


Figure 1.12 Effect of tool rotation rate/traverse speed ratio (defined as heat index in this research) on peak temperature for three different aluminum alloys from Hashimoto [from 140].

Although this research will not attempt to separate the dependence of evolved weld parameters with tool rotational speed and tool traverse speed individually, research by Arbogast and Hartley has shown that for a given tool geometry and depth of penetration, the maximum temperature is a strong function of tool rotational speed while the heating rate is a strong function of the tool traverse speed [139]. The dependence of maximum SZ temperature on tool rotational speed is widely accepted although the discussion of heating and/or cooling rates differs between sources. Using embedded thermocouples in NiAl bronze plates, Swaminathan measured the rate of change of temperature at various points and under various FSW conditions (Figure 1.13) [149]. These results showed that the heating rate (as the pin moved towards a thermocouple) was consistently greater in magnitude than the cooling rate (as the pin moved past a thermocouple); however, both the heating rate and the cooling rate, or more generally, the rate of change of temperature, increased as the tool traverse speed increased. For the research herein, no separation of heating rates or cooling rates will be attempted although

the more general conclusion that rate of change of temperature increases with increasing tool traverse speed will be utilized.

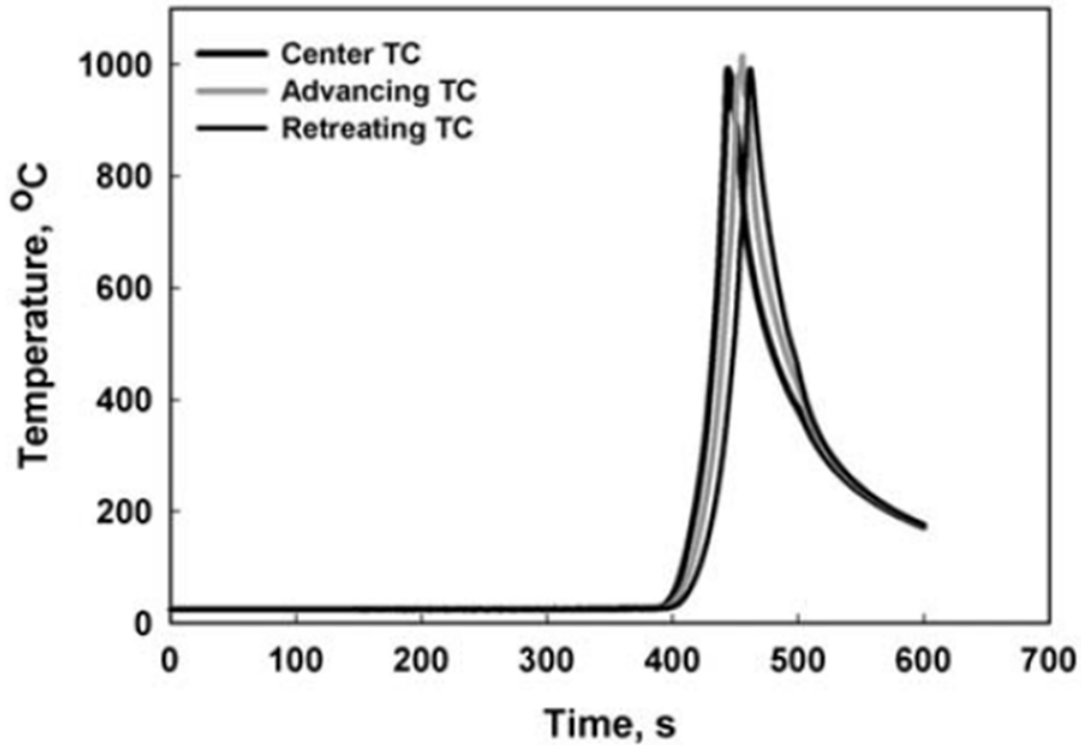


Figure 1.13 Typical heating and cooling rates during friction stir welding from [from 149] during friction stir welding of NiAl bronze plates with embedded thermocouples (TC).

It can be logically hypothesized that the evolved microstructure and material properties will be affected by both the maximum temperature and the rate of change of temperature although the mechanism behind each may differ. This hypothesis and the overall approach of estimating heat input using Equation 1.2 is strongly supported by comparison to traditional fusion welding. The fundamental reference for heat input and cooling rates for traditional fusion welding is work by Rosenthal in 1946 on the theory of moving heat sources and their application to metal treatments [150], and more recent textbooks on welding continue to use Rosenthal's equations as a theoretical basis [151, 152]. A short comparative summary to FSW will be presented here. The heat input due to fusion welding is typically expressed as heat input per unit length ($HI_{\text{fusionwelding}}$) in

units of kJ/mm and is a function of the rate of heat transfer from the heat source to the workpiece (\dot{Q}), typically calculated by multiplying the voltage and the current used during arc welding ($\dot{Q}=EI$ which is analogous to $P=\omega\tau$ in Equation 1.5 for FSW), and the welding speed (v) (Equation 1.5) [151]. In traditional fusion welding, the maximum temperature in the weld pool is strongly related to \dot{Q} (analogous to tool rotational rate in FSW) and the cooling rate is strongly related to v (analogous to tool traverse rate in FSW) [151, 152]. Although fusion welding and FSW are vastly different processes, the similarity in relationships of heat input, maximum temperature, and rate of change of temperature strongly support the methodology presented in this research. Additionally, the final equations for heat input for both methods (Equations 1.2 and 1.5) are theoretically very similar.

$$HI_{fusionwelding} = \frac{\dot{Q}}{v} \left(\frac{kJ}{mm} \right) \quad \text{Equation 1.5}$$

The HI term defined in Equation 1.2 is in units of revolutions per length and is not meant to be a useful dimensional analysis of FSW. The dimensions of HI are the inverse of WP which is defined as the number of revolutions the pin accomplishes per unit length of traverse motion. Other authors have attempted dimensional analysis of the FSW process to produce non-dimensional numbers corresponding to the heat input [131] as well as more fundamental energy balance methods to determine heat input [124, 137]. These methods incorporate several additional variables including material properties of the tool and workpiece such as thermal conductivity and specific heat capacity, as well as additional welding parameters not typically measured such as tool torque and power. Removing the dependence on material properties and the constant value of plunge force normally used in the FSW process, these methods reduce to similar relationships as Equation 1.2 except the dependence on traverse speed (v) in the denominator is often a squared relationship (typical for non-dimensional analyses) or the dependence on tool rotational speed (ω) in the numerator is often a squared relationship (typical for energy balance methods). Because no set standard exists for FSW, the simple and easy to measure relationship of HI in Equation 1.2 will be used to correlate microstructure and material properties following FSW in this research.

c. Friction Stir Welding on Oxide Dispersion Strengthened Steels

Based on the observed problems with traditional joining techniques on ODS steels and the promising capabilities of FSW, joining of ODS steels both in plate and tubular form by FSW has been tested on different ODS steels, and several authors have demonstrated the capability to join different ODS steels via FSW with good success [41, 56, 142, 144-147]. Initial investigation of FSW on ODS steel alloys began as early as 2007 when Feng at ORNL concluded that thin sheets of MA956 could be joined by FSW while preserving the oxide dispersion within the material and thereby preserving the materials high temperature mechanical properties [153]. Similarly, in an early investigation of FSW on MA957, Jashti showed MA957 could be friction stir welded successfully, albeit with a post weld decrease in hardness and potentially an increase in grain size in the weld nugget [144].

Several authors have researched the effects of FSW on the oxide particles in aluminum-containing ODS alloys such as MA956 and PM2000, but the results are inconclusive and do not include analysis of a range of FSW parameter conditions. Using scanning electron microscopy (SEM) and small angle neutron scattering (SANS), West concluded that FSW resulted in the dispersed oxides being slightly coarsened. Similarly using high-spatial resolution scanning transmission electron microscopy (STEM), Chen concluded that FSW did not appear to create a major change in size or distribution of oxides in PM2000 [60, 154]. Finally, in related work Legendre and Mathon used SANS to conclude that FSW using a single parameter condition of 600 RPM and 50 MPM on PM2000 caused oxide particles to grow in vicinity of the SZ [142, 143].

In total, research on FSW of ODS steels has produced some common conclusions: (1) fully consolidated defect-free welds can be achieved in ODS steels using FSW, (2) FSW has a minimal impact on the oxide dispersion in the SZ, (3) the SZ consists of coarsened and equiaxed grains, and (4) hardness in the SZ is reduced compared to the BM. What is missing in published research is a systematic correlation of FSW parameters in concert with microstructural characteristics and evolved material properties. Additionally, most current literature has focused on high heat input welding parameters (high rotational speeds and/or low traverse speeds), but a broader range of

heat inputs during FSW has not been explored. The aim of this research is to correlate FSW parameters of tool rotational speed and tool traverse speed to the evolved microstructure and material properties for MA956 in plate form.

d. Friction Stir Welding Techniques Used in this Research

The FSW geometry used in this research was similar to that shown in Figure 1.8 and was accomplished by MegaStir Technologies using a tool fabricated from an MS 80 grade of PCBN and a convex scroll shoulder step spiral (CS4) tool design which requires no tool tilt (Figure 1.14). FSW parameters of tool rotation rate in RPM and tool traverse speed in MPPM were varied to produce welds of differing quality and consolidation. Plunge force was maintained constant at 17.8 kN (4000 lbf). Four different friction stir welded plates were utilized in this research although the identical MA956 material was used in each (Table 1.4), and the FSW techniques were the same except for specific welding parameters of tool rotational speed and tool traverse speed. An example of a MA956 welded plate used is shown in Figure 1.15. Due to limited availability of MA956 material and the expense of the FSW process, welded plates of MA956 usually consisted of a single bead-on-plate run with FSW conditions varied and annotated on the plate similar to that shown on Figure 1.15. The workpiece was oriented such that the tool rotated in the x-y plane and traversed in the x direction with the z axis outward normal to the plate (Figure 1.16).



Figure 1.14 Friction stir welding tool used in this research. The tool is fabricated using a MS80 grade polycrystalline cubic boron nitride and includes a convex scroll shoulder and step spiral pin.

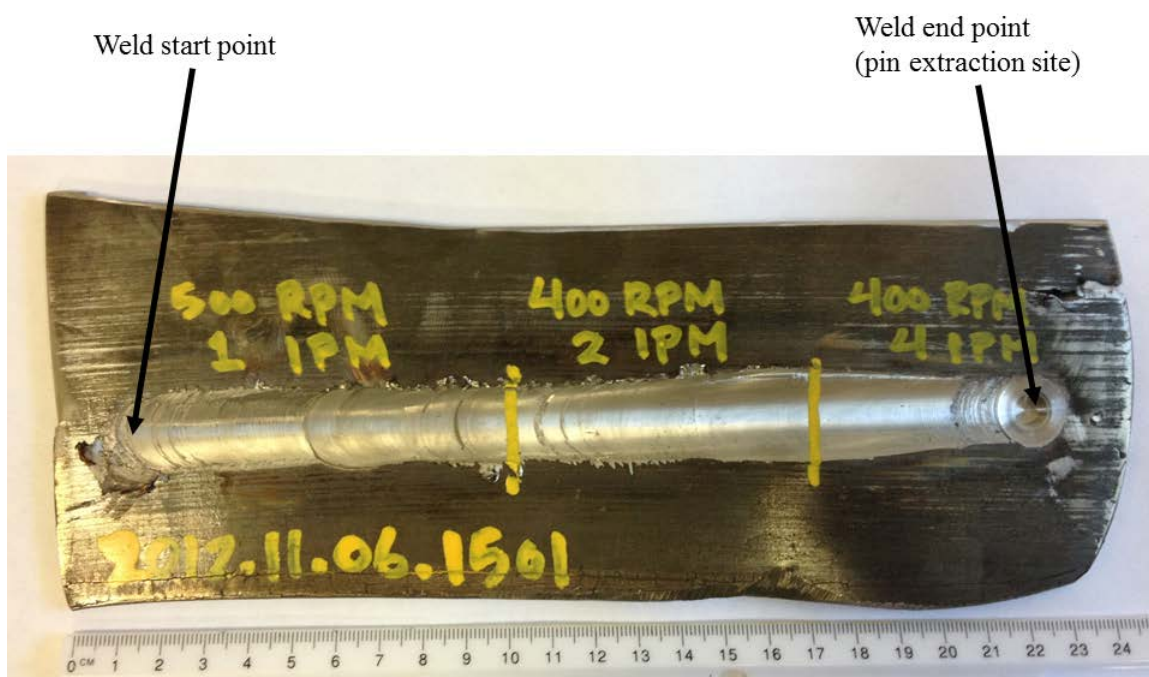


Figure 1.15 Example of a MA956 friction stir welded plate used in this research. Due to limited availability of MA956, single bead-on-plate runs with varying welding conditions were performed on individual plates.

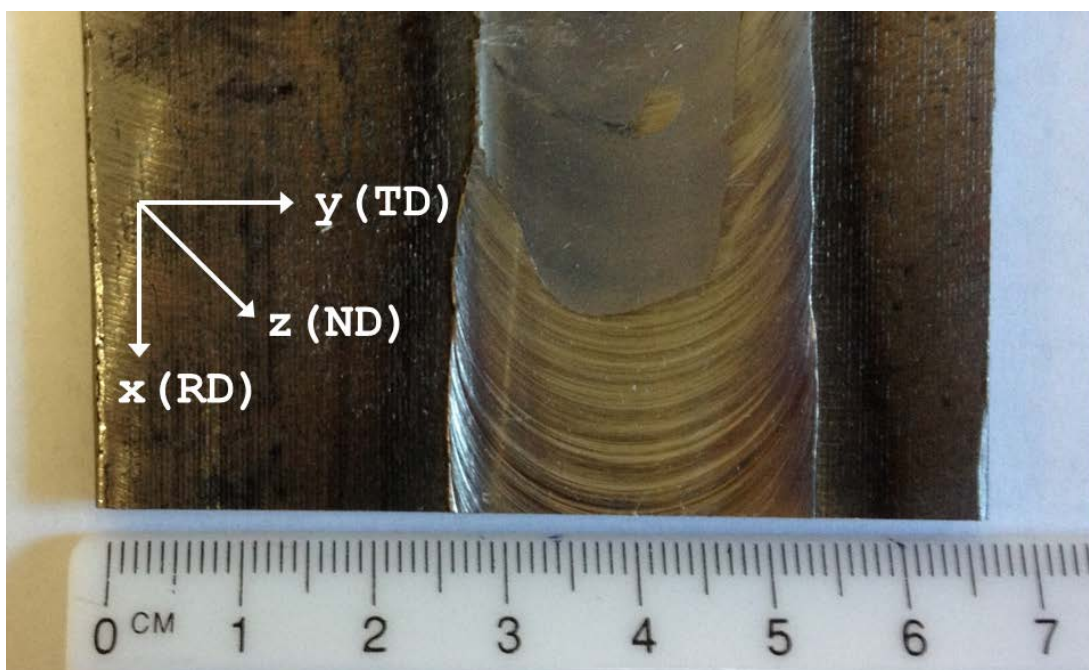


Figure 1.16 Weld orientation.

E. RESEARCH TASKS AND HYPOTHESES

The overall objective of this research is to evaluate FSW as an appropriate joining technique for MA956 steel to be used in high temperature applications including use in extreme coolant conditions such as molten lead and LBE for advanced reactor systems. This objective will be accomplished by establishing the processing, microstructure, and material property relationships following FSW of the ODS steel MA956. As discussed previously, ODS steels such as MA956 are promising candidates for structural materials in advanced fission and fusion reactor designs with one of the few limitations being practical joining methods that preserve the high temperature strength of the welded alloy. FSW is a proven joining method for aluminum and steel that has also shown significant potential for ODS alloys based on maintaining the alloy below its melting temperature thereby preventing agglomeration of oxide particles. While FSW has been successfully demonstrated on ODS steels in general and MA956 in particular, little is known on the effects of welding parameters most notably tool rotational speed and tool traverse speed, and most research to date has been on conditions with high thermal input.

The overall objective of this research is divided into three primary tasks: (1) determine the base metal microstructure and material properties of MA956 as a function of temperature, (2) determine the evolution of the friction stir welded microstructure and resultant material properties as a function of both welding parameters and temperature, and (3) determine the susceptibility of MA956 to LME. A flowchart break down of these three tasks is shown in Figure 1.17 that includes subtasks and a summary of hypotheses based on current literature for each task. The three primary tasks are divided into subtasks focused primarily on experiments required to determine the functional relationships between processing, microstructure, and material properties. For tasks (1) and (2) above the final material properties are assumed to be a function of the evolved microstructure and thus establishing microstructural properties such as grain size and oxide particle size and distribution are critical to the understanding of evolved material properties. Established relationships such as the Hall-Petch grain size strengthening and Orowan particle strengthening mechanisms will be used to relate microstructure to material properties. Additionally, material properties such as hardness, yield strength, and ultimate tensile strength will be compared to evaluate multiple techniques and prove existing relationships. For task (3), emphasis will be on establishing an experimental setup that evaluates the tensile properties of MA956 in a molten lead and LBE environment similar to that which a structural alloy would be exposed to in a lead or LBE-cooled reactor.

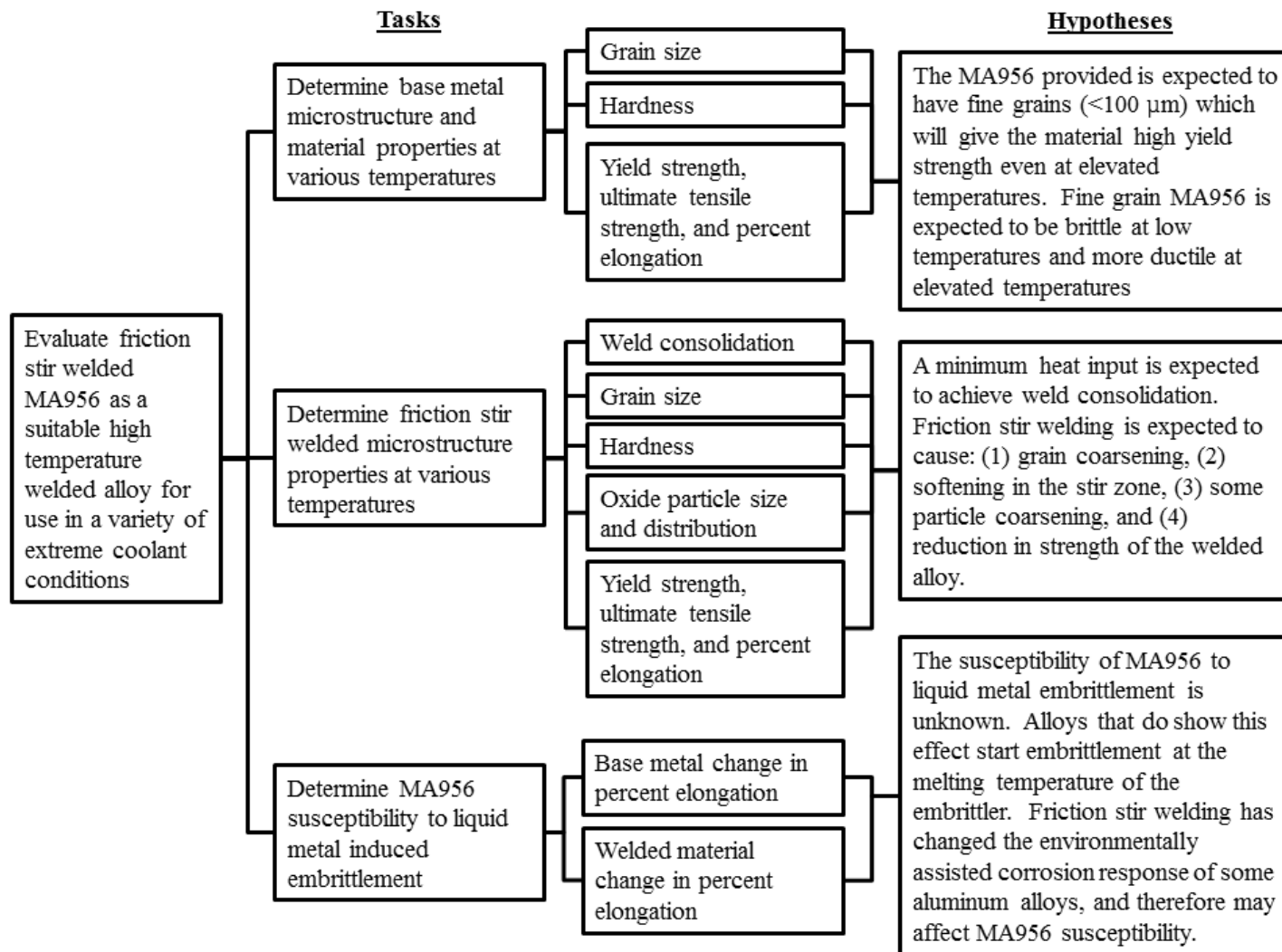


Figure 1.17 Flowchart breakdown of tasks and hypotheses for this research.

Based on the literature already summarized, several hypotheses can be drawn for the objectives in this research. Data on CG MA956 is readily available both from the vendor, Special Metals, and other research groups as previously cited. Although less prevalent, data for FG MA956 is in the literature, and based on the manufacturing process used for the MA956 in this research, it is hypothesized that the MA956 in this study is a FG alloy that will have yield strength greater than the CG MA956. It is also hypothesized that this MA956 will have limited ductility at low temperatures, similar to the CG material. Sufficient data in the literature on ODS steels and specifically MA956 exists to hypothesize that FSW will cause: (1) grain coarsening in the SZ, (2) an asymmetric softening in the SZ, (3) some degree of oxide particle coarsening, and (4) an overall reduction in strength of the welded joint. Comparison of grain size effects in the SZ following FSW must be coupled with the starting microstructure since both grain refinement and grain coarsening have been seen following FSW depending on the starting microstructure. Current research on the effect of FSW on the oxide particles in ODS aluminum-containing steels (such as MA956 and PM2000) is inconclusive and only suggests that some oxide particle coarsening may occur, and data only exists for a limited range of welding conditions. Therefore, the full effect of FSW on oxide particles in ODS aluminum-containing steels has yet to be established and is one of the sub-tasks of this research.

The LME response of ODS steels or other advanced RAFM or FM steels is not well documented in current literature, and insufficient evidence exists to draw detailed hypotheses on if or how MA956 will undergo LME in a molten lead or LBE environment. However, there is data from the late 1970s and early 1980s that addresses LME on previous generations of steels and gives some insight into what conditions might promote LME [155-158]. Similar to SCC and other EAC mechanisms, Shunk determined that some metal to embrittler⁵ couples produced a LME response while others did not [157]. Examples of material couples that cause LME include commercially

⁵ In this context the term “embrittler” refers to the molten material to which the candidate material is exposed. This convention in terminology is consistent with work by Shunk, Asher, Nicholas, and Old, all of whom did extensive research on LME in the late 1970s. Examples of typical molten metal embrittlors are mercury, lithium, gallium, and lead.

available iron (i.e. low purity iron) in molten lead which underwent LME, while higher purity iron did not undergo LME. The other primary factors that determined an LME response were temperature of the embrittler, and intimacy of contact between the metal and the embrittler. For this research, the task of determining MA956 susceptibility to LME will be accomplished by establishing the most likely conditions for LME in a slow strain rate test and evaluating any potential change in percent elongation to determine if LME occurred. This approach is consistent with guidelines in ASTM standards for slow strain rate testing to determine EAC [159].

F. CHAPTER OUTLINES

Although each chapter in this dissertation is intentionally written to stand alone covering a specific aspect of the overall objective, Chapters II through IV are directly related in order to establish the processing, microstructure, and material property relationships that are the core of this research. All chapters in this dissertation use the same baseline MA956 identified in Table 1.4 and the same FSW techniques outlined in paragraph D.3.d of this introduction, and for brevity these discussions are not repeated in subsequent chapters. A summary of the specific FSW parameters used is presented in Chapter II during discussion on weld consolidation, and subsequent to that, the majority of the remaining discussion is on fully consolidated welds. The insights gained in Chapter II and III on microstructure and oxide particle morphology following FSW are critical to the foundations of the material property relationships established in Chapter IV. The LME analysis is mostly distinct from that causal chain and is discussed separately. Similar to the task breakdown chart of Figure 1.17, an overall chapter outline of this dissertation is shown in Figure 1.18 and summarized below.

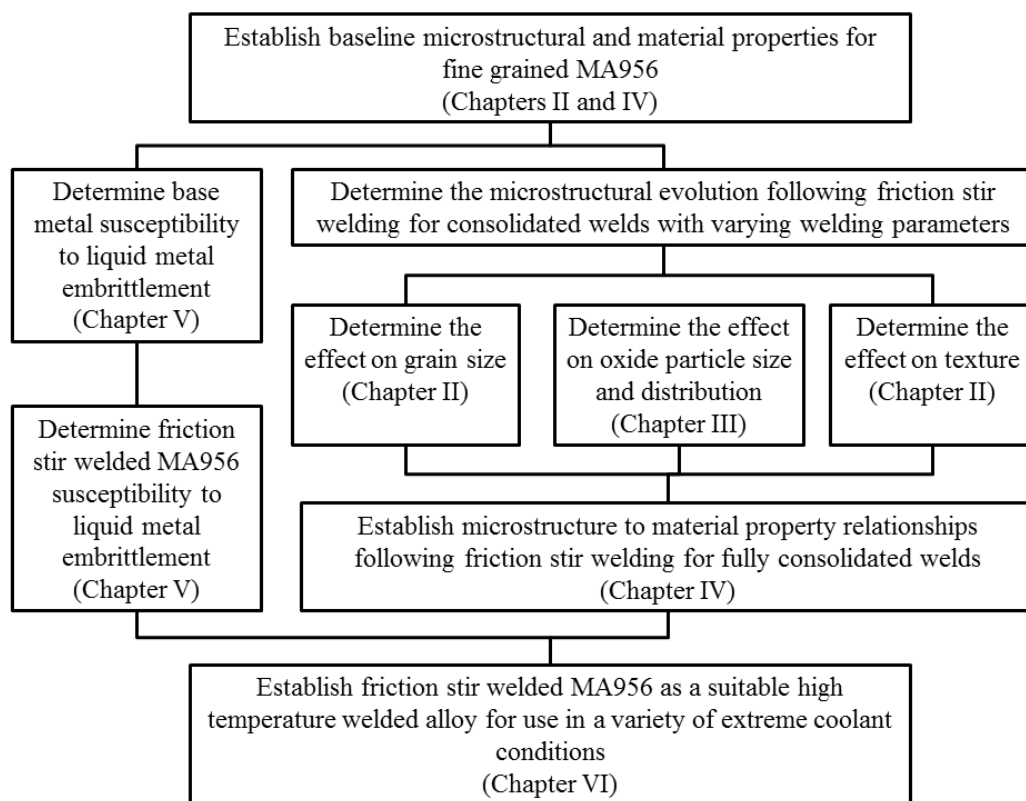


Figure 1.18 Block diagram outline of chapters in this dissertation.

In Chapter II, the processing-microstructure relationships for successful FSW of MA956 are established. This chapter details the MA956 ODS steel and the FSW process parameters used in this research. Comprehensive microstructural characterization methods (optical microscopy (OM), SEM, electron backscatter diffraction (EBSD), and microhardness analyses) were used to connect the evolution in weld microstructure (grain size and texture) with a variety of FSW conditions. These results show that friction stir welds with low tool rotational speeds or high tool traverse speeds produce tunnel defects in the SZ, and that the value of HI can be used as a parameter for predicting defect-free weld consolidation. Data from Chapter II will also show that grains are significantly coarsened in the SZ and the degree of coarsening can also be related to the heat input from FSW. Finally, Chapter II will show a typical asymmetric hardness profile across the weld nugget consistent with other research and will begin an analysis of strengthening contributions using a hardness versus grain size version of the Hall-Petch relationship (as compared to a traditional Hall-Petch plot of yield strength versus grain size).

In Chapter III, a variety of analytical techniques (SEM, STEM, energy dispersive x-ray spectroscopy (EDS), and small angle x-ray scattering (SAXS)) are used to establish the fate of oxide particles following FSW. These results show that FSW causes coarsening of existing Y-Al-O particles far greater than previously reported in open literature. This coarsening is a strong function of the heat input during welding. Mechanisms for this coarsening are proposed and the significance of the coarsening is discussed.

In Chapter IV, constant extension rate tensile testing is used to determine yield strength, ultimate tensile strength, and percent elongation of the BM and SZ as a function of temperature and welding parameters. Material parameters of MA956 including an experimentally determined Hall-Petch constant and strain hardening exponent are provided. The strengthening mechanisms behind the BM MA956 and friction stir welded MA956 are summarized, and using parameters from Chapters II and III, dominant strengthening mechanisms are discussed. Of specific note, the coarsening of oxide particles during FSW is shown to remove essentially all strengthening contribution of the dispersed oxides.

In Chapter V, two different LME experiments are developed to determine the susceptibility of MA956 to LME. A static U-bend experiment is used to determine the long term exposure effects of MA956 under tensile stress to molten lead and a slow strain *in situ* tensile test is designed and discussed. Using the slow strain rate tensile test, three different steels including MA956 are fractured in tension while exposed continuously to molten lead and LBE. Results from these tests are not fully conclusive but suggest that MA956 is not susceptible to LME at the conditions tested.

In Chapter VI, the relevance of this dissertation work, as a whole, is discussed and recommendations for future research as well the general use of ODS steels such as MA956 are made. The effectiveness of FSW as a joining mechanism for MA956 is summarized, and comparative predictions for other ODS steels are made. Recommendations are made for future research based on the results found in this research.

II. PROCESSING-MICROSTRUCTURE RELATIONSHIPS FOLLOWING FRICTION STIR WELDING

A. INTRODUCTION

As discussed in Chapter I, traditional joining methods for ODS steels have proven to be unsuccessful or not viable for all applications while a number of investigations have demonstrated that ODS steels can be joined using FSW [41, 60, 142–147, 153, 154], and even more specifically that MA956 can be successfully joined using FSW [56, 141]. Several common conclusions are made from these investigations while some important differences and disparities can also be found. The most important conclusion from all of the research is that FSW can successfully produce consolidated welds in ODS steels, including MA956. Most of the research uses FSW conditions with high thermal input, and there are no research analyses on ODS steels that use a range of conditions within a single study. A total of twelve references that researched FSW of ODS steels were reviewed. Some of these references do not document welding parameters used and not all fully address or demonstrate weld consolidation. Across all of these references the range of HI, as defined in this research, is 8 to 20. The research in this dissertation will extend the lower limit of HI to 2 and will address weld consolidation for each case individually. Based on the theoretical foundations of FSW established by Mishra and Nandan and the large amount of experimental FSW work on aluminum and traditional steels, FSW is expected to have a significant effect on the microstructure in the SZ. The majority of FSW research on ODS steels is on CG alloys and the microstructure effect of FSW is grain refinement as predicted by Mishra. In the case of FG starting alloys, hardness is noted to be reduced in the stir zone and an overall reduction in strength of the weld has been found.

The objective of this chapter is to determine the processing-microstructure-property relationships and then to connect the microstructural changes to local variations in material properties. This will be accomplished specifically by determining: (1) weld consolidation, (2) grain size in the SZ, and (3) SZ hardness all as a function of the welding parameters tool rotational speed and tool traverse speed. This chapter will

correlate these parameters to overall grain morphology and evolved material properties and will serve as the basis for strengthening mechanisms in Chapter IV. The research in this chapter expands the current literature of FSW of ODS steels by conducting a systematic review of welding conditions, including low to high heat inputs, and by analyzing weld consolidation for each case. Additionally, unlike some other research studies, the ODS alloy in this research is not subjected to heat treatments before or after FSW and thus changes in microstructure are isolated to effects from FSW and not the combined effects of FSW and heat treatments.

B. EXPERIMENTAL PROCEDURE

The MA956 and FSW techniques in this chapter are the same as discussed in Chapter I. Two different plates of MA956 were utilized in this chapter (Figures 2.1 and 2.2) for the majority of data acquisition. A third plate of MA956 (Figure 2.3) from previous collaborative work with LLNL was also utilized to a lesser extent. Figure 2.1 pictures the MA956 plate used for initial trial FSW attempts by MegaStir and shows five different initial FSW conditions used.⁶ This initial plate was only used for weld consolidation analysis done by OM and was utilized to determine optimum welding conditions for subsequent welds. The close proximity of weld passes in Figure 2.1 does not support independent analysis of FSW parameter effects outside of the SZ. This was considered acceptable since the plate in Figure 2.1 was only intended to establish weld consolidation.

⁶ The annotations in Figure 2.1 and other raw data sources from MegaStir list FSW conditions in English Engineering units of RPM and inches per minutes (IPM). For consistency with other literature all discussion in this dissertation will utilize the International System of Units (SI). Use of English Engineering units exists only in raw images where conversion to SI units would cause additional confusion. For simplicity in this research the only conversion necessary is in tool traverse rate where nominally 1 IPM = 25 MMPM.



Figure 2.1 Initial MA956 plate used for friction stir welding consolidation analysis. The white annotations in this image indicate the welding parameters used in English Engineering units of revolutions per minute and inches per minute. The purple outlines indicate areas of optical microscopy samples used in other figures of this chapter.



Figure 2.2 Subsequent MA956 plate used for friction stir welding analysis. Annotations in this image indicate the welding parameters used in English Engineering units. The transverse sections for optical microscopy specimens are visible from three different welding conditions. This friction stir welded plate of MA956 is the basis for data in Chapters II, III, and IV of this dissertation.



Figure 2.3 MA956 plate used from previous collaborative research. This friction stir welded plate utilized the low heat input conditions of 275 RPM and 100 MPPM and was only used for microstructural analysis and hardness determination of that condition in this chapter.

Figure 2.2 shows the friction stir welded plate of MA956 used for most research in this dissertation. Based on initial observations of weld consolidation using Figure 2.1, the FSW parameters of 500 RPM/25 MMPM, 300 RPM/50 MMPM, and 400 RPM/100 MMPM were determined to be optimum selections for welding parameters likely to produce consolidated welds while varying the heat input from a low HI value (400 RPM/100 MMPM) to a high HI value (500 RPM/25 MMPM). The plate depicted in Figure 2.2 was utilized for all microstructure and hardness analysis in this chapter (with the exception of the welding parameter condition of 275 RPM/100 MMPM) as well as oxide particle analysis in Chapter III and all material property and strengthening mechanism analysis of Chapter IV.

Figure 2.3 shows a friction stir welded plate of MA956 that was used in previous unpublished collaborative research with LLNL. This research was conducted only to determine the possibility of using FSW on MA956 and offered no other significant conclusions; however, after initial review of data gathered from research on Figure 2.2, the additional FSW parameter condition of 275 RPM/100 MMPM (the conditions used in Figure 2.3) offered valuable insight into the hardness to grain size relationship following FSW. For this reason data from this sample was gathered. The MA956 material used in Figure 2.3 is identical to other MA956 used in this research, and FSW conditions other than tool rotational speed and tool traverse speed were also similar.

Samples of the friction stir welded MA956 plates in Figures 2.1–2.3 were sectioned and analyzed by OM, SEM, EBSD, and micro-indentation. Transverse cross sections perpendicular to the weld path were metallographically prepared for each welding condition. These sections were prepared by standard metallographic preparation techniques using SiC papers, aluminum oxide polishing solutions, and 0.05 μm colloidal silica solution, followed by electropolishing at 20 V using an electrolyte containing 10% perchloric acid in ethanol maintained at 250°K (-23°C). Microstructural examinations were conducted using a Zeiss Neon 40 field emission SEM operating at 20 keV. All EBSD analyses were carried out using the EDAX-TSL orientation imaging microscopy (OIM) 6.0 system with a Hikari camera at 20 keV using a 60 μm objective aperture with an approximate probe current of 1 nA. EBSD data was de-noised using

TSL OIM software cleanup functions of grain dilation and grain confidence index standardization in accordance with recommended settings. To ensure an adequate number of grains were counted during analyses, all inverse pole figure (IPF) maps and all pole figures were calculated from areas with minimum dimensions of 150x300 μm equating to a minimum of 2000 grains for the most limiting case. For areas of fine grain size, such as the BM, a step size of 0.25 μm was used equating to over 20,000 grains in the analysis area. For other areas with a larger average grain size, a step size of 0.5 μm was used.

Microhardness measurements were performed using a HVS-1000 microhardness tester (Figure 2.4a) with a diamond indenter using a 1 kg-force (2.2 lbf) load and a dwell time of 15 seconds. The hardness tester calibration was verified before and after indentation using a National Institute of Standards and Technology (NIST) certified specimen with a hardness of 726 HV and a certified error of 1.9%. Micro-hardness measurements were taken across the weld nugget at the mid-plane of the transverse section of the weld in a horizontal direction and at RS TMAZ, SZ center, and AS TMAZ in vertical directions. Rectangular specimens from Figure 2.2 (the MA956 plate with weld conditions of 500 RPM/25 MMPM, 300 RPM/50 MMPM, and 400 RPM/100 MMPM) were used for micro-indentation as well as other microstructure analyses and are shown in Figure 2.4b. A typical hardness indentation as seen through the indenter is shown in Figure 2.4c.

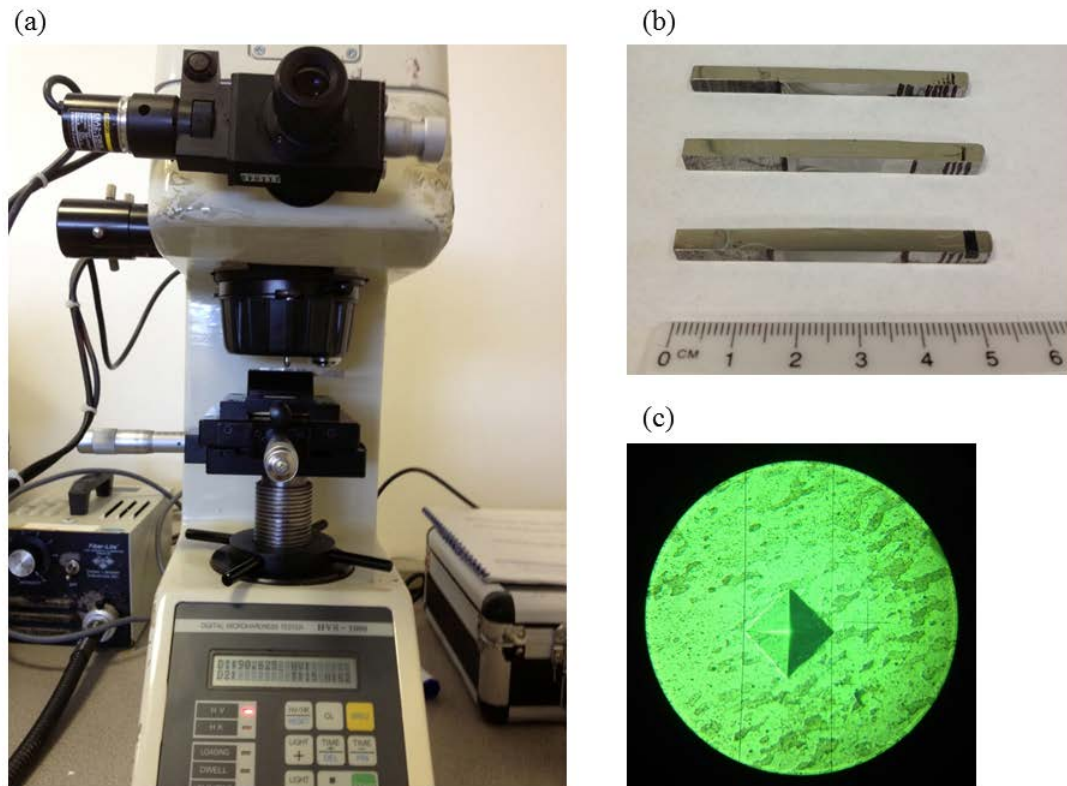


Figure 2.4 (a) HVS-1000 microhardness tester used in this research, (b) specimens from Figure 2.2 used for micro-indentation, and (c) a typical indentation as seen through the indenter.

Based on other research that showed large gradients in hardness across the TMAZ [141, 142, 145], a method for spacing of indentations was developed to assess these gradients without compromising accuracy of the individual indentations. This method included horizontal spacing of 500 μm and vertical spacing of 150 μm and is depicted in Figure 2.5 for the 500 RPM/25 MPPM sample. In addition to showing the arrangement of indentations, Figure 2.5 was taken from the TMAZ of the highest heat input condition (which will be shown later to correlate to the most abrupt change in grain size) and shows a swirling pattern that correlates to the TMAZ. The optical micrograph of Figure 2.5 was taken after metallographic preparation but prior to electropolishing, and was intentionally taken in this configuration to show optically the TMAZ. Figure 2.6 is the indenter image of the inset area in Figure 2.5 and shows the large gradients that exist in the TMAZ, both

in the vertical and horizontal directions. These gradients only exist in the TMAZ as will be shown later in this chapter. To demonstrate that the close spacing used in the vertical direction (150 μm) did not adversely affect hardness values, a test area was performed in the SZ of the 500 RPM/25 MPPM sample (Figure 2.7). At this time, it was known that there was little variation in hardness in the SZ, and thus it was anticipated that any variations in the test area of Figure 2.7 would be due to inaccuracies associated with indentations being too closely spaced. In the horizontal lines of indentations of Figure 2.7 (annotated A, B, and C and highlighted in yellow), the left most, right most, and center indentation of each line were all within the 1.9% accuracy of the indenter and thus it was concluded the close proximity spacing of 150 μm did not affect the indentations. In total each specimen in Figure 2.4b contained a horizontal line of indentations (consisting of 3 indentations in a vertical row as shown in Figure 5) and three vertical lines of indentations at the RS TMAZ, SZ center, and AS TMAZ. In addition to the experimental value of these results, the indentations established visible markers that were very valuable later in subsequent analyses to determine location within the sample.⁷

⁷ It is acknowledged that experimental results are not normally discussed in the experimental procedure sections of research; however, the initial results presented in this paragraph formed the basis for the experimental procedure and are not part of the core results from this chapter. This approach is deemed acceptable and is summarized as follows: an initial hypothesis is made, initial data is gathered, that initial data is used to develop an experimental procedure, and final data is gathered based on the developed procedure. This methodology will be used in remaining chapters so at times initial results will be given in the experimental procedure section to support the procedure developed.

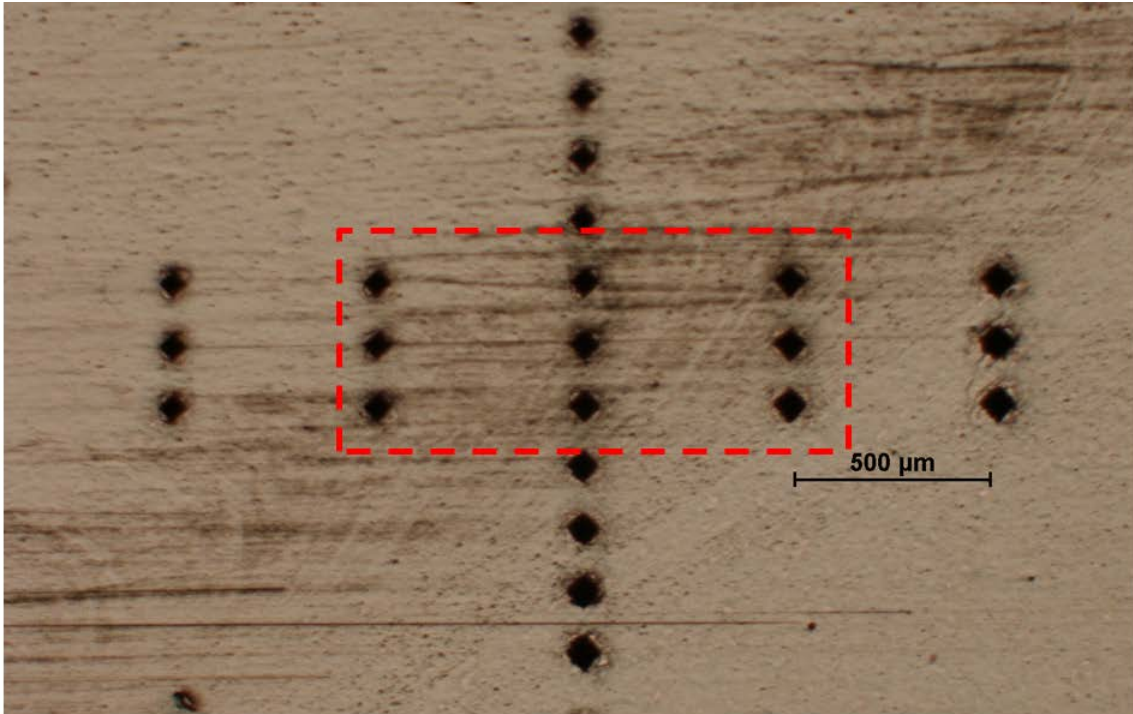


Figure 2.5 Optical micrograph of the thermo-mechanically affected zone for the 500 RPM/25 MPPM condition showing the vertical and horizontal spacing used for indentation. The inset area corresponds to Figure 2.6.

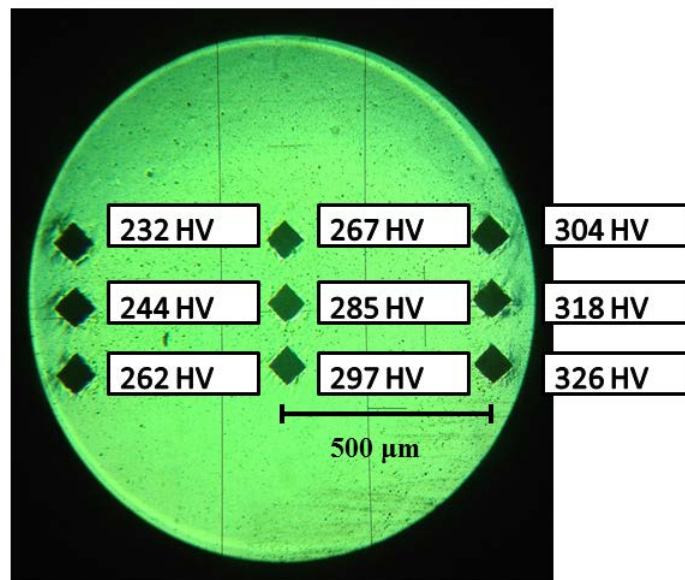


Figure 2.6 Optical micrograph taken through the HVS-1000 microhardness tester showing the large vertical and horizontal gradients in hardness in the vicinity of the thermo-mechanically affected zone. This area correlates to the inset area on Figure 2.5.

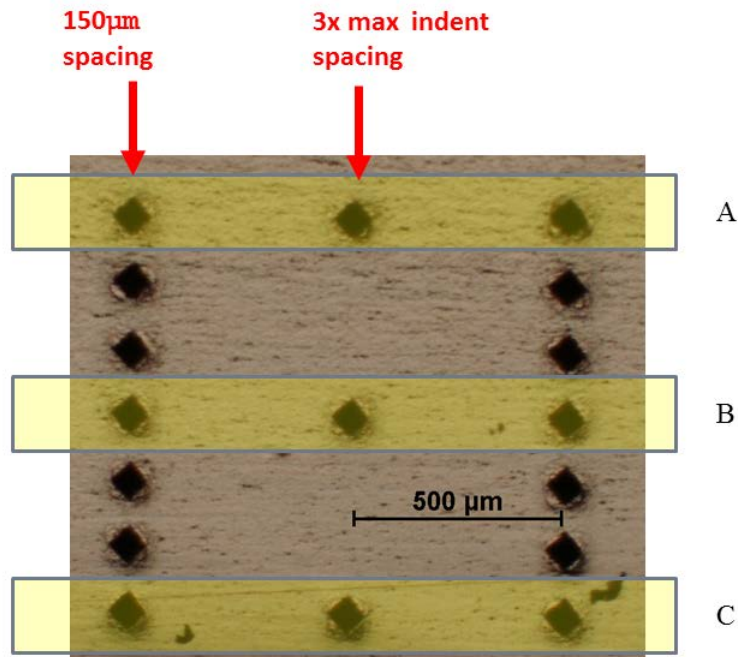


Figure 2.7 Micro-indentation test area used to verify that the proximity of indentations did not adversely affect indentation accuracy. The left most, right most, and center indentations in the lines A, B, and C all had hardness values within the accuracy of the indenter.

C. RESULTS

1. Base Metal Microstructure

BM MA956 consisted of fine ferrite grains (average grain size of $0.89\ \mu\text{m}$) elongated in the rolling direction of the plate (Figure 2.8). The BM texture contained a γ fiber with a strong $\{110\}\langle 111\rangle$ component, consistent with other rolled body centered cubic (BCC) materials (Figure 2.9) [160]. The pole figures of Figure 2.9 are oriented to show transverse views of the welded plate and the axis orientation matches the weld diagram of Figure 1.16, i.e. the y-z plane corresponds to the cross section of the weld. This is different than typical depictions of rolled plate textures since they would normally be oriented in planar views of the plate (x-y plane), but the transverse orientation is intentionally displayed to allow for direct comparison to the evolved texture following FSW which will be shown later. The FG structure of the BM MA956 gave it a high uniform hardness of $346\ \text{H}_v$.

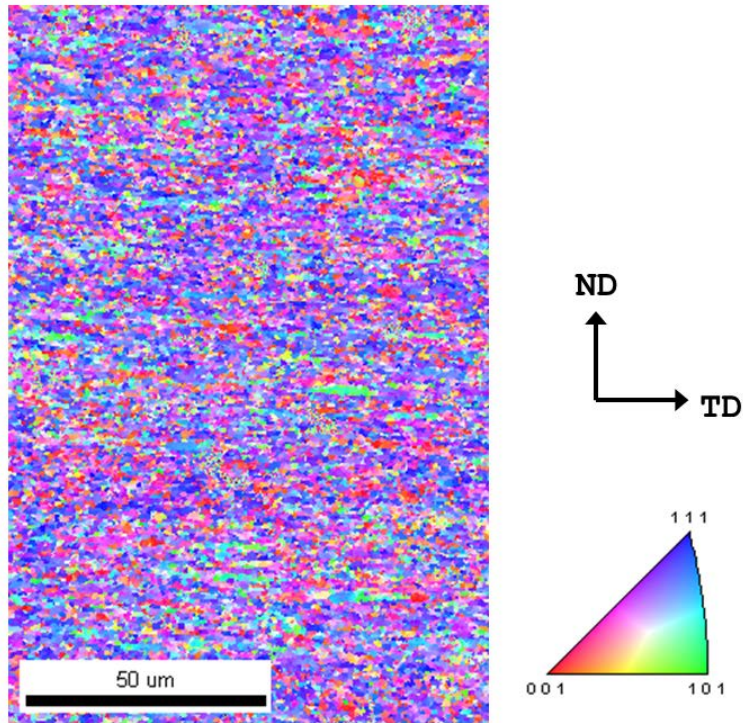


Figure 2.8 Inverse pole figure map for base metal MA956 showing sub-micron grains oriented in the rolling direction of the plate.

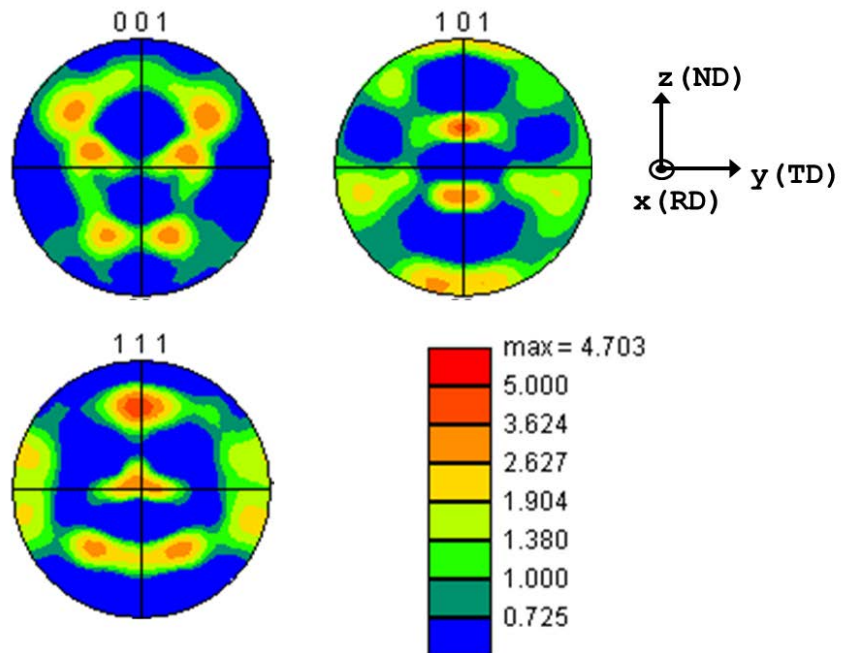


Figure 2.9 Pole figures for base metal MA956 corresponding to rolled texture for a body centered cubic structure.

2. Weld Consolidation

Full-penetration defect-free welds were observed for a range of FSW conditions with higher heat input (Table 2.1 and Figures 2.10 and 2.11). For reference five different sources from the current literature that include FSW on ODS steels have been inserted on Figure 2.10 showing the typically high heat input conditions used in most other cases. Heat input was expressed using the ratio of the rotational speed to traverse speed as discussed in Chapter I (Equation 1.2). Weld quality and penetration were determined by macrographs of the weld nugget as a function of RPM and MPPM combinations in order to establish the weld parameters necessary to achieve defect-free microstructures. Macroscopic metallographic observations are summarized in Table 2.2. A higher heat input, i.e., increasing tool rotation rate or decreasing tool traverse speed, tended to result in a defect-free nugget. Examples of weld consolidation macrographs are shown in Figure 2.11. These macrographs correspond to the specimens taken from Figures 2.1 and 2.2. Defect-free welds were observed when HI was greater than 4 (Figures 2.11a and 2.12b and shaded entries of Table 2.1). For conditions with a HI less than 4, welds were observed to be defective with tunnel defects occurring at the bottom or edges of the SZ (Figures 2.11c and 2.11d). Macrographs taken by MegaStir from all eight FSW parameter combinations are contained in Appendix B.

Table 2.1 Friction stir welding parameter summary. Shaded entries indicate defect-free consolidated welds.

Tool Rotation Rate (RPM)	Tool Traverse Speed (MMPM)	Heat Index	Weld Quality	Weld Penetration
200	50	4	Lack of Consolidation	Incomplete
300	50	6	Defect-free	Full
300	100	3	Lack of Consolidation	Incomplete
300	150	2	Lack of Consolidation	Incomplete
400	50	8	Defect-free	Full
400	100	4	Defect-free	Full
400	175	2.3	Lack of Consolidation	Incomplete
500	25	20	Defect-free	Full

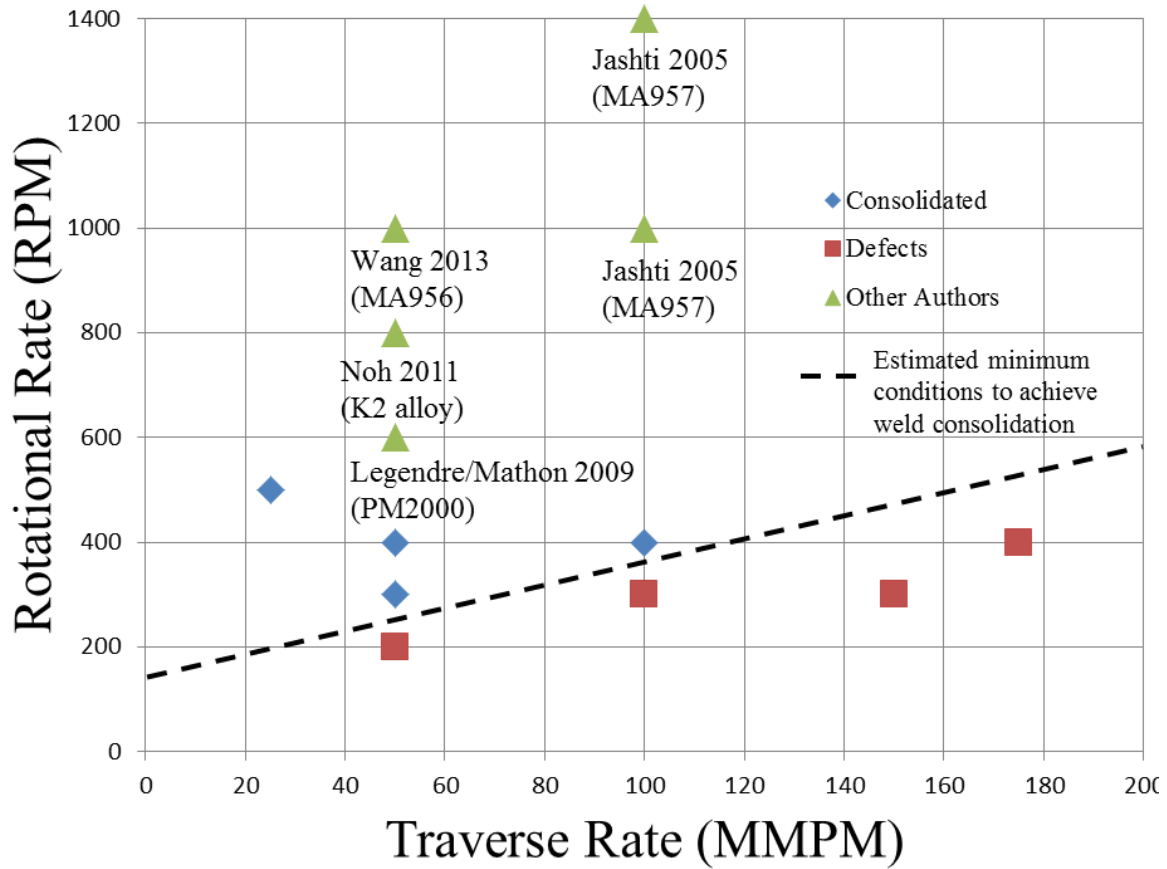


Figure 2.10 Friction stir welding parameter map illustrating weld parameters for defect-free welds. The dotted line is illustrative of an estimated minimum process parameters achieve weld consolidation. Green triangles represent typical high heat input conditions used during friction stir welding of similar oxide dispersion strengthened steels in the current literature.

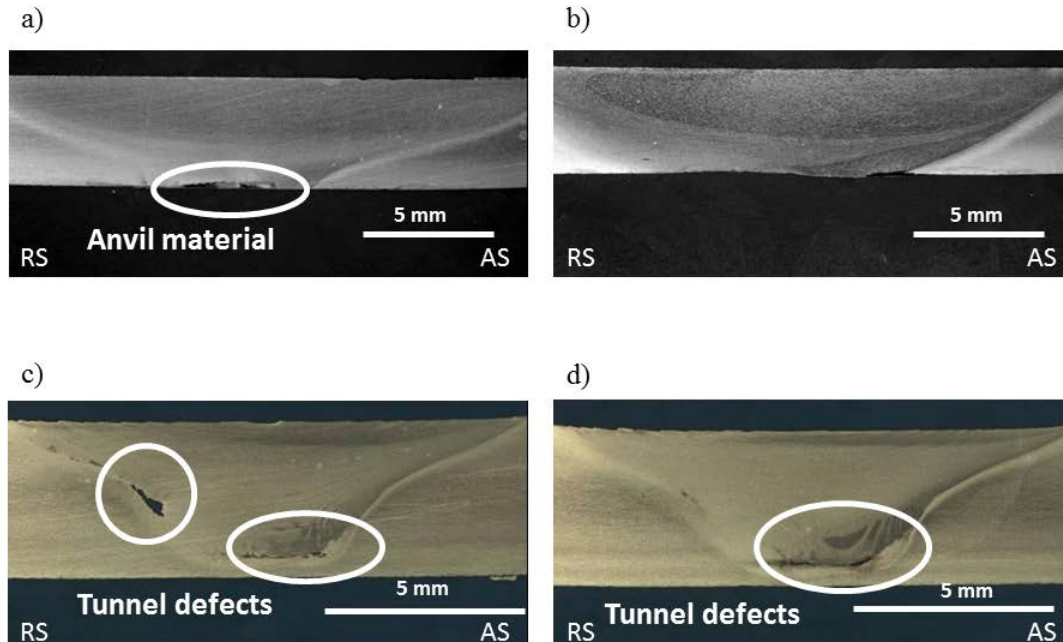


Figure 2.11 Optical macrographs of transverse metallographic cross-sections for (a) 400 RPM/100 MPM and (b) 500 RPM/25 MPM weld parameter combinations showing full penetration defect-free welds and (c) 300 RPM/100 MPM and (d) 300 RPM/150 MPM combinations showing tunnel defects.

A small amount of anvil material (a mild steel) was inadvertently extracted into the bottom of some welds as shown in Figure 2.11a due to variations in thickness of the as received MA956 plate (note the differences in plate thickness in Figure 2.11). In an effort to achieve full penetration, the FSW tool penetrated through the plate thickness and contacted the support anvil. This is not uncommon, especially with variations in the plate thickness, because the tool pin tip is in very close proximity to the bottom of the plate. The material drawn into the weld nugget is not considered to be a defect associated with weld parameters but could be a defect in service. In addition to the defects shown for the 300 RPM/100 MPM and 300 RPM/150 MPM conditions, similar tunnel defects were observed for RPM/MPM combinations of 200 RPM/50 MPM and 400 RPM/175 MPM leading to lack of consolidation in the weld nugget (Appendix B).

The weld nugget zones formed during the welding accomplished in this research were basin-shaped as opposed to elliptical as defined by Mishra (Figure 2.11 compared to

Figure 1.10a). Additionally, as already discussed by Mishra and several authors, the shape of the nugget zone is dependent on FSW parameters [121]. Clearly, for high heat inputs, Figures 2.11a and 2.11b, the weld nugget is very broad both at the weld crown and weld root. In comparison, for low heat input, Figures 2.11c and 2.11d, the width of the weld nugget is narrow at the weld root. This is best visualized by looking at the weld nugget width at the centerline of the plate.

3. Stir Zone Microstructure

Each FSW parameter combination produced a SZ microstructure with coarsened and nearly equiaxed ferrite grains, a significantly lower average hardness value compared to the BM, and a BCC torsional texture. No phase transformations occurred in any of the FSW conditions and the entirety of the weld remained a BCC ferritic structure. Grain size in the SZ for all the different FSW parameter sets illustrate significant grain coarsening in the stir zone compared to the very fine average grain size of 0.89 μm in the BM (Figures 2.12 and 2.13). The data of Figure 2.13 indicates that grain size does not monotonically increase with HI. Specifically, the grain size for HI=6 (300 RPM/50 MPPM) is less than the grain size for HI=4 (400 RPM/100 MPPM); however, grain size did monotonically increase with increasing tool rotational speed suggesting tool rotational speed may be the dominant parameter for grain coarsening. Further analysis using FSW conditions with singular changes in tool rotational speed and tool traverse speed would be required to fully determine this response. For each FSW parameter combination, grain size was highest in the center of the SZ and decreased moving outward to the BM. No abnormal grain growth was noted in any area of any sample. The grain size reduction, traversing from the SZ to the BM, was not symmetric. For example, the grain size reduction was gradual moving from the SZ toward the RS. Similarly, the grain size reduction was gradual moving outward from the SZ to the AS but was sharply reduced at the TMAZ. Similar gradients in grain size existed across all FSW weld parameter sets although the grain size reduction on the AS TMAZ was most dramatic for the 500 RPM/25 MPPM weld parameters corresponding to the highest HI. Grain size as a function of weld position for the 500 RPM/25 MPPM weld parameters along a mid-plane cross-section of the sample is shown in Figure 2.14.

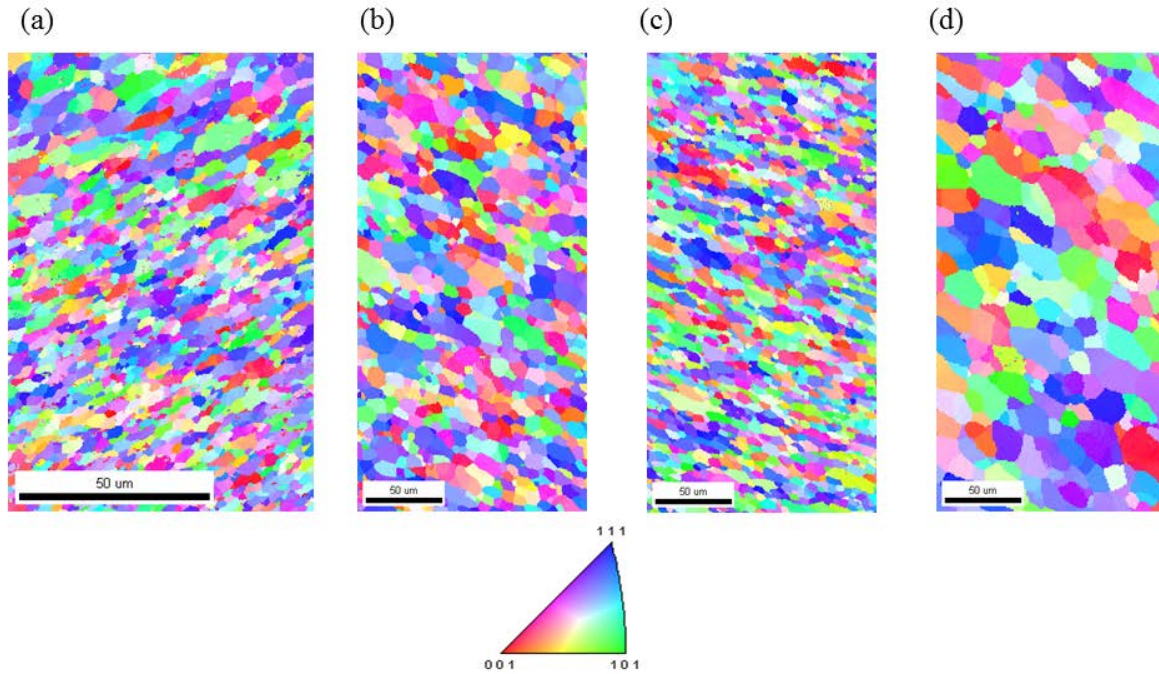


Figure 2.12 Inverse pole figure maps for (a) 275 RPM/100 MPM (HI=2.75), (b) 400 RPM/100 MPM (HI=4), (c) 300 RPM/50 MPM (HI=6), and (d) 500 RPM/25 MPM (HI=10) showing increase in grain size as HI is increased during friction stir welding.

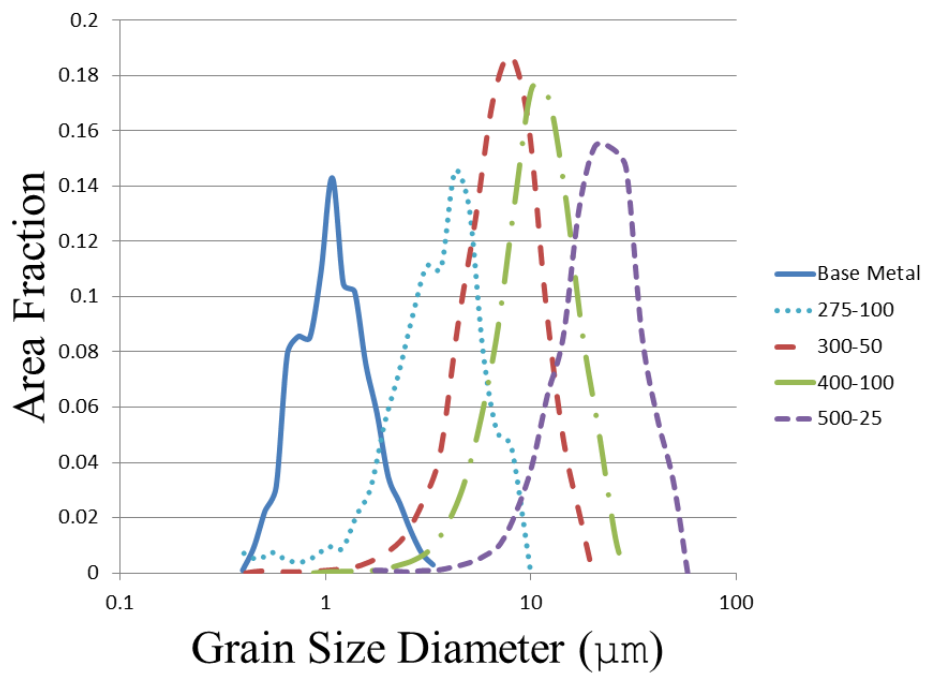


Figure 2.13 Stir zone grain size distribution for different friction stir welding parameters.

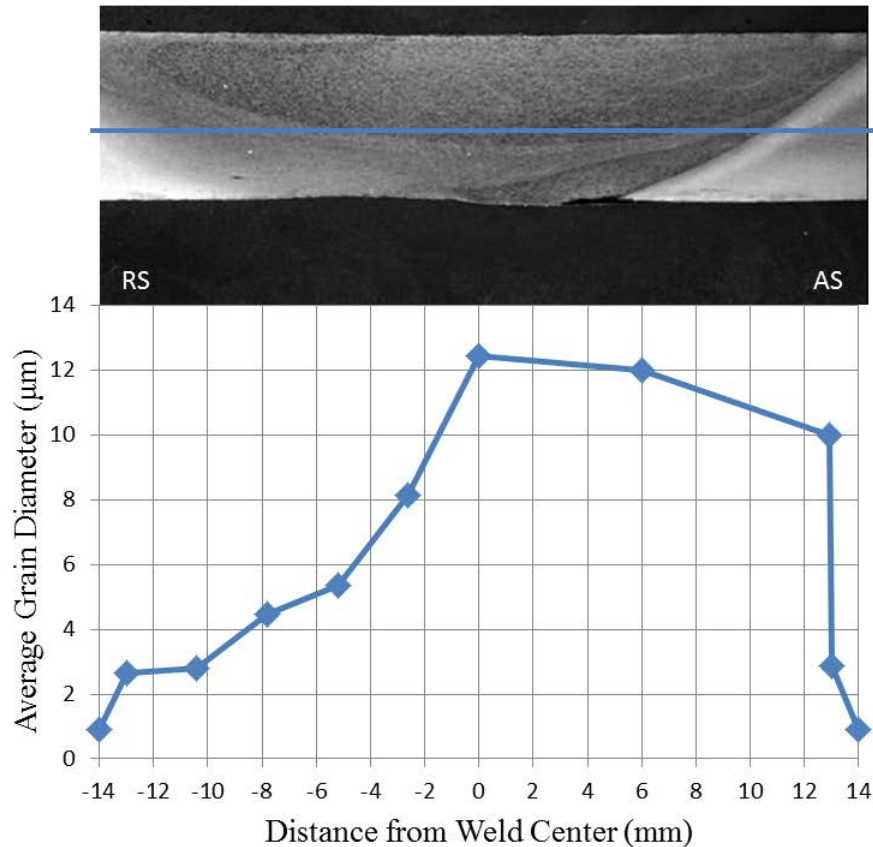


Figure 2.14 Average grain diameter for 500 RPM/25 MPPM weld parameter condition along the mid-plane of the weld.

Closer examination of the high angle and low angle grain boundary (HAGB and LAGB, respectively) structures show that while the grain size defined by HAGBs increased systematically with increasing heat input (black lines in Figure 2.15), a persistent LAGB structure was present for all microstructures. LAGBs are defined here as grain boundaries with scalar misorientations between 1-10° (bold red lines in Figure 2.15). The grain boundary network for each microstructure was comprised of approximately 20% LAGBs (ranging from 17.0% to 23.8%), regardless of heat input. In the 400 RPM/100 MPPM grain boundary map (Figure 2.15c), many of the larger oxide particles were incorrectly detected as grain boundaries and thus the 400 RPM/100 MPPM condition showed an incorrectly high percentage of 38.2% LAGBs.

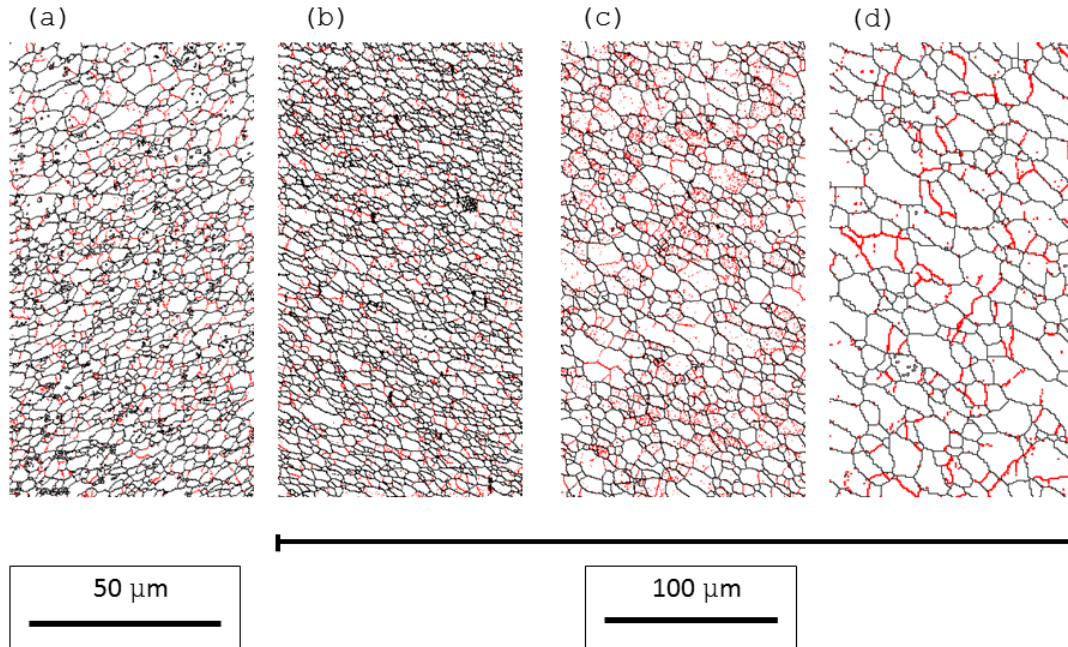


Figure 2.15 Stir zone grain size maps for (a) 275 RPM/100 MMPM, (b) 300 RPM/50 MMPM, (c) 400 RPM/100 MMPM, and (d) 500 RPM/25 MMPM combinations. Bold/red lines indicate low angle grain boundaries ($1 < \theta < 10$ degrees). Black lines indicate high angle grain boundaries ($\theta > 10$ degrees).

For each FSW combination, hardness decreased in the horizontal direction across the weld nugget (Table 2.2 and Figure 2.16). Each hardness data point in Figure 2.16 represents the average of three hardness measurements to account for data scatter. Experimental error associated with hardness measurements was 1.9% for homogeneous areas such as the BM and SZ; however, variations up to 10% were seen in the TMAZ with as little as 300 μm spacing between indentations (Figure 2.17). This data scatter was attributed to actual hardness variations due to the differences in locations of the indentations rather than experimental error on hardness measurements based on the very large gradients in grain size near the TMAZ. Because of this, the hardness indentation spacing method discussed in paragraph II.B and shown in Figure 2.5 was developed and utilized.

Table 2.2 Stir zone hardness and stir zone grain size diameter for friction stir welding parameter conditions.

FSW Condition (RPM/MMPM)	SZ Grain Size Diameter (microns)	SZ Hardness (H _V)
BM	0.89	346 ± 6.6
300/50	4.16	225 ± 4.3
400/100	6.94	221 ± 4.2
500/25	12.5	218 ± 4.2

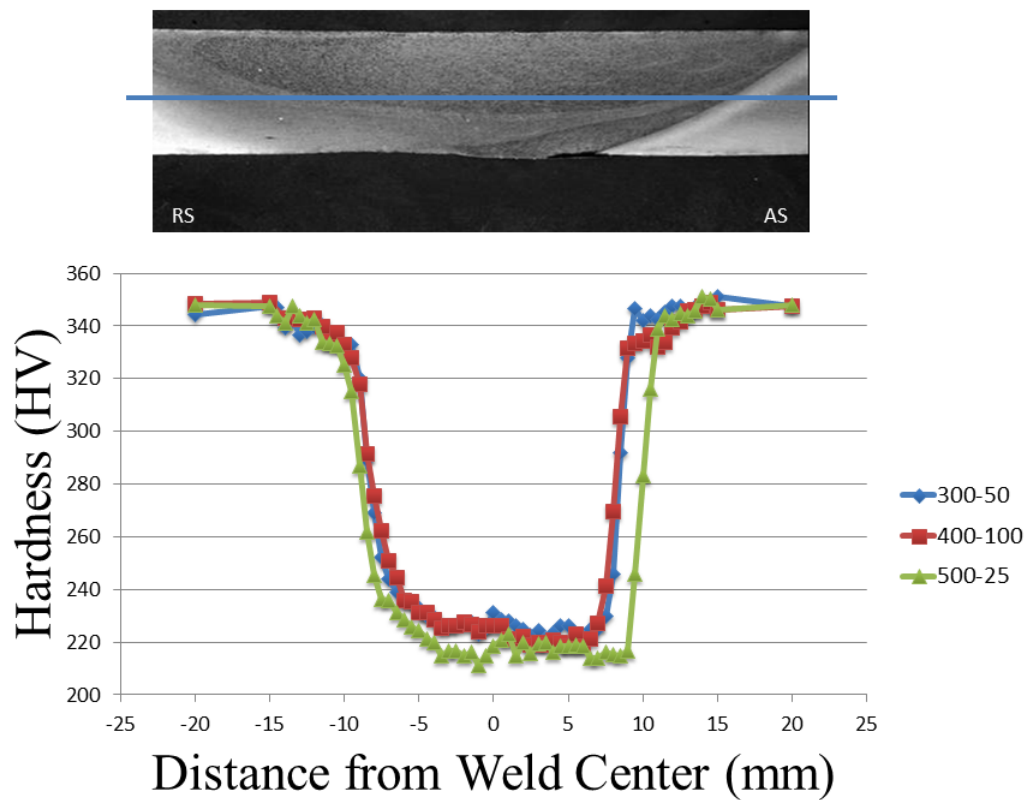


Figure 2.16 Hardness profile across the stir zone for varying friction stir welding parameters.

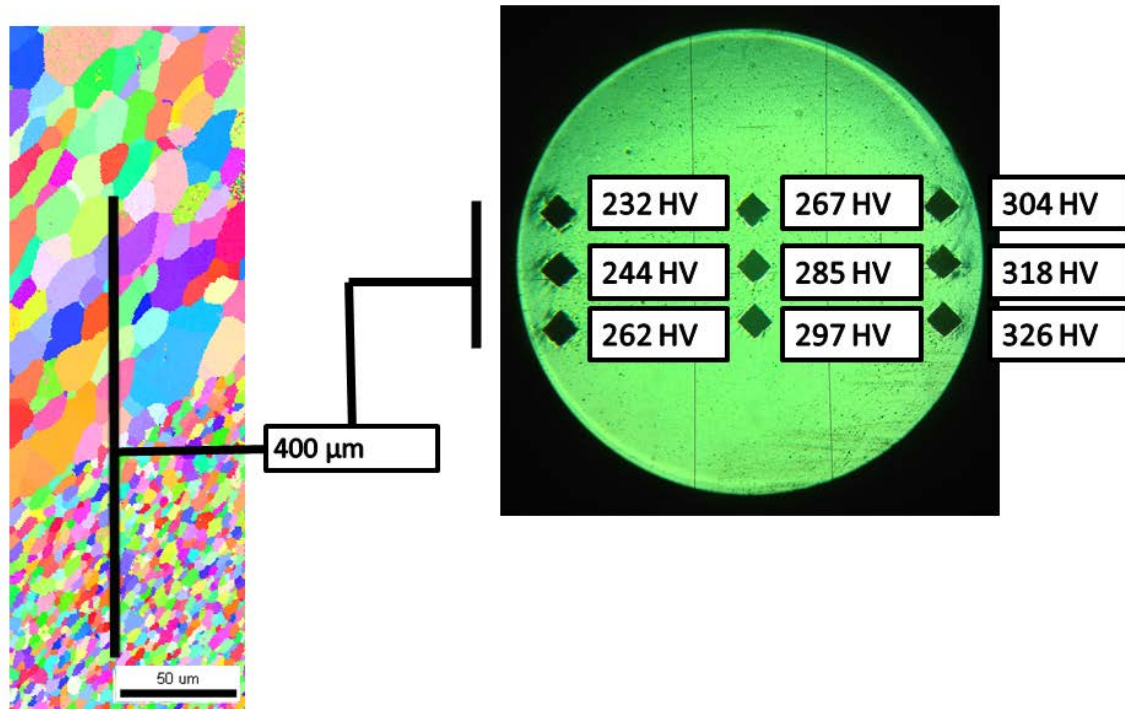


Figure 2.17 Inverse pole figure map and correlated micro-hardness indentation image showing large gradients in hardness in the thermo-mechanically affected zone.

There is little change in hardness in the SZ through the depth of the weld (red lines of Figures 2.18–2.20); however, traversing across the TMAZ along a vertical line at a horizontal distance away from the center of the SZ, dramatic and rapid changes in hardness occur (green and blue lines of Figures 2.18–2.20). This would be expected as the hardness trace crosses through a composite of microstructures, i.e., weld nugget, TMAZ, heat affected zone (HAZ), and BM. This change is most abrupt on the AS TMAZ.

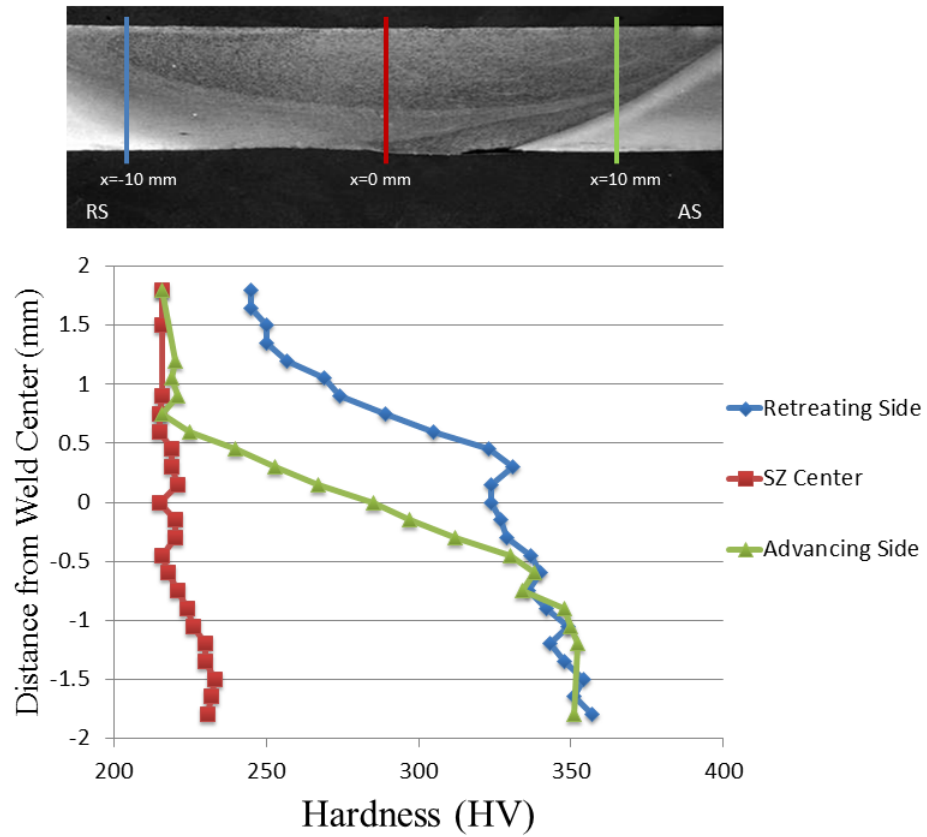


Figure 2.18 Hardness profile as a function of depth along each vertical line in the weld for 500 RPM/25 MPPM weld parameters for the retreating side (blue), stir zone (red), and advancing side (green).

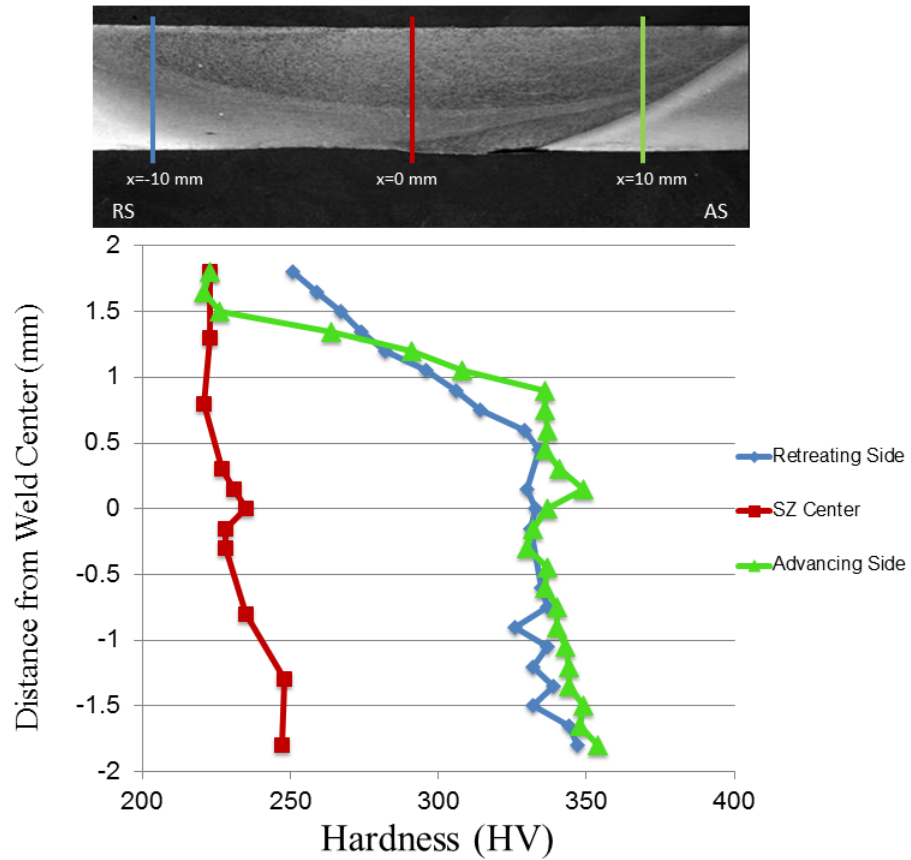


Figure 2.19 Hardness profile as a function of depth along each vertical line in the weld for 300 RPM/50 MPPM weld parameters for the retreating side (blue), stir zone (red), and advancing side (green).

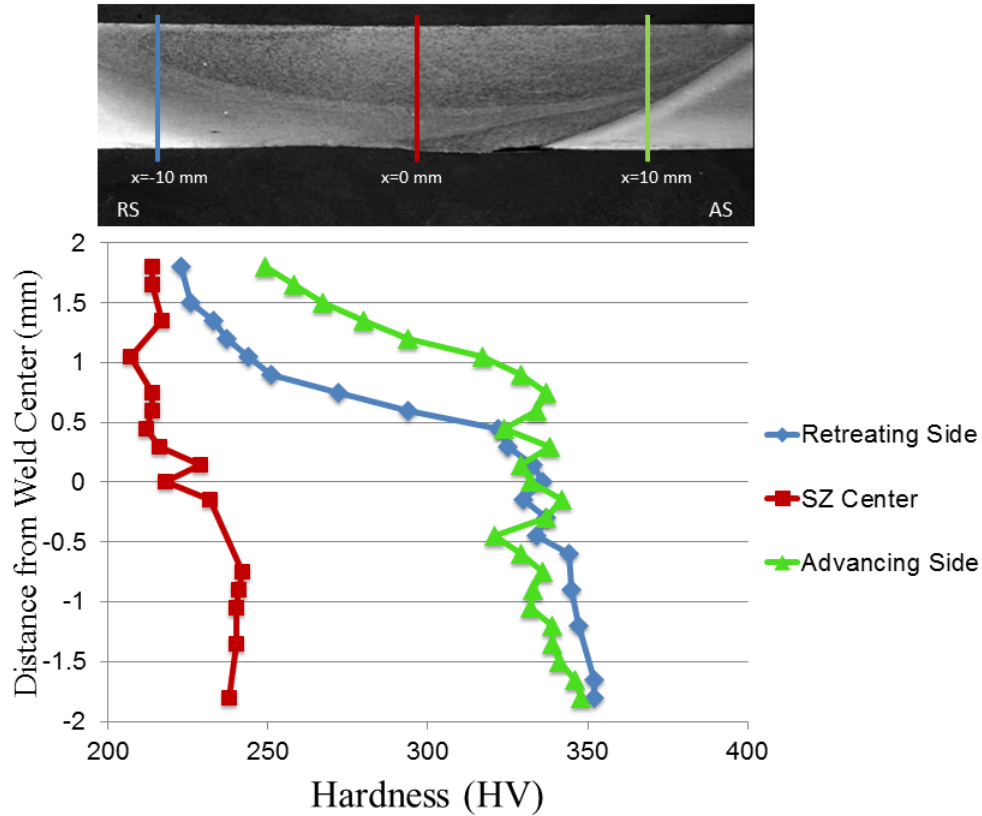


Figure 2.20 Hardness profile as a function of depth along each vertical line in the weld for 400 RPM/100 MPPM weld parameters for the retreating side (blue), stir zone (red), and advancing side (green).

Pole figures from the stir zone for each FSW condition displayed a persistent, torsional texture (Figure 2.21), which is distinctly different from the rolling texture in the base material shown previously (Figure 2.9). The pole figures in Figure 2.21 are oriented similarly to Figure 2.9, i.e. the y-z plane correlates to the cross sectional view of the weld.⁸ The SZ decrease as the heat input is increased suggesting a transition from a deformation based texture as the heat input is increased. Similar experimental results have been shown for both torsional steel textures and FSW SZ textures for other ODS steels [145, 146, 161].

⁸ The orientations of pole figures is intentionally emphasized for later comparison. The orientations of pole figure to this point (Figures 2.9 and 2.21) were selected since they represent the logical cross sectional view of the weld structure; however, as will be discussed later, the angle of the FSW tool causes the actual shear plane of the tool to workpiece to be different from this view. This shear plane will be analyzed in the discussion section of this chapter.

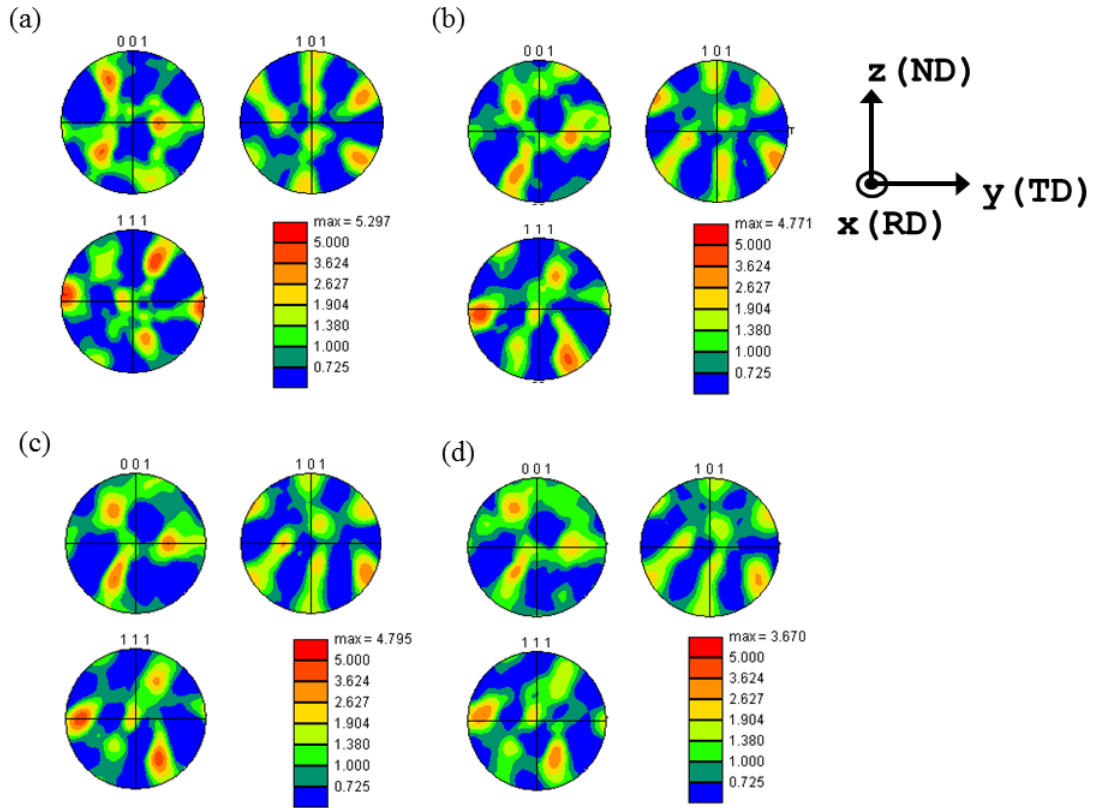


Figure 2.21 Pole figures for (a) 275 RPM/100 MPPM, (b) 300 RPM/50 MPPM, (c) 400 RPM/100 MPPM, and (d) 500 RPM/25 MPPM welding conditions showing a persistent BCC torsional texture following friction stir welding.

4. Thermo-Mechanically Affected Zone

The microstructure changed abruptly at the interface between the SZ and TMAZ. This change was most pronounced for high HI conditions and was consistently greater on the AS versus the RS of the tool for each FSW condition. The most gradual grain size transition at the AS TMAZ occurred for the 400 RPM/100 MPPM combination, corresponding to the lowest HI. The SZ-TMAZ interface for the 400 RPM/100 MPPM combination is shown in Figure 2.22a with contrastingly increasing gradients in grain size as HI increases in Figures 2.22b and 2.22c.

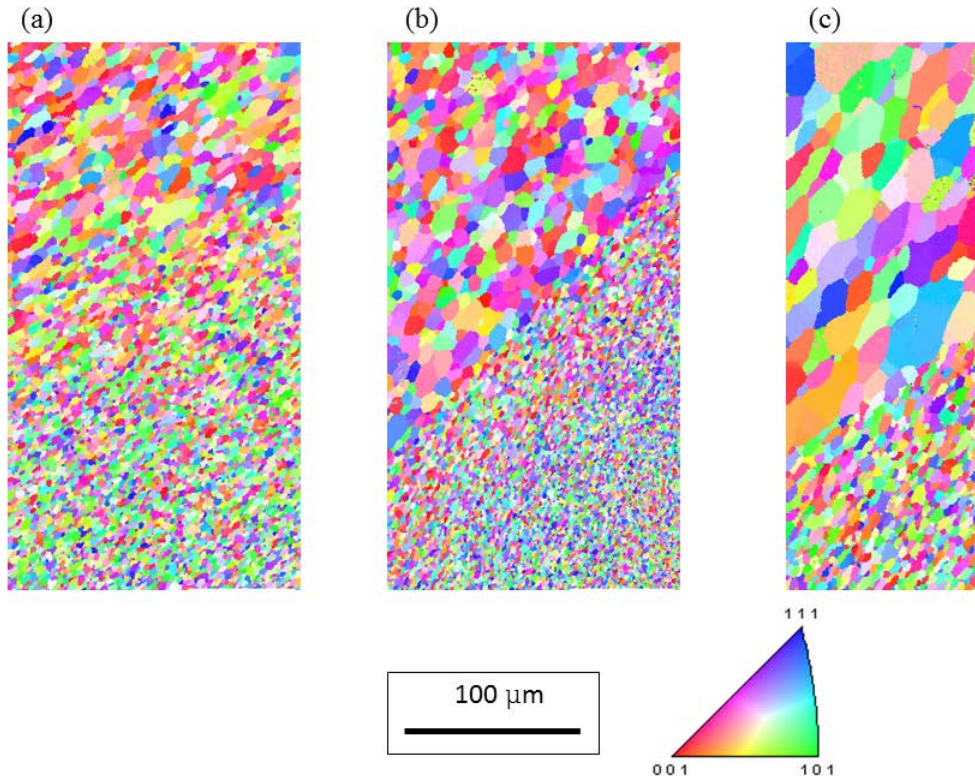


Figure 2.22 Stir zone to thermo-mechanically affected zone interfaces on the advancing side of the weld for (a) 400 RPM/100 MPPM, (b) 300 RPM/50 MPPM, and (c) 500 RPM/25 MPPM conditions showing the increase in microstructural gradient as a function of HI.

Grain size gradients were much lower on the RS for each FSW parameter combination and therefore were not visible on a single IPF map. To compensate for this, a series of smaller IPF maps were analyzed along the RS of each weld. The results show a gradual reduction in grain size across the RS. Figure 2.23 is a representative example of IPF maps across the entire weld nugget. Similar results were observed for all defect-free welds.

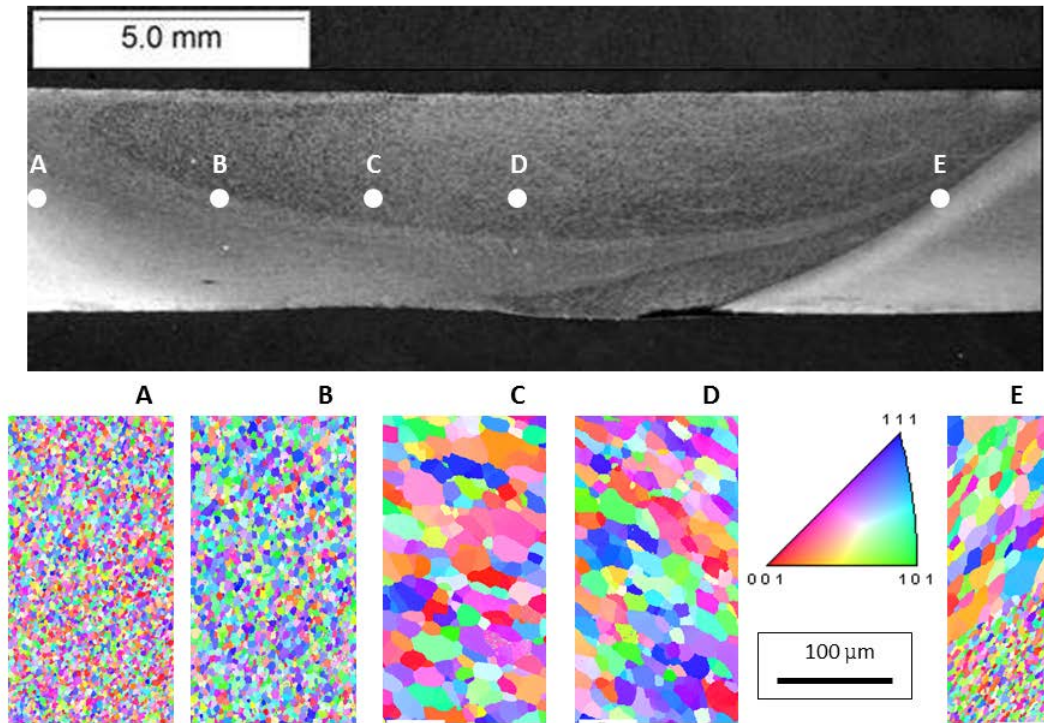


Figure 2.23 Representation of inverse pole figure maps across the weld nugget for 500 RPM/25 MPPM. The same 100 micron scale bar applies to all maps.

D. DISCUSSION

1. Weld Consolidation

This work suggests that HI as expressed by the ratio of tool rotational speed to tool traverse speed (Equation 1.2) may be an effective way to estimate FSW conditions required for successful joining. As shown in the macrographs of Figure 2.11, weld defects occur for low HI conditions. This observed trend is similar to work by Chimbli who discussed the lack of consolidation in friction stir welded aluminum alloys by varying process parameters and subsequent destructive evaluation [132]. The ratio of tool rotation rate to tool traverse rate was found to be a good measure of the ability to form defect-free consolidated welds. For MA956, a HI value between 4 and 6 produced consolidated, defect-free welds. For comparison other research on FSW of ODS steels have used HI values greater than 4 (ranging from 8 to 20) to achieve successful weld conditions (see green triangles on Figure 2.10) [41, 141–146] with the exception of

research by Etienne who used a very low heat input combination to analyze the redistribution of oxide particles following FSW without addressing weld consolidation [147]. This concept is very similar to recent research by Biswas in a review of FSW parameters on an aluminum alloy [133]. In this research, the overall mechanical response of the welded alloy depended on the ratio of tool rotational speed to tool traverse speed. For the aluminum alloy and tool material used, the suitable value of this ratio was between 15 and 16 revolutions per mm. An exact comparison between the values determined in this research and those determined by Biswas is not intended since many variables other than tool rotational speed and tool traverse speed were different (e.g. tool type, workpiece material, geometry, plunge force, etc.); however, the methods used in both studies are similar and suggest that this methodology can be applied to other FSW combinations.

2. Grain Growth in the Stir Zone

The distinction between unrecrystallized FG MA956 and recrystallized CG MA956 is significant since FSW on the two differing conditions produces opposing results. Some previous research utilizes a recrystallized CG MA956 (grain size ranging from hundreds of μm to cm) for both general material property determination [99, 162] and recently for the effects of FSW on microstructure and mechanical properties [56]. In these cases the heat input from FSW causes a refinement in grain size and a corresponding increase in hardness and strength. In other research using unrecrystallized FG MA956 (grain size of μm or less), FSW causes grain coarsening and a corresponding reduction in hardness and strength [141]. Detailed investigations of the differences between CG and FG MA956 show that grain refinement is the dominant strengthening mechanism and the material properties of the opposing starting grain sizes are different in particular at elevated temperatures [101, 102].

Quantifying HI as the simple ratio between rotational and translation speed may not be sufficient for predicting the resultant friction stir weld microstructure. In this work, two FSW conditions with the same HI (400 RPM/100 MPM and 300 RPM/50 MPM) produced successful and defective welds, respectively. In very recent research

by Wang et. al., recrystallized coarse grain MA956 was friction stir welded with a high heat input (1000 RPM/50 MPPM) [56]. Using HI, this welding condition should apply the same heat input as the 500 RPM/25 MPPM condition used in this work; however, the SZ grain size observed by Wang et al. is approximately 1–2 μm , compared with the 12 μm grain size observed in this work. These differences point out the importance of both the starting microstructure and the heat input model for predicting the SZ grain size. More elaborate heat input models have been developed and should be applied to systematic studies connecting FSW conditions with the starting and resultant microstructures [121, 122, 130].

The heat input due to FSW causes significant grain coarsening in the SZ and this degree of grain coarsening can be related to HI. However, the analysis of LAGBs indicates that grain growth is not solely a function of heat input (in which case there should be no LAGBs). A more robust analysis is that continuous dynamic recrystallization is occurring as grains are both growing due to heat input and are sheared by the FSW process. In a review by Doherty et al. [163], the term recrystallization is defined as the formation of new grain structures in a deformed material by the formation and migration of high angle grain boundaries driven by the stored energy of deformation and the term dynamic recrystallization is defined as the occurrence of recrystallization during deformation. This is different from the classical model of recrystallization as a seeded-nucleation and growth process. Expanding further on this theory of recrystallization, Humphreys [164] differentiates between discontinuous processes where grain growth occurs heterogeneously throughout the material and continuous processes where grain growth occurs uniformly with no identifiable nucleation and growth stages. Based on this more descriptive definition, the term continuous dynamic recrystallization is appropriate to describe FSW as defined by Humphreys. In several studies, the observed SZ grain morphology is discussed as equiaxed and coarsened grains due to heat input, but the severe plastic deformation occurring produces near-equiaxed grains that still retain a significant portion of LAGBs. This observation is reinforced during analysis of texture in the SZ.

3. Texture Development in the Stir Zone

The persistent, torsional texture observed, regardless of heat input, further suggests that the stir zone microstructure observed is the result of a continuous dynamic grain coarsening process during deformation. Although it has already been reported that the FSW process produces a BCC torsional texture in the SZ for other ferritic ODS steels [145, 146], the evolved SZ texture in this research compares very closely to theoretical ideal orientations developed for texture developments during torsional testing of steels [165] as well as texture formation during equal angular extrusion of BCC materials [166]. The SZ texture contains a $\{hkl\}\langle 111 \rangle$ fiber and a $\{110\}\langle uvw \rangle$ fiber as shown in Figure 2.24 and matches closely to ideal orientation points as described by Baczynski [165]. Unlike previous pole figures, the pole figure of Figure 2.24 has been rotated by the angle corresponding to the angle of the conical FSW tool (see Figure 1.14) such that the orientation of the pole figure in Figure 2.24 is in the shear plane between the tool and the workpiece. Because of this, axis orientation is not shown on this pole figure. This additional rotation was necessary for comparison to other theoretical and experimental torsional tests. The experimental results in this work also correlate with the ideal shear texture in BCC materials identified in recent research of texture development in friction stir welds by Fonda [167]. The torsional texture is a deformation texture that does not require recrystallization to form. No other, separate “recrystallization” texture was observed in this work or in the literature. Thus, nucleation and growth-based recrystallization may in fact not be responsible for the stir zone microstructure in ferritic ODS steels.

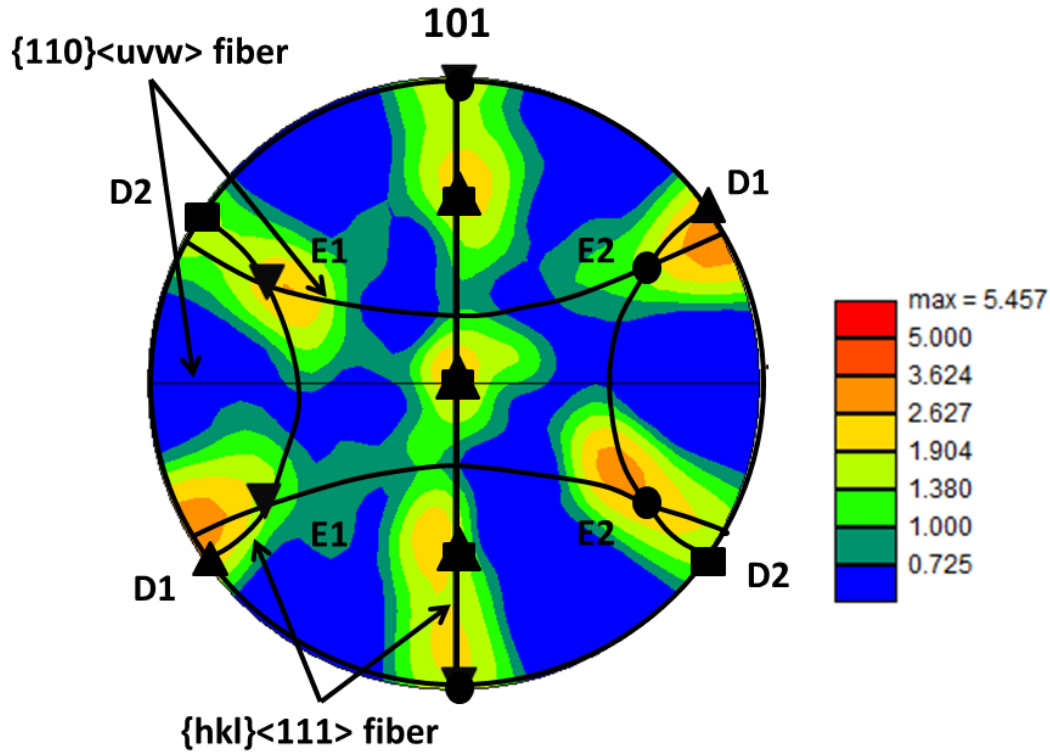


Figure 2.24 Stir zone texture shown with overlaid ideal BCC torsional texture from Baczynski [after 165]. Annotations from Baczynski: D1- $[1\ 1\ \bar{2}]\langle 111 \rangle$ (triangles), D2- $[\bar{1}\ \bar{1}\ 2]\langle 111 \rangle$ (squares), E1- $[0\ 1\ \bar{1}]\langle 111 \rangle$ (inverted triangles), and E2- $[0\ \bar{1}\ 1]\langle 111 \rangle$ (circles). The orientation of this pole figure corresponds to the shear plane between the friction stir welding tool and the workpiece.

4. Hardness Analysis

Micro-indentation results show that FSW reduces the hardness of the BM by approximately 37% compared to the SZ and that the hardness profile across the weld nugget is asymmetric. The average values of hardness within each stir zone show a small, but measurable, difference in hardness between the FSW conditions that may be relatable to grain size. The asymmetry trend in SZ hardness has been observed and commented on by several authors [41, 142, 145]; however, the analysis here also shows that the asymmetry is also a function of HI. The significance of this observation is not immediately apparent, but this research shows that lower values of HI will produce welds

with relatively smaller and more balanced gradients in grain size and hardness on both sides of the weld.

In addition to differences in hardness from the BM to the SZ, large gradients in micro-hardness exist across the weld in particular across the AS TMAZ in both horizontal and vertical directions. This is shown in Figure 2.25 for FSW parameters of 500 RPM/25 MPPM (the highest heat input condition) corresponding to the most abrupt change in both grain size and hardness encountered. Similar processes were conducted for other FSW conditions, and in all cases, the gradients in hardness are higher on the AS vice RS, and the relative gradients are reduced as HI reduced (i.e. lower HI conditions produce smaller gradients in hardness throughout the weld).

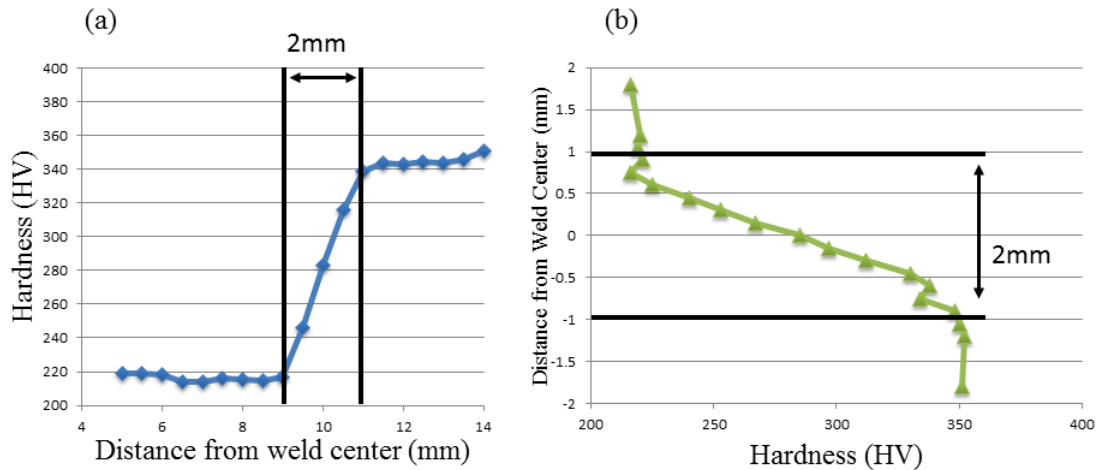


Figure 2.25 (a) Horizontal and (b) vertical gradients in hardness at the advancing side thermo-mechanically affected zone for the 500 RPM/25 MPPM welding combination.

Grain size variations cross the weld, shown in Figures 2.12–2.15 and hardness variations across the weld, shown in Figure 2.16, are directly related for all FSW parameter combinations. The relationship between grain size and hardness can be summarized as follows: (1) traversing from the SZ to the RS, grain size gradually decreases and hardness gradually increases, (2) traversing from the SZ to the AS, grain size and hardness are nearly constant until reaching the TMAZ at which point a very sharp decrease in grain size and increase in hardness occurs, and (3) these effects are

enhanced as HI increases, i.e., the SZ grain size increases for higher HI values and the abruptness of the transitions both on the RS and most noticeably on the AS is more distinct for higher HI values. The change in grain size across the weld explains the asymmetric nature of the hardness profiles and at lower HI values the asymmetry is less noticeable.

The large gradient in grain size may have significant consequence for weld reliability. The large grain size in the stir zone adjacent to the advancing side TMAZ boundary may experience a large amount of strain localization which could lead to crack nucleation at this location during tensile deformation. FSW parameters with high HI may need to be avoided to reduce this large grain size gradient. An assessment of this potential failure location is discussed in Chapter IV during material property evaluation.

The similarity in increase in grain size and reduction in hardness from the BM to the SZ suggests that a relationship such as the Hall-Petch relationship exists across the weld nugget. It is recognized that hardness is a measure of a material's plastic flow resistance and therefore is a function of both yield strength and strain hardening; however, the direct correlation of hardness to inverse square root of grain size shown in Figure 2.26 for the four successful FSW conditions tested in this research suggests that application of the Hall-Petch equation adequately describes the correlation between microstructural evolution and macrostructural material properties during FSW. A more robust support of this hypothesis is conducted in Chapter IV during tensile testing of specimens from the BM and SZ of each FSW condition. For now, however, the hardness results clearly indicate a Hall-Petch relationship exists amongst the FSW specimens even though the data is based on hardness data vice yield strength data. It is worth noting that the BM condition (a much lower grain size and much higher hardness condition) does not fall on the line presented in Figure 2.26. This significance of this fact was not

immediately apparent, but will be discussed in detail in Chapter IV and leads to a critical conclusion on the effect of FSW on the oxide particles in MA956.⁹

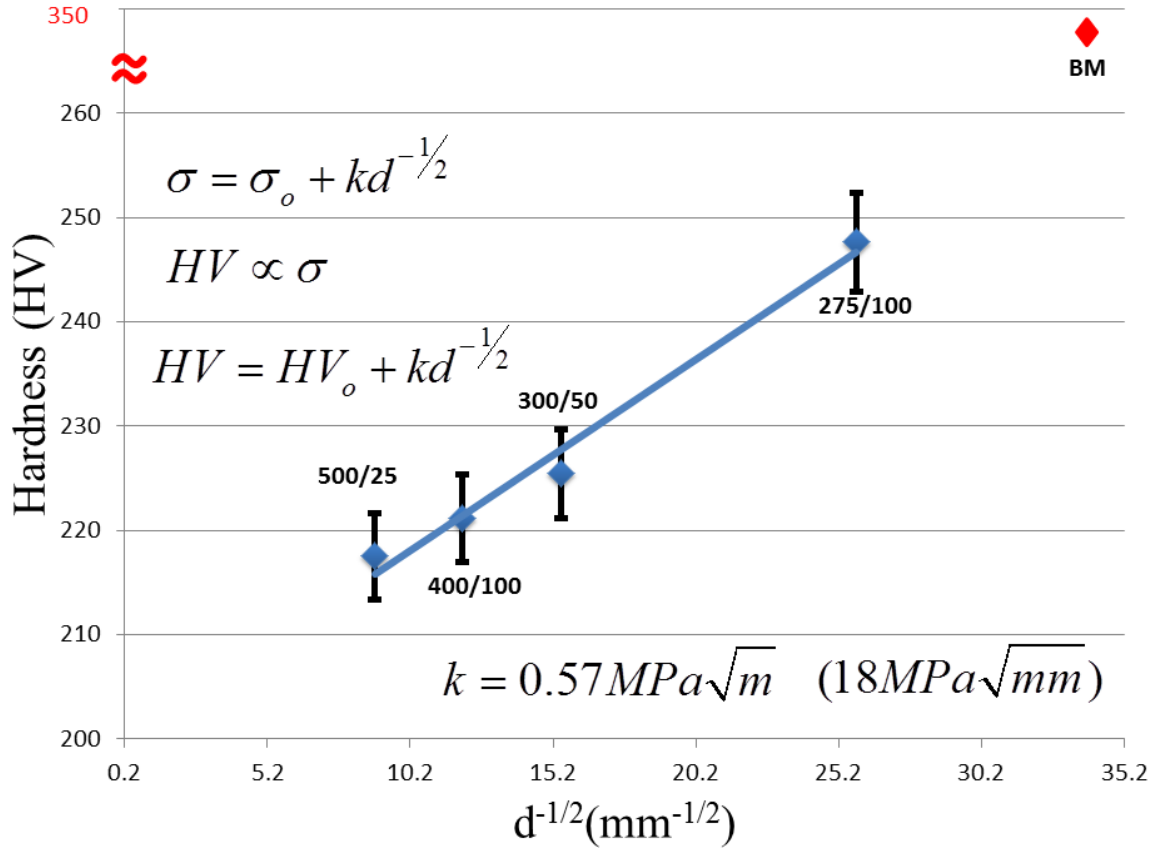


Figure 2.26 Application of the Hall-Petch equation using hardness and grain size following friction stir welding. The base metal condition (red) does not correlate with the Hall-Petch line. The y-axis is broken to show the base metal condition without vertical compression of the remaining data.

After conversion from hardness to stress using the acceleration due to gravity and unit conversion, the hardness data allows for calculation of the Hall-Petch constant (k) which corresponds to the slope of line in Figure 2.26. This conversion is shown in

⁹ The methodology of hardness/strength to grain size relationships presented in this chapter is presented chronologically as it was experimentally determined, and is not intended to be redundantly repeated in later chapters, but the initial insight into material property evolution following FSW achieved by micro-indentation became the basis for hypotheses on oxide particle morphology and overall strengthening mechanisms during FSW. Because of this important fact, the results are presented in this chapter and correlated to final material properties in Chapter IV.

Equations 2.1 and 2.2 and yields a value of k of $0.57\text{MPa}\cdot\text{m}^{-1/2}$ which is consistent with published values of k for typical steels [168]. This value of k is also consistent with values used in strengthening contribution calculations of MA956 specifically [56, 100, 101]. A more detailed analysis of the Hall-Petch plot as well as appropriate values of k will be presented in Chapter IV.

$$\text{slope} = \frac{HV}{\text{mm}^{-1/2}} = HV\text{mm}^{1/2} \left(\frac{\text{kg}}{\text{mm}^2} \text{mm}^{1/2} \right) \quad \text{Equation 2.1}$$

$$\frac{1.8\text{kg}}{\text{mm}^2} \text{mm}^{1/2} \left(9.8\text{m}/\text{sec}^2 \right) \left(\frac{1000^2 \text{mm}^2}{1\text{m}^2} \right) \left(\frac{1\sqrt{\text{m}}}{\sqrt{1000\text{mm}}} \right) \left(\frac{\text{N sec}^2}{\text{kgm}} \right) \left(\frac{\text{Pam}^2}{\text{N}} \right) \left(\frac{\text{MPa}}{10^6 \text{Pa}} \right) = 0.57\text{MPa}\sqrt{\text{m}}$$

$$\quad \text{Equation 2.2}$$

E. CONCLUSIONS

This chapter has provided a systematic study of the processing-microstructure relationships for the friction stir welding of MA956 ODS steel. The heat input during FSW was controlled and described by a heat index, which was a simple ratio of the rotational speed in RPM to the traverse speed in MPM. Four of eight welding conditions produced defect-free full penetration welds. Conditions with high thermal input produced defect-free welds that were then analyzed by OM, SEM, EBSD, and micro-indentation to determine the resulting microstructure-mechanical property relationships. The following conclusions were drawn:

(1) Welds with low tool rotational speeds or high tool traverse speeds produced tunnel defects on either the retreating edge or weld root. The ratio of tool rotation speed to tool traverse speed, denoted here as HI, can be used as a parameter for predicting defect-free weld consolidation.

(2) Grains in the SZ are substantially coarsened by higher heat input conditions. Although grain growth in the SZ is directly related to heat input, near-equiaxed grains with a non-negligible constituency of LAGBs still exist in the SZ

indicating continuous dynamic recrystallization of grains due to the combined effects of heat input and intense shearing plastic deformation.

(3) A persistent, simple torsional texture in the SZ was observed for all FSW conditions. The intensity of this texture decreases as heat input is increased.

(4) An abrupt change in grain size and hardness exists across the TMAZ to SZ interface. This change is systematically more pronounced on the advancing side of the tool for each welding condition. Higher heat input conditions produce a more abrupt change in both grain size and hardness equating to a smaller but steeper TMAZ. Although the weakest area of each weld is in the center of the SZ, the interface between the SZ and TMAZ is hypothesized as a potential failure location due to possible strain localization at the TMAZ to SZ interface.

(5) Hardness decreases from the BM to the SZ by 37% for each welding condition and may be correlated to observed grain growth in the SZ using the Hall-Petch relationship. This result suggests that grain coarsening is the dominant, low-temperature strengthening mechanism of the welded material.

(6) The asymmetric hardness profile in the weld nugget from the RS to the AS is also attributed to grain growth in the SZ and is a function of HI. Lower heat input conditions produce a more symmetric profile for both grain size and hardness across the weld nugget.

III. OXIDE PARTICLE COARSENING DURING FRICTION STIR WELDING

A. INTRODUCTION

The category, ODS steels, gets its name from the homogenous distribution of small oxide particles that exist in the base metal matrix. This dispersion of particles is the core feature of these materials and is one of the primary reasons for the high temperature strength and radiation damage resistance of these alloys. The dispersed oxides give these materials exceptional high-temperature strength due to the pinning of dislocations while also providing sites for the accumulation of hydrogen and helium atoms to mitigate radiation swelling in nuclear applications. The improved strength of ODS steels relative to traditional steels has been well established [55, 63], as has the improved radiation damage resistance of these steels [17, 33]. As discussed in Chapter I, the primary disadvantage of traditional joining techniques for ODS steels is the agglomeration of oxide particles which results in degraded material performance in depleted areas. Preserving the uniform distribution of oxide particles following joining is necessary to ensure that welded ODS steels can be used in high temperature applications.

The formation of oxide particles during manufacture of ODS alloys that contain aluminum such as MA956, PM2000, and various K-alloys developed by Kimura at Kyoto University has been studied by several authors, and the evolution of complex Y-Al-O particles from the base Y_2O_3 powder during the PM process is well documented [37, 103, 169–172]. In an early study of oxide particles in MA956, Cama concluded that the original Y_2O_3 powder used during the PM processing reacts with oxidized aluminum in the metal matrix producing various Y-Al-O particles, including yttrium aluminum perovskite (YAP), yttrium aluminate (YAT), and yttrium aluminum hexagonal (YAH) and that these particles coarsen as a function of both temperature and exposure time over thousands of hours without further chemical change [169]. Further research on MA956 has shown that other potential Y-Al-O particles may form including yttrium aluminum garnet (YAG) and yttrium aluminum monoclinic (YAM), and each specific oxide formation is dependent on temperature during manufacture and processing [103, 171,

172]. In a very recent study of oxide phases in PM2000, Shen used TEM, electron micro-diffraction, and EDS to identify YAP particles as well as two additional Al-Fe-O particle phases in PM2000 [173]. These phases have not been previously reported in any ODS steel, and the significance of this finding as well as its existence in other alloys is not immediately evident. In a comprehensive analysis of oxide formation in aluminum-containing ODS steels, Hsiung at LLNL used high-resolution transmission electron microscopy (HRTEM) to document the crystal structure, density population, size distribution, and interfacial structure of oxide particles in MA956 and in a similar aluminum-containing ODS alloy, K3 [37]. Hsiung proposed a three-stage formation mechanism of oxide particles in both alloys: (1) fragmentation of starting Y_2O_3 particles during the early stages of ball milling, (2) agglomeration and solid-state amorphization of Y_2O_3 fragments mixing with oxidized aluminum during later stages of ball milling, and finally (3) crystallization of the agglomerates to form oxide particles during consolidation. Furthermore Hsiung delineates three specific formation reactions dependent on temperature that determine which Y-Al-O particle is formed (Table 3.1). The ODS alloys used in Hsiung's research were consolidated at temperatures far below the formation temperature range of 1400°C to 1600°C for YAG (consolidation temperatures of 1100°C for MA956 and 1150°C for K3), and during HRTEM all oxide particles were determined to be YAM or YAP, and specifically not YAG. Of particular note, the progression of oxides from YAM to YAP to YAG (Table 3.1) occurs for increasing temperature and decreasing yttrium to aluminum concentrations. This important fact is utilized to differentiate between the oxides following FSW.

Table 3.1 Proposed oxide formation reactions from Hsiung [after 37].

Oxide	Chemical Reaction	Formation Temperature Range
YAM ($Y_4Al_2O_9$)	$2Y_2O_3 + Al_2O_3 \rightarrow Y_4Al_2O_9$	900°C-1100°C
YAP ($YAlO_3$)	$2Y_2O_3 + 2Al_2O_3 \rightarrow 4YAlO_3$	1100°C-1250°C
YAG ($2Y_3Al_5O_{12}$)	$3Y_2O_3 + 5Al_2O_3 \rightarrow 2Y_3Al_5O_{12}$	1400°C-1600°C

Although researched in far less detail, TiCN particles also exist in MA956 and other ODS alloys, but are of less importance in aluminum-containing alloys since Y-Al-O particles preferentially form over Y-Ti-O particles [105, 106]. It is notable that several other ODS alloys such as MA957 and 12/14YWT do not contain aluminum, and in these cases Y-Ti-O particles that form by different mechanisms potentially evolve differently during FSW [58, 78, 174]. Because of the known significance of aluminum in oxidation and corrosion prevention of ODS alloys in a wide variety of environments including air [170], super-critical water (SCW) [75], molten lead [158], and LBE [90], the research herein focuses on aluminum-containing ODS alloys.

Several authors have researched the effects of FSW on oxide particles in aluminum-containing ODS alloys such as MA956 and PM2000, but the results across this literature are inconclusive and do not include an analysis of a range of FSW parameter conditions. Using SEM and SANS, West concluded that FSW resulted in the dispersed oxides being slightly coarsened [141]. Similarly, using high-spatial resolution STEM, Chen concluded that FSW did not appear to create a major change in size or distribution of oxides in PM2000 [60, 154]. Finally in related work Legendre and Mathon used SANS to conclude that FSW on PM2000 caused oxide particles to grow in vicinity of the SZ [142, 143].

Because of the nm size of oxide particles present in MA956 as well as other ODS steels, most research on oxide particle morphology has focused on nano-scale techniques

including transmission electron microscopy (TEM), SANS, and atom probe tomography (APT) appropriate for nano-scale measurements while neglecting micro-scale level effects. Due to the hypothesized coarsening effects of FSW on ODS materials, the research herein utilizes both nano-scale and micro-scale measurements. For this research the term nano-scale is used to denote measurements of less than 100 nm (typical of BM MA956 oxide particles), and the term micro-scale is used to denote measurements greater than 100 nm. This denotation is not intended to classify MA956 as a nanostructured ferritic alloy (NFA) as that term is typically reserved for more refined particle sized alloys such as MA957 [147].

The objective of this chapter is to determine both qualitatively and quantitatively the fate of both Y-Al-O particles and TiCN particles in MA956 following FSW for a range of parameter conditions from low heat input to high heat input. Additionally this research will analyze particle response at both a nano and micro-scale. The results from this chapter combined with the microstructural data from Chapter II will be used to determine the active strengthening mechanisms following FSW in Chapter IV to help determine suitability of FSW as a joining mechanism for MA956 and other aluminum-containing ODS steels.

B. EXPERIMENTAL PROCEDURE

The MA956 and FSW techniques in this chapter are the same as discussed in Chapters I and II. The MA956 plate shown in Figure 2.2, which included the three fully consolidated weld conditions, was utilized for all analyses in this chapter. Additionally the BM MA956 used throughout this research came from the same lot of MA956 used by Hsiung in his review of nanoparticles in Fe-Cr steels.¹⁰ In this chapter only fully consolidated welds were analyzed. The three defect-free FSW parameter conditions analyzed in this chapter were: (1) 400 RPM/100 MPPM (the lowest heat input

¹⁰ The similarity between the MA956 used in this research and that used by Hsiung is important for later comparison. Prior to 2010, LLNL acquired MA956 from Special Metals in a variety of forms including plate form and U-bend configurations. The plate form MA956 was used by Hsiung in his research as well as initial unpublished research on FSW of MA956 (Figure 2.3). Starting in 2011, MA956 in both plate and U-bend configurations began to be used for this research. Because of these similarities, the material composition and manufacturing processes are considered identical and therefore the base microstructure including initial oxide particle size and distribution are also considered identical.

condition), (2) 300 RPM/50 MPPM (slightly higher heat input condition), and (3) 500 RPM/25 MPPM (the highest heat input condition).

1. Microscopy techniques

Samples of the friction stir welded MA956 plate shown in Figure 2.2 were sectioned and analyzed by SEM, EBSD, EDS, STEM, and SAXS. Cross sections across the weld path were metallographically prepared for each welding condition by standard metallographic preparation as discussed in Chapter II. Microstructural examinations were conducted using a Zeiss Neon 40 field emission SEM at 20 keV. All EBSD analyses were carried out using the TSL orientation imaging microscopy (OIM) 6.0 system with a Hikari camera at 20 kV using a 60 μm objective aperture with an approximate probe current of 1 nA.

Quantification of oxide particle growth was accomplished by digital stereology using SEM imaging. Software counting was conducted on 67 μm by 67 μm square sections (corresponding to a SEM analysis area at 1000x magnification) representative of the SZ for each FSW parameter combination. SZ SEM images containing visible oxide particles were counted using two different digital stereology software packages: (1) ImageJ, a public domain image processing solution developed by National Institute of Health and previously used in a variety of microscopy techniques [175], and (2) a MATLAB code designed by Woertz specifically for measuring particle distribution and homogeneity in FSW of two-phase alloys containing non-deformable particles in a soft matrix [176].¹¹ For both methods no image adjustments other than small changes in brightness or contrast were made. Baseline settings as discussed in reference material for both methods were used and identical images were used in both techniques for each FSW parameter combination. The MATLAB code written by Woertz was in particular

¹¹ The research by Woertz was also done at the Naval Postgraduate School overlapping the period of this research. Good collaboration between the two works was achieved and the strong theoretical basis established by Woertz was valuable to this research. Additionally, the code by Woertz was designed to analyze non-deforming silicon particles in an aluminum matrix following FSW. This strong similarity to the non-deforming oxide particles in the Fe-Cr matrix following FSW in this research made Woertz's approach easily adaptable. The additional data from Woertz's code is considered to be a significant improvement to the data provided by ImageJ and the similarity in results between the two helps validate Woertz's code.

effective, and the only reason for using ImageJ was to provide a well-established reference for comparison. Woertz discusses the methodology behind his code in detail in his research, but important aspects are summarized here. Woertz's code takes any image (ideally an image with high contrast particles) such as the SEM image in Figure 3.1a, converts that image into a purely binary image (Figure 3.1b), and then conducts a series of calculations based on subdivisions within that image. The results produced by Woertz's code used in this research are population (i.e. number of particles), average particle size, and particle spacing (particle spacing is not calculated by ImageJ and this was a parameter of significant interest in this research.) Woertz's code also calculates area fraction, aspect ratio, orientation, and a newly defined homogeneity index. While of interest in the theoretical aspects of FSW as discussed by Woertz, these parameters were not of significant concern in this research.

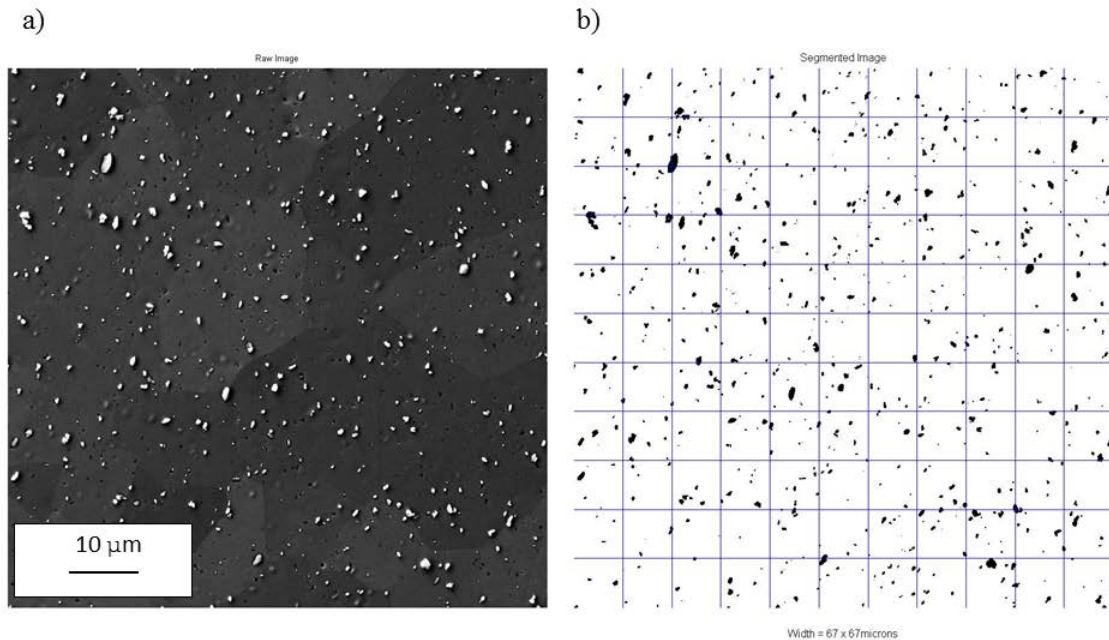


Figure 3.1 (a) Secondary electron microscopy image showing Y-Al-O particles distributed homogeneously in MA956 following friction stir welding and (b) subsequent image created by Woertz's MATLAB code for optical counting techniques [after 176].

STEM images were obtained using the same Zeiss Neon 40 field emission SEM at 30 keV, a 60 µm objective aperture, and an approximate probe current of 1.4 nA on

thin foil samples prepared by twin jet electropolishing of 3 mm discs thinned to less than 100 μm . Electropolishing was accomplished using a Struers Tenupol-5 with 10% perchloric in ethanol solution maintained at a temperature below 250°K (-23°C) and 20 V_{DC}. Although high magnification imaging techniques such as STEM and TEM are required to view nano-scale features, the sample preparation techniques for these methods often cause larger particles to fall out during preparation, and thus STEM or TEM alone are not recommended as sole techniques to evaluate particle distribution of various scales such as those encountered in this research. The use of multiple techniques is considered to be one of the primary advantages of the methods used in this research. The nano-scale preparation techniques (primarily TEM) used by most authors on friction stir welded specimens cause large oxide particles to fall out of the matrix, and thus the presence of large particles, even though acknowledged, is not fully included in some studies [142, 143]. This same process was seen in this research during preparation of TEM and STEM samples in this research, and thus these techniques were primarily used as qualitative assessments.

Specimens for SAXS were sectioned and analyzed across the weld path in a similar manner as discussed above. Specimens were cut perpendicular to the weld direction so as to include cross sections of the base and weld material for both the AS and RS of the weld. The specimens were then metallographically thinned and polished on both sides down to a final thickness of approximately 50 μm using a Southbay Labs TEM polishing jig. Polishing was performed by sequentially grinding using SiC papers followed by a 6 μm and 1 μm diamond slurry polish on a nylon cloth, and a final polish using 0.05 μm colloidal silica on a neoprene cloth.

SAXS analysis was conducted at the Advanced Photon Source at Argonne National Laboratory (ANL) using the USAXS beamline (15-ID). This beamline allowed for an extremely large q range to be examined (10^{-4} to 0.3 inverse angstroms), thereby allowing the collection of scattering data from angstroms to tens of microns. Specimens were loaded into a multi-specimen paddle and scattering data was collected using a beam energy of 16.9 keV, with the precise location of data collection determined using the USAXS in radiography mode. This energy choice maximizes the transmitted signal

without approaching the absorption edge of yttrium (17.04 keV), while at the same time satisfying the q-range needs. Data analysis was performed using the Indra and Irena SAXS analysis data packages for IgorPro [177]. Blank (air scattering) data was subtracted from the scattering data obtained for each specimen location, and the scatterer size distribution was obtained by iteratively fitting a spheroid scatterer model (assuming an aspect ratio of 1) using the maximum entropy approach.

2. X-ray Energy dispersive spectroscopy techniques

EDS analysis was conducted at 12 keV for both individual particles, map areas, and line scans. All EDS maps were taken from representative areas of either the BM or SZ areas and were 23 μm by 17 μm rectangular sections (corresponding to a SEM analysis area at 5000x magnification.) All EDS point, map, and line spectra were counted for 200 seconds and had a dead time of approximately 6% equating to a live count time of approximately 188 seconds. This resulted in typical peaks of 10000 counts or more for elements of interest. Initial EDS results were used to establish experimental techniques. Three different spectra were typically observed: (1) the base metal matrix (Figure 3.2) which was typical of non-particle areas, (2) complex Y-Al-O particles (Figure 3.3) corresponding to bright white areas on SEM images, and (3) TiCN particles (Figure 3.4) corresponding to dark areas on SEM images. Based on these initial results the following energies were analyzed for all EDS analyses: O-K (0.523 keV), Fe-L (0.705 keV), Al-K (1.486 keV), Y-L (1.922 keV), Ti-K (4.510 keV), Cr-K (5.414 keV), and Fe-K (6.403 keV). Low energy values for C-K (0.277 keV) and N-K (0.392 keV) were attempted and can qualitatively be seen in the TiCN particle of Figure 3.3, but resolution did not fully support conclusive use of these low energies. Additionally the low energy for O-K (0.523 keV) and its proximity to the large Fe-L peak (0.705 keV) prevented quantitative use of oxygen results. The separation between the energies of interest (most notably Al-K and Y-L) allowed for good qualitative and quantitative comparison at 12 keV. Lower beam voltages of 10 keV and 5 keV were attempted but did not offer improved spatial resolution (5 keV resulted in an insufficient count rate). For this reason a beam voltage of 12 keV was established and used throughout this chapter for EDS analysis.

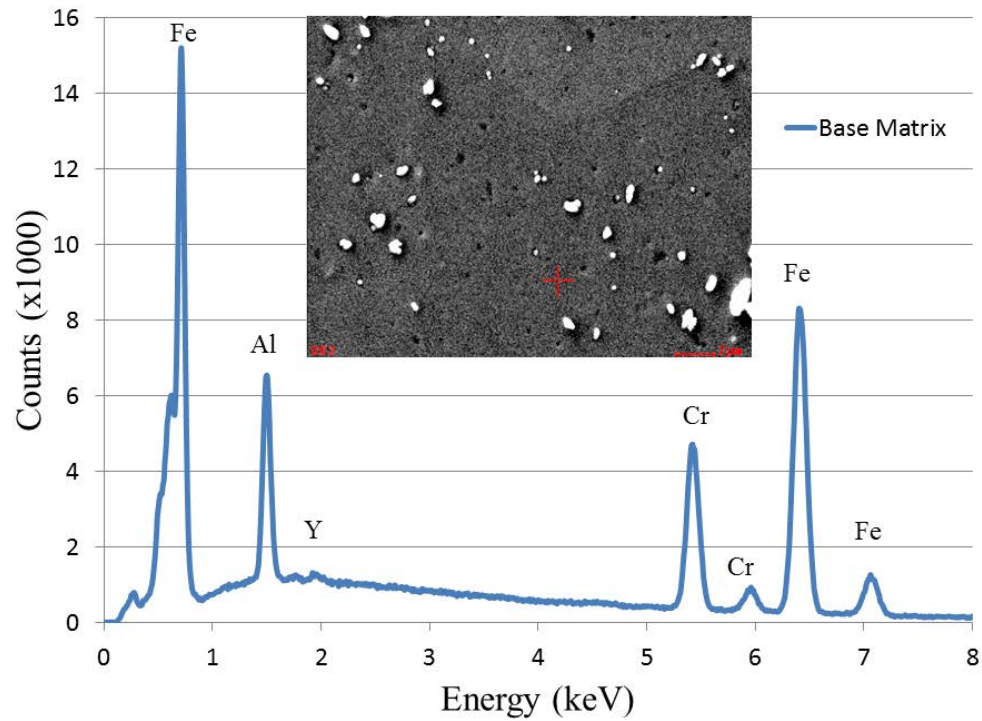


Figure 3.2 Energy spectrum typical of the base matrix for MA956.

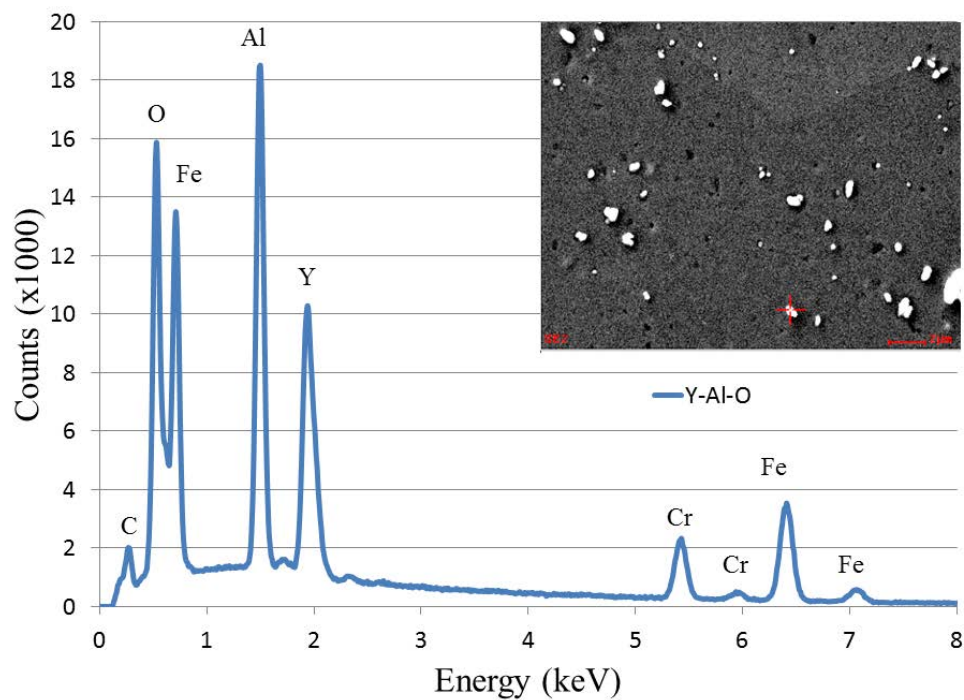


Figure 3.3 Energy spectrum typical of a complex Y-Al-O particle (white on inset) within MA956 following FSW.

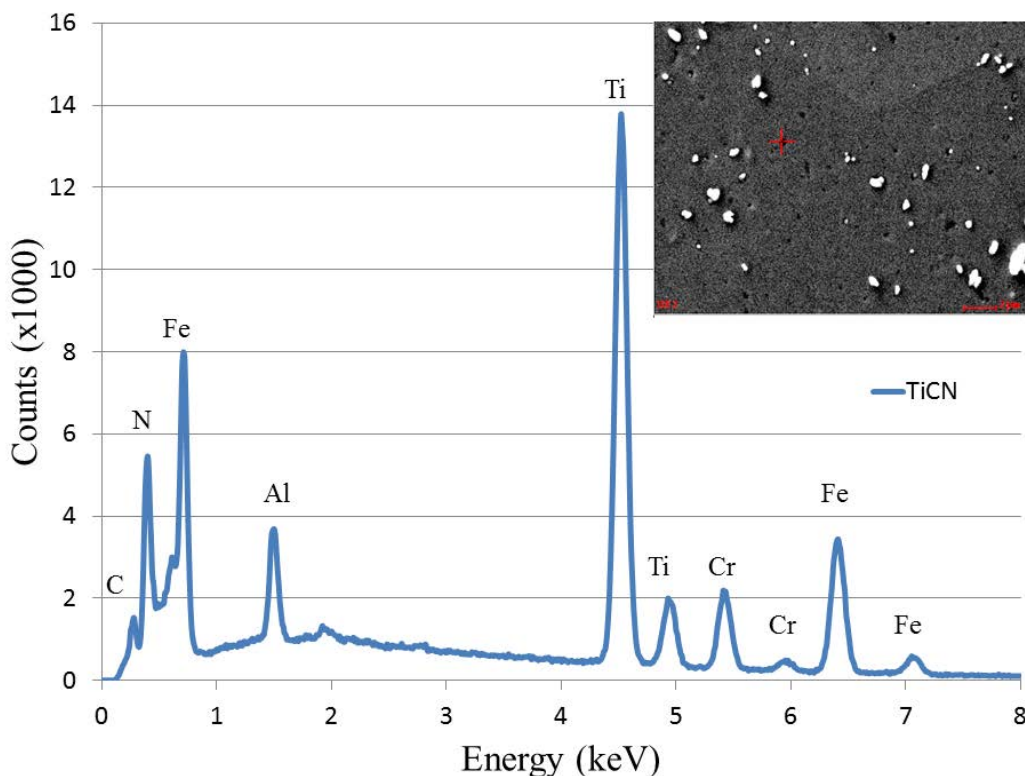


Figure 3.4 Energy spectrum typical of a TiCN particle (black on inset) within MA956.

The phase of Y-Al-O particles following FSW was determined by quantitative raw intensity data comparison to simulations using the DTSA-II x-ray microanalysis software written by Ritchie at NIST [178] and quantitative EDS analysis using EDAX Genesis software. YAM, YAP, and YAG are all line compounds on the Al_2O_3 - Y_2O_3 phase diagram so the transition between each phase was readily identifiable. The phase diagram of the alumina-rich portion of the Al_2O_3 - Y_2O_3 system is shown in Figure 3.5 and depicts the phase lines for YAP and YAG [179]. This phase diagram was selected since the transformation of interest in this research was to YAG. Research that shows the full phase diagram is available elsewhere [180]. The EDAX Genesis software package uses measured intensity and applies ZAF corrections for atomic number (Z), x-ray absorption (A), and x-ray fluorescence (F) which vary by element to calculate atomic or weight percent of measured areas. The quantitative analysis procedure used including the ZAF corrections are discussed in detail by Goldstein [181]. The EDAX Genesis software was

selected to analyze for oxides Y_2O_3 and Al_2O_3 vice individual elements yttrium and aluminum. Because of this, final calculations do not include the low O-K energy (0.523 keV), but rather are based on the higher Al-K (1.486 keV) and Y-L (1.922 keV) energies which were deemed more accurate and discrete. For line scans across particle a step size of 0.02 μm was used. To prevent reliance on these software corrections alone, a comparative method between raw measured intensity and simulated intensity using DTSA-II was utilized. The DTSA-II software is a robust microanalysis software package that was used to simulate the spectra that would be generated by different Y-Al-O particles (YAM, YAP, and YAG) on a Fe-Cr-Al substrate matching that of MA956. In particular, DTSA-II allows for simulations including complex surface topologies such as oxide particles sitting on top of a flat substrate, a rough description for the geometry of the current samples. For the DTSA-II simulations, a Monte Carlo model of a 250 nm diameter sphere (corresponding to a typical particle found during the high heat input conditions) on a bulk homogenous substrate (Fe-Cr-Al) was used. Microscopy settings such as beam voltage, approximate beam current, exposure time, and geometry were applied to simulate the spectra from the welded samples. Parameters used to perform simulations in DTSA-II are listed in Table 3.2. Simulation results from DTSA-II were used to calculate total intensity of yttrium and aluminum for three different potential particles: YAM, YAP, and YAG.

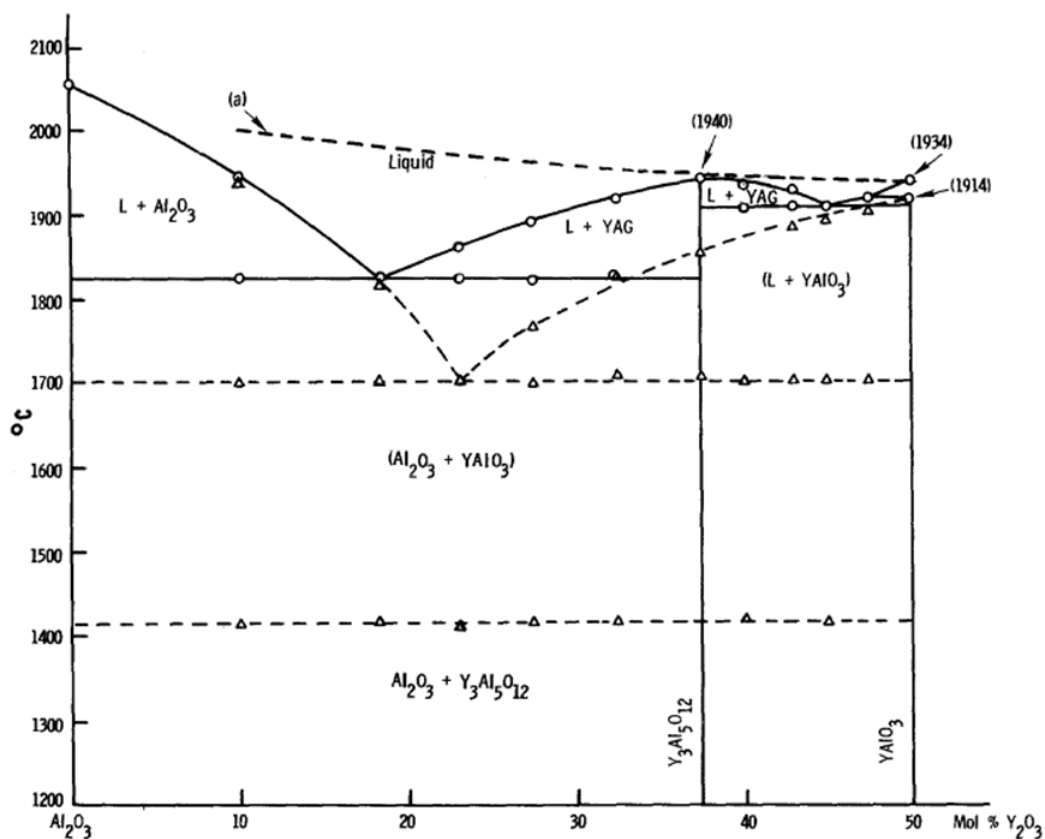


Figure 3.5 Phase diagram of the alumina-rich portion of the Al_2O_3 - Y_2O_3 system from Caslavsky [from 179].

Table 3.2 Parameters used for DTSA-II simulation

Parameter	Value/Condition
Simulation Mode	Monte Carol model of a sphere on a bulk homogenous substrate
Number of Simulations	10
Substrate	Fe (75.5%), Cr (20%), and Al (4.5%)
Sphere Material	YAM, YAP, and YAG separately
Sphere Diameter	250 nm
Beam Energy	12.0 keV
Probe Dose	188 nAsec
Incident Angle	0°
Take-Off Angle	30°
Working Distance	5.0 mm
Specimen-to-detector Distance	50 mm

Two parameters were utilized to distinguish between phases of the Y-Al-O particles: (1) yttrium to aluminum integrated intensity ratio ($IR_{Y/Al}$) and (2) yttrium to aluminum atom ratio ($AR_{Y/Al}$). Theoretical values for $IR_{Y/Al}$ were determined using DTSA-II simulations. Exact values for $AR_{Y/Al}$ were determined by stoichiometric relationships of the different oxides (Table 3.1). Theoretical results for these values are summarized in Table 3.3 and experimental measurements were compared to these results for phase determination.

Table 3.3 Theoretical yttrium to aluminum intensity ratio ($IR_{Y/Al}$) and yttrium to aluminum atom ratio ($AR_{Y/Al}$) values for Yttrium Aluminum Monoclinic (YAM), Yttrium Aluminum Perovskite (YAP), and Yttrium Aluminum Garnet (YAG) as determined by DTSA-II software and stoichiometric relationships respectively.

Oxide Particle Phase	$IR_{Y/Al}$	$AR_{Y/Al}$
YAM	1.671	2
YAP	1.208	1
YAG	0.814	0.6

C. RESULTS

1. Base Metal Particle Distribution

BM MA956 has a uniform distribution of nano-scale Y-Al-O particles as well as a uniform distribution of micro-scale TiCN particles that are often not discussed in literature. BM MA956 contained YAM and YAP particles with a range of particle diameters from 2–80 nm, an average particle diameter of 8 nm, and a particle density of 1.0×10^{20} particles/m³ [37]. This distribution is similar to other reported research on BM MA956 [103, 171, 172]. On similar fine grain MA956, Regle reported a range of TiCN particle sizes from 100–200 nm [106]. In this chapter, quantification of particle size was only attempted for Y-Al-O particles and only at the micro-scale using analysis of SEM imaging although SEM (Figure 3.6) and STEM (Figure 3.7) imaging suggests nano-scale initial Y-Al-O particles as well as larger micro-scale TiCN particles in the BM consistent

with results from Hsiung and Regle respectively. In the micro-scale SEM imaging of Figure 3.6, there are no Y-Al-O particles visible in the BM. All of the visible white particles in Figure 3.6 are Al-O particles (Al_2O_3) with negligible yttrium or other elements, whereas the dark particles are TiCN particles barely visible at the micro-scale. STEM imaging of MA956 (Figure 3.7) shows a fine BM grain size, nano-scale particle distribution, and large dislocation density in the BM due to the hot rolling fabrication prior to FSW. SAXS results for the BM (Figure 3.8) show similar results in that two peaks are visible, one at 6.4 nm and a second at 17.9 nm both correlating to Y-Al-O particles.

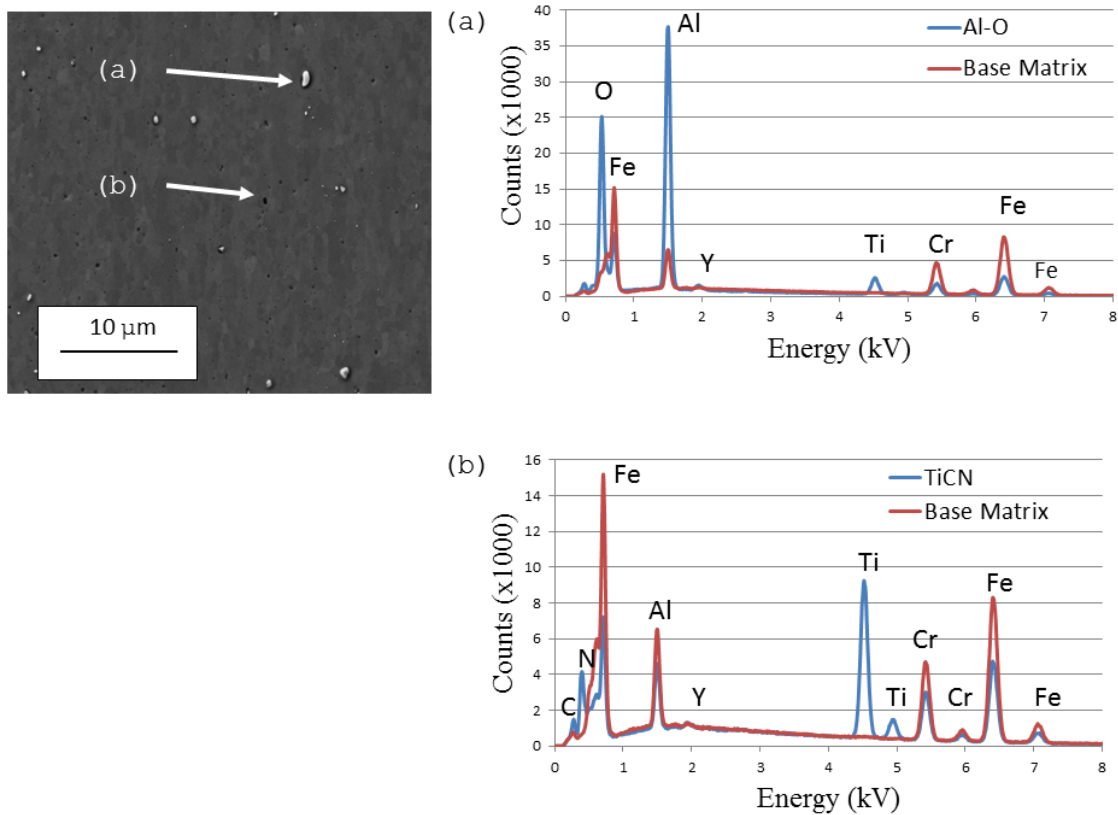


Figure 3.6 Scanning electron microscopy imagery of base metal MA956 with energy dispersive x-ray spectroscopy spectra showing (a) Al-O particles (white) and (b) TiCN particles (dark) uniformly distributed in the base metal.

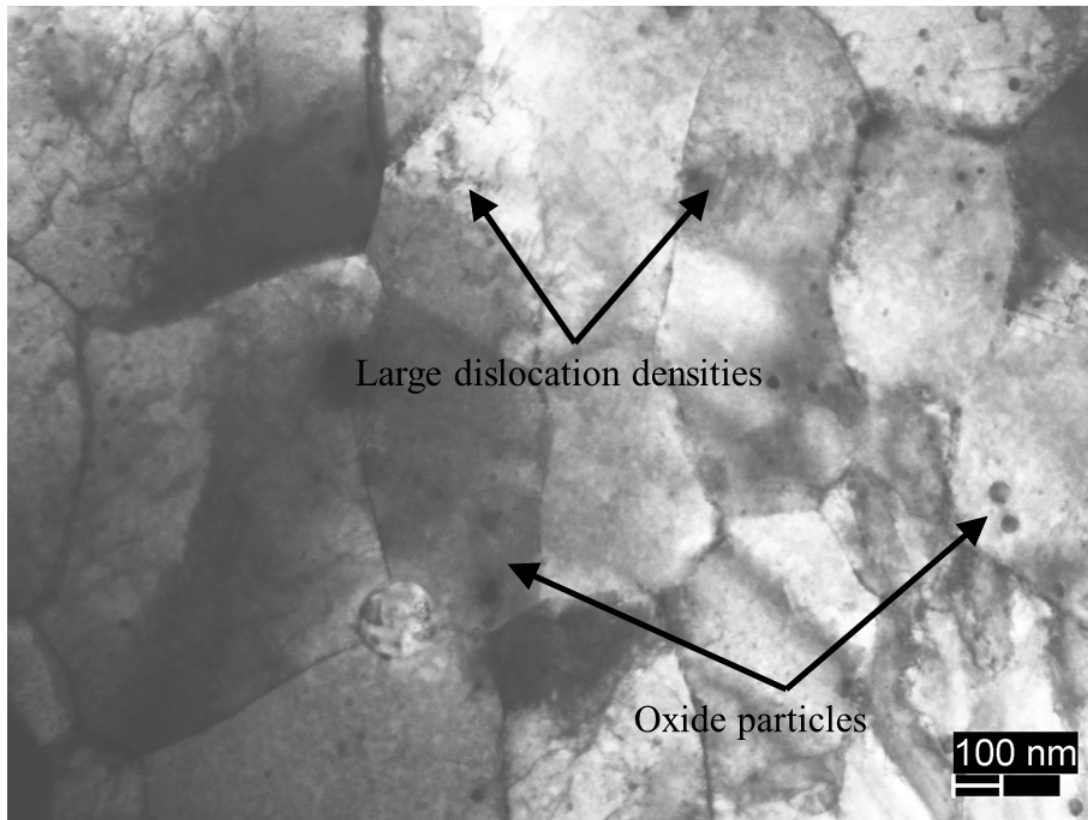


Figure 3.7 Scanning transmission electron microscopy image of base metal MA956 showing fine grains, nano-scale particles (small dark particles), and large dislocation densities in the base metal.

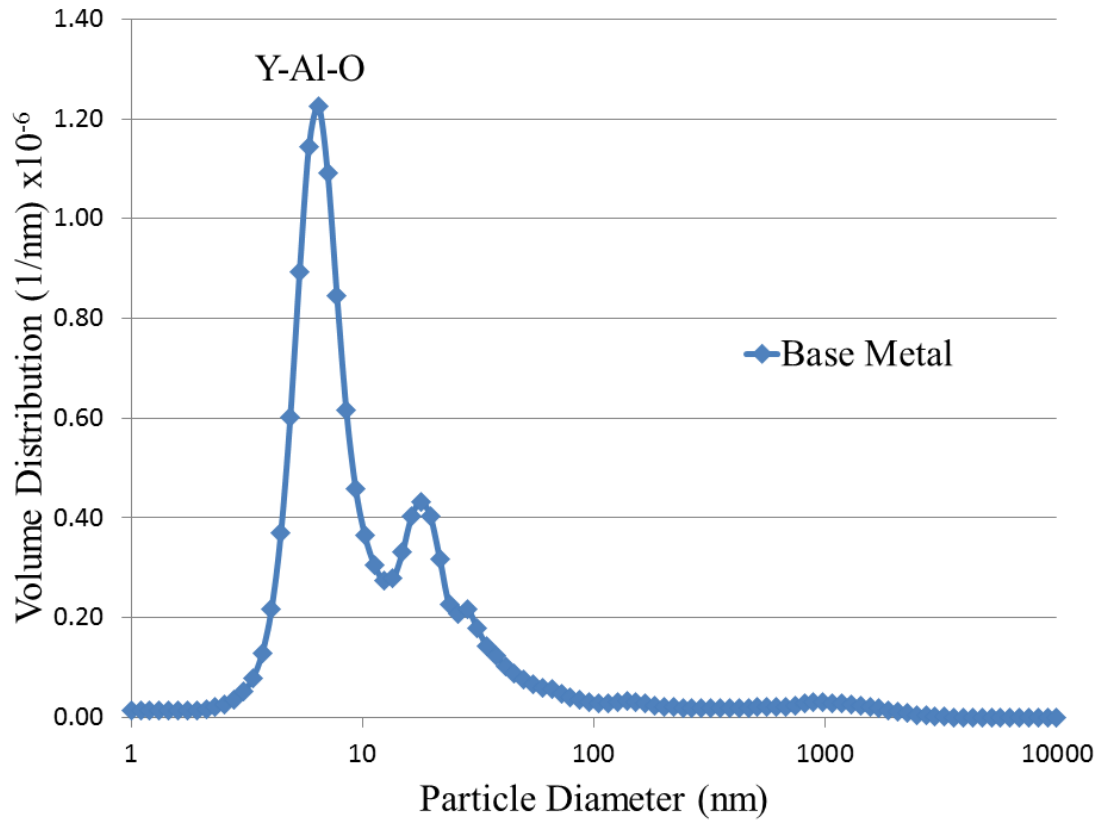


Figure 3.8 Small angle x-ray scattering data for base metal MA956.

2. Stir Zone Particle Distribution

In sharp contrast to the BM, the SZ sections of each FSW parameter combination contain a uniform distribution of visible, micro-scale Y-Al-O particles and a similar size distribution of TiCN particles to that of the BM (Figures 3.9 and 3.10). In the SZ of each FSW parameter combination micro-scale Y-Al-O particles are clearly visible with average particle sizes ranging from 160 nm (low heat input conditions) to 343 nm (high heat input condition). STEM imaging of the SZ for each FSW parameter combination (Figure 3.10) also showed significant grain growth in the SZ, oxide particle coarsening, and significant reduction in dislocation density due to the continuous dynamic recrystallization during FSW.

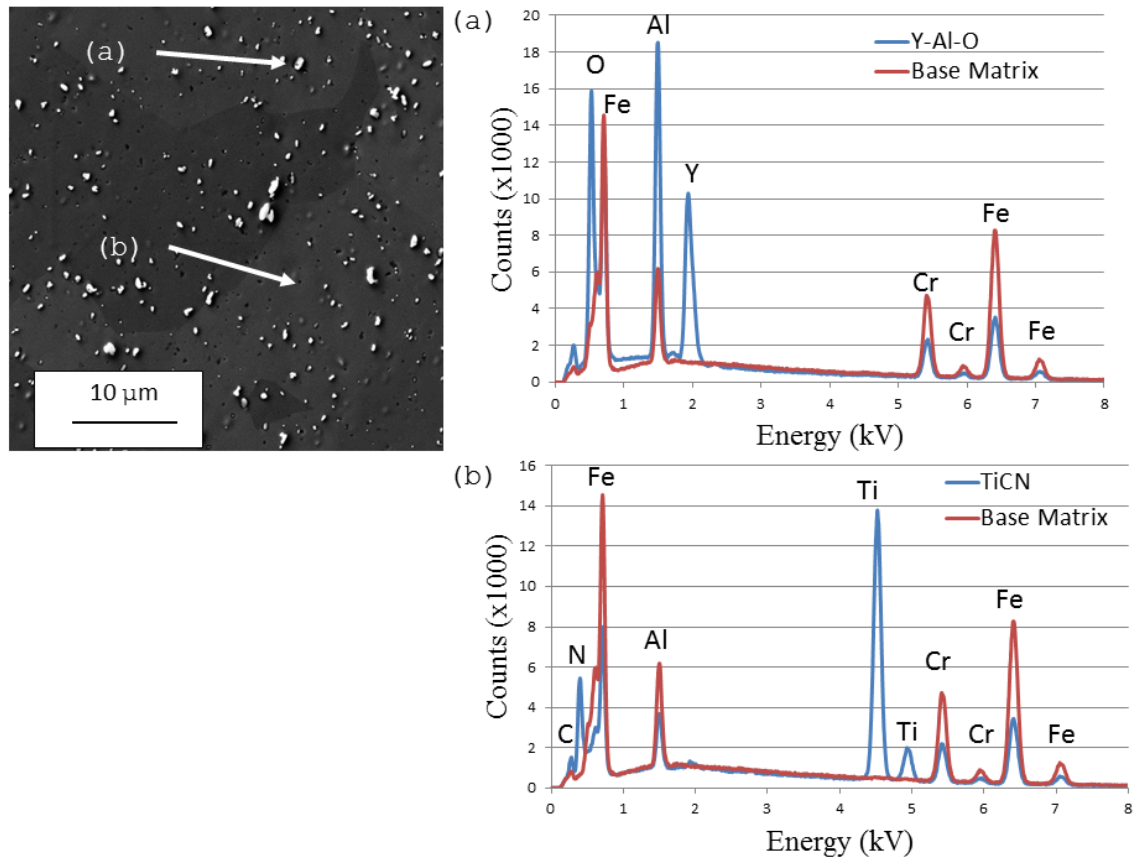


Figure 3.9 Scanning electron microscopy imagery of the stir zone for 500 RPM/25 MPM friction stir welding combination with energy dispersive x-ray spectroscopy spectra showing (a) coarsened Y-Al-O particles (white) and (b) similar sized TiCN particles (dark) uniformly distributed in the base metal.

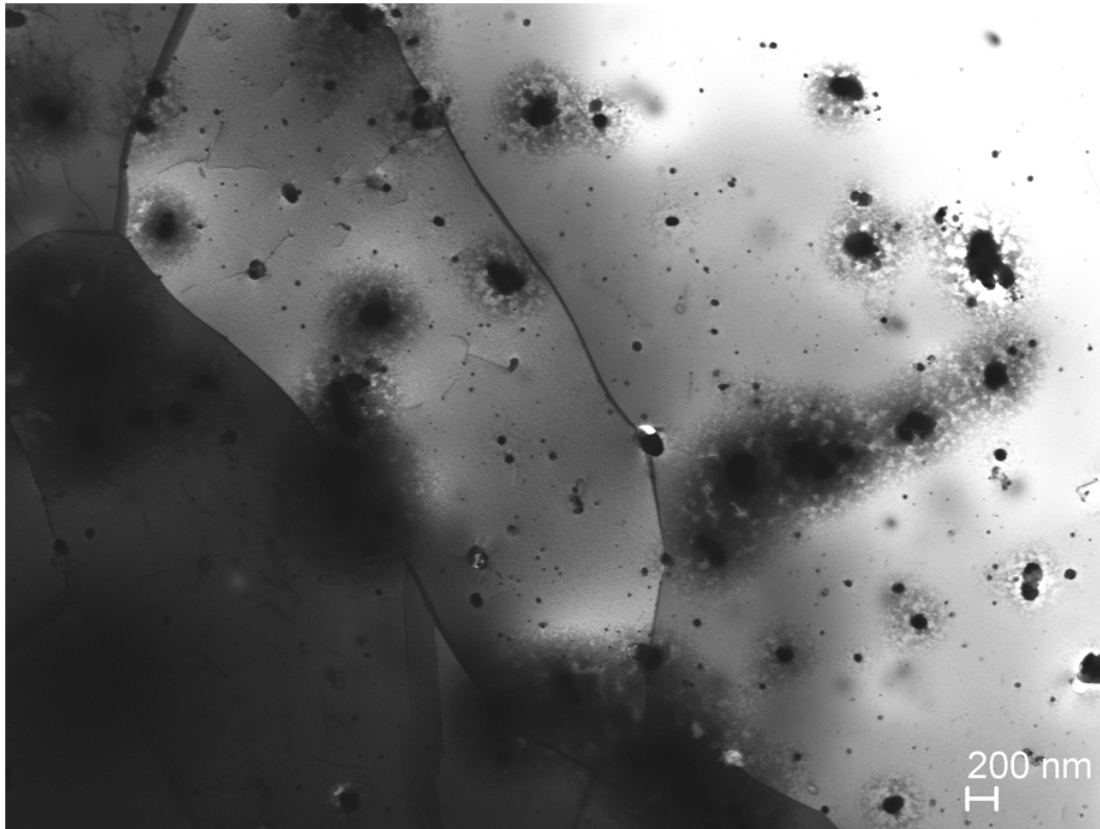


Figure 3.10 Scanning transmission electron microscopy imagery of the stir zone for 300 RPM/50 MPPM friction stir welding combination showing grain growth, oxide particle coarsening, and reduction in dislocation density following friction stir welding.

In addition to the comparison possible using SEM imaging alone (Figure 3.11), EDS analysis of the SZ of each FSW combination showed a clear spectral difference indicating Y-Al-O particle coarsening following FSW (Figure 3.12) that increased as the heat input increased. For EDS analysis a higher magnification image was utilized to allow for better discrimination of spectral maps whereas a lower magnification image was utilized for optical analysis to ensure a sufficient number of particles were present. In addition to the coarsening of Y-Al-O particles, Figures 3.11 and 3.12 show a negligible change in TiCN particle distribution following FSW for each parameter combination.

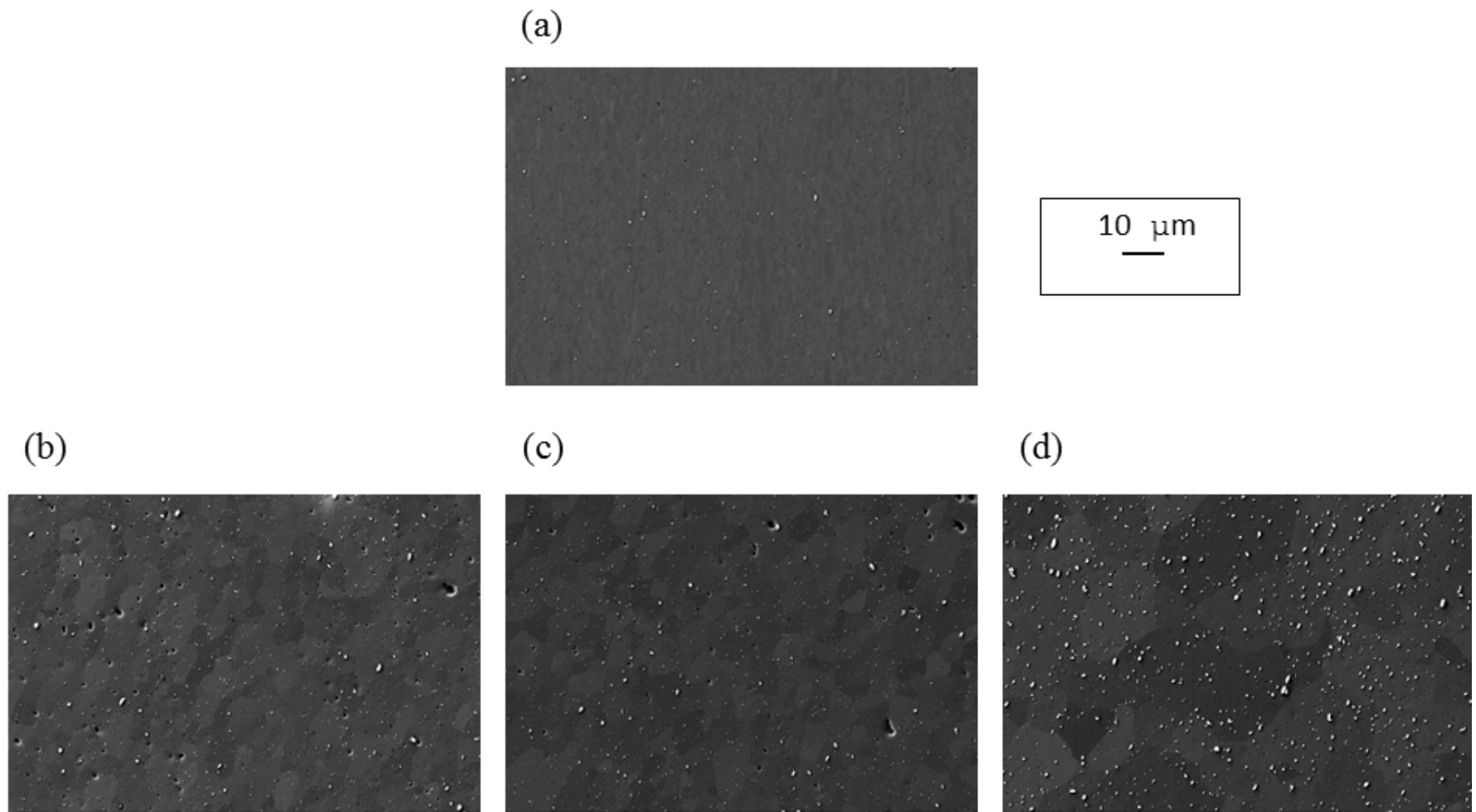


Figure 3.11 Scanning electron microscopy image comparison of (a) BM, (b) 400 RPM/100 MPM, (c) 300 RPM/50 MPM, and (d) 500 RPM/25 MPM showing oxide particle coarsening following friction stir welding.

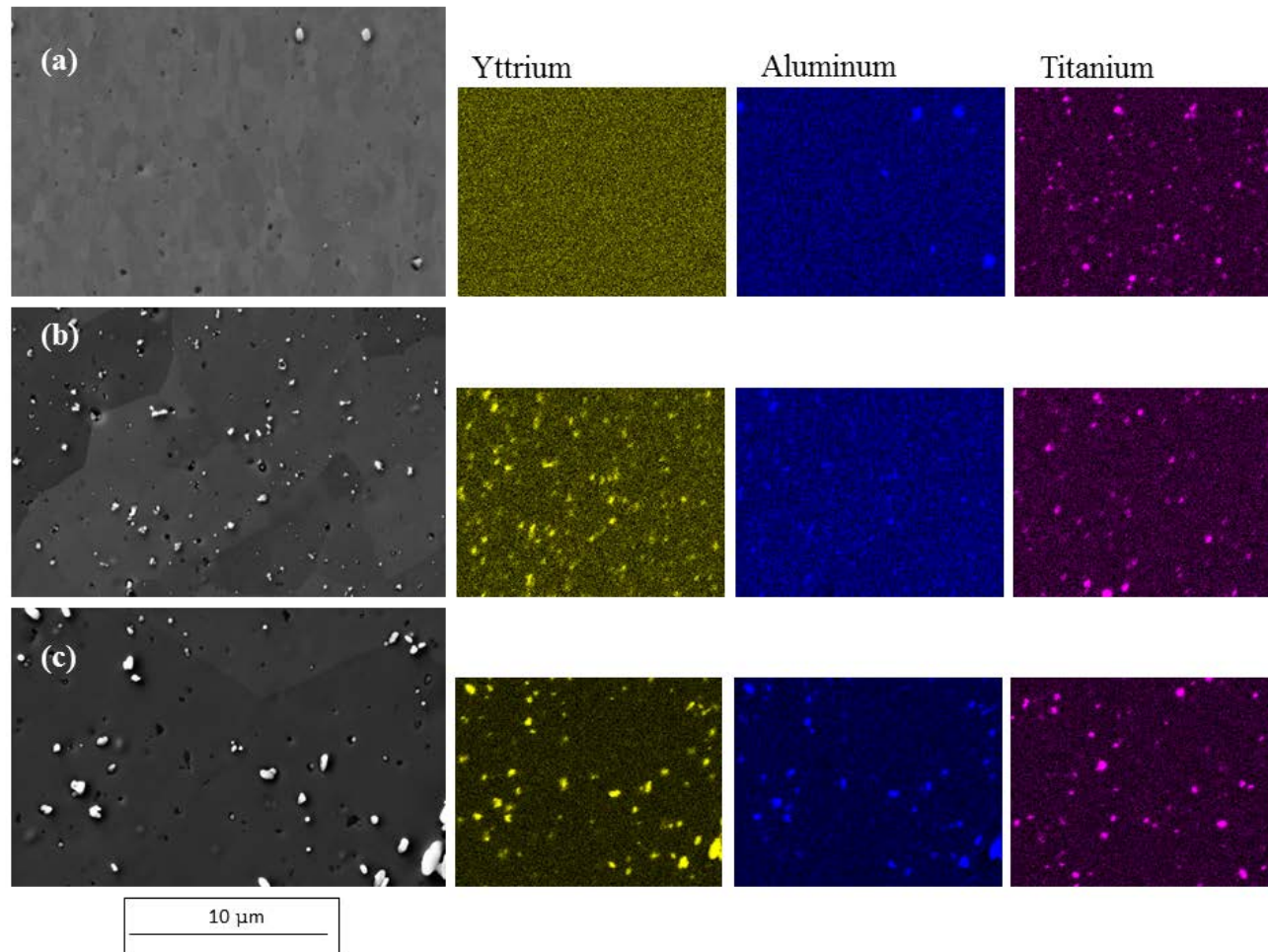


Figure 3.12 Scanning electron microscopy imagery and energy dispersive x-ray spectroscopy spectral maps for yttrium (left side-yellow), aluminum (center-blue), and titanium (right side-purple) for (a) base metal, (b) 400 RPM/100 MPPM (low heat input), and (c) 500 RPM/25 MPPM (high heat input) showing increasing oxide particle coarsening as heat input was increased during friction stir welding.

SAXS analysis of the SZ for each welding condition shows both a reduction in volume distribution and an increase in particle diameter from the BM to the SZ for each FSW combination corroborating the particle coarsening evidence seen in the SEM imaging and EDS mapping (Figure 3.13). The SAXS data from Figures 3.13 strongly substantiates the SEM and EDS analyses of Figures 3.11 and 3.12. The SAXS data alone suggests that the number of nm sized particles is nearly eliminated in all friction stir welded specimens regardless of heat input, and the overall particle size is increased traversing from the BM to the SZ which serves as an independent display of particle coarsening from the SEM and EDS data in Figures 3.11 and 3.12.

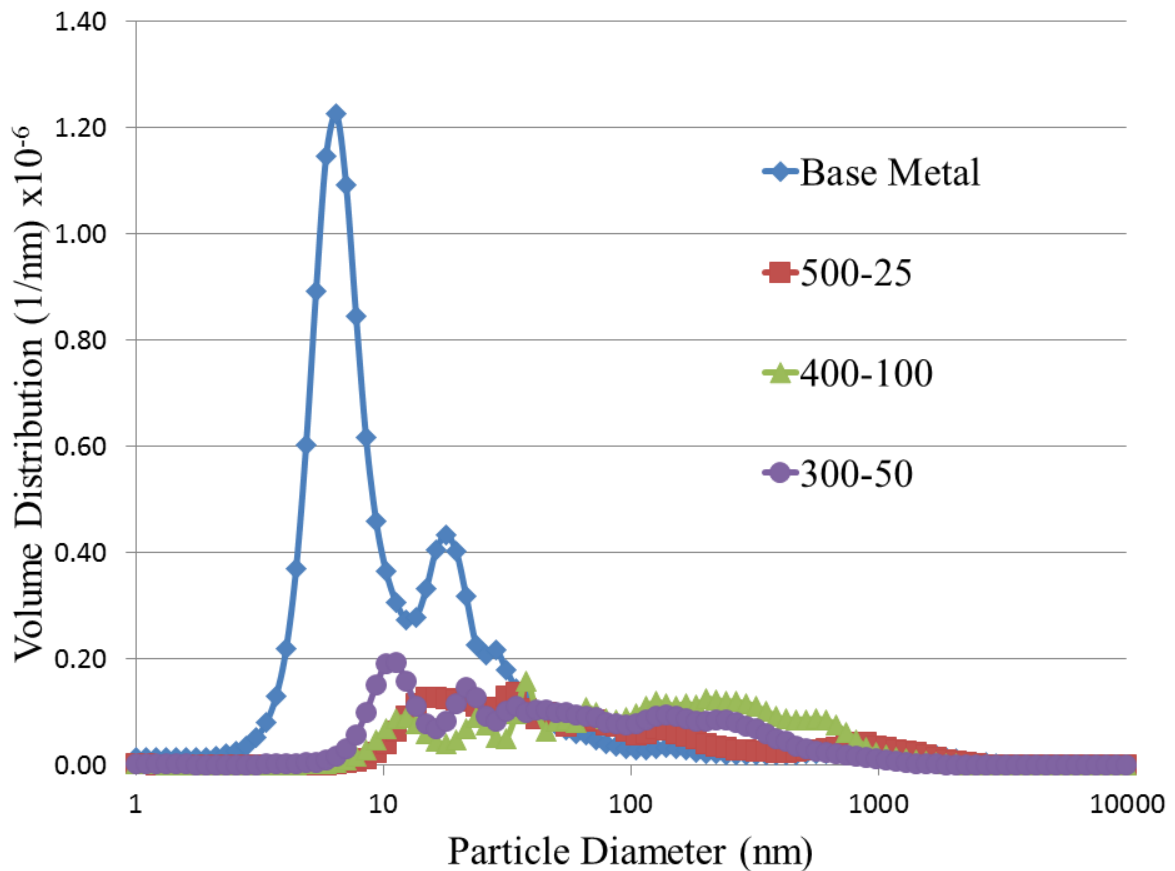


Figure 3.13 Small angle x-ray scattering data from the stir zone material for friction stir welding conditions.

3. Thermo-Mechanically Affected Zone Distribution

In Chapter II large gradients in grain size and hardness were observed across the TMAZ in particular on the AS of the weld nugget for high heat input conditions. Consistent with that analysis a small but noticeable change in particle size was evident across the TMAZ on the AS for each parameter combination (Figure 3.14). On the RS of each parameter combination, no such gradient in particle size, grain size, or hardness is evident (Figure 3.15).

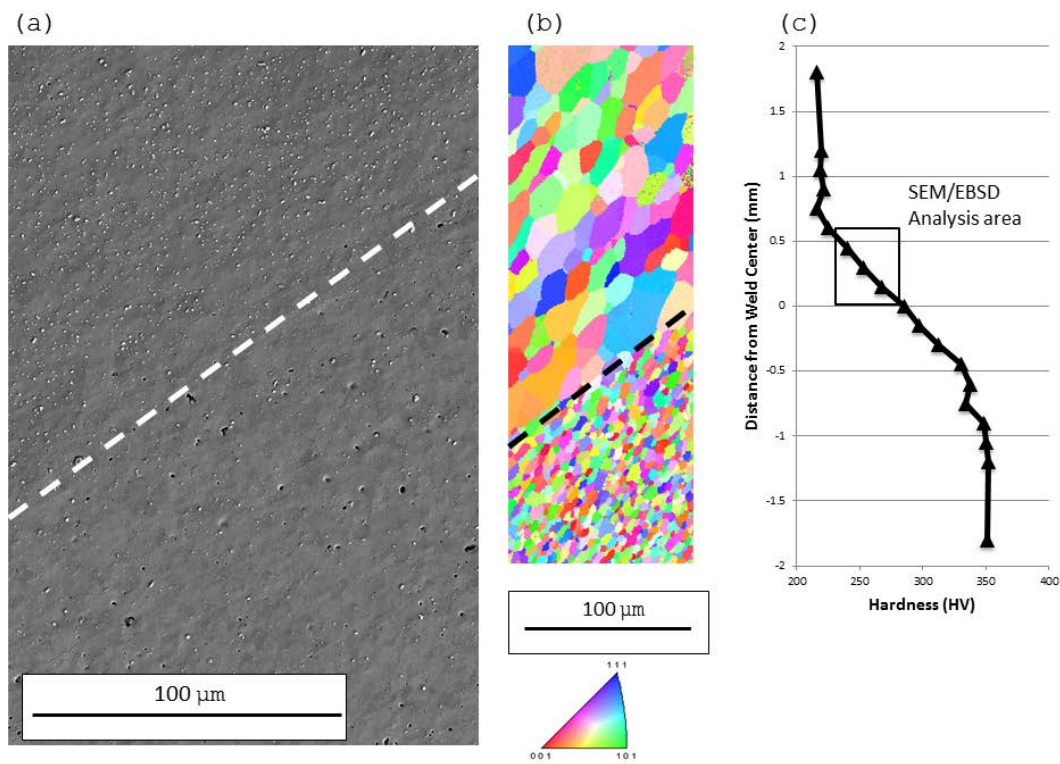


Figure 3.14 Gradients in (a) oxide particle size, (b) grain size, and (c) hardness at the advancing side thermo-mechanically affected zone (top left) for the 500 RPM/25 MPPM parameter combination. Dotted lines on (a) and (b) are illustrative of the separation that exists at the thermo-mechanically affected zone. The annotation on the hardness graph (c) indicates the approximate area for the images in (a) and (b).

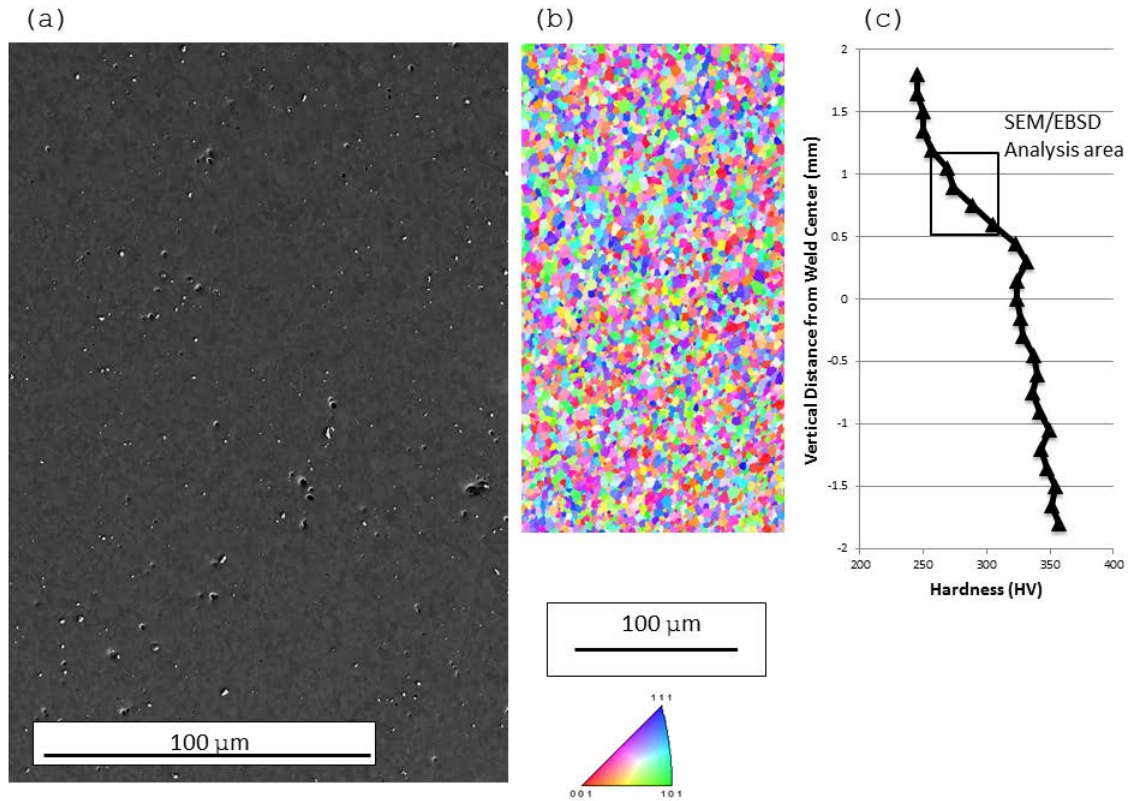


Figure 3.15 (a) Oxide particle size, (b) grain size, and (c) hardness at the retreating side thermo-mechanically affected zone (bottom right) for the 500 RPM/25 MPM parameter combination. The annotation on the hardness graph (c) indicates the approximate area for the images in (a) and (b).

4. Oxide Particle Phase Determination

Using raw intensity comparisons to DTSA-II simulated spectra and quantitative EDS analysis, oxide particles in MA956 were determined to be predominantly YAG for high heat input conditions and a mixture of YAG and other lower yttrium concentration particles for low heat input conditions. BM oxide particle phase determination was not attempted; however, since the results by Hsiung were based on the same MA956 as used in this research with no additional heat treatments or processing, the oxides existing in the BM are assumed to be YAM, YAP, and specifically not YAG as previously discussed [37].

For the high heat input welding condition, 500 RPM/25 MMPM, a total of 10 particles in the SZ were analyzed by EDS (Figure 3.16) including a range of particle sizes from large particles (longest axis approximately 500 nm or greater) and small particles (longest axis less than 500 nm).¹² Of these 10 particles, 9 were determined to be YAG with the remaining particle determined to be YAM (Table 3.4). This conclusion was based on both quantitative EDS analysis and DTSA-II simulation comparison. The maximum error of the 9 particles determined to be YAG was 16.5% with an average of error of 8.1% using $AR_{Y/Al}$ and 23.0% maximum error and 10.9% average error using $IR_{Y/Al}$.

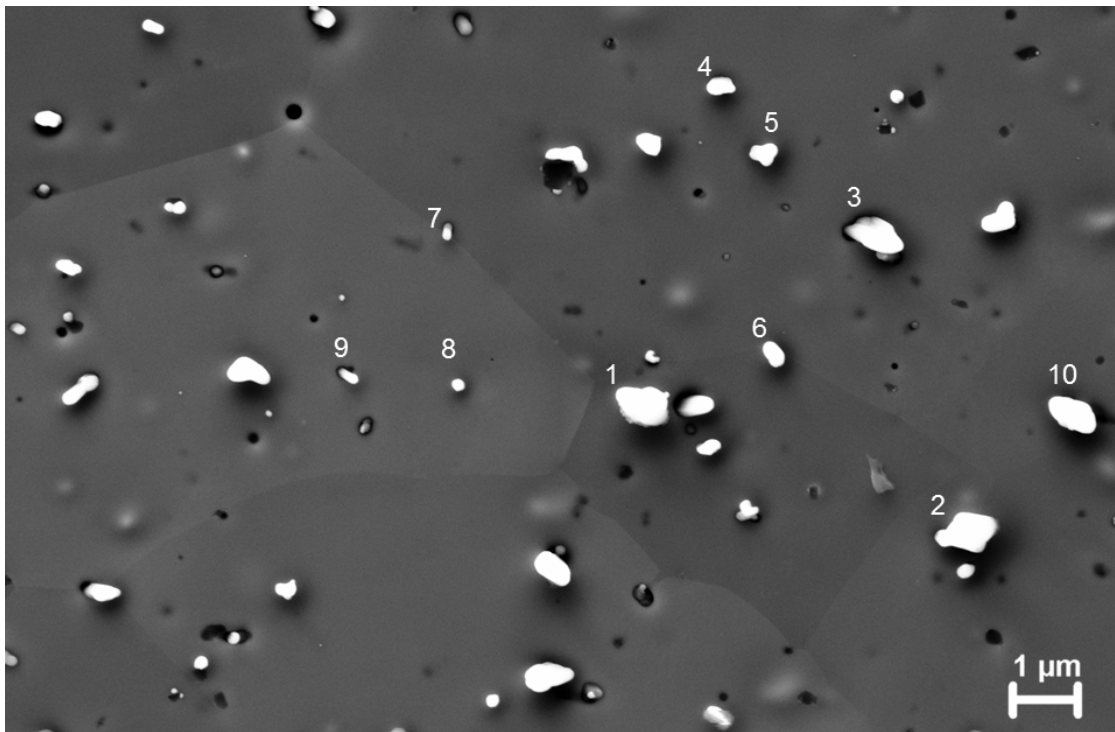


Figure 3.16 Scanning electron microscopy image of the stir zone from the high heat input condition (500 RPM/25 MMPM) showing particles analyzed by energy dispersive x-ray spectroscopy. Particle numbering refers to Table 3.3.

¹² Although the scales in Figure 3.16 (and subsequent Figure 3.21) are accurate, the discussion of particle size in this section dealing with oxide particle phase determination is considered to be less accurate and very different in approach than the particle size determination in paragraph C.2 and Figures 3.11 and 3.12. The most accurate particle size calculation is achieved by measuring the area of the particle and determining the equivalent diameter of a circle of the same area. The particle size approach mentioned in this section is based on a single line estimate across the largest axis of the particle, and thus is in most all cases an overestimate of the true particle size.

Table 3.4 Parameters used to identify phase of complex Y-Al-O particles in friction stir welds with high heat input parameters.

Particle Number (Corresponding to Figure 3.16)	Yttrium to Aluminum Atom Ratio ($AR_{Y/Al}$) (YAM=2) (YAP=1) (YAG=0.6)	Yttrium to Aluminum Intensity Ratio ($IR_{Y/Al}$) (YAM=1.671) (YAP=1.208) (YAG=0.814)	Determined Phase
1	0.535	0.672	YAG
2	0.570	0.720	YAG
3	0.551	0.694	YAG
4	0.592	0.750	YAG
5	0.501	0.627	YAG
6	0.525	0.659	YAG
7	0.626	0.796	YAG
8	0.635	0.808	YAG
9	2.057	2.803	YAM
10	0.648	0.826	YAG

EDS line scans were conducted across both YAG (Figure 3.17) and YAM (Figure 3.18) particles in the high heat input condition. Inset areas of both of these Figures show the corresponding particle to the overall particle map of Figure 3.16 as well as the line profile used for the measurement. Both of these line scans show the good spatial resolution achieved using the field-emission SEM combined with EDS. The y-axis of Figures 3.17 and 3.18 were intentionally converted to weight percent to allow for direct comparison to the known weight percentages of MA956 (Table 1.4). This depiction shows that YAM forms at an aluminum weight percent that was consistent with the

uniform distribution of aluminum within MA956 (4.75%) while YAG requires a concentration of aluminum well above that seen in the base alloy.

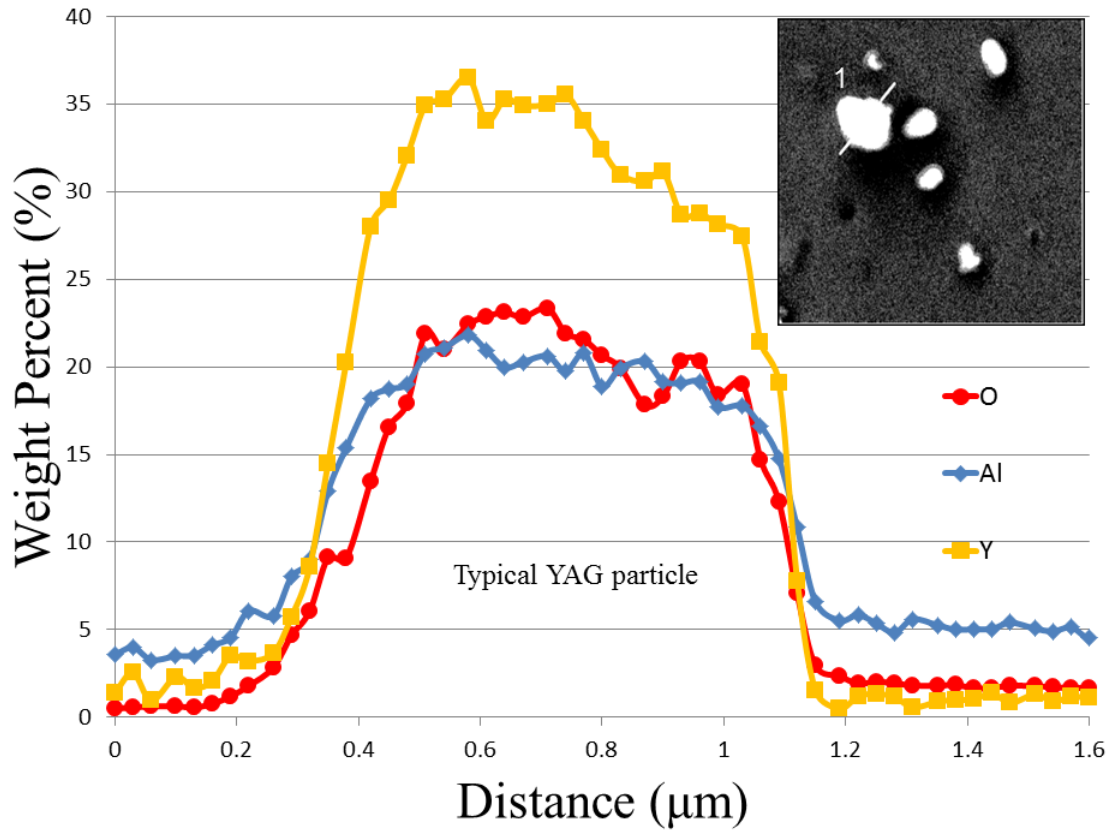


Figure 3.17 Energy dispersive line scan across an yttrium aluminum garnet particle in the stir zone of the high heat input condition. The inset area corresponds to Figure 3.16 and depicts the orientation of the scan.

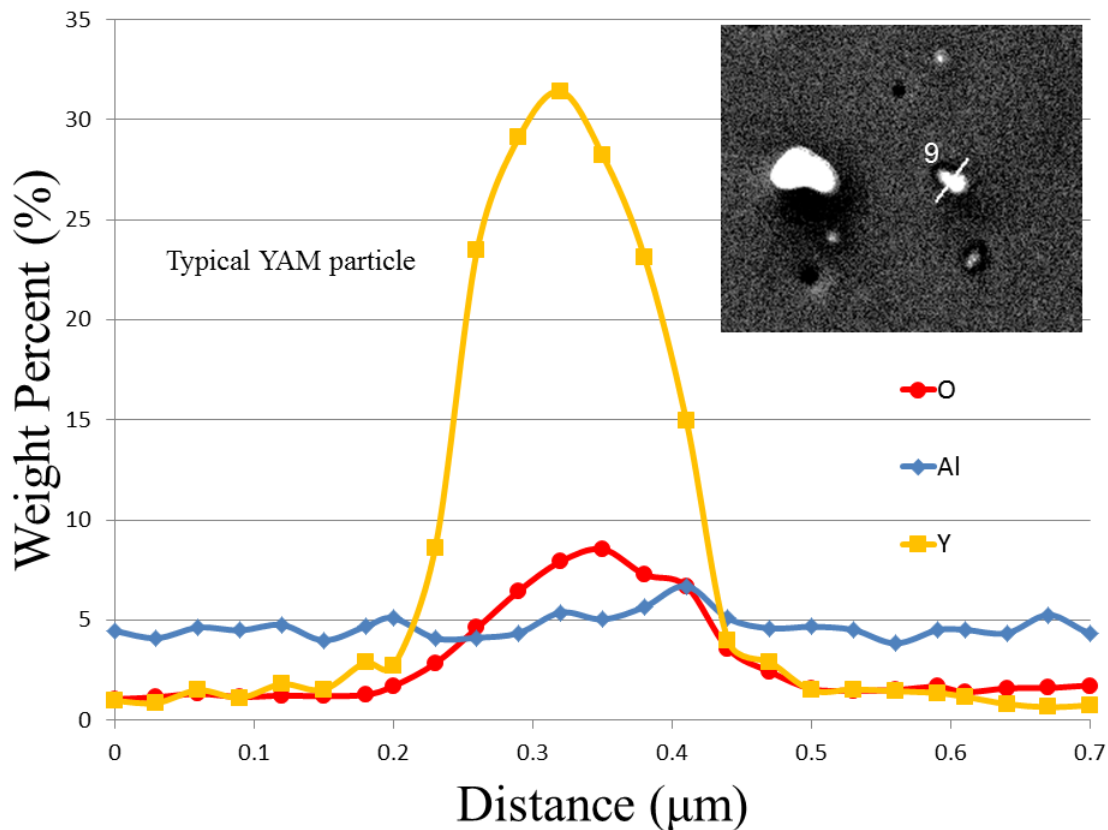


Figure 3.18 Energy dispersive line scan across an yttrium aluminum monoclinic particle in the stir zone of the high heat input condition. The inset area corresponds to Figure 3.16 and depicts the orientation of the scan.

Reasonable agreement was noted between the theoretical and experimental data of the DTSA-II simulated spectra and EDAX Genesis spectra. Comparison spectra for the EDAX Genesis and DTSA-II data are shown in Figure 3.19 for YAG and Figure 3.20 for YAM. The intensities used for the ratios in Table 3.3 come from these spectra (although only shown for particles 1 and 9 in Figure 3.19 and 3.20 respectively.) To allow for comparison between the theoretical predictions and experimental results, the data for Figure 3.19 and 3.20 is normalized to the maximum intensity for each. As discussed previously, the low energies associated with C-K and N-K visible on the experimental results are below the minimum energy considered accurate and are thus neglected. These C-K and N-K peaks do not exist on the DTSA-II theoretical predictions because C and N were intentionally not included in the substrate.

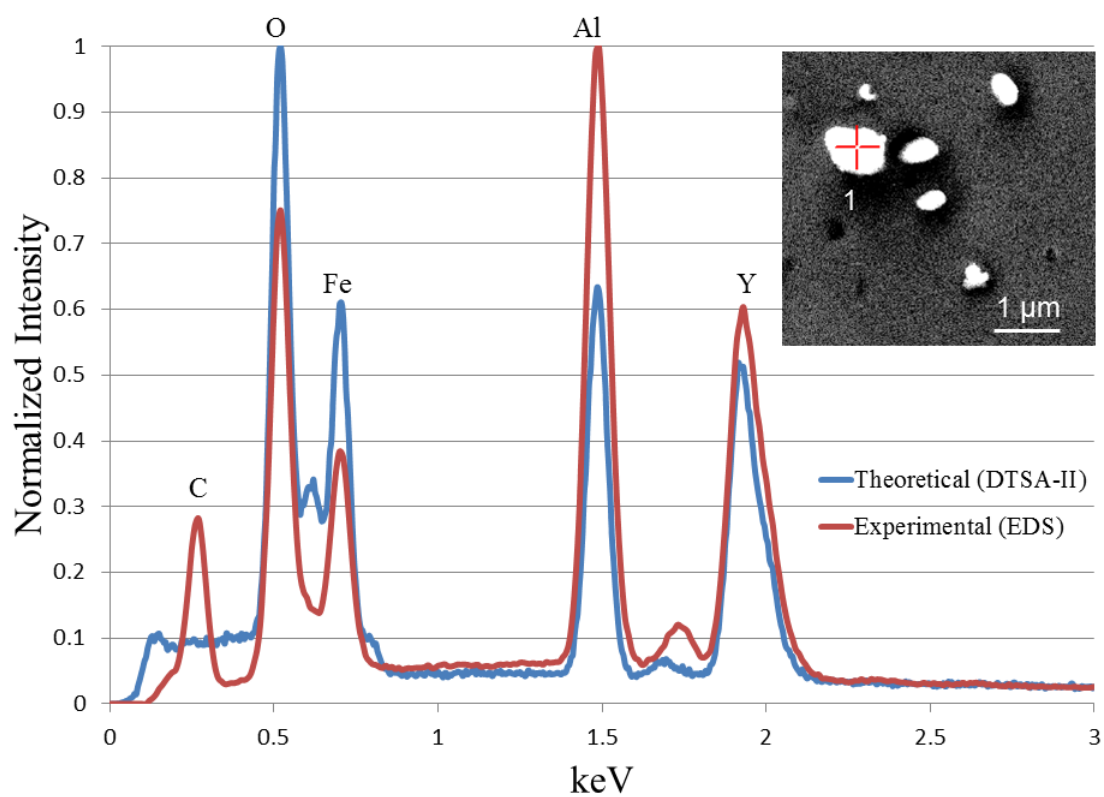


Figure 3.19 Energy spectrum for a yttrium aluminum garnet particle from experimental data from the EDAX Genesis software and theoretical simulations using DTSA-II.

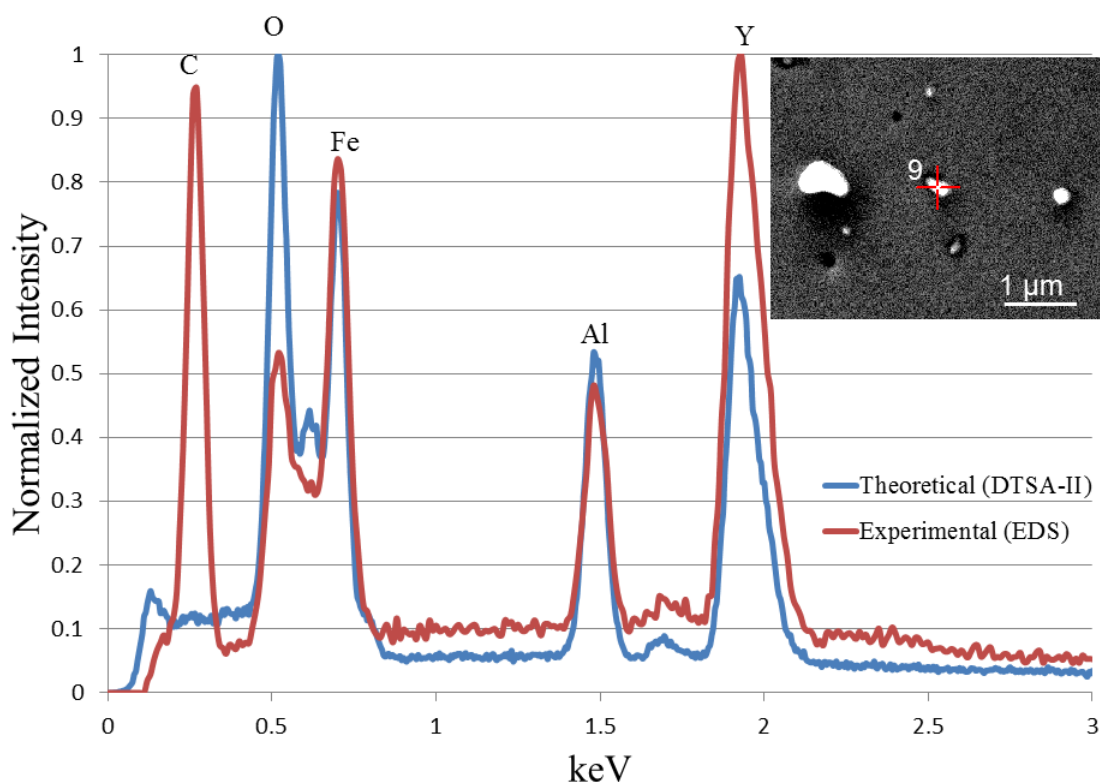


Figure 3.20 Energy spectrum for a yttrium aluminum monoclinic particle from experimental data from the EDAX Genesis software and theoretical simulations using DTSA-II.

For the low heat input welding condition, 400 RPM/100 MMPM, a total of 10 particles in the SZ were analyzed by EDS (Figure 3.21) including a range of particle sizes similar to that of the high heat input condition. As can be clearly seen between the Figures 3.16 and 3.21, the particles in the low heat input condition are in general much smaller than the high heat input condition. Of these 10 particles, 7 were determined to be YAG and the remaining 3 (all of which corresponded to larger particles) could not be conclusively be determined to be YAM, YAP, or YAG (Table 3.5). The maximum error of the 7 particles determined to be YAG was 32.7% with an average of error of 16.0% using $AR_{Y/Al}$ and 38.7% maximum error and 17.4% average error using $IR_{Y/Al}$.

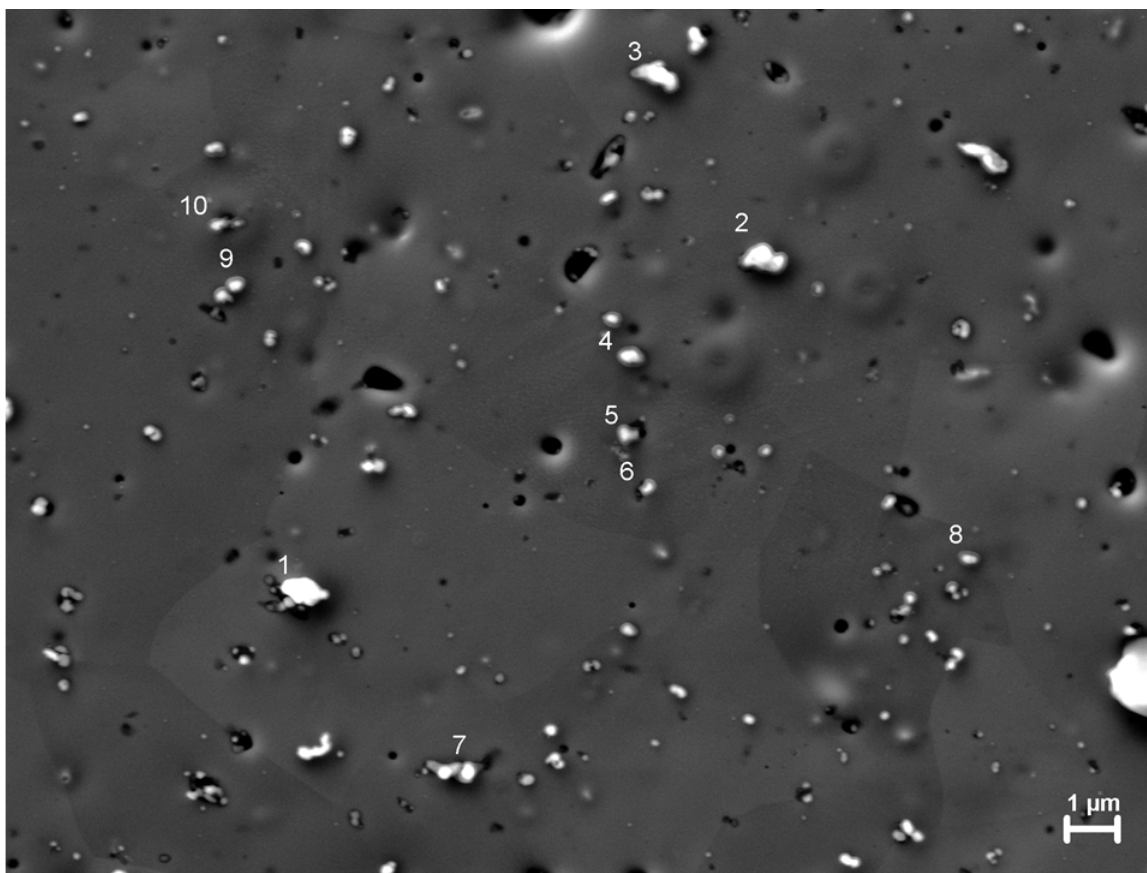


Figure 3.21 Scanning electron microscopy image of the stir zone from the low heat input condition (400 RPM/100 MPPM) showing particles analyzed by energy dispersive x-ray spectroscopy. Particle numbering refers to Table 3.4.

Table 3.5 Parameters used to identify phase of complex Y-Al-O particles in friction stir welds with low heat input parameters.

Particle Number (Corresponding to Figure 3.23)	Yttrium to Aluminum Atom Ratio ($AR_{Y/Al}$) (YAM=2) (YAP=1) (YAG=0.6)	Yttrium to Aluminum Intensity Ratio ($IR_{Y/Al}$) (YAM=1.671) (YAP=1.208) (YAG=0.814)	Determined Phase
1	0.075	0.084	Indeterminate
2	0.156	0.181	Indeterminate
3	0.231	0.274	Indeterminate
4	0.716	0.920	YAG
5	0.490	0.613	YAG
6	0.497	0.622	YAG
7	0.404	0.499	YAG
8	0.626	0.798	YAG
9	0.538	0.678	YAG
10	0.658	0.839	YAG

Similar to the EDS line scans done for the high heat input condition, line scans across particles in the low heat input condition were conducted and produced mixed results. Smaller particles in the low heat input condition were determined to be YAG and had EDS line profiles very similar to YAG particles seen in the high heat input condition (Figure 3.22 compared to Figure 3.17). Larger particles in the low heat input condition, however, had inconsistent EDS line profiles as shown in Figures 3.23 and 3.24. The line profiles, atom ratios, and intensity ratios of these particles did not conclusively match to YAM, YAP, or YAG and seem to suggest a non-uniform distribution of yttrium within the particles that was not seen in any of the particles from the high heat input condition.

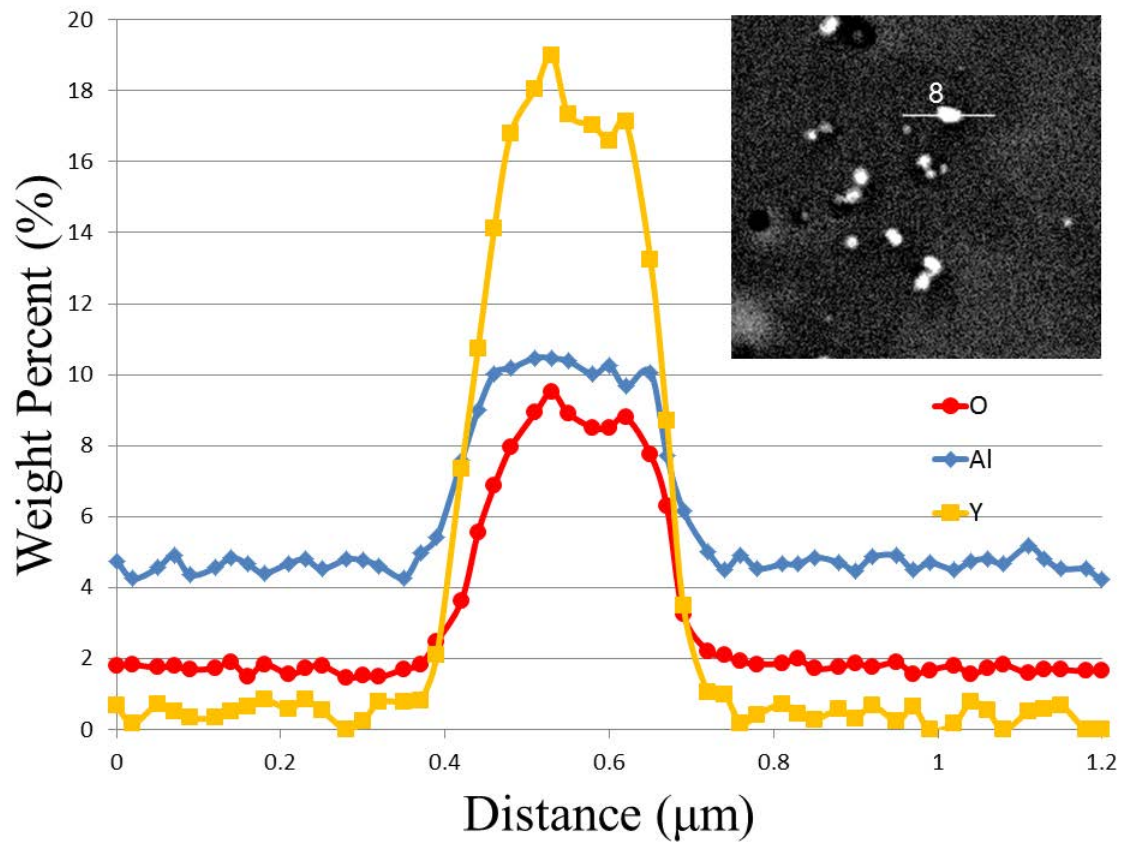


Figure 3.22 Energy dispersive line scan across a yttrium aluminum garnet particle in the stir zone of the low heat input condition. The inset area corresponds to Figure 3.21 and depicts the orientation of the scan.

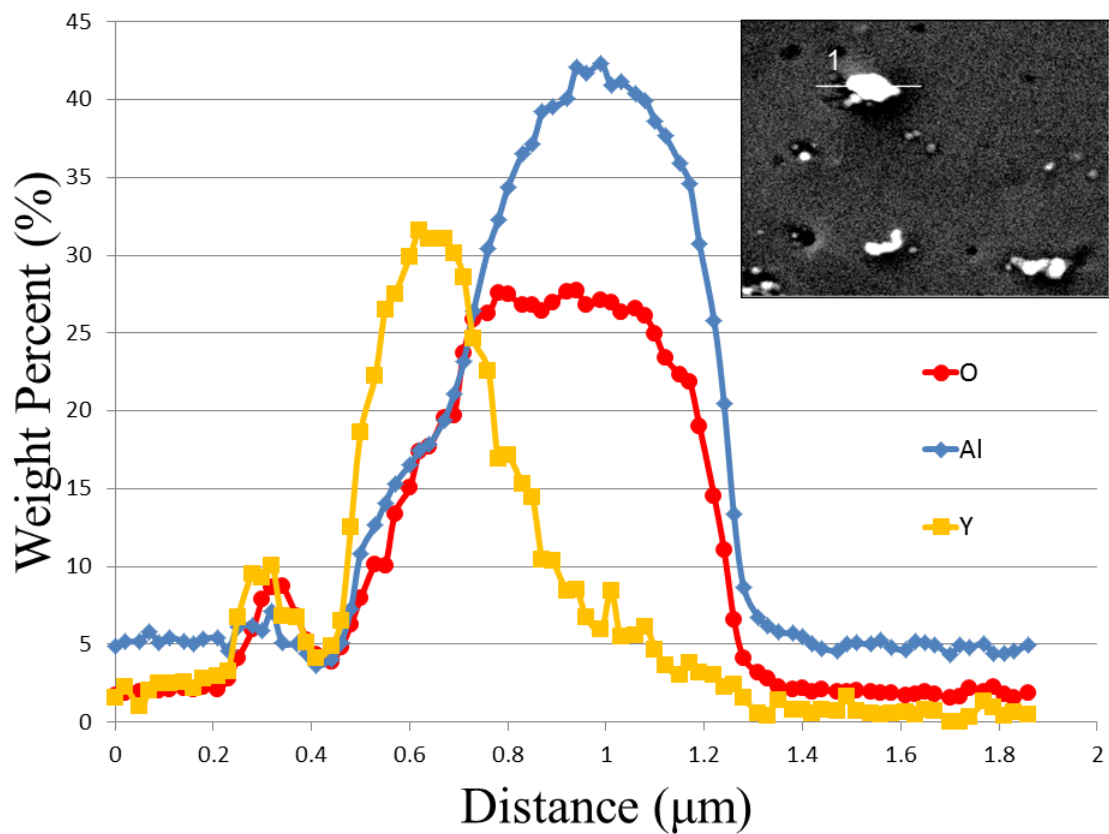


Figure 3.23 Energy dispersive line scan across an indeterminate particle in the stir zone of the low heat input condition. The inset area corresponds to Figure 3.21 and depicts the orientation of the scan.

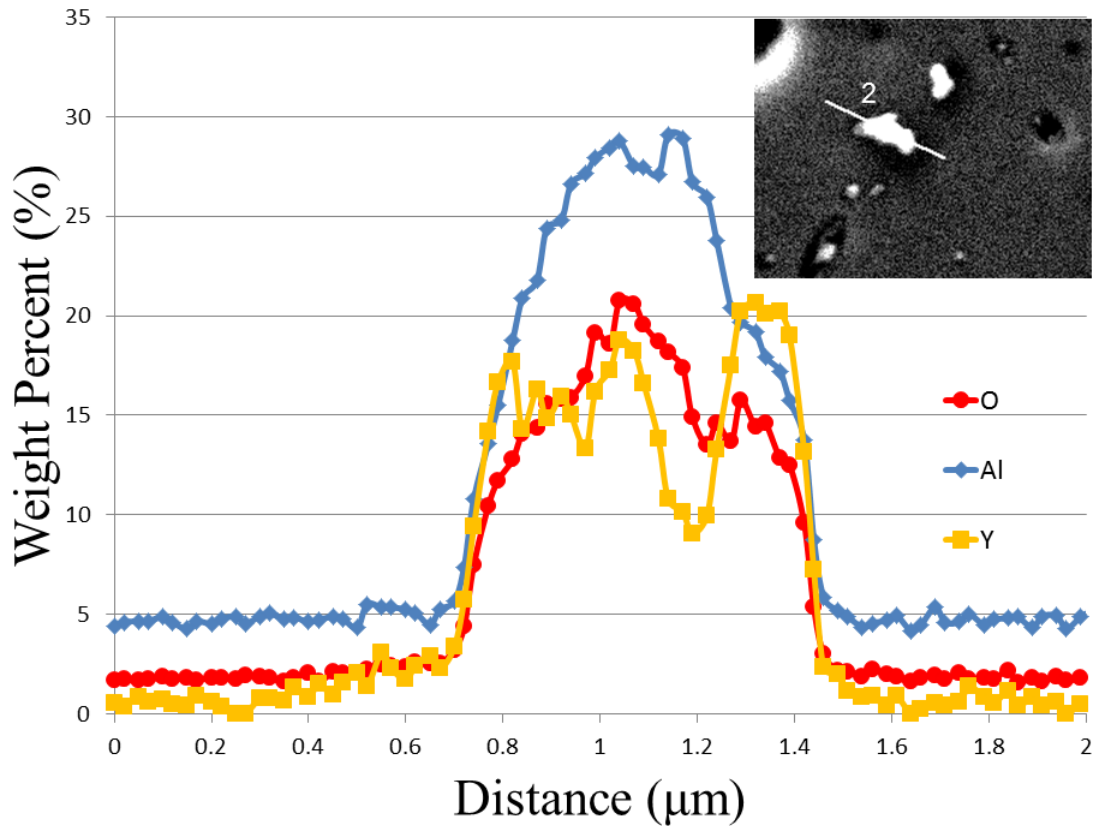


Figure 3.24 Energy dispersive line scan across an indeterminate particle in the stir zone of the low heat input condition. The inset area corresponds to Figure 3.22 and depicts the orientation of the scan.

D. DISCUSSION

1. Oxide Particle Coarsening

Using nano and micro-scale techniques, oxide particle coarsening clearly occurs following FSW over a range of heat input conditions. At the nano-scale, STEM images show oxide particle growth from the BM to the SZ during FSW (Figure 3.7 compared to Figure 3.10). Similarly, micro-scale SEM imaging shows only Al-O particles visible prior to FSW, while subsequent SZ areas for all conditions show Y-Al-O particles clearly visible at this scale (Figure 3.11). Similarly, the reduction in number of small particles and corresponding increase in number of larger particles following FSW seen in SAXS analysis (Figures 3.13) clearly indicate oxide particle coarsening. Results show a significant reduction in the population of nano-scale particles and a corresponding

increase in micro-scale particles. Combining SEM imaging with EDS analysis (Figure 3.12), the spectral maps clearly show a coarsening of yttrium and aluminum that becomes more pronounced as the heat input is increased.

To quantify this coarsening, two independent optical counting techniques were used on the SEM images of Figure 3.11 (Table 3.6). Data for Table 3.6 is presented in terms of oxide particle density in the analysis area in particles/m² (N), average particle diameter (d_{avg}) in nm, and inter-particle centroid to centroid spacing (S) in μ m for different values of HI with FSW parameter conditions listed for reference. The data for the BM is taken from results by Hsiung [37]. For clarity Hsiung's particle counting includes nano-scale particles that are well below the size that can be counted using the techniques in this research, and thus a direct comparison of the absolute particle density between the BM and the SZ is not intended; however, the order of magnitude difference between the two and the SAXS results herein suggest oxide particle coarsening following FSW. The similarity in welding conditions of 400 RPM/100 MPPM and 300 RPM/50 RPM cause the data distribution between these two low heat input conditions to be indistinguishable, but the difference between the low heat input conditions and the high heat input condition of 500 RPM/25 MPPM is significant as is the disparity between the BM and any of the FSW conditions. The results from Woertz's code and ImageJ are comparable and the trends between the two methods are consistent. Overall the data from Table 3.6 combined with the qualitative results of Figures 3.11 and 3.12, i.e. particle population density decreasing and average particle diameter increasing, clearly demonstrate that Y-Al-O particles are coarsened during FSW and that this coarsening is dependent on welding parameters, specifically that higher heat input conditions cause greater particle coarsening.

Table 3.6 Oxide particle density (N), average particle diameter (d_{avg}), and inter-particle spacing (S) for different friction stir welding conditions for the same sample area.

FSW Parameter Condition (RPM/MMPM)	HI	N (particles/m ²)		d_{avg} (nm)		S (μm)
		Woertz	ImageJ	Woertz	ImageJ	
400/100	4	4.32×10^{11}	4.02×10^{11}	166	226	3.23
300/50	6	4.39×10^{11}	4.13×10^{11}	163	202	3.19
500/25	20	1.75×10^{11}	1.44×10^{11}	343	410	3.41
BM[37]	-	1×10^{13}		8.1		-

The oxide particle coarsening during FSW presented here is similar to particle coarsening shown by both Cama and Kruk during extended high temperature exposure of MA956 at temperatures below its melting temperature [169, 171]. Using quantitative EDS, Cama observed a three times increase in average particle size (from 15 nm to 50 nm) during exposure at 1300°C (88% of the melting temperature for MA956) over 1000 hours and, using electron tomography, Kruk observed in excess of a two times increase in particle size (from 3–60 nm to 92–192 nm) during exposure at 1350°C over 1000 hours. Both of these results show particle increases of roughly the same magnitude seen in this research and are both at temperatures at or near the top of the expected temperature range of typical metal FSW conditions with the primary difference being the time in which the coarsening occurs [121, 122, 130]. As opposed to the 1000 hours of exposure time of Cama and Kruk, the coarsening during FSW occurs during the short term welding process. The cause of this difference in coarsening rate is attributed to the proposed coarsening mechanism presented later in this chapter.

2. Titanium Particle Effects

Dispersed TiCN particles appear to be unaffected by FSW up to the HI values used here (Figures 3.11 and 3.12). Research similar to that completed herein for MA957 (an ODS alloy without aluminum) with a singular FSW condition has shown that FSW had relatively little effect on the number density and size distribution of Y-Ti-O particles [58, 147]. Whether or not Y-Ti-O particles are stable during all FSW conditions is unknown, but the difference in response of Y-Al-O ODS alloys and Y-Ti-O ODS alloys may give additional options when considering various alloys for design applications.

3. Proposed Coarsening Mechanisms

Before discussing possible mechanisms behind the oxide particle coarsening seen in this research, a more detailed summary of current literature on oxide particle coarsening in aluminum-containing ODS steels will be presented in order to establish hypotheses for the effects of FSW on the oxide particles. This review includes research on FSW of the ODS steels PM2000 and MA956 which are very similar in composition (Table 1.3) and initial processing. Using SANS and SEM, West analyzed the change in microstructure of MA956 following FSW with conditions of 400 RPM/50 MPPM (a comparatively low heat input condition) and 600 RPM/13 MPPM (a comparatively high heat input condition) and concluded that “dispersoids were slightly coarsened during welding” without any quantification of the degree of coarsening or any attempts to determine the phase of the particles either before or after FSW [141]. Using comparisons of grain size and hardness to analyze the change of oxide particle size and distribution, West suggests that oxide particles may have dissolved and re-precipitated during FSW leading to the slight coarsening effect observed.

Using TEM and STEM, Wang researched the change in microstructure and mechanical properties of MA956 following FSW with the comparatively very high heat input condition of 1000 RPM/50 MPPM [56]. Although oxide particle phase composition determination was not attempted, Wang observed dispersoid coarsening and commented “fine dispersoids were noticed to attach to coarse ones, and typical diameter was about 140 nm, which was not observed in the as-received material under TEM [sic]”

[56]. In his conclusions, Wang describes this effect as particle-coalescence induced coarsening. Although he does not state it as such, Wang's theory for coarsening can also be described as Ostwald ripening.

Using TEM, high resolution STEM, and EBSD, Chen concluded that FSW "appears to make only a small difference to the size and distribution of the oxide dispersion in PM2000," but he did not include the FSW conditions used and also did not address weld consolidation so a full analysis of the effect of heat input from FSW cannot be ascertained [60, 154]. Chen measured the size, composition, and microstructure of the oxide particles by extraction replication of particles onto a carbon support film. While an accurate method of measuring individual particles, this approach may bias measurements to smaller particles. Similar TEM and STEM foil preparation techniques were utilized in this research and it was noted that often large particles fell out of the samples during preparation and thus would not be included in this nano-scale analysis. Additionally Chen analyzed phases of Y-Al-O particles during initial heat treatments after consolidation prior to FSW. This analysis showed transformations within the Al_2O_3 - Y_2O_3 system (Figure 3.5) that were similar to those presented by Hsiung [37]. In this analysis Chen concluded that the high temperatures during consolidation and post manufacture heat treatment caused continued phase transformations between Y_2O_3 powders, YAG, and YAP, but due to the aggregate response of FSW and heat treatments, changes in particle phase or composition cannot be directly attributed to either condition separately.

In related work Mathon and Legendre analyzed the effects of FSW on the microstructure of PM2000 using SANS and concluded that oxide particles "grow larger as one approaches the SZ. In the nugget of the weld joint, the size of the particles is too large to allow quantifying their size and volume fraction" [142, 143]. For this research Mathon and Legendre used a singular high heat input condition (600 RPM/50 MPPM) comparatively similar to the high heat input condition used in this research (500 RPM/25 MPPM). Similar to the work by Chen, the methods used by Mathon and Legendre are biased to particles of smaller size so a complete analysis of both nano-scale and micro-scale particles cannot be accomplished. Mathon even notes this fact stating "only the

smallest particles are detected [by SANS] corresponding to a volume fraction of 0.5%” [143]. Unlike the EDS analysis used in this research, the SANS techniques by Mathon do not support the direct identification of different elements or phases within the alloy, and thus, although Mathon concludes that oxide chemical composition is different than in the BM, he concludes the particles in the SZ may be Y-Ti-Al-O without definitive data to support this suggestion. None of the EDS data in this research has shown a change in titanium distribution following FSW that supports the formation of a Y-Ti-Al-O phase. Although neither Mathon nor Legendre propose a mechanism behind the effect of FSW on the oxide particles in PM2000, both of their results suggest a change in the chemical composition of particles following FSW.

From this literature review three mechanisms are proposed for the coarsening of Y-Al-O particles seen in this research: (1) particle coarsening due to the dissolution and subsequent re-precipitation of Y-Al-O particles, (2) particle coarsening due to Ostwald ripening, and (3) particle coarsening due to the continued phase transformation within the Al_2O_3 - Y_2O_3 system similar to that seen during initial alloy consolidation and processing. The first coarsening mechanism proposed is that Y-Al-O particles are dissolved and subsequently re-precipitated during FSW as proposed by West. Although temperature was not measured during the FSW of this research as previously discussed, theoretical and other experimental research has shown that FSW raises an alloy to approximately 80–90% of its melting temperature (equating to a temperature range of 1178°C to 1326°C for MA956) [121, 122, 129–131]. This temperature is insufficient to cause dissolution of any phase in the Al_2O_3 - Y_2O_3 system (Figure 3.5), and other experimental work has even shown the ability to melt the base metal alloy while preserving the oxides intact for analysis [101]. Additionally the enthalpies of formation for YAG (-7,197 kJ/mol), YAM (-5,545 kJ/mol), and YAP (-1,827 kJ/mol) are sufficiently low to suggest that dissolution of any of these phases is unlikely even during FSW [182]. Additional research on the phase stability of YAG, YAM, and YAP also suggests these phases would not undergo dissolution at the temperatures typically seen during FSW [183]. For these reasons, dissolution and re-precipitation is not considered to be viable mechanism for the oxide particle coarsening seen in this research.

The second proposed mechanism, Ostwald ripening, proposes that smaller particles dissolve, and through solid state mass transport, large particles grow which is slightly different than the particle-coalescence theory proposed by Wang. The theory of Ostwald ripening is discussed in detail by Voorhees [184] but can be summarized as the reduction in total energy of a two-phase system (base matrix and a Y-Al-O particle) by an increase in the size of the second phase (the Y-Al-O particle) which causes a decrease in total interfacial area. This reduction in total energy is thermodynamically favorable leading to the coarsening effect. Taken on their own, the SAXS results in this research (Figure 3.13), or any method that does not include an analysis of phase, suggest Ostwald ripening as a mechanism for oxide particle coarsening. These methods show a reduction in population of smaller particles and an increase in population of larger particles and inherently assume a constant volume fraction process of the second phase, i.e. the Y-Al-O particles.

The volume fraction (f) of a precipitate is directly related to the diameter of the precipitate (d) and the inter-particle spacing (S) of the precipitates (Equation 3.1) [168]. Using this relationship and assuming a constant volume fraction process, any increase in particle size (d), such as due to Ostwald ripening, must cause a directly proportional change in inter-particle spacing (S). This criterion was evaluated for two different sets of conditions (Tables 3.6 and 3.7) and in both conditions the constant volume fraction process assumption is not supported. Data in Tables 3.6 and 3.7 is presented with the first condition being an initial condition from which coarsening occurs. From this initial condition the change in average particle size is used to calculate a constant volume fraction theoretical inter-particle spacing which can then be compared to the measure inter-particle spacing for the second condition. Table 3.6 shows this comparison for the BM to the SZ of the high heat input condition (500 RPM/25 MPM). For this comparison, if the particles from the BM were coarsened as shown (from 0.008 μm to 0.343 μm) the inter-particle spacing should be 1.59 μm ; however, this value was measured to be 3.41 μm indicating that the transition from the BM to the SZ was not a constant volume fraction process. Similarly, Table 3.7 shows a comparison of the low heat input condition (400 RPM/100 MPM) to the same high heat input condition. This

comparison is even more dramatic and shows that if particles were coarsened as shown (from 0.166 μm to 0.343 μm) the corresponding final inter-particle spacing should increase to 6.67 μm ; however, the inter-particle spacing was found to be only 3.41 μm and changed very little from the low heat input condition. These comparisons shows two very important details: (1) particle coarsening during FSW does not follow a constant volume fraction process and (2) the inter-particle spacing amongst vastly different FSW conditions is unchanged. A visualization of the particle coarsening mechanism by Ostwald ripening is shown in Figure 3.25 that is similar to the data presented in Tables 3.7 and 3.8. Figure 3.25 shows that for both the high and low heat input conditions, the theoretical predictions based on Ostwald ripening alone do not match the experimental results specifically that the inter-particle spacing does not correspond to the prediction.

$$f = \frac{1/6 \pi d_{avg}^3}{S^3} \quad \text{Equation 3.1}$$

Table 3.7 Evaluation of Ostwald ripening by comparison of oxide particle parameters for base metal and stir zone of high heat input condition.

Condition	Average particle diameter (d_{avg}) (μm)	Measured inter-particle spacing (S) (μm)	Constant volume fraction theoretical inter-particle spacing (S) (μm)
BM	0.008	0.037	-
Stir zone high heat input condition	0.343	3.41	1.42

Table 3.8 Evaluation of Ostwald ripening by comparison of oxide particle parameters for stir zones of low heat input and high heat input conditions.

Condition	Average particle diameter (d_{avg}) (μm)	Measured inter-particle spacing (S) (μm)	Constant volume fraction theoretical inter-particle spacing (S) (μm)
Stir zone low heat input condition	0.166	3.19	-
Stir zone high heat input condition	0.343	3.41	6.67

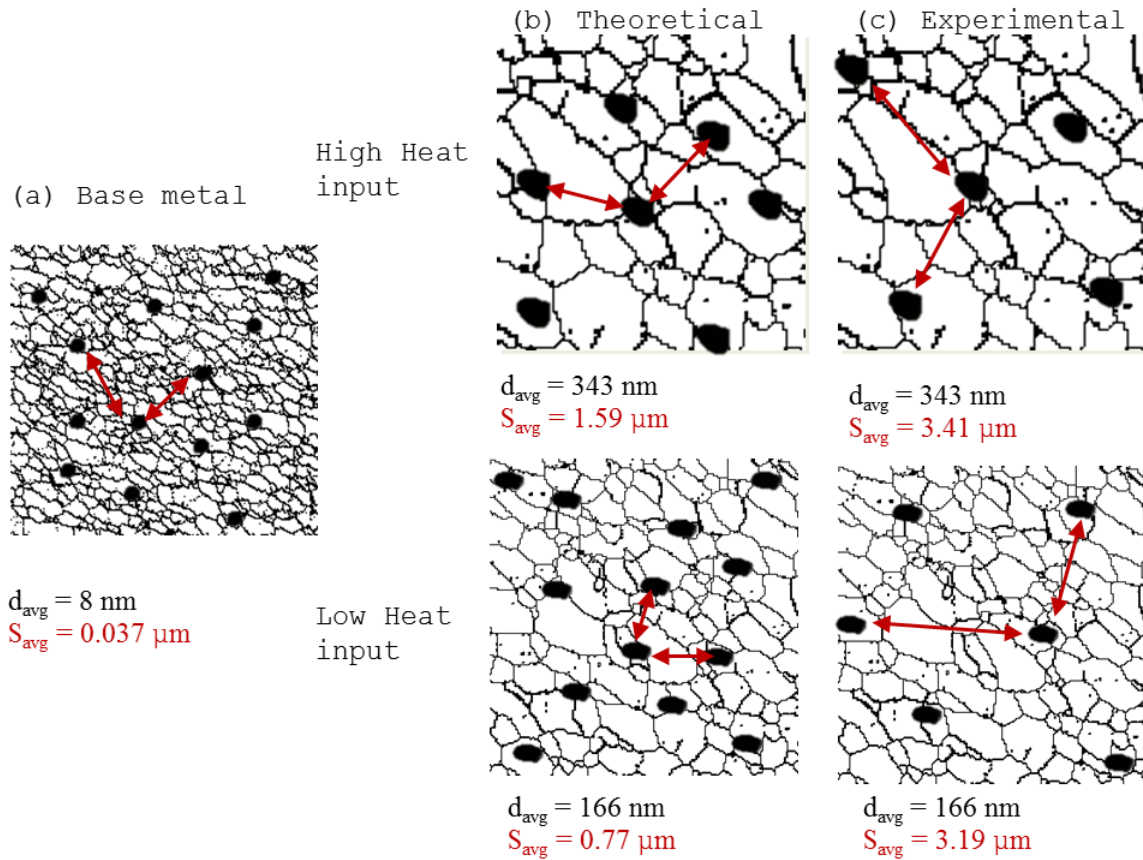


Figure 3.25 Visualization of (a) oxide particle distribution in the base metal, (b) theoretical oxide particle coarsening predicted by Ostwald ripening alone, and (c) experimental oxide particle coarsening seen in this research. Grain and oxide particle sizes are not to scale and are meant to be an approximation of data previously reported.

The SAXS data in this chapter strongly suggests a reduction in the number of nm scale particles and an increase in the number of larger (100s of nm) particles following FSW that is entirely independent of the EDS data also presented here. The SAXS data alone suggests an Ostwald ripening mechanism as previously discussed; however, SEM imagery such as that seen in Figure 3.11, 3.12, 3.16, and 3.21 and summarized in Table 3.5 shows a near uniform distribution of particles regardless of the particle size. If Ostwald ripening was the only active mechanism, the inter particle spacing would be expected to increase at the same rate as the particle size to achieve a consistent volume fraction of the same phase. Similar to the homogeneity discussion by Woertz [176], it is suggested that the FSW process establishes the uniform spatial distribution of particles

regardless of size, and the change in particle size is due to other proposed mechanisms discussed below.

Although FSW is a highly non-equilibrium process, reasonable estimates of time at temperature and time of exposure to the intense plastic deformation can be made which help establish the feasibility of diffusion and mass transport necessary to cause the particle coarsening seen herein. From the work previously cited by Swaminathan (Figure 1.13) on nickel aluminum bronze, the time at elevated temperature can be estimated conservatively high as 200 seconds with a similar conservatively high estimate of time at peak temperature of 10 seconds [149]. Using an adjustment to account for the differences in thermal conductivity of MA956 ($k_{MA956}=10.9 \text{ W/m}^\circ\text{C}$) and nickel aluminum bronze ($k_{NiAlBronze}=39.1 \text{ W/m}^\circ\text{C}$), it can be reasonably estimated that during FSW, MA956 is exposed to a thermal cycle lasting approximately 12 minutes with a sustained peak temperature time of approximately 1 minute. Using the size of the SZ and the welding speed, a particle is exposed to plastic deformation and the motion of the tool for approximately 1 minute for low tool traverse speeds (25 MPPM) or for 15 seconds for high tool traverse speeds (100 MPPM). The combined effects of elevated temperature and plastic deformation make accurate calculations of diffusivity or mass transport problematic, but the estimation of thermal cycle and plastic deformation exposure times suggest that particle motion during FSW would be sufficient to cause the particle coarsening seen in this research.

The third proposed coarsening mechanism, particle coarsening due to the continued phase transformation within the Al_2O_3 - Y_2O_3 system, by itself does not explain the specific reasoning behind the coarsening and also does not fully address whether the YAG particles are formed from existing YAM and YAP particles or whether they originate from the original Y_2O_3 and Al_2O_3 reactants; however, the EDS data from this chapter does conclusively demonstrate that a new Y-Al-O phase (i.e. YAG) has formed that did not formerly exist in the BM. It is proposed that during the thermal and plastic deformation cycles of FSW, aluminum and oxygen in the metal matrix diffuse to form the new YAG phase thus increasing the size of the particle. Because of these effects, the coarsening of oxides in MA956 is concluded to be from a combination of Ostwald

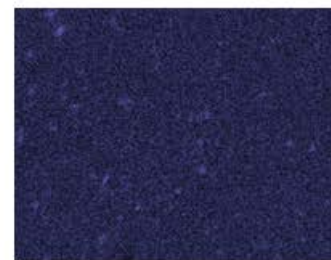
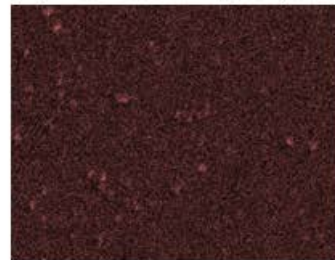
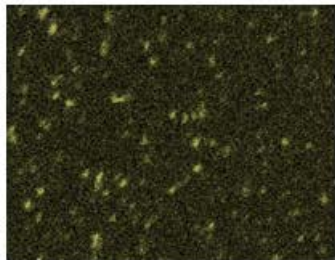
ripening and a continuance of phase transformations within the $\text{Al}_2\text{O}_3\text{-Y}_2\text{O}_3$ system. A summary of the oxide particle coarsening observed with delineation of phases as determined by the quantitative EDS analyses of Figures 3.16–3.24 is shown in Figure 3.26. The phase transformation chronology is shown in Table 3.1 and was observed by Hsiung on the same MA956 as used in this research although the manufacturing treatments used (1100°C maximum) did not expose the MA956 to temperatures in the range of YAG formation (approximately 1400°C); however, the same MA956, now friction stir welded, can be expected to have reached temperatures up to 90% of the melting temperature and thus very close to the range of YAG formation. Although the exact temperature in the high heat input condition or the low heat input condition is not known, it is expected that the higher heat input condition would reach a higher stir zone temperature and thus may be expected to achieve a more full transformation to YAG as was seen in Table 3.3. Although not conclusively proven, the mixed phase results of the low heat input condition (Table 3.4) as well as the non-uniform yttrium distribution seen in the EDS line profiles of Figure 3.23 and 3.24, suggest that in the low heat input condition, the phase transformation to YAG may not be complete.

Base metal



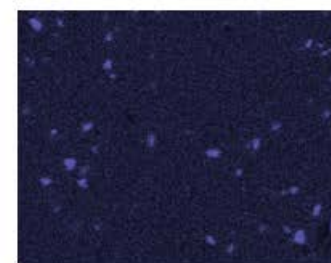
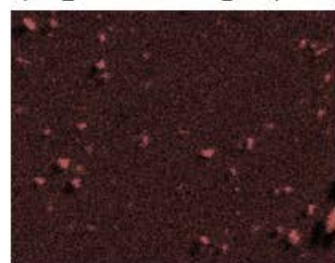
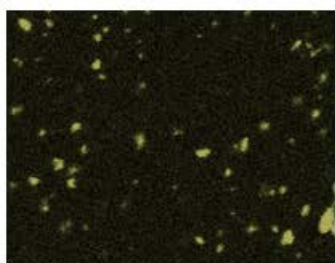
Very fine YAM and YAP particles. Some larger Al_2O_3 particles.

400 RPM/100 MPPM (low heat input)



Coarsened particles. 70% YAG and 30% mixed $\text{Y}_2\text{O}_3\text{-Al}_2\text{O}_3$ phase particles.

500 RPM/25 MPPM (high heat input)



Coarsened particles. 90% YAG and 10% YAM and other mixed $\text{Y}_2\text{O}_3\text{-Al}_2\text{O}_3$ phase particles.

5 μm



Figure 3.26 Summary of oxide particle coarsening observed in this research.

E. CONCLUSIONS

This chapter has provided a systematic analysis of oxide particle coarsening during FSW of the ODS steel MA956. Oxide particle transformation begins during PM manufacture of the base alloy and subsequently these particles are coarsened by further phase transformation as a function of the heat input during FSW. The degree of coarsening is expected to have a significant effect on the strengthening contribution of the oxide particles and will be discussed in detail in Chapter IV. The following conclusions were drawn:

(1) FSW causes coarsening of existing Y-Al-O particles within the base alloy. The coarsening is evident both at the nano-scale by a reduction in nano-sized particles and at the micro-scale by an observed increase in micro-sized particles. This oxide particle coarsening is attributed to a combination of Ostwald ripening and a continuance of phase transformations within the Al_2O_3 - Y_2O_3 system.

(2) The degree of oxide particle coarsening is a function of welding conditions. FSW conditions with high thermal input can cause up to a two times increase in average particle size as compared to low heat input conditions. Increased heat input did not change the inter particle spacing of particles suggesting that a constant volume fraction process assumption is not appropriate.

(3) TiCN particles in ODS alloys containing aluminum are unaffected by FSW and qualitatively do not change in size nor form Y-Ti-O particles due to the preferential formation of Y-Al-O particles.

IV. MATERIAL PROPERTIES AND STRENGTHENING MECHANISMS FOLLOWING FRICTION STIR WELDING

A. INTRODUCTION

Chapters II and III have shown that the MA956 used in this research is a FG alloy with a hardness of approximately 346 Hv which undergoes significant grain and particle coarsening in the SZ as well as significant softening in the SZ following FSW. It can logically be hypothesized that these effects will cause a reduction in both yield and ultimate tensile strength in the SZ; however, the exact relationship between the microstructure and final evolved material properties has yet to be determined since the final macroscopic material properties are dependent on several factors including grain size, oxide particle distribution, and strain hardening. Additionally, previous chapters have focused only on room temperature response since the techniques used were all conducted at room temperature only. This chapter will utilize the foundations set in Chapters II and III and expand on that data to determine the overall tensile behavior of MA956 both before and after FSW for a range of temperatures up to 600°C. This methodology will help determine the suitability of friction stir welded MA956 in high temperature applications such as those proposed in Chapter I.

Although it is well established that MA956 has limited ductility at room temperature [93, 96, 98], the tensile behavior of FG MA956 at room temperature or elevated temperatures is not as well established. The tensile behavior of friction stir welded MA956 at room temperature or elevated temperatures is also not known. Based on Special Metals published data [93], it is expected that the strength of MA956, both BM and following FSW, will decrease with increasing temperature; however, as previously discussed MA956 was originally designed as a CG alloy and the alloy used in this research is a FG alloy, and therefore the MA956 in this research is expected to have an increased strength compared to Special Metals published data. Based on the grain and particle coarsening seen in Chapters II and III, it is hypothesized that FSW will cause a reduction in strength in the SZ. The degree of this reduction is unknown although based on hardness changes seen following FSW, it is hypothesized that strength will be reduced

by approximately 37%. The relationships between hardness, yield strength, and ultimate tensile strength will also be analyzed in this chapter to help determine the utility of using hardness to determine material properties of alloys without having to conduct full tensile testing.

Although the hardness measurements in Chapter II strongly suggest a Hall-Petch relationship in the SZ, these measurements have not fully established what strengthening mechanisms are responsible for the reduction in hardness following FSW. The research in this chapter will not only help establish the corresponding reduction in strength, but will also establish the mechanism(s) behind this expected reduction. Research by other authors has analyzed the strengthening contributions from solid solution strengthening, grain boundary strengthening, oxide particle dispersion strengthening, and dislocation strengthening in MA956 and has shown that grain boundary strengthening is the dominant strengthening mechanism with oxide particle dispersion strengthening being the second most dominant strengthening mechanism [56, 100, 101]. Based on the results of Chapters II and III, both the grain and particle coarsening caused by FSW are expected to have large effects on the yield strength of MA956.

The overall objective of this chapter is to characterize the tensile deformation properties of FG MA956 as a function of mechanical testing temperature for both the BM and the SZ following FSW. As the welded microstructure evolves significantly from the base plate material, special attention is given to the role of welding conditions on the resultant tensile properties and their temperature dependence. Using the data from Chapters II and III, the overall processing, microstructure, and tensile deformation relationships following FSW are presented. The results show that FG MA956 is a useful high strength alloy for elevated temperature applications and that FSW is a viable joining technique for MA956 that maintains most of the alloy's high temperature strength, while sacrificing a significant amount of the lower temperature strength of the joint.

B. EXPERIMENTAL PROCEDURE

The most important experimental consideration throughout this chapter is the limited amount of MA956 both in BM form and even more importantly in welded form

available for destructive tensile testing analysis as opposed to the non-destructive microscopy and hardness techniques used in preceding chapters. Of the seven plates of MA956 available (Appendix A) only five were suitable for tensile testing analysis, and of these, one was reserved for related research on residual stress formation during FSW. This left four available plates of relatively limited size (plates 2, 4, 6, and 7 of Appendix B) that were available to create tensile specimens for the BM condition and the three primary defect-free FSW conditions (500 RPM/25 MPM, 300 RPM/50 MPM, and 400 RPM/100 MPM) all as a function of temperature. Because of the limited amount of MA956 available, the methodology and experimental techniques used during tensile testing were critical, and an extensive preparation program was planned and executed prior to any MA956 tensile testing. The details of this preparation program are discussed in detail in this section to help establish the validity of MA956 data presented later in this chapter.

Prior to any MA956 tensile testing the following steps were completed: (1) a specific tensile specimen design was established, (2) a finite element model of that specimen designed was constructed and analyzed using the expected experimental conditions, (3) an experimental setup and procedure was developed, and (4) an experimental verification of the entire process was conducted on a similar non-ODS alloy (SS316). In order to establish the baseline conditions for MA956 testing, both methods and results related to establishing final testing conditions for MA956 are discussed in detail in this section; however, the remaining portions of this chapter (results, discussion, and conclusions) contain data only from MA956 testing.¹³ The preparations for MA956 testing were deemed as very successful. No tensile test of MA956 was evaluated as an unsatisfactory result due to experimental setup or procedural errors, and thus, all MA956 material was effectively utilized.

¹³ There is one exception to this statement that will be discussed later. Due to the limited amount of MA956, an insufficient number of MA956 specimens were available for error calculation. Because of this an experimental error routine was established using SS316 of the exact same geometry and experimental conditions. The variance in these SS316 tests was utilized as experimental error for MA956.

1. Tensile Specimen Design

A total of five different specimen geometries and five different alloys were used during initial preparation and final MA956 testing. A summary of these geometries and alloys is contained in Figure 4.1 and Table 4.1 with detailed manufacturing specifications listed in Appendix C. Two aluminum alloy (AA1100 and AA5052) specimens were used from available stock material at Naval Postgraduate School (NPS) and represent a typical large tensile specimen (Figure 4.1d and e). These specimens were utilized for initial experimental setup and final experimental verification. The remaining three geometries (Figure 4.1a-c) are miniature tensile specimens and were constructed from a range of alloys including MA956 as shown in Figure 4.1 and Table 4.1. The miniature specimen forms were selected primarily for material conservation reasons.



Figure 4.1 Summary of materials and geometries used in this research with corresponding description of use discussed in Table 4.1.

Table 4.1 Summary of materials and geometries of tensile specimens used in this research.

Material	Geometry	Use
MA956	Miniature tensile geometry (standard) (Figure 4.1b)	This was the standard tensile specimen used in this research. All MA956 stress-strain curves were generated from this specimen. For FSW specimens, the gage section of this specimen was comprised entirely of SZ material.
	Miniature tensile geometry (narrow) (Figure 4.1a)	This specimen geometry was made based on initial concerns with the radius of curvature of the grip to gage section of the standard geometry. Further evaluation determined this adjustment was not necessary. This geometry was only used in the experimental procedure portion of Chapter IV.
	Miniature tensile geometry (long) (Figure 4.1c)	This geometry was designed to evaluate tensile behavior across the entire weld. This geometry was also used in Chapter V for LME analysis.
SS316	Miniature tensile geometry (standard) (Figure 4.1b)	This specimen was generated to evaluate the experimental methods of this chapter prior to conducting test on MA956.
	Miniature tensile geometry (long) (Figure 4.1c)	This specimen was generated as a control for the LME analysis of Chapter V.
1018 Steel	Miniature tensile geometry (standard) (Figure 4.1b)	This specimen was generated to evaluate the experimental methods of this chapter prior to conducting test on MA956.
	Miniature tensile geometry (long) (Figure 4.1c)	This specimen was generated as a control for the LME analysis of Chapter V.
AA5052	NPS custom geometry (Figure 4.1e)	This specimen was used for initial testing and strain gage experimental analysis.
AA1100	NPS custom geometry (Figure 4.1d)	This specimen was used for initial testing and verification of system operation. No data from this specimen is presented.

Miniature geometry tensile specimens (Figure 4.1a-c) were machined via wire electrical discharge machining (EDM) by Full Spectrum Machining, Gilroy, CA with manufacturing tolerances of 0.0508 mm (0.002 inches). The advantages of EDM in general [185] and specifically for tensile sample preparation [186, 187] are discussed in other literature. For this research EDM was selected based on the small tolerances desired, the smooth surfaces produced that required no additional treatment, and the lack of distortion during specimen fabrication.

The three miniature tensile geometries (Figure 4.1a-c) all have identical geometries in the grip regions so that they each may fit into the same tensile grips. The three geometries vary in their gage section dimensions and purpose. The final geometry selected for MA956 tensile specimens (Figure 4.1b) is shown at a larger scale in Figure 4.3a. Unless specifically noted otherwise, this sample geometry was used for all tensile results. Samples of this geometry from 1018 steel and SS316 were also utilized for preparation and comparison. During initial evaluation of this geometry on MA956, there was concern that the radius of curvature from the grip to gage section may be insufficient and may cause stress concentration outside of the gage section sufficient to cause fracture near the grip which could lead to erroneous results.¹⁴ Because of this concern, a new geometry with an increased radius of curvature from the grip to the gage section (and correspondingly narrower and shorter gage section) was designed (Figure 4.1a). This new design was intentionally planned to be a machinable derivative of the original design that could still mate with the grips of the experimental setup (Figure 4.2b). During verification of the experimental setup it was determined that this modification to curvature of the grip to gage section was not required since all failures for both geometries occurred within the gage section (Figure 4.3). Because of this, results from the narrow gage section specimens do not factor into the results of this chapter and are no longer discussed. The long gage section geometry (Figure 4.2c) was designed for two reasons: (1) to evaluate across the entire weld section which will be discussed in this chapter and (2) to conduct LME testing in Chapter V.

¹⁴ The basis for this concern is discussed later in the finite element modeling of paragraph B.3. Despite the final conclusion that this new geometry was not required, the discussion of this alternate geometry is intentionally left in this section to show the depth of analysis conducted.

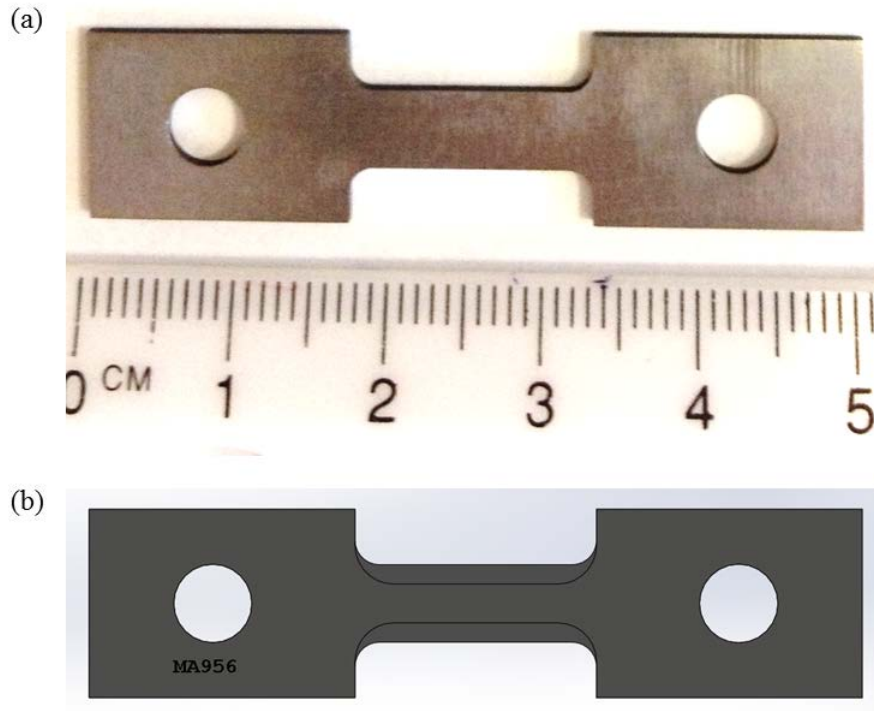


Figure 4.2 (a) Miniature tensile specimen geometry used for all MA956 tensile test data in this research and (b) SolidWorks image to scale of the same geometry overlaid with a machinable new geometry with an increased radius of curvature and narrower gage section.

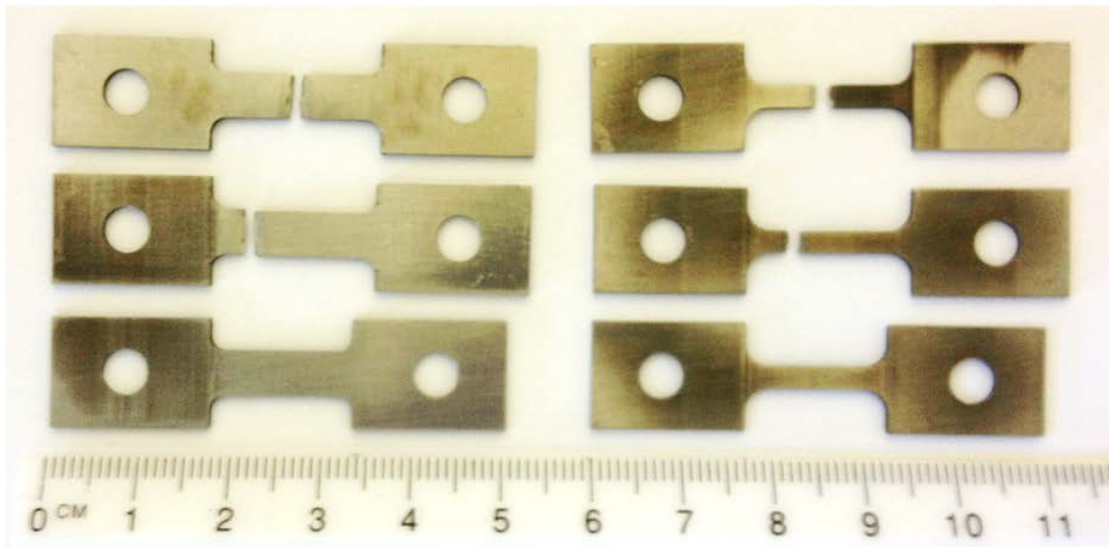


Figure 4.3 Tensile specimens fractured from the original miniature tensile geometry (left) and increased radius of curvature tensile geometry (right) all showing proper fracture in the gage section. Based on these results, the increased radius of curvature sample (right) was deemed not required.

2. Finite Element Verification of Design

In order to help ensure proper specimen performance during tensile testing, finite element modeling of all geometries was accomplished prior to the performance of any testing. The goal of this modeling was to ensure uniform stress distribution through the sample which would lead to failure in the gage section. Finite element modeling was conducted using ANSYS 14.0 on models built with SolidWorks 2012–2013. The same SolidWorks models were used to create the manufacturing drawings (Appendix C) for all miniature tensile specimens.¹⁵ Finite element modeling was only attempted in the elastic region and was not intended to be used to determine or estimate any plastic response. All ANSYS images presented in this research are shown at conditions that are approximate to yield conditions for the given material, and all stress values are equivalent (Von Mises) stress. Additional details of ANSYS modeling including meshing used and application of forces and restraints is contained in Appendix D.

The results of ANSYS modeling are presented in terms of a stress concentration factor (k_t) which is the ratio of the maximum stress anywhere in the specimen to the stress in the gage section (Equation 4.1). This presentation of k_t is identical to that presented in textbooks [168, 188] and has been applied to tensile testing specimens as well [186] although most tensile testing research does not report this factor. The intent of modeling to determine k_t is to determine if there are local areas of high stress, such as the junctions between the specimen grip and gage sections, that may cause fracture and to determine if the testing conditions are establishing a uniform stress in the gage section necessary for a good fracture.

$$k_t = \frac{\sigma_{max}}{\sigma_{gage}} \quad \text{Equation 4.1}$$

The significance of stress concentration can be shown in the extreme condition of no fillet from the grip to gage section of a tensile specimen. Although certainly not

¹⁵ The AA1100 and AA5052 specimens (Figure 4.1d and e) had already been manufactured and therefore the corresponding SolidWorks models for these specimens were made after specimen manufacture. This statement is only made for clarity of presentation and does not affect any result in this research.

appropriate for a tensile specimen, this condition is shown in Figure 4.4. The specimen shown in Figure 4.4 is identical to the miniature tensile specimen used in this research (Figure 4.2a) except there is no fillet between the grip and gage section. At first glance the uniform distribution of stress in the gage section of this specimen looks encouraging, but as expected the sharp transition from the grip to the gage section produces a very high localized stress (Figure 4.5). This results in the extreme condition of $k_t=6.4$ and is indicative of a worst possible geometry case.

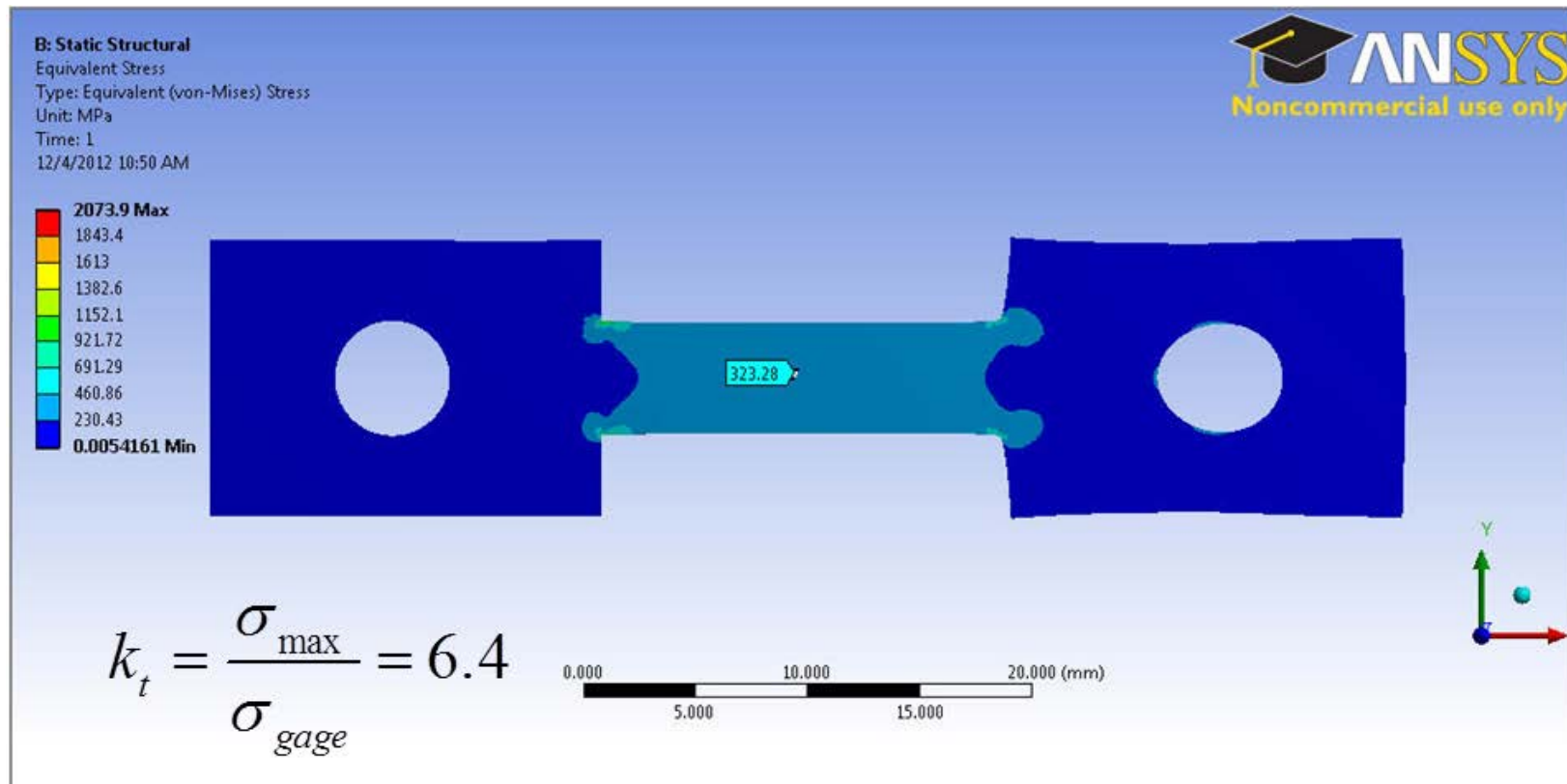


Figure 4.4 ANSYS modeling results showing stress distribution in a tensile specimen with no fillet between grip and gage sections.

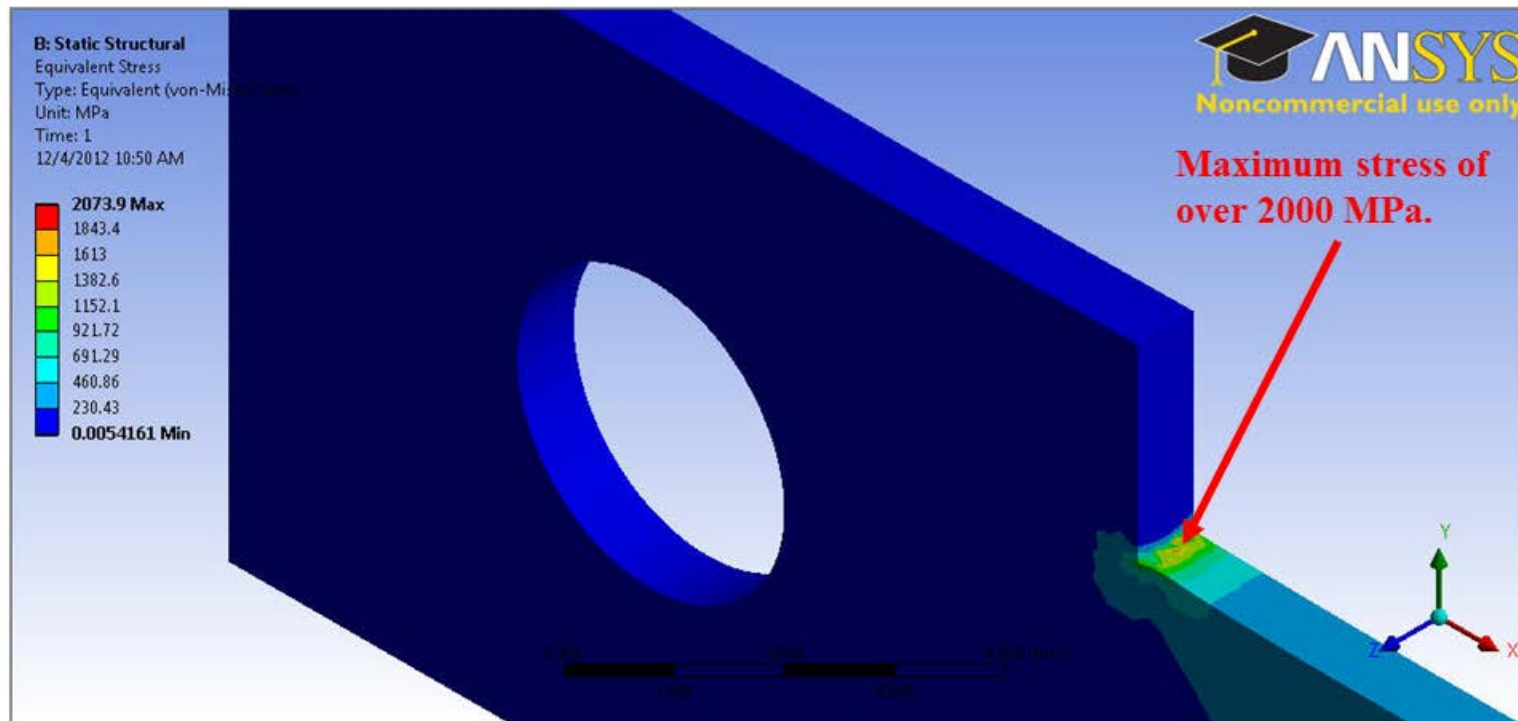


Figure 4.5 ANSYS modeling results showing high stress concentration at the intersection between the grip and gage section.

Contrastingly, an ANSYS model was created from the geometry of a commonly used miniature rectangular tensile specimen used to evaluate nanostructured metals and alloys (Figure 4.6) [189]. In this model, the very gradual transition from the grip to the gage section produces a uniform distribution of stress throughout the gage section and a low value of $k_t=1.3$. Using a similar approach, the k_t values of three of the specimen geometries used in this research are shown in Figures 4.7–4.9.¹⁶ The modeling results from Figures 4.7–4.9 show that all three of these geometries have stress profiles that would be expected to produce good tensile results comparable to those used in other research [189]. Although the increased radius of curvature of the narrow miniature tensile design did produce a lower value of k_t , the fracture results in Figure 4.3 show this further reduction was not required.

¹⁶ The geometry used for the AA1100 was not modeled in ANSYS since this specimen was only used for initial testing evaluation. The long mini tensile specimen (Figure 4.1c) has an identical distribution of stress and k_t since it is identical in geometry to the normal mini tensile specimen except that it has a longer gage length which is in the line of the applied force.

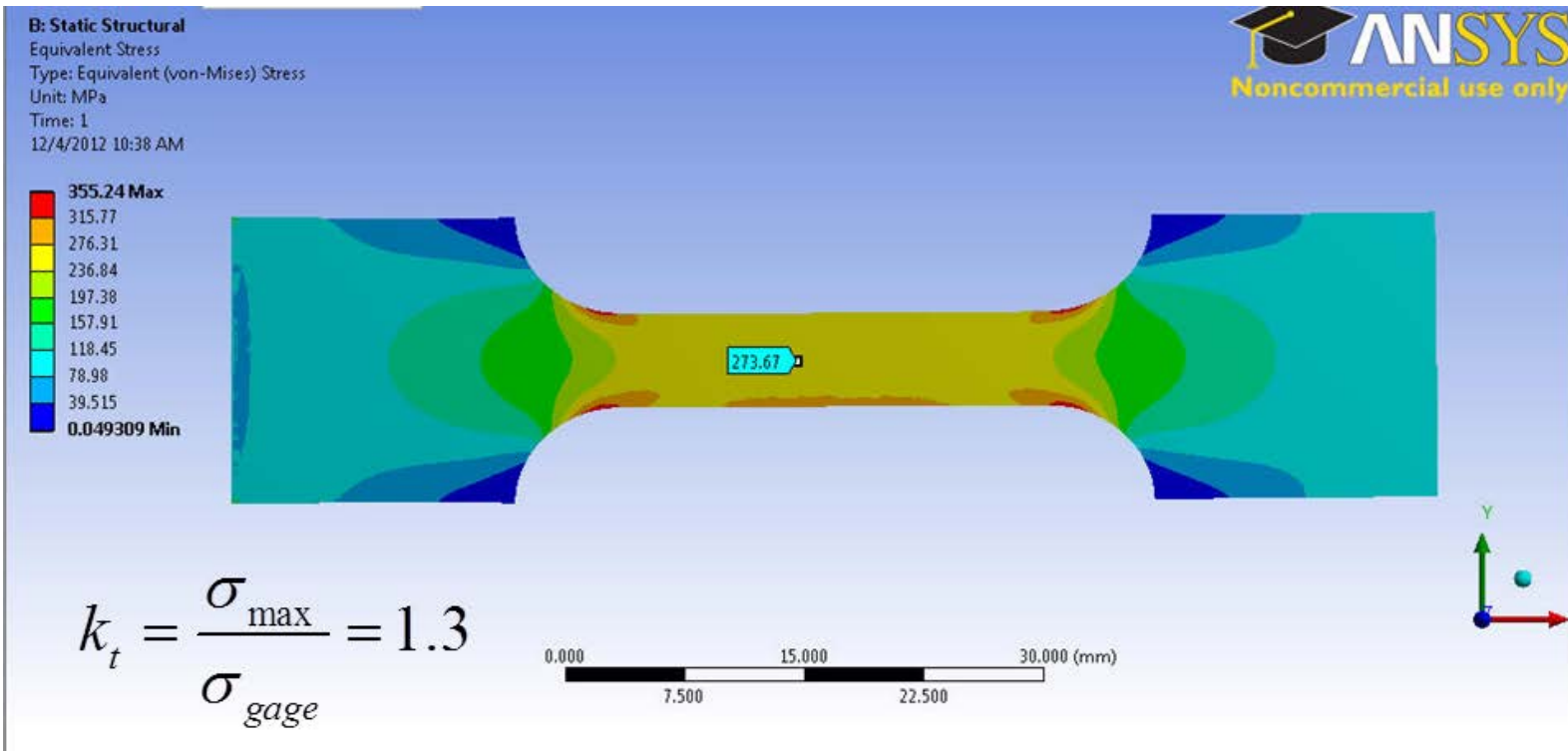


Figure 4.6 ANSYS modeling results of a miniature rectangular tensile specimen used to evaluate nanostructured metals and alloys [after 189] showing a low stress concentration due to the fillet between the grip and gage section.

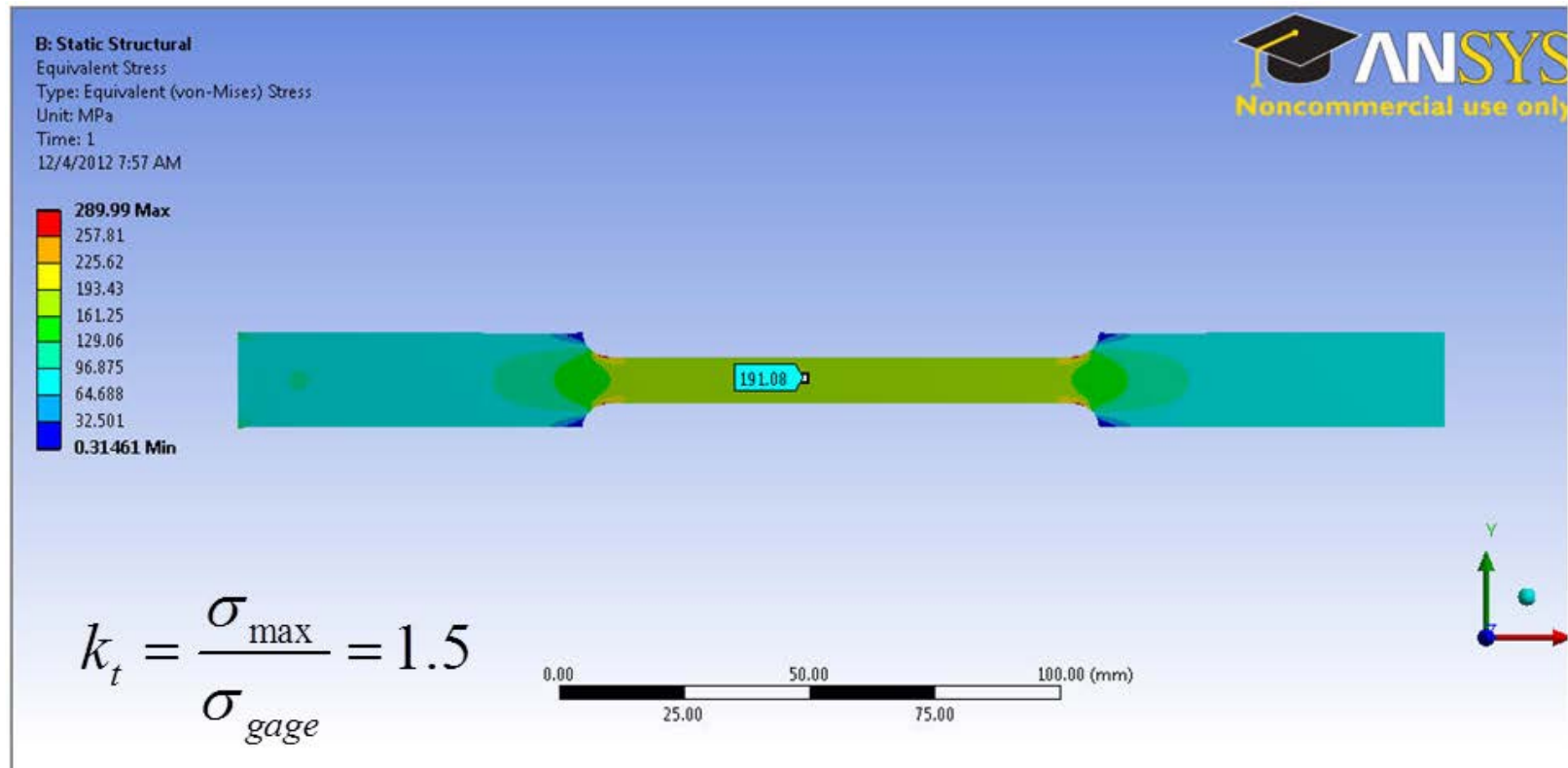


Figure 4.7 ANSYS modeling results for the AA5052 sample used in this research (Figure 4.1d).

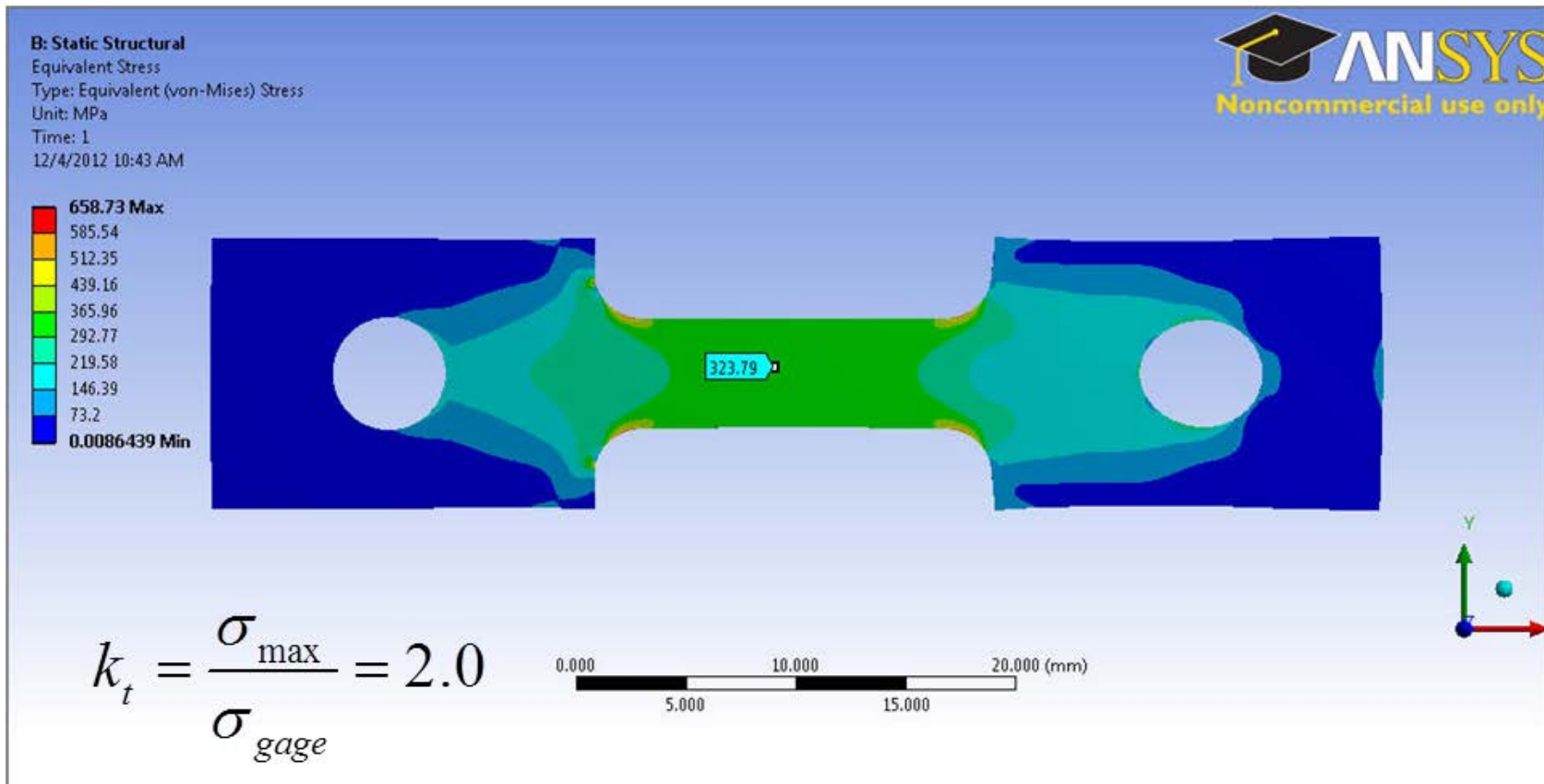


Figure 4.8 ANSYS modeling results for the standard miniature tensile sample used throughout this research (Figure 4.1b).

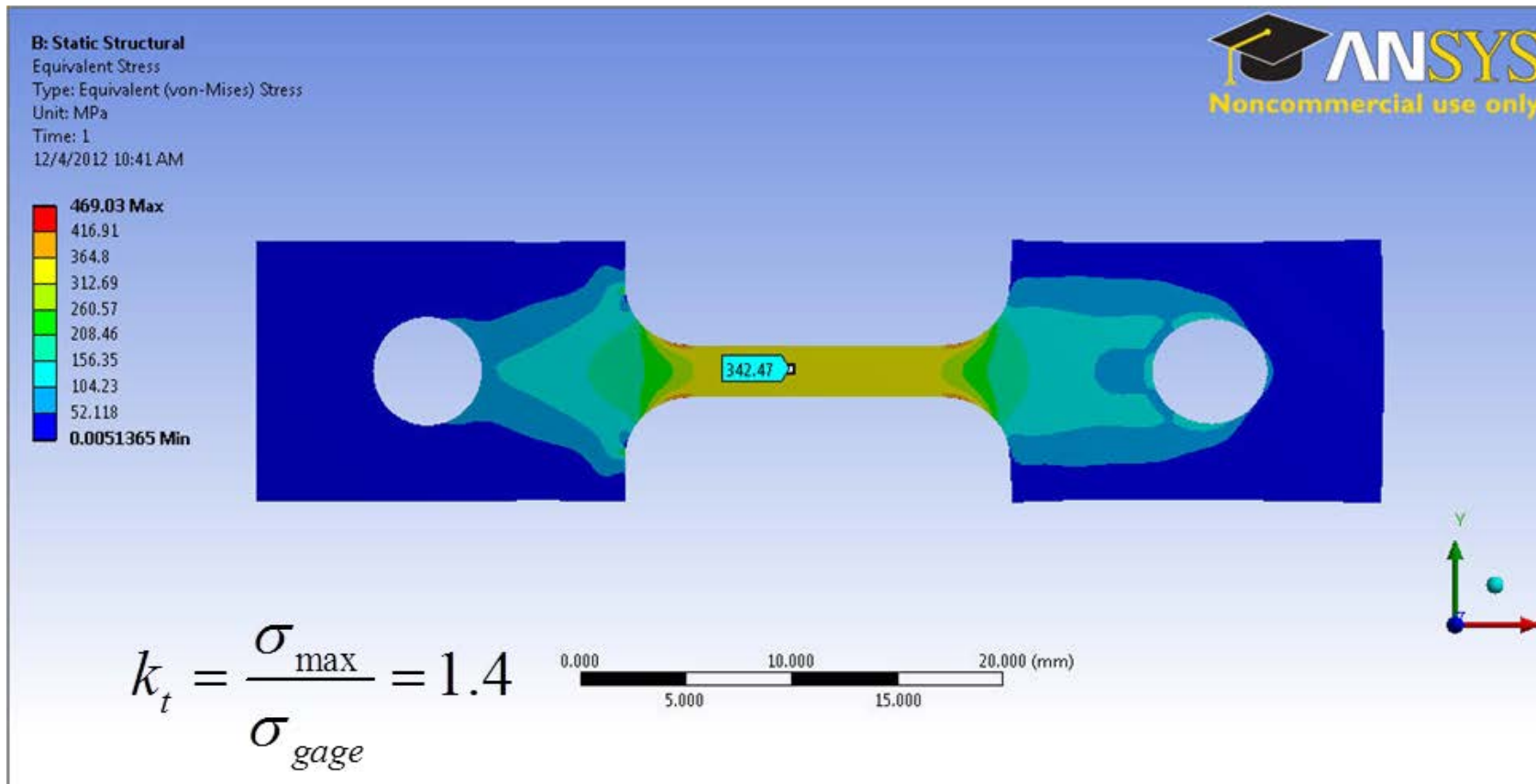


Figure 4.9 ANSYS modeling results for the new increased radius of curvature miniature tensile sample analyzed in this research (Figure 4.1a).

Restraint of tensile specimens during tensile testing is a critical and well established factor during tensile testing. Specimen restraint is accomplished by a variety of grips including screw action grips, wedge type grips, pneumatic action grips, and bolt action grips. Advantages and disadvantages of each of these types of grips are discussed in other literature [190] and the process of grip selection is described as trial and error. To eliminate this trial and error process, specific attention was applied to the restraints used in the actual experimental setup and the finite element modeling done in ANSYS. The ANSYS results confirm the importance of proper grip restraint and demonstrate how this could be accomplished in this specific experimental setup. The restraint process utilized during this research includes three restraint surfaces (Figure 4.10): (1) a bolt restraint, (2) a seating restraint, and (3) a grip compression restraint. The tensile specimen fits within the grip in a recessed surface and the specimen seats on the grip on the flat portion of the tensile specimen, i.e. the grip does not contact the fillet between the grip and gage section of the specimen.

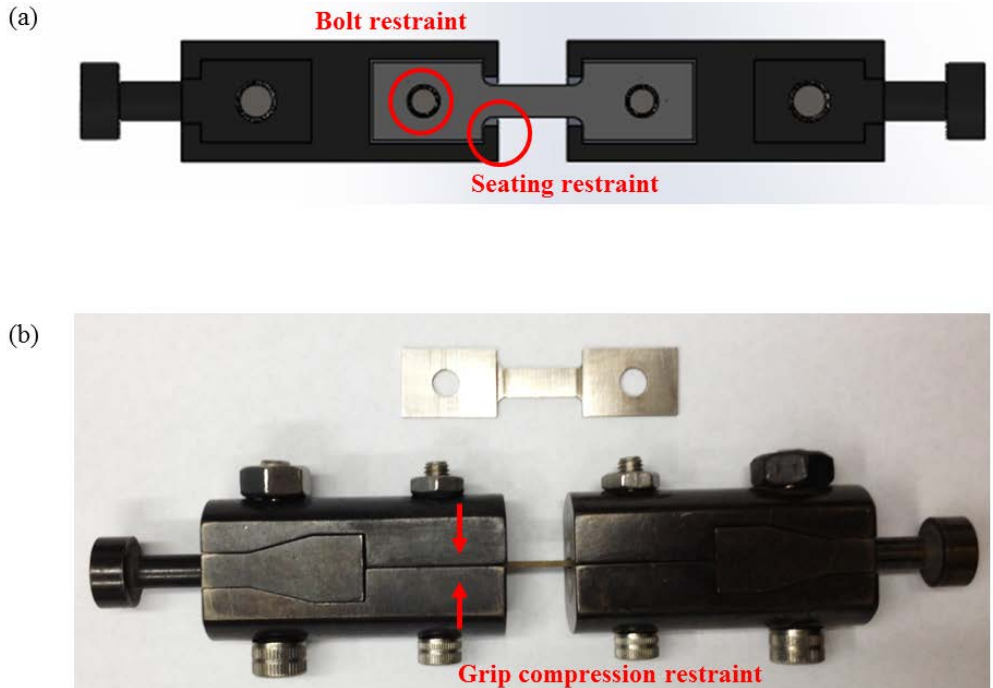


Figure 4.10 (a) Cutaway SolidWorks model showing bolt restraint and seating restraint and (b) photograph of a tensile specimen fully assembled in its grips showing grip compression restraint.

Finite elements results with all three restraint mechanisms analyzed individually and collectively show that the seating restraint (Figure 4.10a) is the most critical restraint, and fortunately this is easily achieved with proper specimen insertion. The grip compression restraint (Figure 4.10b) was found to negligibly contribute to response during ANSYS modeling and experimental data by varying the value of the compressive force of the grips on the specimen. Values of grip compression forces up to 500 N did not result in any changes in response during finite element analysis. Based on this theoretical result, the torque applied to the bolts of the grips was not measured. The lower grip bolts that clamp the grips together were hand tightened only. The upper grip bolts were also only hand tightened. Over-tightening of the upper grip bolts must be specifically avoided to allow the grips to align with the tensile axis. ANSYS modeling using bolt restraint only (Figure 4.11) showed a largely non-uniform distribution of stress in the gage section as opposed to the uniform distribution of stress when both the bolt restraint and seating restraint were applied (Figure 4.12). With proper specimen insertion into the grips, the condition of Figure 4.11 should never occur.

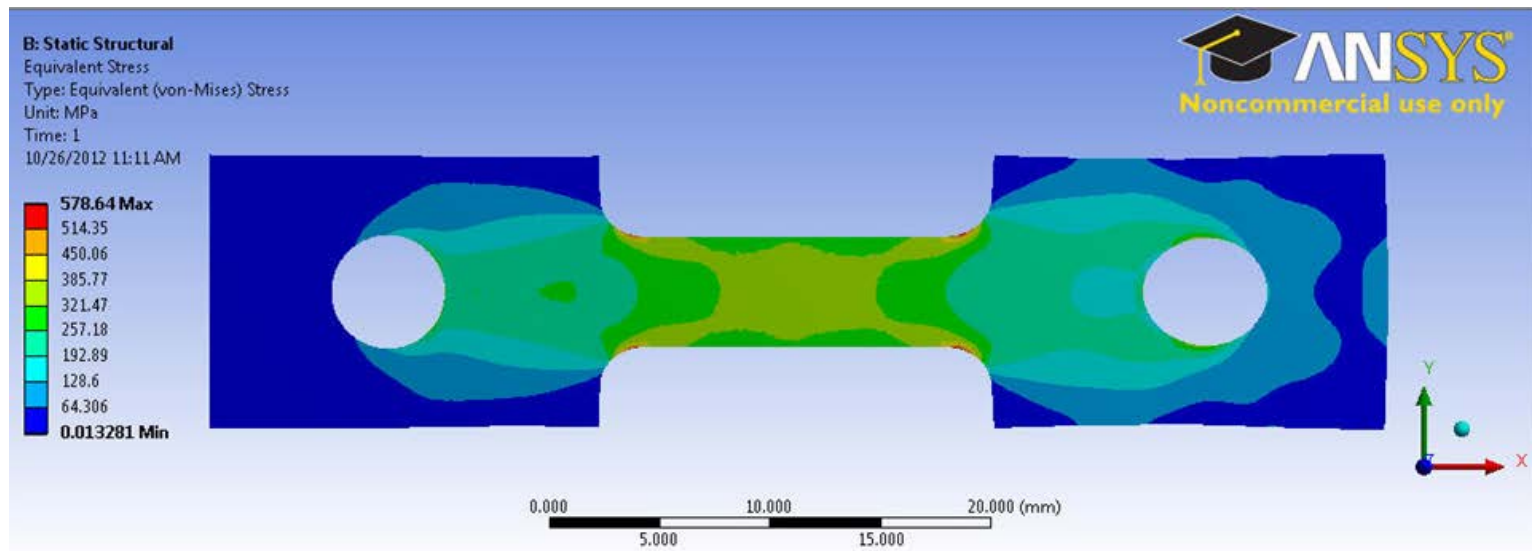


Figure 4.11 ANSYS finite element models showing non-uniform stress distribution in the gage section when using bolt restraint alone.

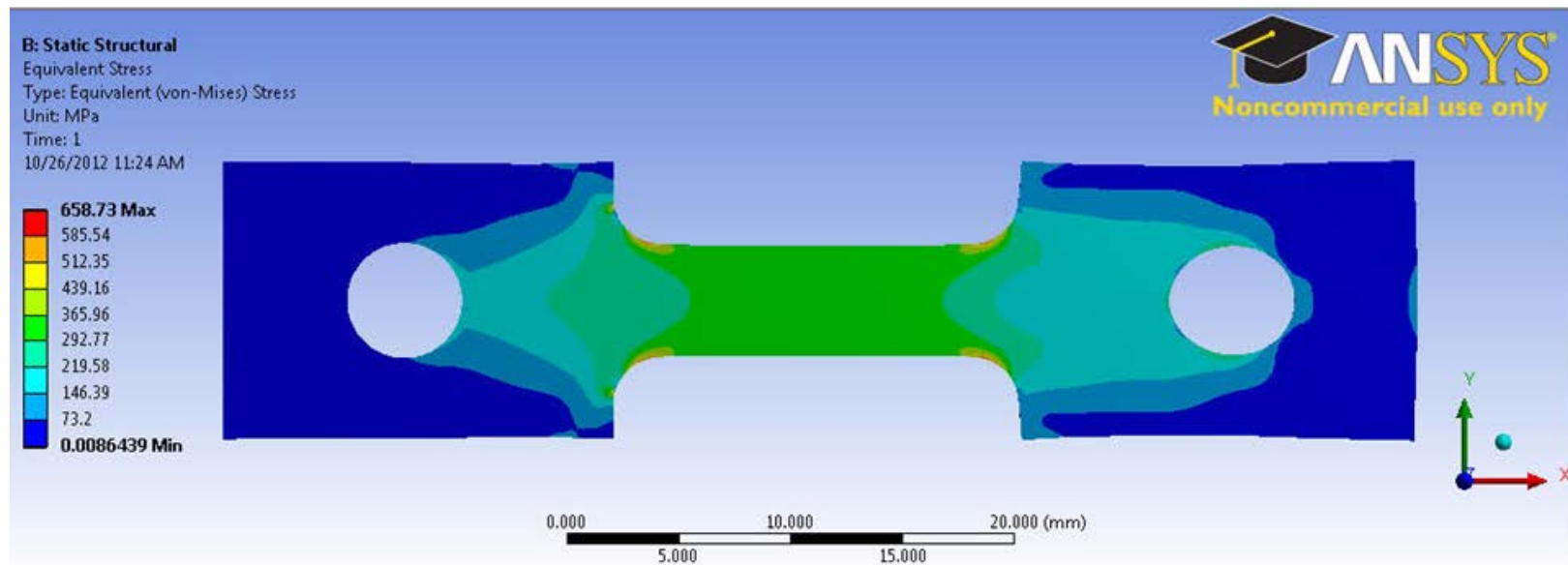


Figure 4.12 ANSYS finite element models showing uniform stress distribution in the gage section when using both bolt and seating restraint.

3. Initial Tensile Testing Setup

The standard tensile testing setup (Figure 4.13) consisted of: (1) load cell, (2) furnace, (3) specimen area, (4) grips and (5) crosshead. Tensile testing on the larger AA1100 and AA5052 specimen geometries required a different grip setup and larger load cell (Figure 4.14). The physical nature of the grips used for the miniature tensile specimens requires care during testing to avoid grip slippage which can lead to poor experimental performance. This poor performance would normally occur in the elastic region as load is increased in the entire machine, grip, and specimen line of axis, but could also occur in the plastic region if relative motion occurs anywhere in this axis after specimen yielding not due to actual deformation of the specimen. Relative motion between components in the tensile line of axis is most likely to occur in the seating surfaces inherent in the grips (Figure 4.15). Slippage between the specimen and grips was minimized by the restraints mentioned in B.2. Grip slippage leads to load drops in experimental data which can be corrected by applying a foot correction but should be avoided (Figure 4.16) [190]. In addition to proper restraint, preloading of samples was utilized to prevent grip slippage. Preloading consisted of applying a small load ($<10\%$ of the load at yield) at a fixed rate (equating to a strain rate of approximately $1 \times 10^{-3} \text{ sec}^{-1}$) prior to recording data. This preload placed the entire line of axis in tension and is normally sufficient to fully seat all surfaces in the load line. Grip slippage, restraint, foot corrections, use of preload, and other tensile testing techniques are discussed in detail by the American Society for Metals (ASM) [190].

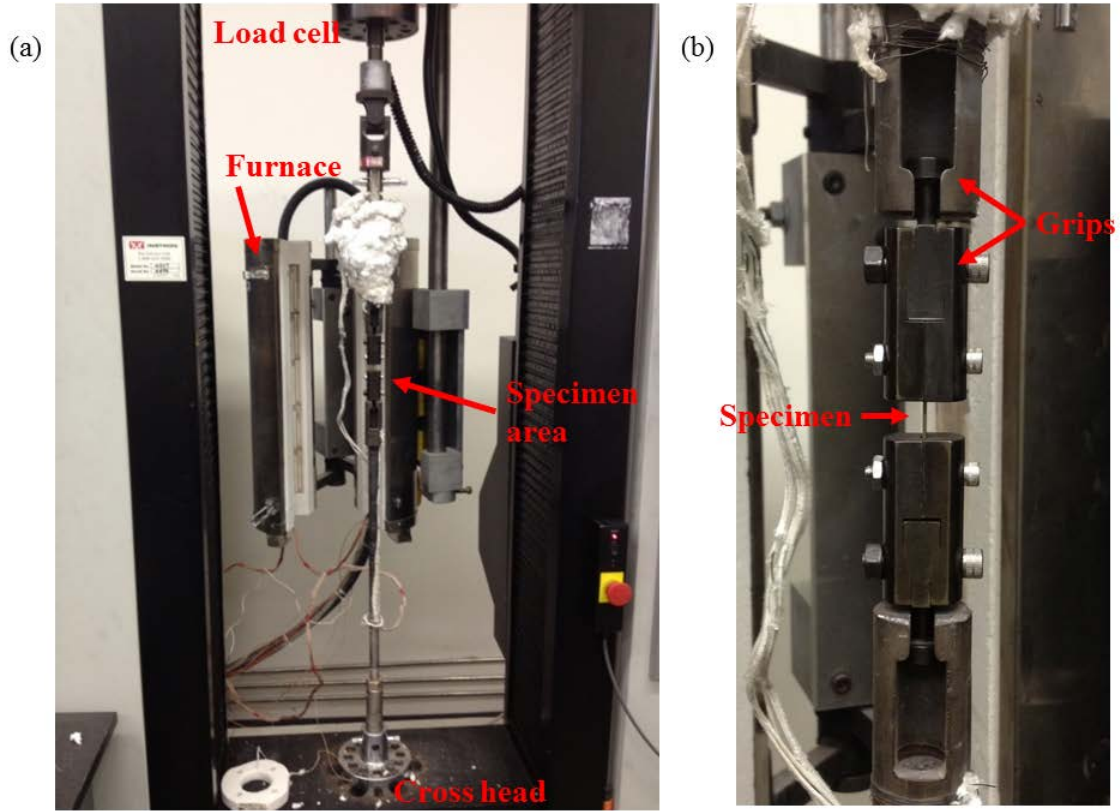


Figure 4.13 (a) Standard tensile testing setup used for miniature tensile specimens and (b) close up view of the specimen area.



Figure 4.14 Tensile testing setup used for AA1100 and AA5052 specimens.

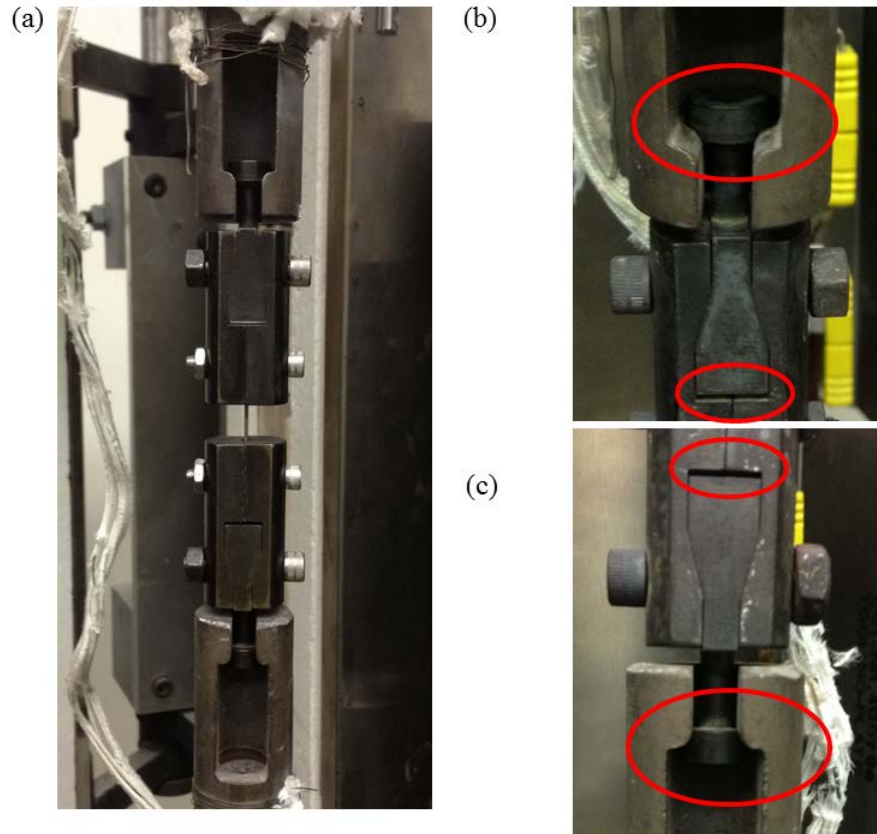


Figure 4.15 (a) Standard miniature tensile setup, (b) upper section grip slippage locations (red circles), and (c) lower section grip slippage locations (red circles).

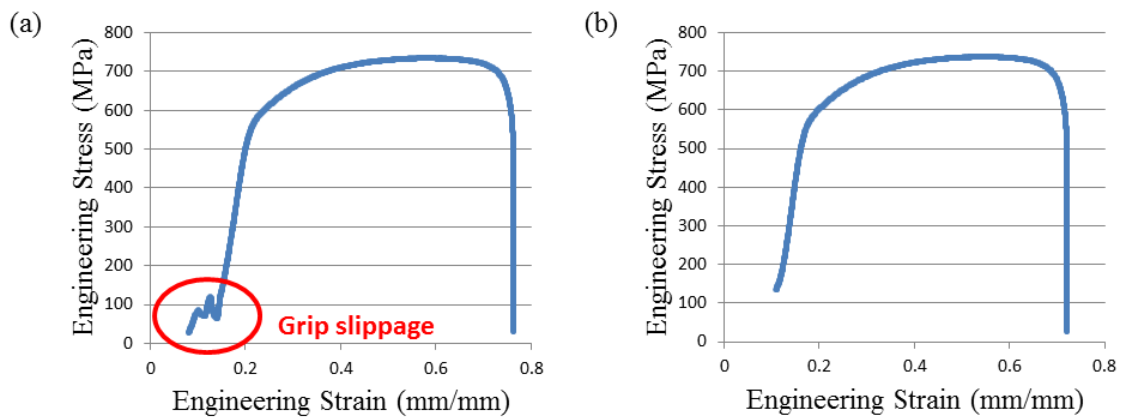


Figure 4.16 Raw MA956 data showing (a) load drops due to grip slippage in the elastic region and (b) smooth elastic region for the sample alloy and geometry with preload applied to prevent grip slippage.

Because of the small specimen size and the elevated temperature testing, an extensometer was not used and strain was calculated using crosshead displacement. The potential errors in strain measurement using crosshead displacement alone are discussed in detail elsewhere in the literature [189, 190]; however, key aspects are summarized here. The lack of ability to measure specimen elongation directly leads to the inability to accurately measure specimen modulus of elasticity (E) accurately as well as inherent errors in strain at failure (also called percent elongation) since the displacement of the machine is also included in the overall displacement calculated via crosshead speed. The compliance of the machine (which includes the grips and essentially everything but the specimen) was significant, and a procedure was developed that included experimental calculation of machine compliance in order to produce final results that removed the machine response. This process significantly improves accuracy in the elastic region, gives a more accurate measure of E (although not needed and never utilized in this research) and gives a more accurate measure of strain at failure. The process developed produces negligible change on yield strength measurements and has no effect on ultimate tensile strength measurements.

To compensate for machine compliance, instrumented testing at room temperature using strain gages was conducted initially on AA5052 samples (Figure 4.17) to prove the validity of the approach and then on SS316 samples of identical geometry as planned MA956 samples (Figure 4.18). General purpose linear pattern strain gages (gage length=1.57 mm, grid width=1.57 mm, strain range= $\pm 1.5\%$, 350 ohm) were used for measuring strain. Data from the instrumented AA5052 testing shows the improved accuracy of the strain gage in the elastic region (Figure 4.19) and calculation of E from this data was within 5% of the published value. The strain gages used in this research all fell off the specimen shortly after the yield point (hence the abrupt stop in strain gage data such as in Figure 4.19) due to elongation of the specimen, but this was deemed acceptable since only the elastic response was used. Yield strength calculations using the 0.2% offset method from both the strain gage data (Figure 4.20a) and INSTRON data (which uses crosshead speed to calculate strain) (Figure 4.20b) show that although the

calculation method may look more accurate using the strain gage, the actual difference in measured yield strength is less than 10%.



Figure 4.17 AA5052 specimen instrumented with a strain gage to measure strain vice using crosshead speed.

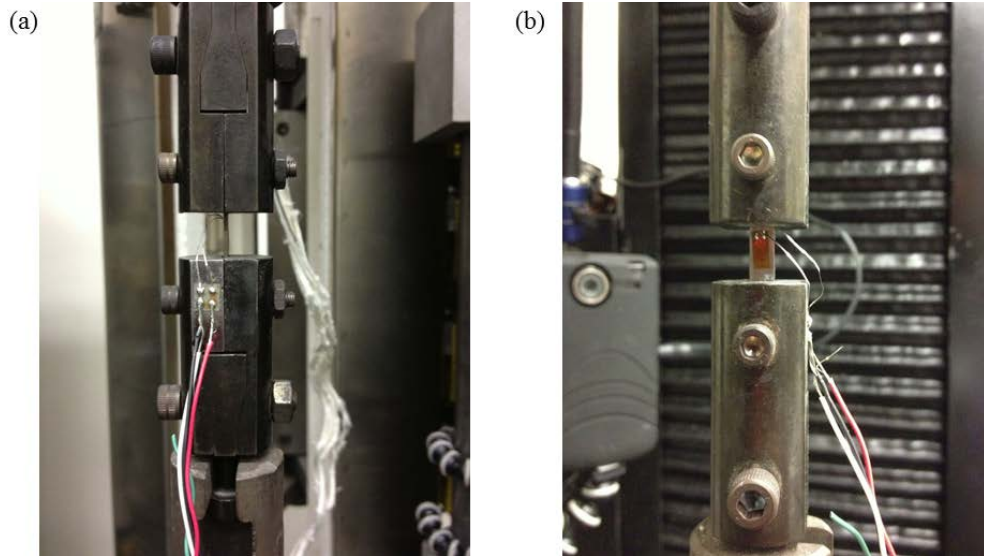


Figure 4.18 (a) Front and (b) side views of a SS316 specimen instrumented with a strain gage to measure strain vice using crosshead speed.

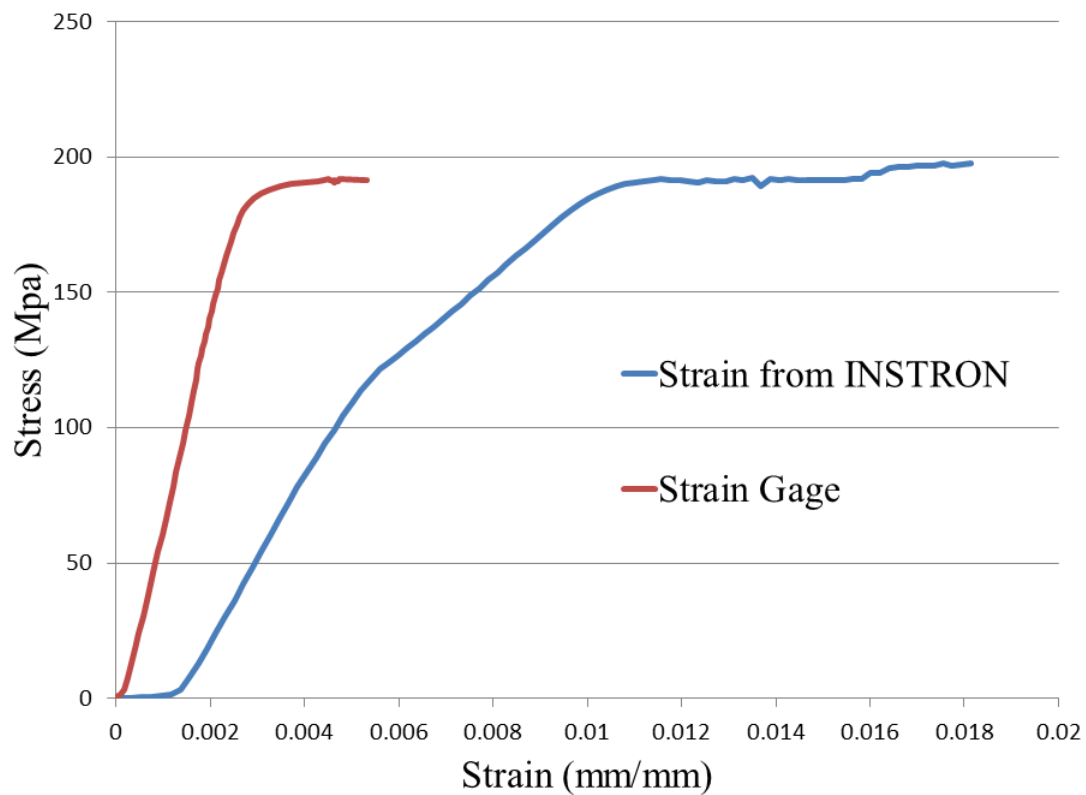


Figure 4.19 Data from AA5052 tensile test showing the improved response in the elastic region when using a strain gage. The strain gage fell off the sample shortly after the yield point due to specimen elongation. The difference in the slopes of these two lines is due to machine compliance.

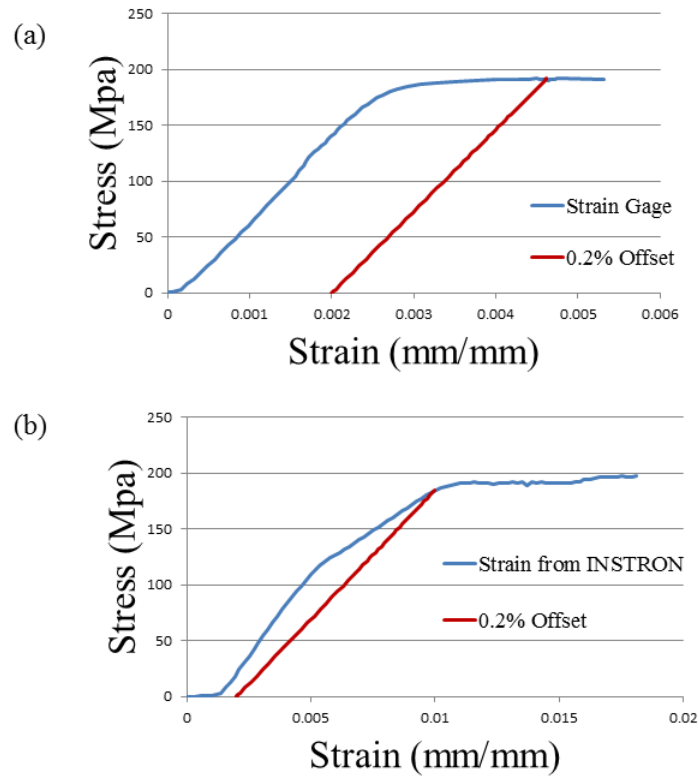


Figure 4.20 Comparison plots of AA5052 yield strength calculation using (a) a strain gage to measure strain and (b) crosshead speed to measure strain that show a negligible difference in measured yield strength.

The primary purpose of the strain gage experiments in this research was to remove machine compliance as a source of error as discussed in [190] and is summarized in Figure 4.21. This approach assumes that the entire system consists of two springs in series with one spring representing the specimen and the second spring representing everything outside of the specimen to include the aggregate response of the machine and grips (Figure 4.21a). By calculating strain using crosshead speed, the INSTRON data represents an equivalent response, whereas a strain gage (or any extensometer) measures strain from the specimen response alone. From both of these values the machine compliance can be calculated (Figure 4.21b). With this machine compliance, further non-instrumented samples can be adjusted using the method previously in reverse. This adjustment corrects the elastic response as shown in Figure 4.21c. It is acknowledged

that this process is highly setup specific, i.e. any difference in machine setup such as different grips will cause machine compliance to be altered. Once this process was successfully proven on the AA5052 geometry, it was repeated on the miniature tensile geometry using a SS316 specimen. Results comparable to the AA5052 results of Figures 4.19 and 4.20 are shown for SS316 in Figures 4.22 and 4.23.

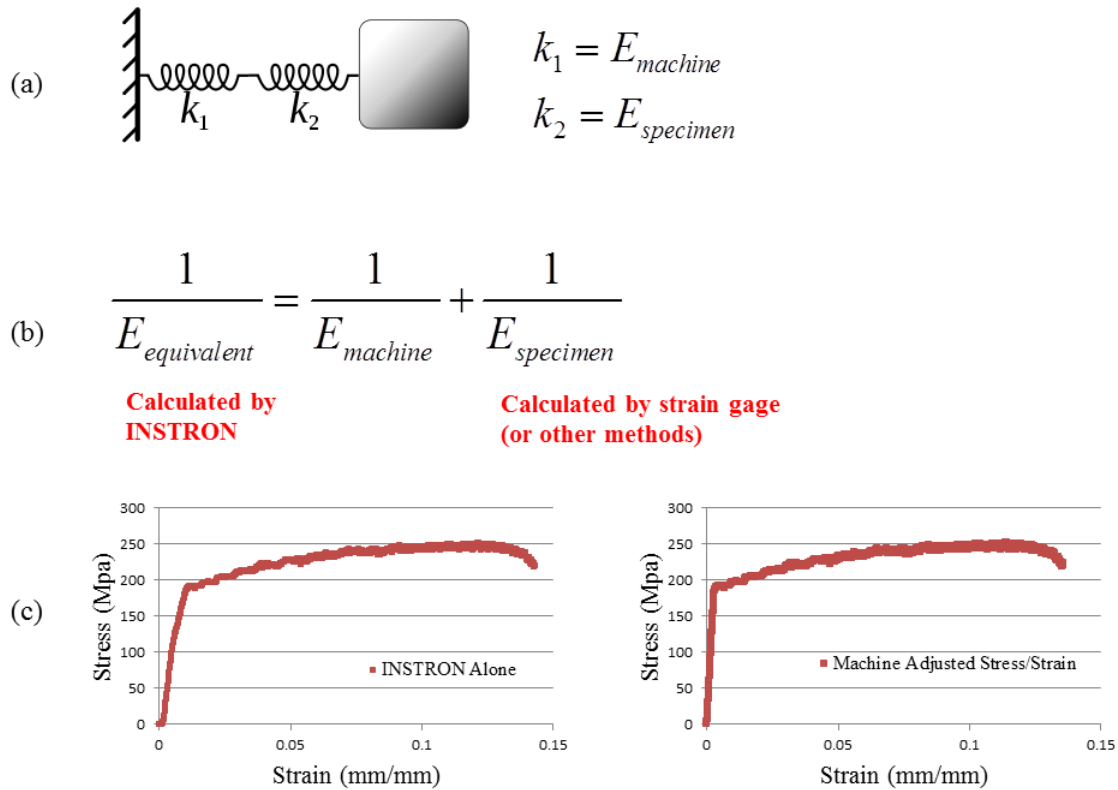


Figure 4.21 Use of a strain gage to calculate and adjust for machine compliance that includes: (a) simple modeling as a two spring system, (b) calculation of machine modulus from experimentally measured data, and (c) adjustment of stress strain curves removing machine compliance.

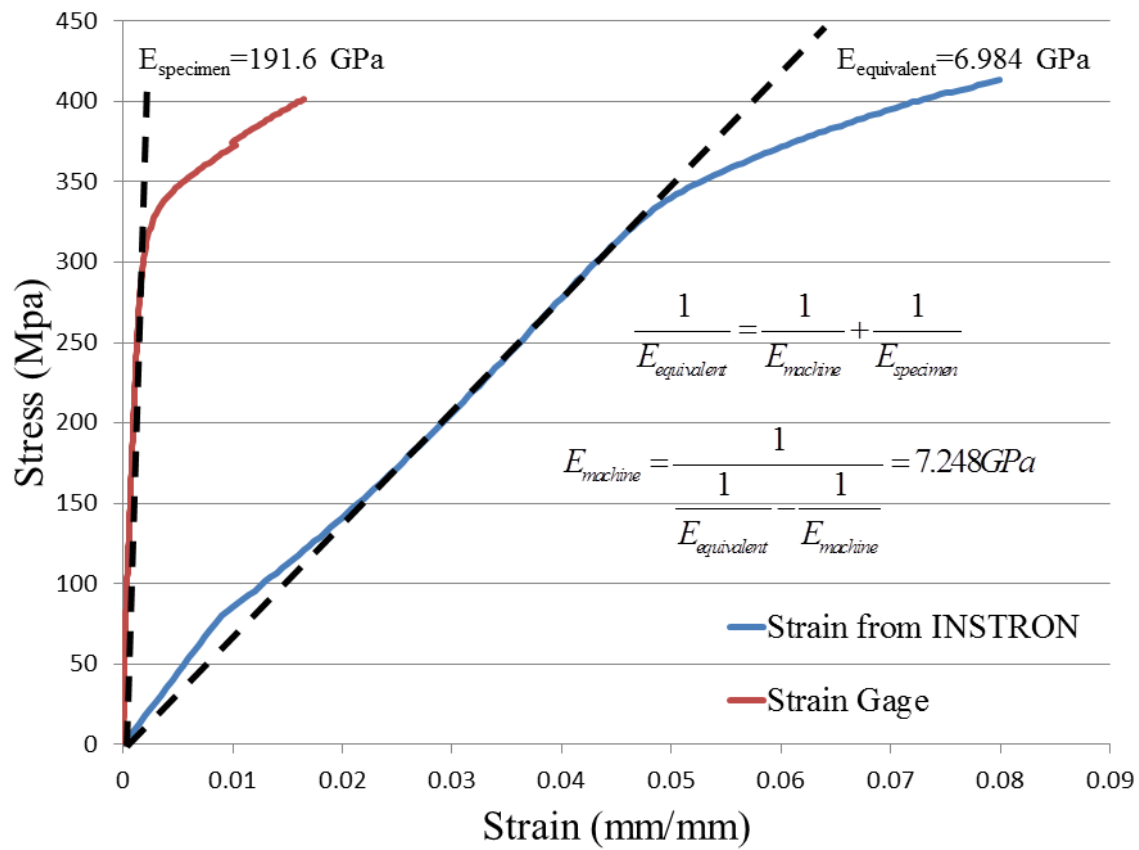


Figure 4.22 Data from SS316 tensile test showing the improved response in the elastic region when using a strain gage. The strain gage fell off the sample shortly after the yield point due to specimen elongation. The difference in the slopes of these two lines is due to machine compliance.

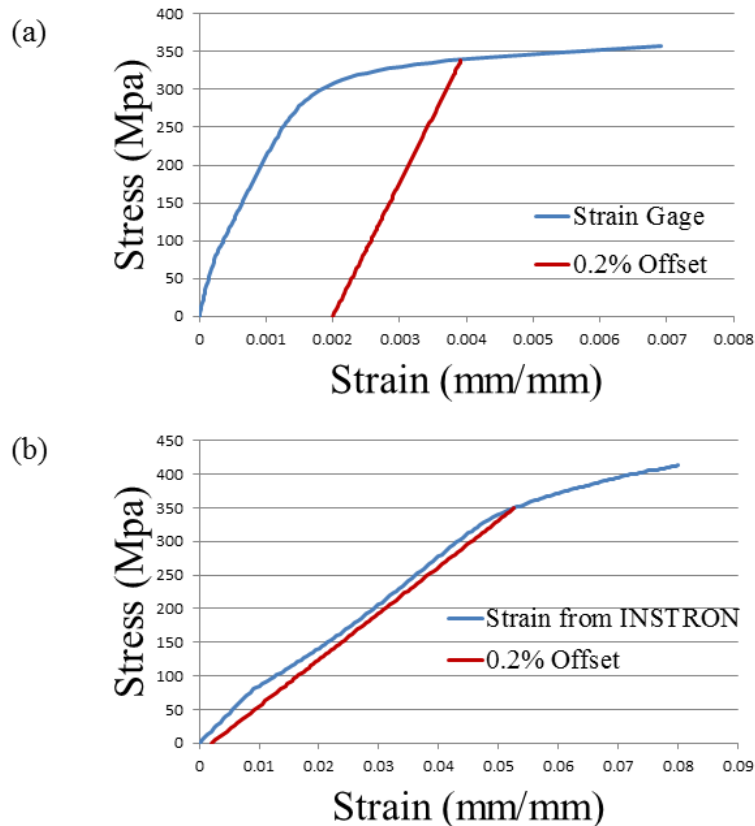


Figure 4.23 Comparison plots of SS316 yield strength calculation using (a) a strain gage to measure strain and (b) crosshead speed to measure strain that show a negligible difference in measured yield strength.

Based on the initial results reported so far, a final experimental method was developed and utilized for all remaining tensile testing in this chapter which includes all tensile testing for MA956. These preparations lead to consistently good results for MA956. A summary of major points is shown in Figure 4.24, which is representative of all of the tensile results on MA956. The non-zero starting point of Figure 4.24 is due to preloading of the specimens. No significant grip slippages were noted during any MA956 testing, but small variations in the elastic regions such as shown in Figure 4.24 were corrected with a foot correction which also establishes a zero stress/strain starting point as discussed in [190]. Good tensile performance was noted in the elastic and plastic regions as shown in Figure 4.24. A low end of test threshold was intentionally established to ensure proper fracture and excess data beyond fracture such as that shown in Figure 4.24 was removed.

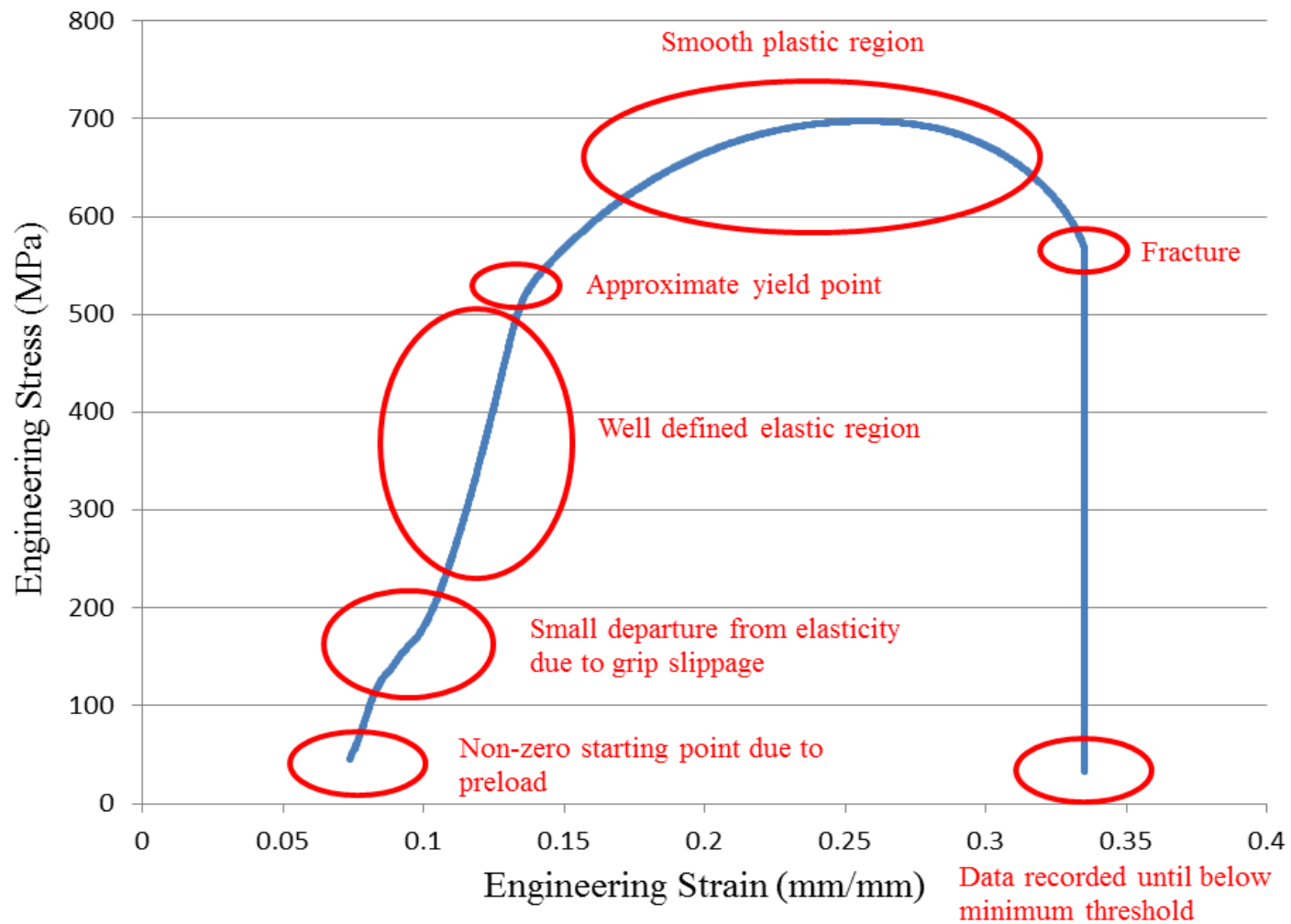


Figure 4.24 Typical raw data from a MA956 tensile test using the experimental methods developed.

As discussed previously, raw data such as that shown in Figure 4.24 was corrected using a foot correction, and machine compliance was removed using the previously described method. This process was done consistently for all SS316 and MA956 tensile testing in this chapter. This experimental process is shown in chronological order in Figure 4.25 and consisted of: (a) recording of raw data, (b) determination of the slope of the elastic region (this is the equivalent response and therefore includes machine compliance), (c) application of a foot correction and elimination of data beyond fracture, (d) calculation of the 0.2% offset yield strength, and finally (e) removal of machine compliance in the elastic region.

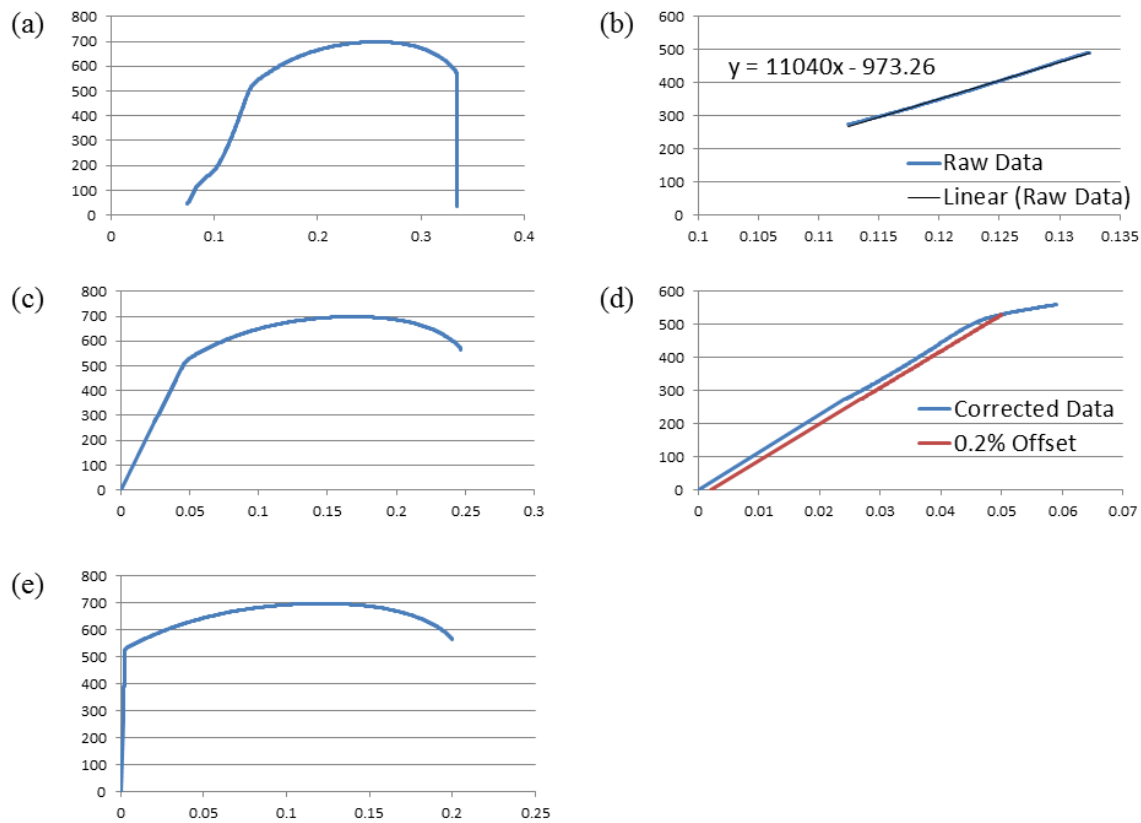


Figure 4.25 Summary of data reduction steps for all SS316 and MA956 tensile tests in this chapter. These steps included: (a) recording of raw data, (b) determination of the slope of the elastic region (note: this is the equivalent response), (c) application of a foot correction and elimination of data beyond fracture, (d) calculation of the 0.2% offset yield strength, and finally (e) removal of machine compliance in the elastic region. All vertical axis shown are Engineering Stress in MPa and all horizontal axis are Engineering Strain in mm/mm.

4. Experimental Verification of Design

To verify the tensile procedures described above, tensile testing was conducted on a series of SS316 samples of identical geometry prior to testing on MA956. A work-hardened SS316 was selected as a candidate test material based on its similarity to MA956, availability, and abundance of data in the open literature. Appropriate tensile property values and trends in performance were observed for SS316 at temperatures up to 600°C including yield strength, ultimate tensile strength, percent elongation, work hardening, ductility minima, and serrated flow regimes. Since insufficient MA956 material was available for multiple specimen testing at each condition, the variations in experimental data for SS316 at room temperature were applied as experimental error for MA956. The variations in yield strength, ultimate tensile strength, and percent elongation for SS316 at room temperature were all less than 5% (Figure 4.26 and Table 4.2).

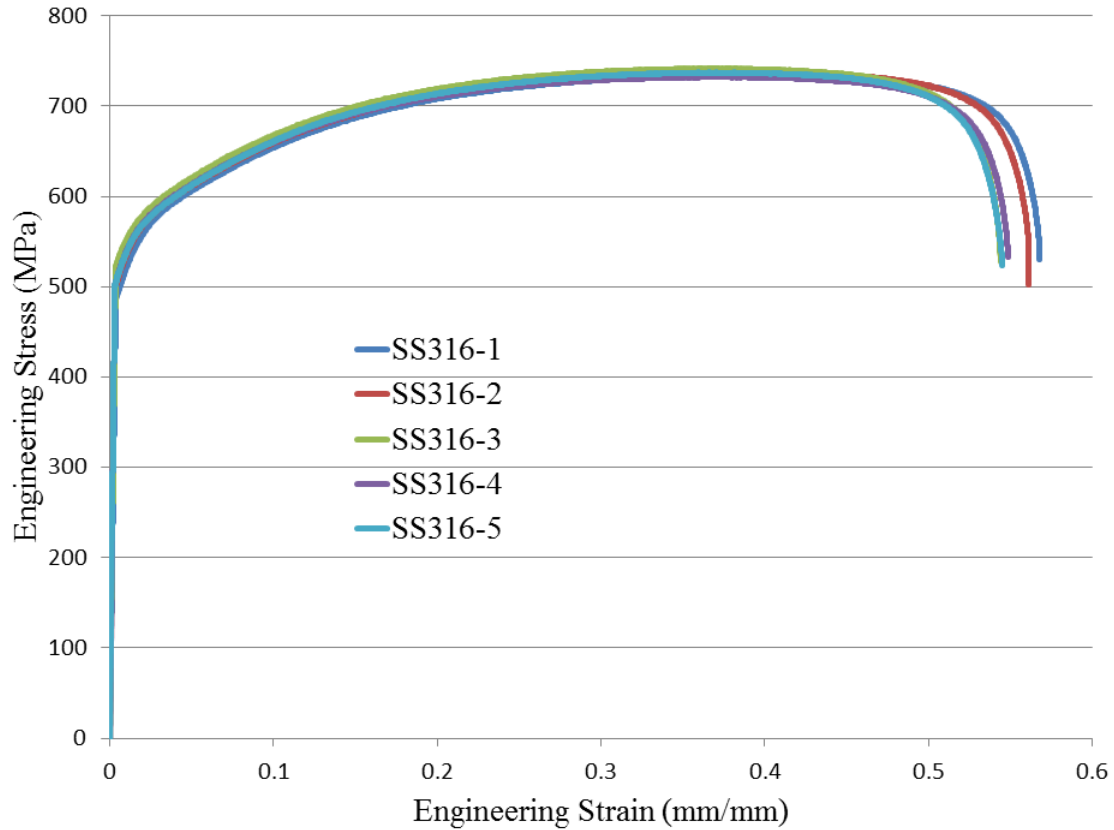


Figure 4.26 Stress strain curves for five identically tested SS316 specimens showing limited variation in experimental results.

Table 4.2 Variability of SS316 tensile testing at room temperature showing less than 5% variation in tensile parameters for the given experimental setup.

Sample	Yield Strength (MPa)	Ultimate Tensile Strength (MPa)	Percent Elongation (%)
SS316-1	502	735	56.8
SS316-2	499	737	56.1
SS316-3	522	742	54.4
SS316-4	501	732	54.9
SS316-5	501	737	54.5

5. Final Tensile Setup

The previous discussion has included tensile testing setup and results from a variety of materials and geometries (Table 4.1). With the experimental methodology

fully described, the remainder of this chapter will discuss MA956 tensile testing results exclusively. Unless specifically noted otherwise, the tensile specimen geometry used was the standard miniature tensile geometry (Figure 4.2a).

MA956 tensile specimens (gage section dimensions: length=12.7 mm, width=5.08 mm, and thickness=1.09 mm) were manufactured from BM and SZ sections of MA956 plate via EDM. Friction stir welded specimens were oriented such that the specimen gage length was perpendicular to both the welding and rolling direction and the entire gage length consisted of SZ material (Figure 4.27). BM specimens were similarly oriented from non-welded plates. To maximize material usage, two tensile specimens were machined from each location indicated in Figure 4.27 (i.e. one specimen on top of the other through the thickness of the plate). This decision was based on previous hardness research on the same plate that showed that there was minimal vertical hardness variation in the center of the SZ corresponding to the gage section of the tensile specimen.

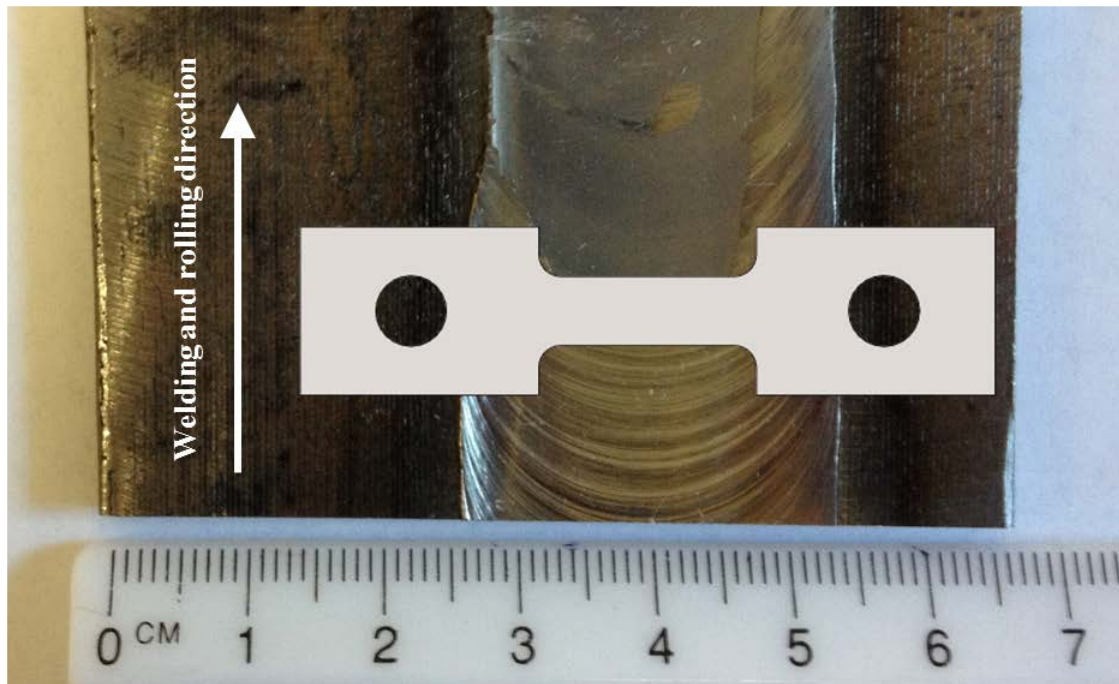


Figure 4.27 Tensile specimen geometry (gage section measurements: length=12.7 mm, width=5.08 mm, and thickness=1.09 mm) shown with corresponding location with respect to welded MA956 plate.

Tensile tests were conducted using an INSTRON 4507 load frame with a 10 kN load cell. Constant extension rate tests were conducted at a crosshead speed of 0.762 mm/min equating to a maximum tensile strain rate of 10^{-3} sec^{-1} for the specimen geometry. Although considered, insufficient material existed to conduct strain rate sensitivity tests; therefore, all tensile tests were conducted at the same crosshead speed. Additionally research by Salomon on MA956 concluded that strain rate sensitivity began at temperatures around 600°C which was the upper end of the temperature range for this research [102]. Tests were conducted at room temperature (20°C) and at temperatures up to 600°C (+5°C) using a 4800 Watt, Applied Test Systems five-zone tubular furnace that enclosed the entire specimen and grip connections of the load frame. For tests at temperatures above room temperature, specimens were manually maintained at a small tensile load (<50 N equating to less than 5% of the yield stress) for 1 hour to allow for thermal equilibration prior to testing. Specimens were preloaded to <10% of the yield point at 250 N/min (corresponding to a strain rate of approximately $1 \times 10^{-3} \text{ sec}^{-1}$) to minimize grip slippage. BM specimens were tested at room temperature, 400°C, 500°C, and 600°C. Due to limited availability of friction stir welded specimens and the relative consistency of the BM response between 400°C and 600°C, the three FSW conditions were tested at room temperature, 400°C and 600°C.

6. Fractography

Fractography of specimens was conducted using a Zeiss Neon 40 field emission SEM operating at 20 keV. High magnification imaging was conducted with no specimen tilt and at a low working distance (5 mm) to allow for improved resolution. High magnification imaging was taken in representative areas of the fracture surface near the center of the specimen. Low magnification imaging was conducted with specimens tilted at 10 degrees and at a larger working distance (approximately 15 mm) to allow for full visualization of the fractured sample.

C. RESULTS

1. Base Metal Tensile Behavior

Similar to the CG results published by Special Metals [93], FG MA956 at room temperature had limited ductility ($\epsilon_f=0.118$ mm/mm), but a significantly higher strength ($\sigma_y=909$ MPa and $\sigma_{uts}=991$ MPa) due to grain refinement (Figure 4.28). At 400°C FG MA956 exhibited little change in ductility but a significant reduction in strength. Increasing the test temperature to 600°C caused an increase in ductility ($\epsilon_f=0.485$ mm/mm) and further reduction in strength ($\sigma_y=292$ MPa and $\sigma_{uts}=309$ MPa) (Figure 4.24). Unlike SS316, no serrated flow regimes were observed in FG MA956 at any temperature up to 600°C.

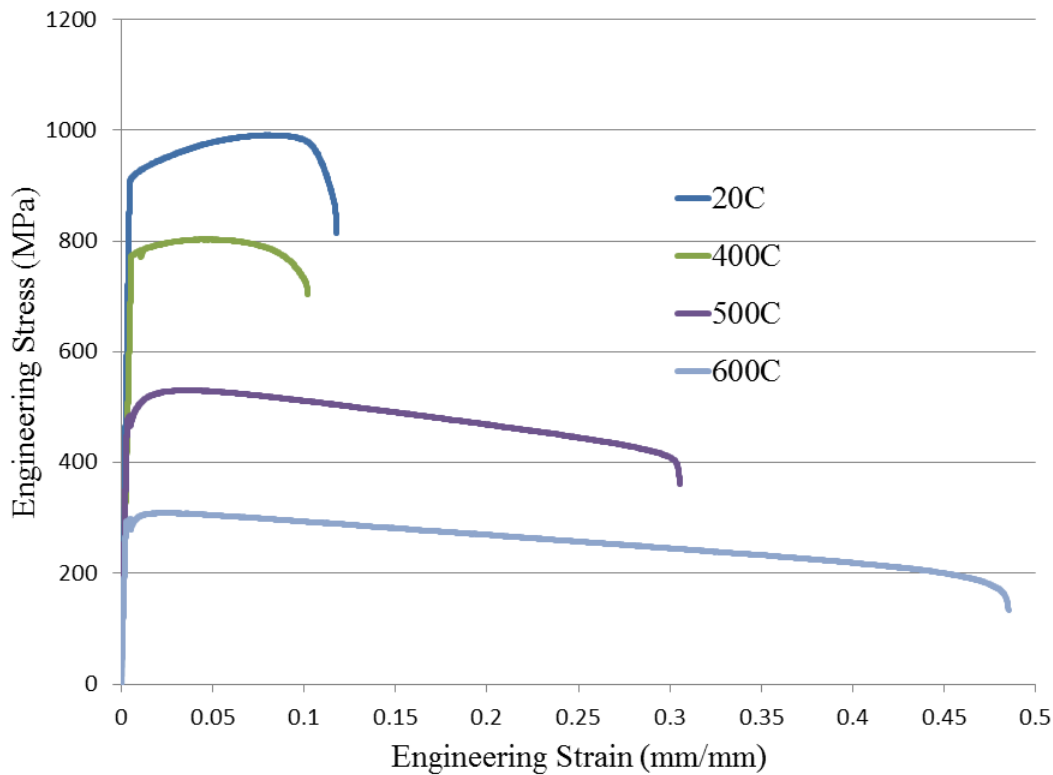


Figure 4.28 Engineering stress-strain curves for base metal MA956 at various temperatures.

Fractography of BM specimens was consistent with observations during tensile testing at all temperatures. At room temperature, MA956 exhibited very limited reduction in area and the fracture surface was characterized by large faceted transgranular fracture surfaces indicative of brittle failure (Figure 4.29a). For comparison, SS316 was much more ductile at room temperature and showed a noticeable reduction in cross-sectional area and dimpled fracture surfaces indicative of microvoid coalescence and ductile failure (Figure 4.29b). The brittle behavior of MA956 at room temperature was consistent with other reported results and is one of the primary disadvantages for its use in room temperature applications [93, 96, 98]. At elevated temperatures, MA956 exhibited noticeable reduction in cross-sectional area and very fine microvoid coalescence indicating a more ductile fracture than that observed at room temperature, a result consistent with the improved ductility observed during tensile testing (Figure 4.30).

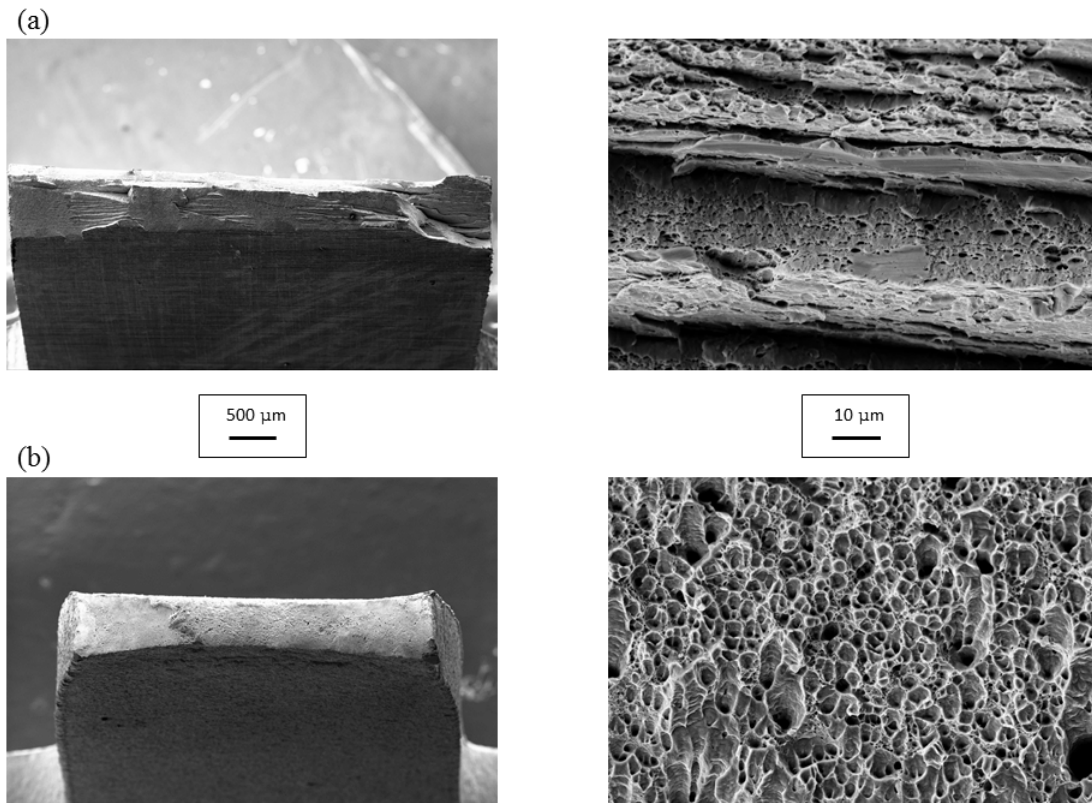


Figure 4.29 Fractography of (a) base metal MA956 and (b) SS316 at room temperatures showing the brittle behavior of MA956 at room temperature.

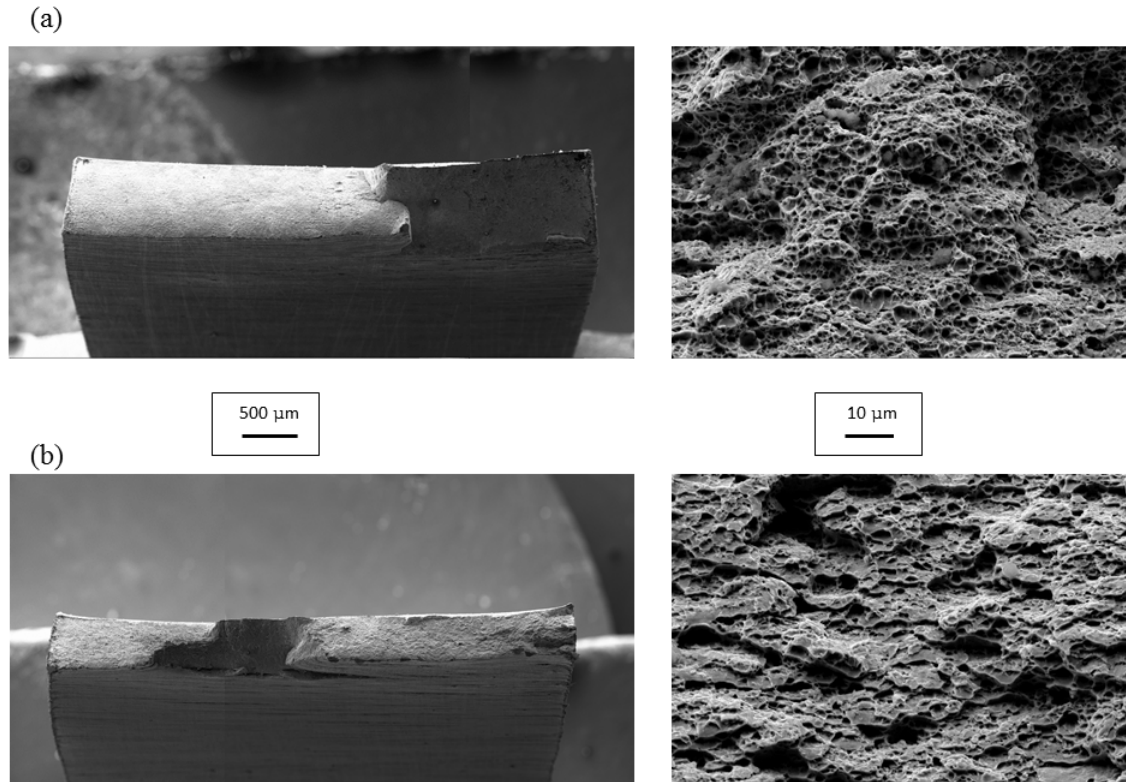


Figure 4.30 Fractography of base metal MA956 at (a) 400C and (b) 600C showing the change in fracture mode from brittle to ductile of MA956 at elevated temperatures compared to the brittle fracture at room temperature in Figure 4.29.

As shown in the stress strain curves of Figure 4.28 and the fractography of Figure 4.29, FG BM MA956 has limited ductility and exhibits moderate strain hardening at room temperature. True stress and true strain were calculated from the engineering stress and engineering strain curves in Figure 4.28 up to the onset of necking for all temperatures tested (Figure 4.31). Using the Holloman relationship (Equation 4.1) [168], values for the strain hardening coefficient (k) and strain hardening exponent (n) were calculated as a function of temperature (Figure 4.32). The results demonstrate that, as temperature is increased, MA956 undergoes significantly less strain hardening, and at the maximum test temperature of 600°C, FG MA956 exhibits almost perfectly plastic behavior.

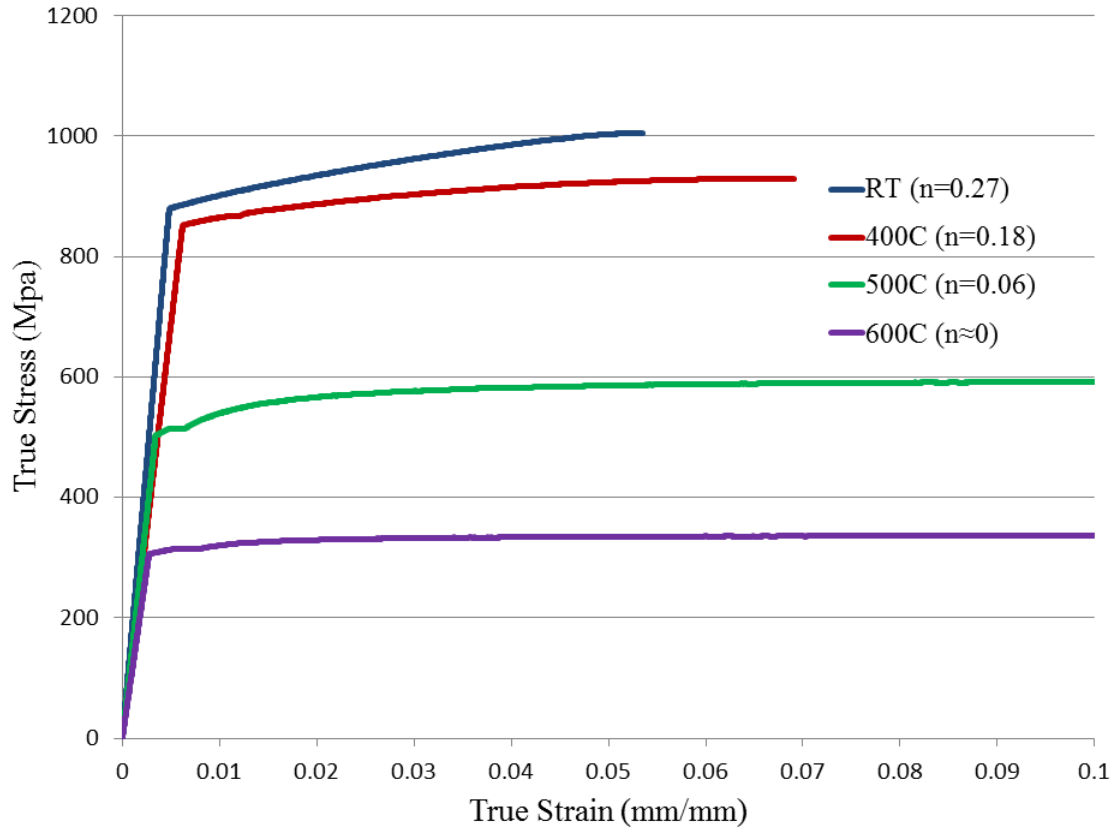


Figure 4.31 True stress-strain curves for base metal MA956 at various temperatures. True stress-strain values were calculated from the engineering stress-strain values (Figure 4.28) to the onset of necking allowing for calculation of strain hardening exponent (n).

$$\sigma_{true} = k\epsilon_{true}^n \quad \text{Equation 4.1}$$

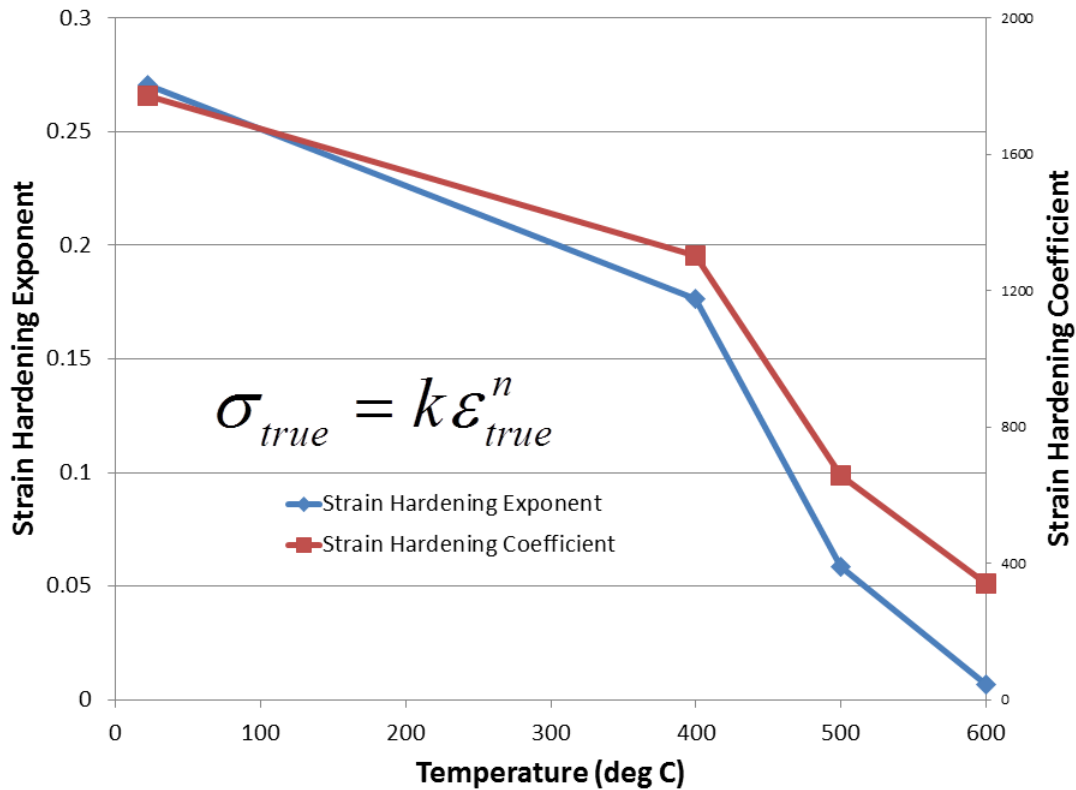


Figure 4.32 Strain hardening exponent (n) and strain hardening coefficient (k) as a function of temperature for base metal MA956 using the Holloman equation (Equation 4.1).

2. Tensile Behavior of the Stir Zone in Friction Stir Welded Material

At room temperature, all FSW specimens showed a significant reduction in strength and an increase in ductility compared to BM specimens (Figure 4.33). It should be noted that the gage section was comprised of only stir zone material, and thus, this result reflects the change in the tensile behavior of the stir zone material, not the entire weld structure. The maximum reduction in strength was 42% compared to the BM and occurred for the highest heat input condition (500 RPM/25 MPM). This value compared very closely to the observed 37% reduction in hardness for the same conditions reported in Chapter II. The differences in strength at room temperature between the FSW conditions were small but support the overall conclusion presented previously that higher heat input conditions produce softer SZ microstructures based predominantly on the

increased grain size as heat input is increased; however, these previous conclusions did not fully address changes from the BM to the stir zones of the friction stir welded conditions which will be analyzed in this research.

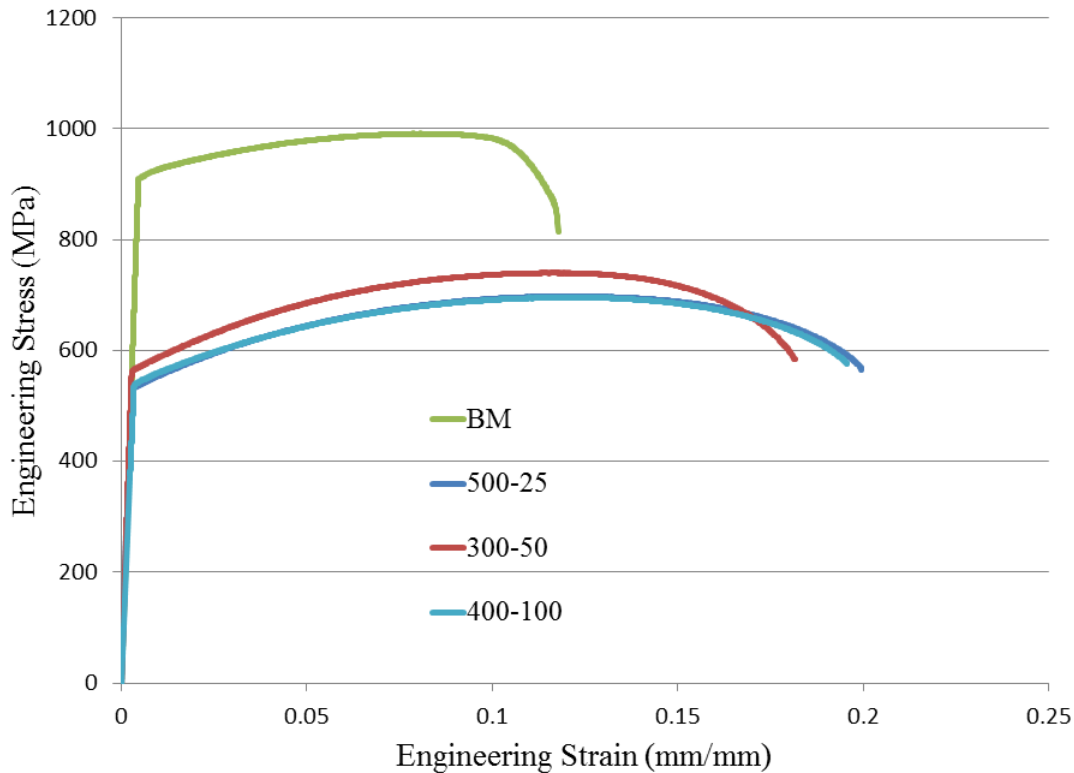


Figure 4.33 Room temperature engineering stress-strain curves for base metal MA956 and friction stir welded MA956 showing a reduction in strength and increase in ductility following friction stir welding.

The results for the elevated temperature tests at 400°C and 600°C both showed that FSW reduces the strength of the BM at each temperature; however, the lowest heat input condition (400 RPM/100 MMPM) resulted in only a 19% reduction in strength at 600°C compared to a 33% reduction in strength for the highest heat input condition (500 RPM/25 MMPM) at the same temperature. This trend is consistent with results in Chapters II and III which demonstrated that lower heat input conditions produce more favorable SZ conditions (less grain coarsening, less oxide particle coarsening, and a harder SZ profile). The trend in ductility following FSW is less consistent at elevated temperatures than at room temperatures. The consistency of yield and ultimate tensile

strength measurements and relative inconsistency of percent elongation measurements for miniature tensile specimens is discussed in other literature [191]. For brevity, the results of FSW samples at the maximum temperature of 600°C are shown in Figure 4.34 although the trends were similar for 400°C.

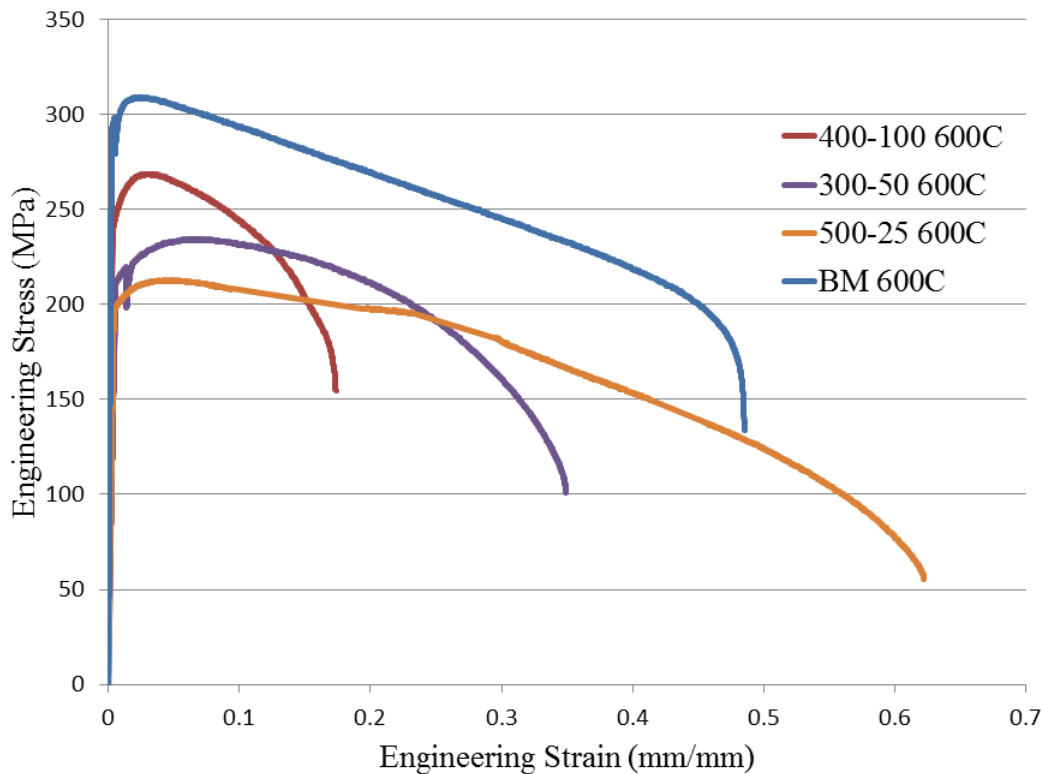


Figure 4.34 Engineering stress strain curves of friction stir welded MA956 at 600°C.

Fractography of FSW specimens was consistent with observations during tensile testing at all temperatures including the change in ductility seen on the stress-strain curves from the BM condition. At room temperature, friction stir welded MA956 displayed a noticeable reduction in cross-sectional area, and fracture surfaces were no longer dominated by the faceted transgranular appearance seen in the BM, but rather showed very fine microvoid coalescence throughout most of the fracture surface, indicating a predominance of ductile failure. This type of fracture surface occurred for all FSW conditions and is shown in Figure 4.35. At elevated temperatures, all FSW

specimens showed ductile behavior with the most marked change occurring for the highest heat input condition at the highest test temperature (Figure 4.36) which also corresponds to the largest elongation measured in Figure 4.28. As shown in Figure 4.33 and Figure 4.35, FSW caused an increase in ductility at room temperature; similarly the degree of strain hardening increased following FSW. The effect of FSW on ductility is less pronounced at elevated temperatures and thus the strain hardening behavior of FSW MA956 is similar to BM MA956 above room temperature.

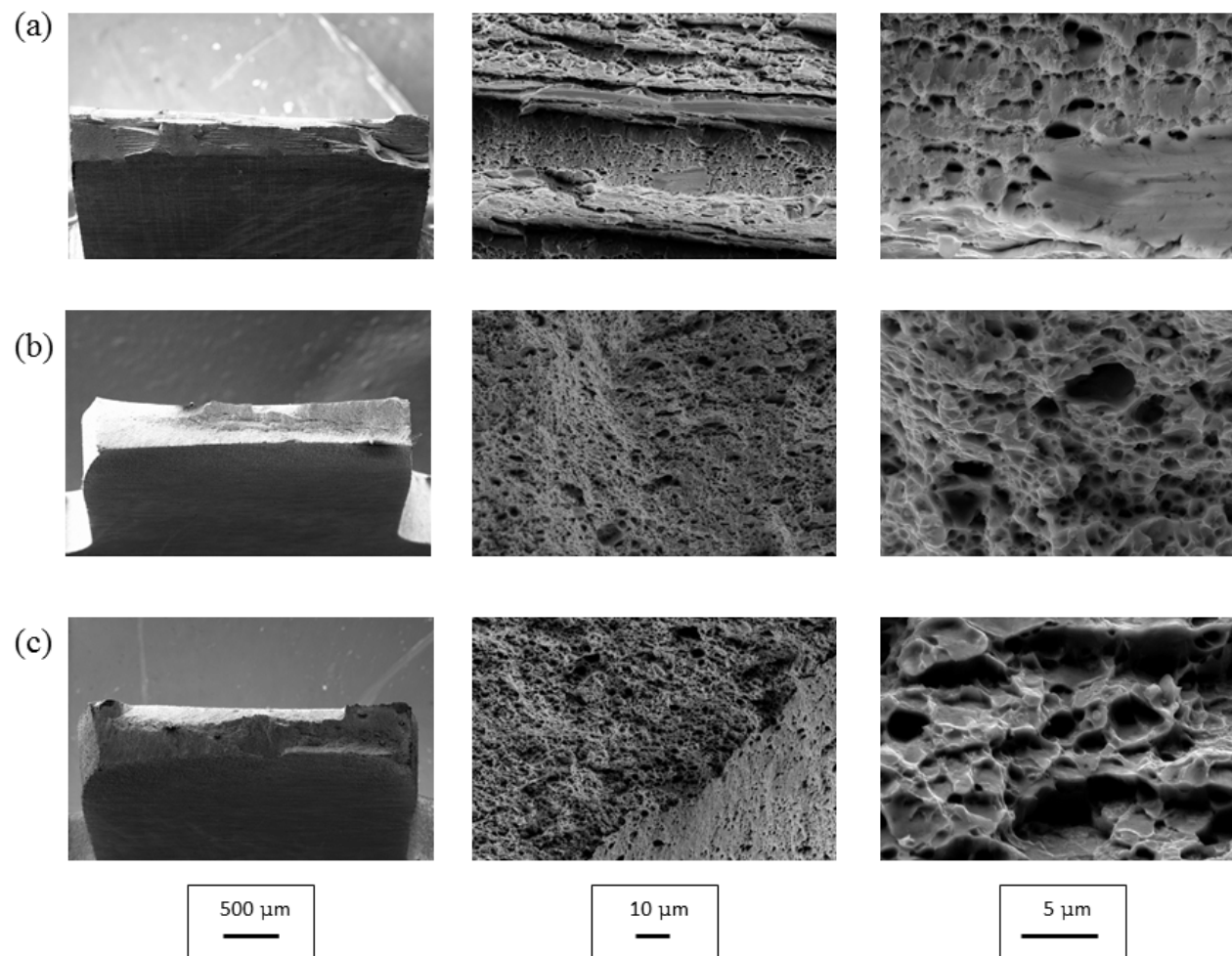


Figure 4.35 Fractography of MA956 at room temperature for (a) base metal, (b) low heat input condition (400 RPM/100 MPPM) and (c) high heat input condition (500 RPM/25 MPPM).

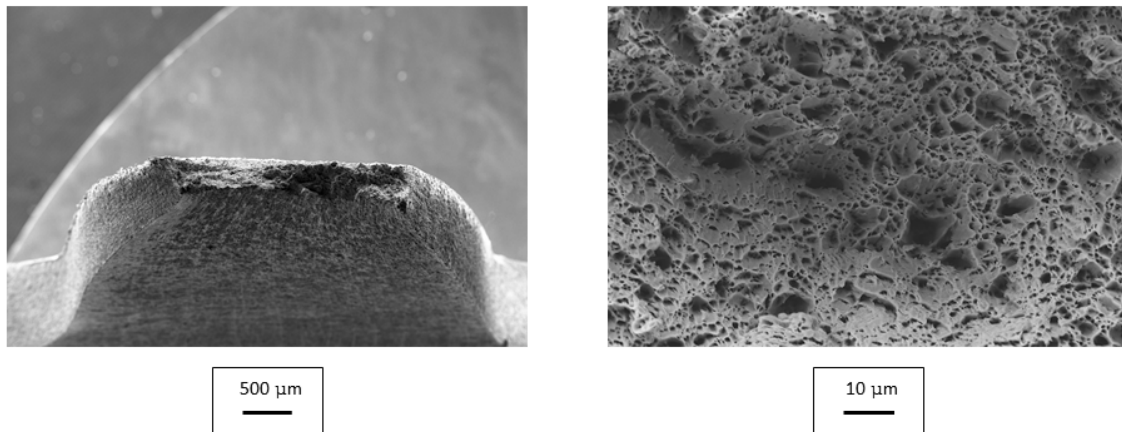


Figure 4.36 Fractography of MA956 friction stir welded with high heat input conditions (500 RPM/25 MMPPM) fractured in tension at 600C showing the largest amount of ductility corresponding to the highest test temperature and highest heat input condition.

3. Thermo-Mechanically Affected Zone

The large gradients in grain size seen on the AS of the high heat input condition did not appear to cause strain localization and systematic failure on the AS during tensile loading as hypothesized in Chapter II (paragraph E conclusion (4)). This was evaluated using the long miniature tensile specimen (Figure 4.1c) which had a gage section that encompassed the entire weld nugget. Tensile testing of this specimen evaluated the entire weld structure from BM, RS, SZ center, and AS and produced failure near the center of the SZ consistent with the area of lowest hardness (Figure 4.37). Based on this result, the large gradients at the AS are not considered to be potential failure location in the tensile conditions tested; however, other failure mechanisms that depend on grain boundaries could still be exacerbated by these gradients.

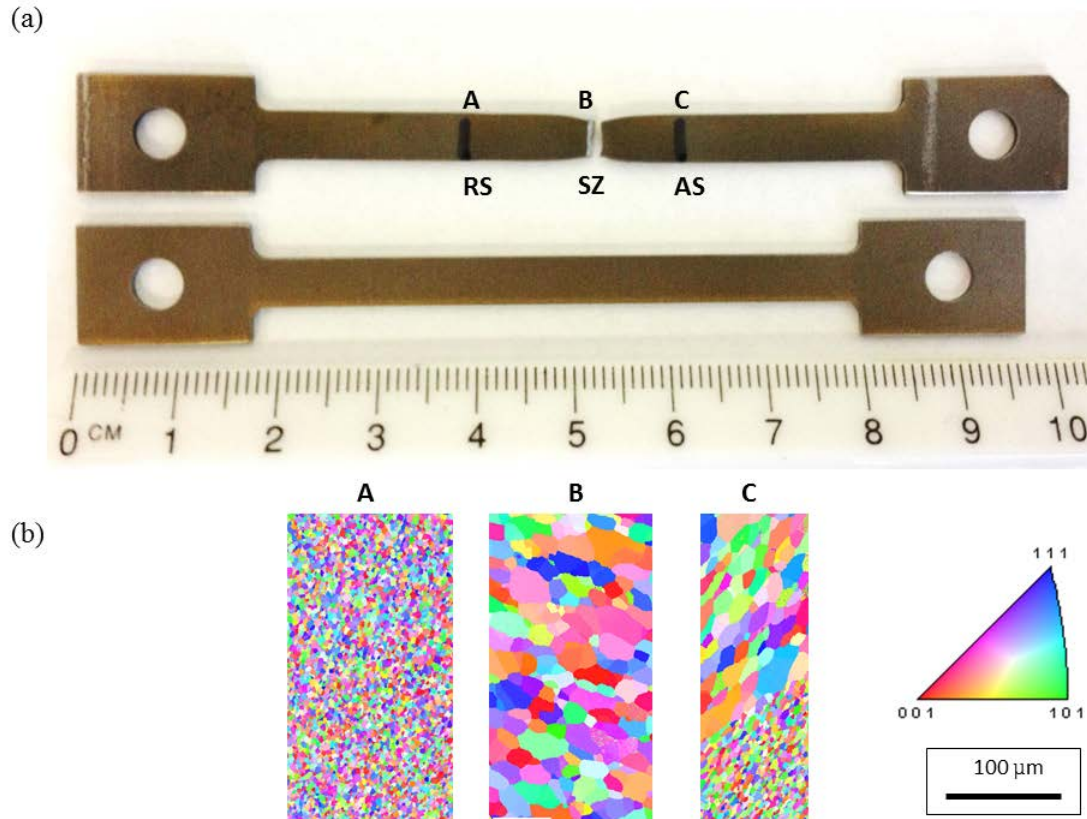


Figure 4.37 (a) Failure in the stir zone for the high heat input condition (500 RPM/25 MPPM) as opposed to failure at the advancing side as hypothesized in Chapter II with (b) corresponding inverse pole figure maps at each location from Chapter II for reference.

D. DISCUSSION

Simple but reasonable qualitative conclusions on ductility can be drawn solely by looking at comparison images of the fractured specimens for the various conditions with no magnification (Figure 4.38). This comparison shows a negligible change in ductility of the BM at 400°C and an increase in BM ductility at 600°C when compared to room temperature. Similarly FSW with high heat input conditions at 600°C caused an increase in ductility and a pronounced degree of necking not seen in other samples. These simple conclusions are expanded upon during full analysis of tensile results.

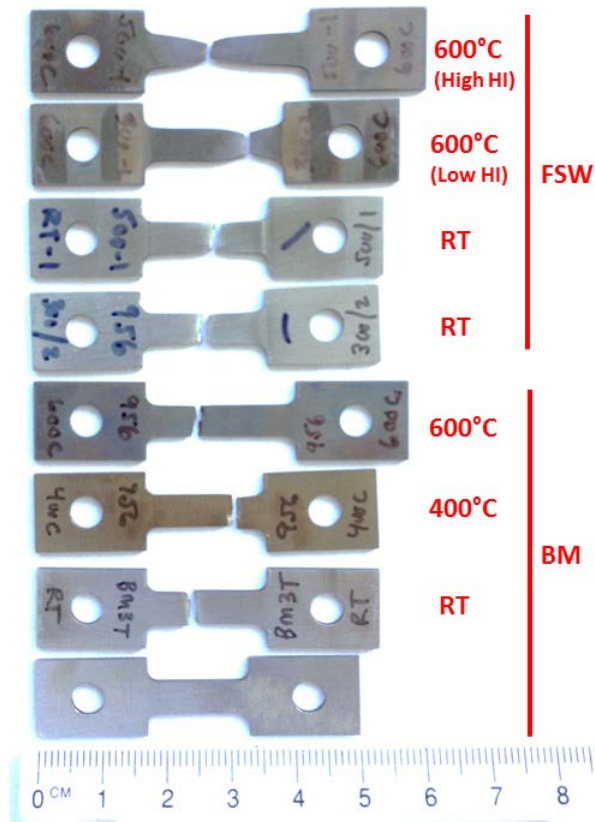


Figure 4.38 MA956 tensile specimens after fracture showing qualitative changes in ductility for different conditions.

The grain size of MA956 is a dominant factor in controlling the tensile properties at room temperature. As mentioned previously, the MA956 used in this research is significantly finer in grain size (1–10 μm) than that normally supplied by Special Metals (>100 μm). Comparative plots of strength (Figure 4.39) and percent elongation (Figure 4.40) show the differences between the FG alloy used in this research and the nominal CG alloy produced by Special Metals. The limited ductility at room temperature of both FG and CG MA956 shown in Figure 4.40 and the fractography of Figure 4.29a is due to the low DBTT of MA956 which is stated as in the range of 0–100°C by Special Metals [93] and corroborated by other sources [96, 97, 104].

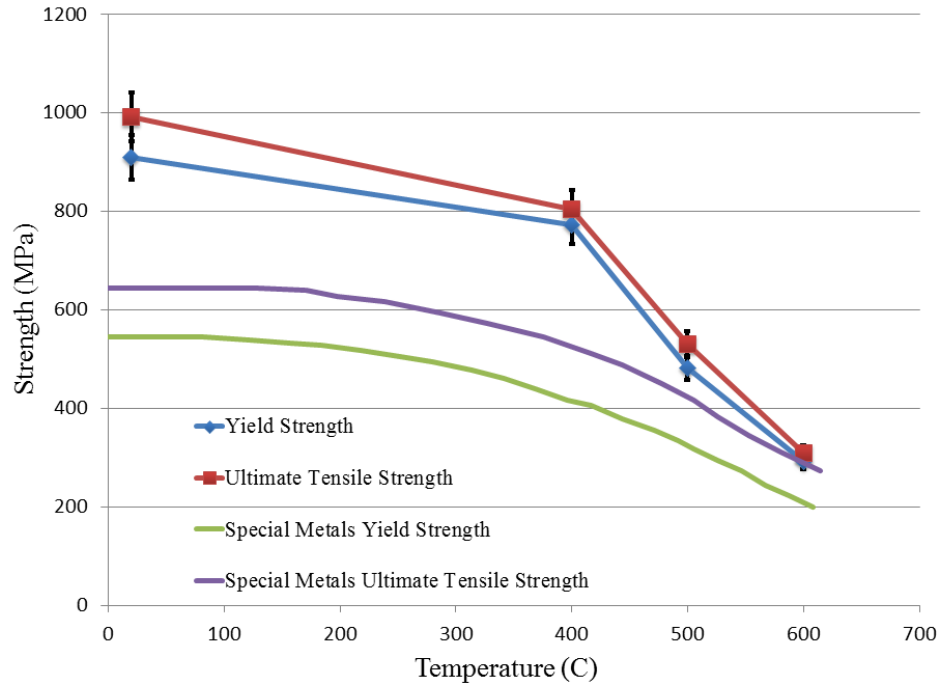


Figure 4.39 Yield and ultimate strengths of fine grain unrecrystallized MA956 with comparison to manufacture's specifications for coarse grain recrystallized MA956 [after 93] (error bars show 5% variation based on SS316 test results).

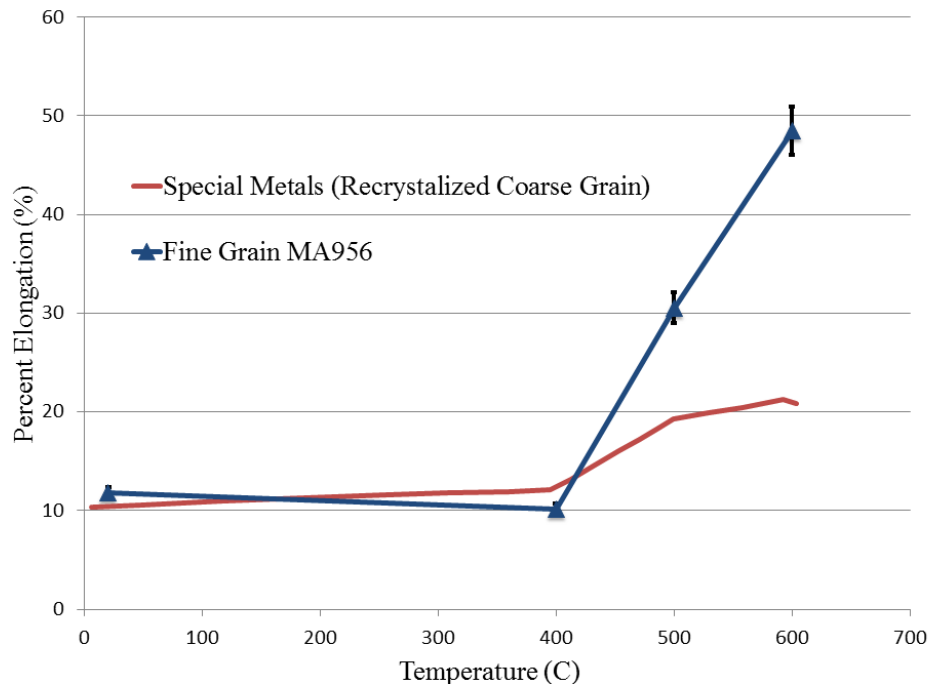


Figure 4.40 Percent elongation of fine grain unrecrystallized MA956 with comparison Special Metals manufacture specifications of coarse grain recrystallized MA956 [after 93] (error bars show 5% variation based on SS316 test results).

1. Temperature Effects

FG MA956 is considerably stronger at lower temperatures than CG MA956, but this difference disappears as the temperature approaches 600°C (Figure 4.39). This difference in yield behavior can be entirely attributed to grain boundary strengthening described by the Hall-Petch relationship. Both FG and CG MA956 have limited ductility at room temperature (Figure 4.40); however, FG MA956 shows improved ductility as the temperature increases. These trends combined with the improved radiation damage resistance of FG materials and comparable creep performance in some situations suggests that FG ODS alloys such as MA956 could be of benefit in nuclear material applications. Overcoming the obstacles in joining of these alloys would further promote their utility in these applications.

2. Friction Stir Welding Effects

While FSW has already been demonstrated as a successful joining mechanism for MA956 and other ODS alloys, this research shows that FSW reduces the room temperature strength of MA956 significantly but improves the room temperature ductility of MA956 over a range of FSW heat inputs (Figure 4.33). The overall strength comparison of BM to friction stir welded MA956 at elevated temperatures is shown in Figure 4.41 and shows that at elevated temperature the effect of FSW on the yield strength of MA956 is much less noticeable. This initial observation suggests that the mechanisms behind the reduction in strength of friction stir welded MA956 are more complex than Hall-Petch grain boundary strengthening alone; however, these initial results are encouraging and support the use of both BM and friction stir welded FG MA956 at the elevated temperatures required for nuclear applications due to the relatively high retained strength of the weld.

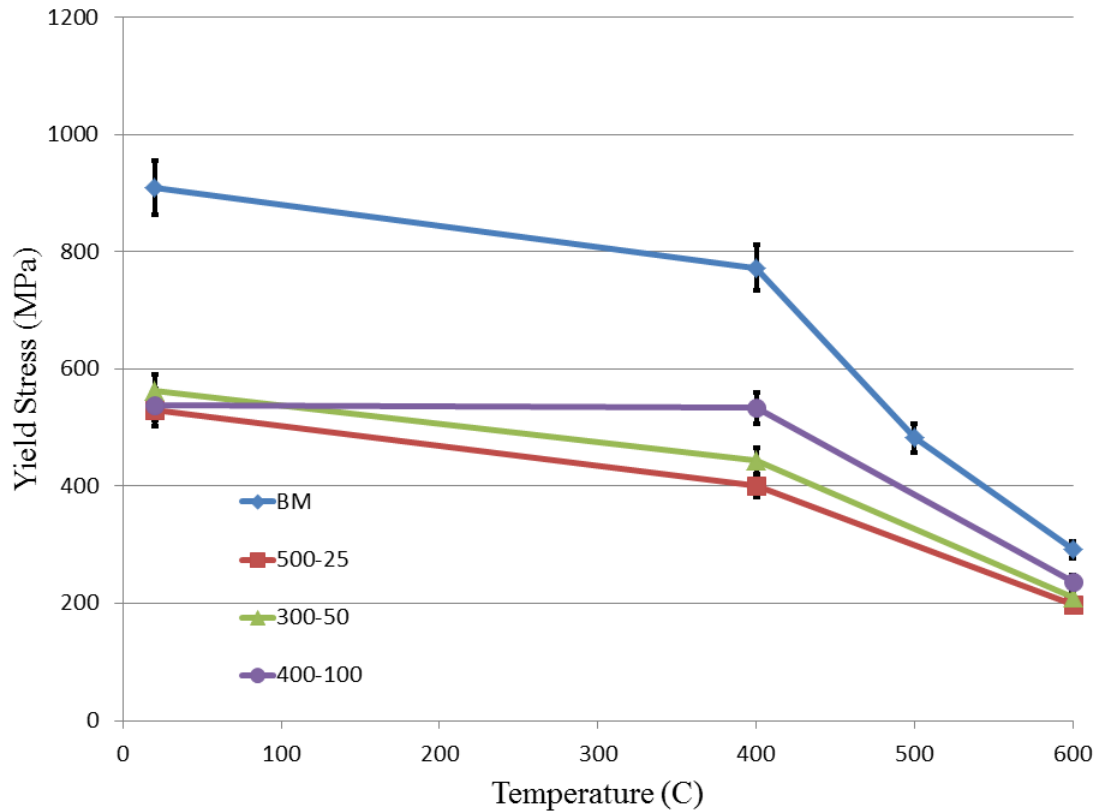


Figure 4.41 Yield strength versus temperature for consolidated friction stir welded conditions. The softening effect of FSW is less evident at high temperature.

The reduction in yield strength of the friction stir welded material compared to the base plate material can be explained primarily through a loss of dispersion strengthening and secondarily by grain coarsening. In Chapter II, the grain size of the stir zone material was shown to increase systematically with increasing FSW heat input, most notably increasing tool rotational speed. Using SEM backscatter electron imaging (Figure 4.42) and the results of Chapter III, the Y-Al-O particles increase in size in the SZ. In addition, the dislocation density was qualitatively much less in the stir zone material following FSW (Figure 4.43). These results are presented here again because oxide particle coarsening is paramount to the understanding of changes in tensile behavior following FSW. Table 4.3 contains a consolidated list of material and microstructural data on MA956 at room temperature as a function of FSW conditions with values of HI included for reference. The BM value of average particle size was obtained from research by

Hsiung on identical FG MA956 during research on nanoparticles in MA956 [37] as discussed in Chapter III. Table 4.3 shows several important room temperature results that occur following FSW: (1) yield strength, ultimate tensile strength, and hardness all decrease, (2) percent elongation increases, (3) ferrite grains are significantly coarsened, and (4) yttrium aluminum oxide particles are significantly coarsened. All of these effects, with the exception of percent elongation, are enhanced as the heat input during FSW is increased from a low heat input condition to a high heat input condition. Similar to the discussion on grain coarsening in Chapter II, the parameters in Table 1.3 do not all monotonically change with HI, but they all do monotonically change with tool rotational speed suggesting that tool rotational speed is the governing parameter in the range of conditions tested. Insufficient data – such as changes in tool rotational speed for a singular tool traverse speed – exists to prove that tool traverse rate is the dominant parameter for all conditions; however, what remains clear is the distinct difference between high heat input conditions (500 RPM/25 MPPM) and low heat input conditions (400 RPM/100 MPPM and 300 RPM/50 MPPM).

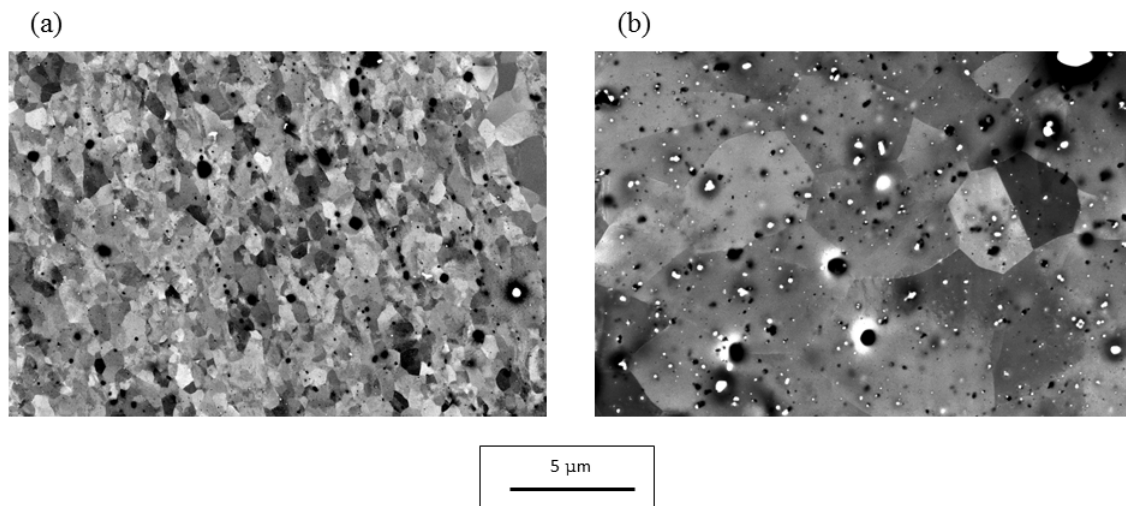


Figure 4.42 Scanning electron microscopy backscatter images of (a) base metal MA956 and (b) friction stir welded MA956 with high heat input (500 RPM/25 MPPM) showing grain and oxide particle coarsening following friction stir welding.

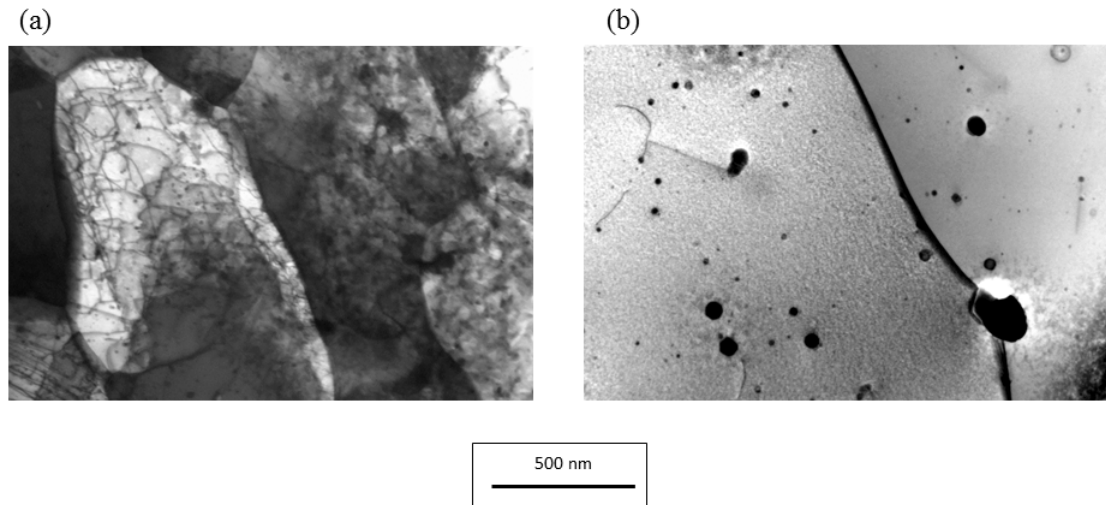


Figure 4.43 Scanning transmission electron microscopy images of (a) base metal MA956 and (b) friction stir welded MA956 with low heat input (300 RPM/50 MMPM) showing a qualitative increase in grain size and reduction in dislocation density following friction stir welding.

Table 4.3 Summary of processing, microstructure, and material property relationships of MA956 at room temperature following friction stir welding with varying process parameters.

Weld Condition	Heat Index (-)	σ_{YS} (MPa)	σ_{UTS} (MPa)	Hardness (HV)	PE (%)	Ferrite Grain Size (μm)	Average Oxide Particle Size (nm)	Average Inter-Particle Spacing (μm)
BM	-	909	991	346	12	0.890	8.07 [51]	-
400-100	4	539	696	221	20	6.94	166	3.23
300-50	6	563	740	225	18	4.16	163	3.19
500-25	20	530	698	218	20	12.5	343	3.41

3. Strengthening Mechanisms

The change in yield strength of the SZ material following FSW can be explained in terms of its microstructural evolution. The yield strength of a material can be estimated as its intrinsic material yield strength summed with contributions by various strengthening mechanisms. This approach has been utilized by Badmos and Wang independently on both FG and CG MA956 to compare theoretical estimates to experimental processes [56, 100, 101]. For the research herein, the approach of

approximating the overall strengthening response as a linear superposition of strengthening terms (Equation 4.2) is used, although a root mean-square method has been proposed by Kocks [192] and used on MA956 [56] as well as other dispersion strengthened alloys such as 14YWT [65].

$$\sigma_y = \sigma_O + \sigma_{SS} + \sigma_{GB} + \sigma_P + \sigma_D \quad \text{Equation 4.2}$$

The strengthening contribution method proposed in Equation 4.2 is defined as follows: the yield strength of a given material (σ_y) is equal to the sum of Peierls-Nabarro stress representing the stress due to resistance of dislocation motion within the crystal lattice (σ_O), the strengthening contribution from solid solution strengthening (σ_{SS}), the strengthening contribution from grain boundary strengthening in accordance with the Hall-Petch relationship (σ_{GB}) (Equation 4.3), the strengthening contribution from oxide particle dispersion strengthening (σ_P), and the strengthening contribution from dislocation strengthening (σ_D). Because FSW is a solid state joining mechanism and MA956 maintains its single ferritic phase, BCC structure, and average composition throughout the welding process, both σ_O and σ_{SS} are assumed not to change significantly during FSW. The remaining terms σ_{GB} , σ_P , and σ_D all vary following FSW as suggested by data in Table 4.3 and the STEM images of Figure 4.43.

$$\sigma_{GB} = kd^{-1/2} \quad \text{Equation 4.3}$$

The change in yield strength as the grain size changes is well-described by the Hall-Petch relationship. Using the data from Table 4.3, a Hall-Petch plot of MA956 was generated and the value of the Hall-Petch constant (k) in Equation 4.3 was calculated to be $0.164 \text{ MPam}^{1/2}$. Other research by Badmos and Wang both used estimated values of k ($0.5 \text{ MPam}^{1/2}$) based on MA956 being a ferritic stainless steel [56, 101]. Figure 4.44 shows that the yield strength for stir zone material from all three FSW conditions falls on the Hall-Petch line; however, the yield strength of the BM condition does not fall on this line, but is instead 255 MPa higher in yield strength than its corresponding location on the Hall-Petch line for its grain size. This difference indicates that the reduction in strength from the BM to any of the FSW conditions is due primarily to changes in oxide

particle dispersion strengthening and dislocation strengthening which combined should be approximately 255 MPa.

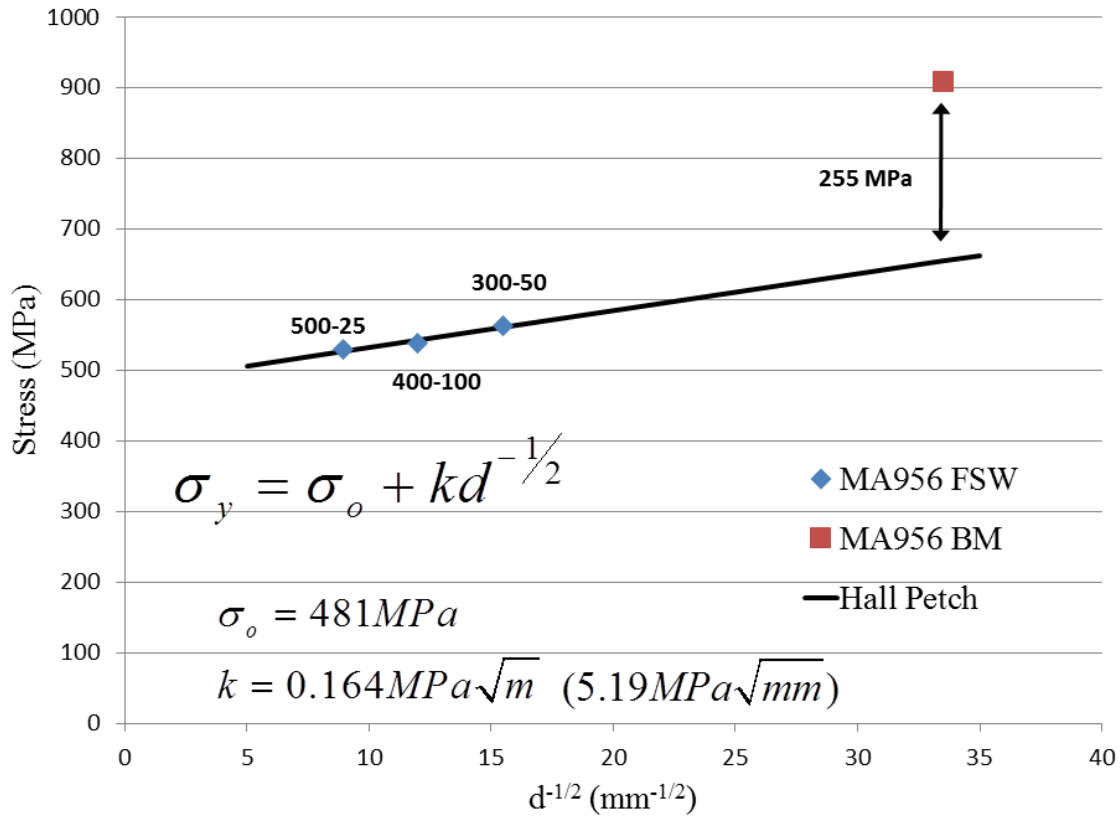


Figure 4.44 Hall Petch plot of MA956 with varying grain size achieved by friction stir welding. The difference in strength of the base metal compared to the Hall Petch line is attributed to changes in particle and dislocation strengthening mechanisms.¹⁷

This estimate for strength loss is remarkably close to previous work examining strengthening mechanisms in MA956. Table 4.4 contains summary data from both Badmos and Wang for strengthening terms in Equation 4.2 [56, 101]. These papers estimate the yield strength contribution due to oxide particle strengthening to be between 248 and 258 MPa respectively, quite similar to the value of 255 MPa presented here. Research by Badmos was based on BM MA956, and the method used to calculate the 248

¹⁷ As mentioned previously, the MA956 specimen with FSW conditions of 275 RPM/100 MMPM (Figure 2.3) was not suitable for tensile specimen fabrication, and thus there is no corresponding point for that condition exists on the Hall Petch plot for MA956.

MPa contribution of particle strengthening was achieved by arc melting MA956 in argon causing the oxides to float off producing a resulting alloy that was no longer particle strengthened. The yield strength contribution due to oxide particle dispersion was estimated by Wang using an Orowan-type relation (Equation 4.4 [56]), where the Taylor factor, M , was 2.7, the shear modulus, G , was 60 GPa, the Burgers vector, b , was 0.25 nm, and the Poisson's ratio, ν , was 0.3. The oxide particle dispersion strengthening component can be estimated from the present data using Equation 4.4 and values from Table 4.3 for average particle radius (r) and inter-particle spacing (λ). The present results show σ_p for stir zone material is only 13.2 MPa for the low heat input condition (400 RPM/100 MPM) and 13.9 MPa for the high heat input condition (500 RPM/25 MPM). This estimate compares very favorably to the data in Figure 4.44 which suggests that FSW causes the complete loss of particle strengthening even for the low heat input condition. This overall conclusion is also strongly supported by research by Kim on 14YWT which concluded that oxide particles greater than 100 nm in size (comparable to all oxide particles following FSW in this research) would result in σ_p being less than 50 MPa [64, 65]. It is worth noting that particles in 14YWT are Y-Ti-O particles as opposed to the Y-Al-O particles in MA956 and the work by Kim did not include any conditions that would cause a comparable degree of particle coarsening as that seen here, but the calculation method used by Kim is very similar to that presented by Wang and used here in Equation 4.4.

Table 4.4 Theoretical strengthening contributions used by other authors for MA956 prior to FSW (σ_O -Peierls-Nabarro stress, σ_{SS} -strengthening contribution from solid solution strengthening, σ_P -strengthening contribution from particle strengthening, and σ_D -strengthening contribution from dislocation strengthening). Contribution from grain boundary strengthening (σ_{GB}) was calculated by each author using an assumed value of $0.5 \text{ MPam}^{1/2}$ for the Hall-Petch constant, k and varied depending on the grain size.

Author	σ_O (MPa)	σ_{SS} (MPa)	σ_P (MPa)	σ_D (MPa)
Badmos[101]	36	116	248	31
Wang [56]	50	130	258	47

$$\sigma_{Orowan} = M \frac{0.4}{\pi} \frac{Gb}{\sqrt{1-\nu}} \frac{\ln\left(\frac{2r}{b}\right)}{\lambda} \quad \text{Equation 4.4}$$

4. Relationship to Hardness

The tensile response data in this research compares favorably with the previous Vickers hardness measurements reported in Chapter II, suggesting that Vickers hardness is a reliable method for estimating the tensile properties in friction stir welded steels. The most striking comparison of hardness and yield strength is the comparison of the Hall-Petch plot presented in Chapter II (Figure 2.26) and the plot presented in this chapter (Figure 4.44). For direct comparison, the hardness data from Chapter II and the yield strength data from this chapter are plotted in a single Hall-Petch plot in Figure 4.45.¹⁸ The data and trends from these two sources are virtually indistinguishable substantiating the hardness analysis in Chapter II and clearly establishing a relationship between hardness, yield strength, and grain size.

¹⁸ As discussed in Chapter II, the MA956 material used for the 275 RPM/100 MPM condition (Figure 2.3) was not suitable for tensile specimen fabrication, and thus no tensile data exists for this condition while grain size and hardness data was available.

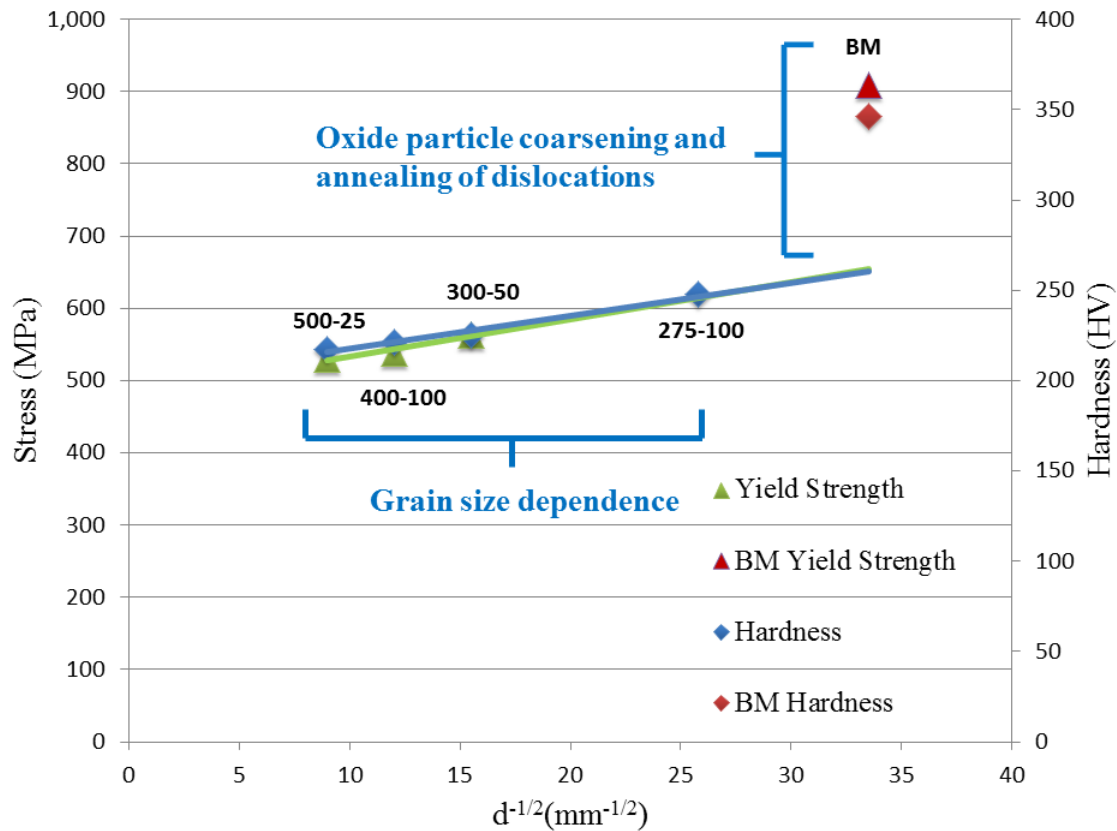


Figure 4.45 Comparison of hardness Hall-Petch data from Chapter II (Figure 2.26) and yield strength Hall-Petch data from Chapter IV (Figure 4.44).

In Chapter II, the Hall-Petch plot was comprised of hardness data only and was therefore not a true Hall-Petch plot. Additionally the only microstructure information known at that point was grain morphology. The reasons behind the hardness BM condition not correlating to the Hall-Petch line for its grain size were not immediately apparent, but lead to the in depth analysis of oxide particle morphology since it appeared that a strengthening mechanism other than solely grain boundary strengthening was significant. Now with the full yield strength data available from this chapter, it is clearly seen that both oxide particle dispersion strengthening and grain boundary strengthening are significant, and the contribution of oxide particle dispersion strengthening was able to be calculated using the Hall-Petch data. This entire process was predicated on the knowledge and insight gained during hardness analysis which was possible with far less effort and expense than the full tensile testing analyses conducted in this chapter.

Although hardness is a measure of a material's plastic flow resistance and therefore a function of both yield strength and strain hardening, it can be used as an effective metric for changes in material performance following FSW. The maximum reduction in strength and hardness following FSW occurred for the highest heat input condition used (500 RPM/25 MPM) which was consistent with hypotheses based on evolved microstructure. For the highest heat input condition (500 RPM/25 MPM) room temperature yield strength was reduced by 42% with a corresponding 37% reduction in hardness reported previously.

The data from Figure 4.45 clearly suggests a relationship between hardness and yield strength, but before defining this relationship, a review of units and unit conversion is necessary to ensure correct values are being compared.¹⁹ The most commonly used relationship between hardness (H) and yield strength (σ_y) is the Tabor relationship (Equation 4.5); however, the Tabor relationship is normally written with H in equivalent units as σ_y which for SI units would be MPa. For Vickers hardness measurements (H_V), this is not the case since the true units for H_V are kgf/mm^2 which comes directly from the force divided by area measurement of the Vickers hardness procedure. The conversion from H_V to MPa requires the multiplication by the acceleration due to gravity and conversion from mm to m (Equation 4.6). To allow for correct comparison to this and other research, the Tabor relationship is converted to the ratio of H_V to σ_y (Equation 4.7). For comparison to the Tabor relationship, the hardness and yield strength values experimentally determined in this research (tabulated in Table 4.3 and shown graphically on Figure 4.45) can be used to determine the same ratio directly. As can be readily seen by the ratio of the axes in Figure 4.45, the ratio of H_V to σ_y for MA956 in this research is 0.4 (Equation 4.8) which is comparable to the 0.31 value calculated from the Tabor relationship when converted to appropriate units. It is known, however, that differences

¹⁹ The distinction between units on hardness and yield strength is critical. Throughout this and most other research that analyzes and reports hardness data specifically, hardness values are typically reported in Vickers Hardness (H_V); however, many literature sources that analyze the ratio of hardness to yield strength such as Tabor and Jung typically use hardness in units of MPa annotating hardness as H without fully establishing this conversion. For consistency throughout this research the term H_V is utilized to indicate units of Vickers Hardness (with true units of kgf/mm^2), the term H is used to indicate units of MPa, and the ratio of yield strength to hardness (σ_y/H_V) will be used even though the true units of this ratio are MPa/Vickers Hardness.

in strain hardening can cause deviation from the Tabor relationship, so Jung developed best fit relationships between yield strength, hardness (H) and the strain hardening exponent (n) for several metallic materials including aluminum, iron, stainless steel, and copper in a variety cold worked and annealed conditions [191]. Using these relationships and the value of n for MA956 experimentally determined at room temperature in this research (n=0.27 from Figures 4.31 and 4.32), Jung's methods result in overestimates of the ratio of H_V to σ_y (Equation 4.9) whereas the Tabor relationship was shown to be an underestimate. The reason for these disparities is the low (but non-zero) strain hardening of MA956 (Figure 4.31). The Tabor relationship is best suited for materials with negligible strain hardening while Jung's methods were established to account for typical strain hardening in metals. In summary, the Tabor relationship (Equation 4.7) is based on a theoretical relationship, Jung's relationship (Equation 4.9) is based on experimental evidence of typical metals, and the relationship presented herein (Equation 4.8) is based on experimental data for MA956 specifically. The relationship in Equation 4.8 is considered to be the most accurate relationship with deviation from the other methods based on differences in strain hardening between the three methods.

$$\left(\frac{H}{\sigma_y} \right)_{Tabor} \approx 3 \quad \text{Equation 4.5}$$

$$1H_V \left(\frac{kg}{H_V mm^2} \right) \left(\frac{9.8m}{sec^2} \right) \left(\frac{1000^2 mm^2}{1m^2} \right) \left(\frac{N sec^2}{kgm} \right) \left(\frac{Pam^2}{N} \right) \left(\frac{1MPa}{10^6 MPa} \right) = 9.8MPa \quad \text{Equation 4.6}$$

$$\left(\frac{H_V}{\sigma_y} \right)_{Tabor} \approx 0.31 \quad \text{Equation 4.7}$$

$$\left(\frac{H_V}{\sigma_y} \right)_{MA956} = 0.4 \quad \text{Equation 4.8}$$

$$\left(\frac{H_V}{\sigma_y} \right)_{Jung} = 0.50 \quad \text{Equation 4.9}$$

E. CONCLUSIONS

The tensile properties of FG MA956 as function of temperature and FSW conditions were investigated. The following conclusions were drawn:

(1) Finite element modeling of tensile specimens was effective to ensure specimen geometry created uniform loading conditions. Specimen geometries with a stress concentration factor of 2.0 or less produced failures in the gage section of the specimen.

(2) Similar to CG MA956, FG MA956 has limited ductility at room temperature, but FG MA956 has a higher yield and ultimate tensile strength than CG MA956 primarily due to grain refinement. At room temperature FG MA956 undergoes moderate strain hardening ($n=0.27$). Above 400°C FG MA956 shows improved ductility over CG MA956 up to the maximum temperature tested of 600°C. At elevated temperatures FG MA956 exhibits very limited strain hardening and demonstrates nearly perfectly plastic behavior at 600°C.

(3) FSW on FG MA956 results in up to a 42% reduction in yield strength of the stir zone material for high heat input conditions. Reducing the heat input during FSW lessens this reduction in strength and at higher testing temperatures, the reduction in strength is less severe. FSW also causes an increase in ductility that is predominantly apparent at lower temperatures. When combined with microstructural data on the same FG MA956, the following effects are observed following FSW: yield and ultimate tensile strength at all temperatures are reduced, room temperature ductility is increased, hardness in the SZ is reduced (by approximately the same percent as strength), dislocation density in the SZ is reduced, grains in the SZ are significantly coarsened, and oxide particles in the SZ are significantly coarsened. All of these effects are enhanced as the heat input due to FSW is increased.

(4) Reduction in yield strength due to FSW is due to the combined effects mentioned above; however, the majority of the loss of strength when comparing the BM to the welded condition stems from the complete loss of oxide particle strengthening due to oxide particle coarsening following FSW. The differences in yield strength and

hardness in stir zone material amongst FSW conditions are well described by the Hall-Petch relationship.

(5) Material property evaluation by hardness measurements can be an accurate assessment method without having to conduct full tensile testing. Using established relationships of hardness to strength can produce accurate results while also showing correct trends following FSW.

(6) MA956 can be manufactured in a FG or CG form. FSW can produce consolidated welds in FG MA956 that can maintain up to 80% of the base material's strength at 600°C. Control of grain size during manufacture and the welding conditions during joining by FSW may produce a final welded material condition sufficient to meet high temperature material specifications.

(7) The strong gradients at the AS TMAZ for the high heat input conditions did not cause a change in tensile behavior of friction stir welded MA956. In all cases, welded specimens failed in the SZ corresponding to the area of lowest hardness and similarly lowest yield strength.

V. LIQUID METAL EMBRITTLEMENT OF MA956

A. INTRODUCTION

Like most corrosion resistant steels, MA956 and other ODS steels get their corrosion and oxidation resistance due to passive protective oxide layers that form between the metal and corrosive environments. The general corrosion resistance of MA956 and other similar aluminum-containing ODS alloys (PM2000 and various K-alloys) has been demonstrated to be good in a wide variety of environments including air [111], SCW [75], LBE [52, 53, 90, 91], and molten salts [34–36]. In each of these environments, a thin, tightly adherent Al_2O_3 protective oxide layer formed on the metal that protects the alloy from corrosion and oxidation. Although important in many other material properties of ODS alloys, the yttrium in the original Y_2O_3 powders and subsequent Y-Al-O particles does not play a significant role in the corrosion resistance of ODS steels [75] and the aluminum concentration in these alloys (nominally 4.5–5.5 wt%) is sufficient to form both the Y-Al-O particles in the metal matrix and the protective Al_2O_3 outer layer. In ODS steels without aluminum (MA957, 12/14 YWT, and 9/12 Cr-ODS), chromium reacts with oxygen to form a similar Cr_2O_3 protective oxide layer; however, in comparative studies the corrosion resistance of these alloys has been shown to be inferior to that of aluminum-containing ODS alloys [53, 70, 75, 90, 91]. This improved general corrosion and oxidation resistance is the primary reason for aluminum addition in some ODS alloys although as shown in Chapter III, aluminum also plays a significant role in oxide particle formation.

In addition to the importance of aluminum in corrosion resistance of ODS steels, oxygen concentration is also a critical component in the formation of the protective oxide layers, and oxygen has been found to be an effective non-metallic corrosion inhibitor in liquid lead and LBE systems. In these systems, oxygen reacts with major constituents of the steel (Fe, Cr, and Al) to form stable protective oxide layers. Research studies have shown that there is a balance between enhanced liquid metal corrosion at low oxygen concentrations and enhanced oxidation that occurs at high oxygen concentrations. The optimal range for oxygen concentration has been shown to be between 0.1–1 ppm oxygen

concentration for lead or LBE systems (Figure 5.1) [193]. In depth reviews of general corrosion of metals in lead and LBE systems have been done at LANL and are available in other sources [193–195].

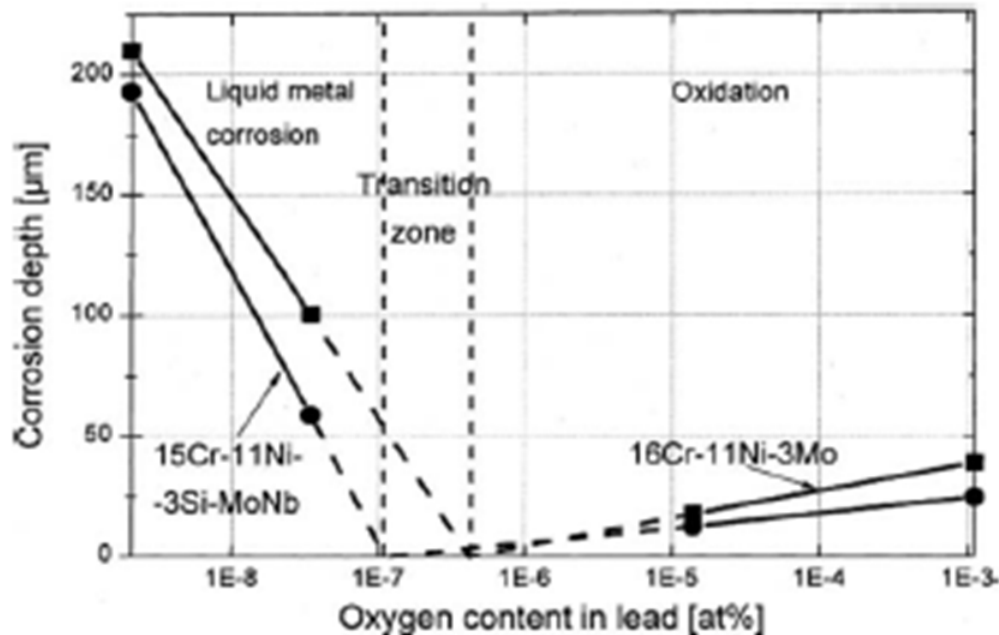


Figure 5.1 Oxygen concentration effect on corrosion of steels in molten lead from Zhang [from 193].

Although the general corrosion and oxidation behavior of ODS steels is well documented, there is limited research into environmental effects on these steels under tensile loading. For consistency and clarity, the following definitions are provided from standard terminology and acronyms relating to corrosion [196]:

Environmentally assisted cracking: cracking of a material wherein an interaction with its environment is a causative factor in conjunction with tensile stress, often resulting in brittle fracture of an otherwise ductile material.

Liquid metal cracking: environmental cracking caused by contact with a liquid metal.²⁰

Stress corrosion cracking: cracking of a material produced by the combined action of corrosion and sustained tensile stress (residual or applied).

For the research herein, the preceding definitions are considered synonymous when referring to the effect of liquid metals on other metals, and the more prevalent current term, LME, will be used in this research. Although research on the effects and mechanisms behind LME is not as prevalent in current literature, research in the late 1970s and early 1980s has helped establish the foundations of what is known about LME, particularly for reactor steels. That research has established the following common principles about LME: (1) similar to SCC in other systems, certain embrittler-to-metal couples are susceptible while others are immune, (2) LME requires dislocation motion and thus only occurs following plastic deformation, (3) LME does not occur under compression loading conditions, (4) the presence of a notch (or crack) is often an exacerbating condition for LME, (5) LME usually results in intergranular fracture, and (6) although the exact mechanism is still unknown, the same theories behind brittle fracture of reactor steels have been applied to LME [155–158, 197]. Additionally, the same research has established the following major criteria necessary to show experimentally a LME response: (1) a susceptible embrittler to metal couple, (2) operating temperature near the melting temperature of the embrittler, and (3) intimate contact between the embrittler and the affected metal. The nominal effect of temperature is shown in Figure 5.2 from Nicholas [155].

²⁰ NACE/ASTM G193-11a does not list a definition for LME, but the definition provided for liquid metal cracking is consistent with definition of LME. Most research sources use the term LME or liquid metal induced embrittlement and not liquid metal cracking.

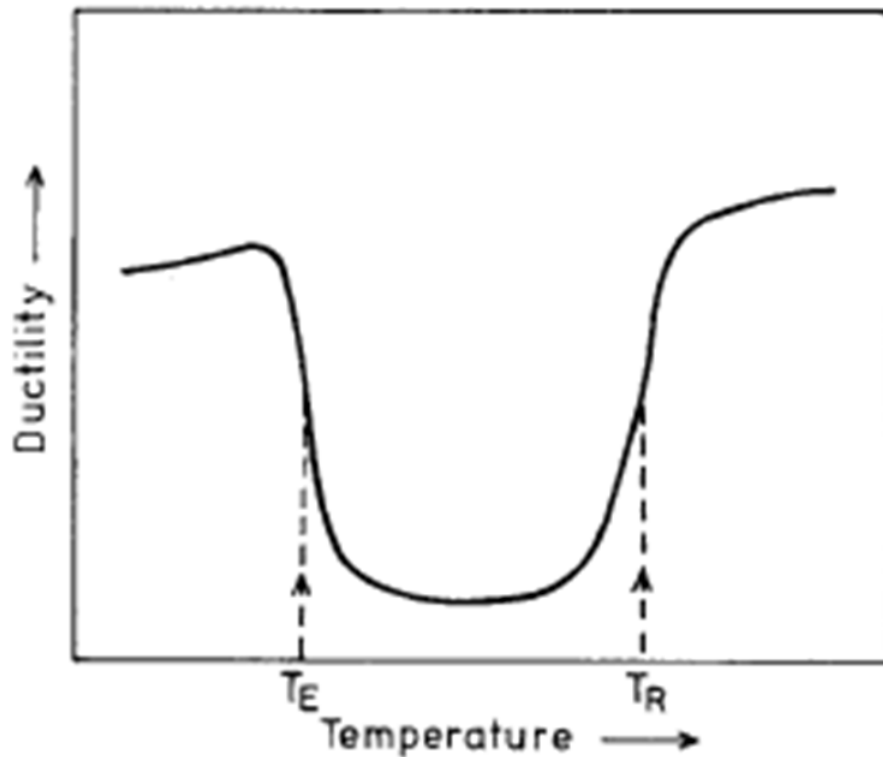


Figure 5.2 Typical ductility trough for a liquid metal embrittlement couple from Nicholas [from 155]. T_E is defined as the temperature corresponding to the onset of the reduction in ductility and T_R is defined as the temperature corresponding to the recovery of ductility.

The effect of temperature on ductility in Figure 5.2 has been observed in all LME couples and is described as a “ductility trough.” Citing several different embrittler to metal couples, Nicholas concluded that the onset of the ductility trough (T_E) never occurred above the melting temperature of the embrittler and similarly, the recovery of the ductility trough (T_R) never occurred below the melting temperature of the embrittler. This observation supports a very important hypothesis: operation at the melting point of the embrittler should place the couple within the ductility trough and should cause a notable LME effect as long as other conditions are met. In similar LME research, Old makes an analogous observation and conclusion: “Embrittlement is often restricted to a limited temperature range. This has important technological implications because it prevents the identification of susceptible systems by simple high temperature screening tests carried out on the assumption that higher temperatures are likely to exacerbate any

detrimental effects” [156]. This temperature effect has significant implications for this research and for potential operation of alloys susceptible to LME. For this research, the intent is to determine the susceptibility of MA956 to LME, and thus operation within a potential ductility trough is desired; however, for applications where MA956 or other ODS steels are likely to be used, the operating temperature is likely to be significantly above the melting temperature of a potential embrittler and thus potentially outside of the ductility trough. While encouraging for operating conditions, strong consideration must be given to transition stages (e.g., plant heat-up and plant cool-down) to ensure that material limitations are not exceeded during these transitions. Research by Nicholas and Old also determined that some other experimental factors did not factor into LME results. The applied strain rate was found to not affect the occurrence of LME. Although most LME failures were due to intergranular fracture, some cases of transgranular fracture have been observed, and the overall effect of grain size variation for the metal was inconsistent [155, 156].

With the development of advanced FM steels over the last two decades, there has been renewed interest in SCC and LME of structural steels for reactor designs with alternate coolants. This has included research on FM steels in a variety of environments including oxygenated or hydrogenated water [198], aqueous environments with a range of pH [89], SCW [86], liquid lead [199], and LBE [200–203]. All of these research studies have used miniature samples of different geometries under tensile load in the environment desired and evaluated SCC or LME by analyzing change in ductility from the results of the *in situ* environment to the results from a controlled environment (air or inert gas). For conditions where immunity to SCC or LME was found, the immunity was attributed to the same passive protective oxide layers that are effective at protecting against general corrosion and oxidation. In these cases the protective oxide layers remained intact during exposure until failure coincident with the failure of the base alloy at tensile yield conditions.

For the research studies specifically on LME [199–203], mixed results with respect to immunity or susceptibility have been found. A 9% Cr-1% Mo steel in molten lead at 350°C was found to be immune to LME by Legris [199]. Researching different

steels in LBE environments, Van den Bosch determined that the FM steels T91 and EUROFER97 (both non-ODS steels) showed immunity to LME due to their native Cr_2O_3 oxide layers [200] while a silicon enriched steel (2.75% Si) showed a susceptibility to LME and an observed ductility trough very similar to that proposed by Nicholas and Old (Figure 5.3) [202]. Researching LME on T91, Auger determined that T91 showed a “small but noticeable” change in ductility consistent with an LME response [203]. These mixed results confirm the empirical nature of LME as noted by Nicholas and Old and highlight the importance of experimental conditions, most notably temperature, in determining the susceptibility of alloys to LME. No research on SCC or LME of any ODS steel could be found in the literature.

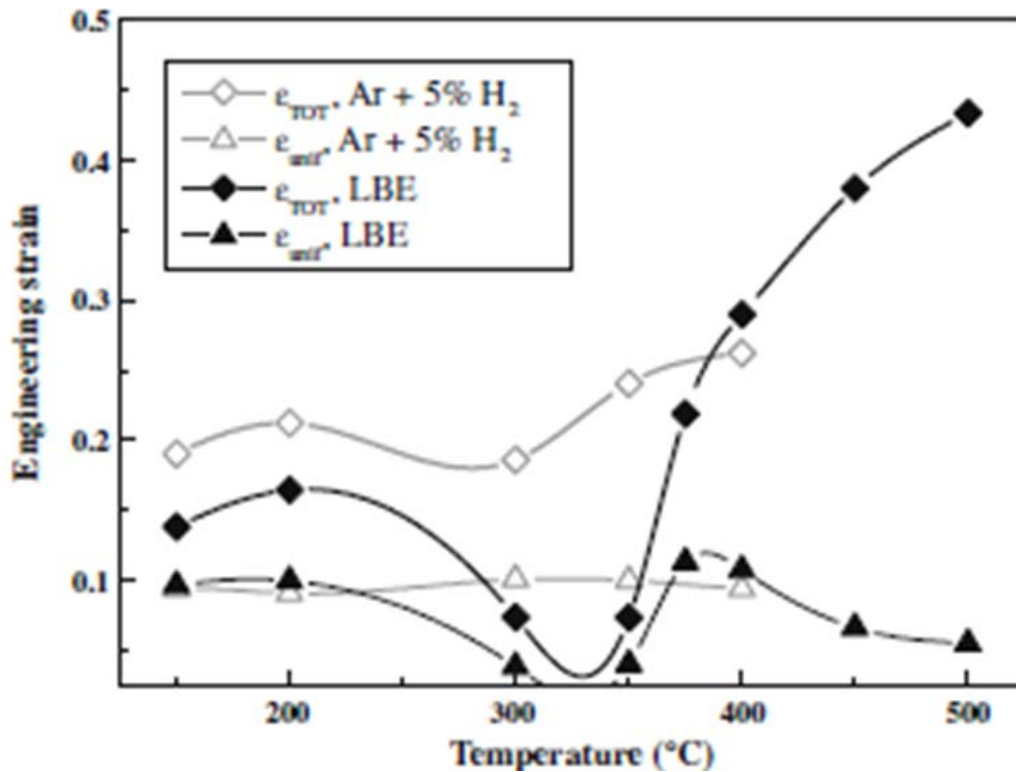


Figure 5.3 Ductility trough observed during liquid metal embrittlement of a silicon enriched steel in lead-bismuth eutectic from Van den Bosch [from 202]. Full black symbols represent results in lead-bismuth eutectic. Empty white symbols represent results in inert gas (Argon). Triangles represent uniform strain. Diamonds represent total strain.

The overall objective of this chapter is to determine the susceptibility of MA956 to LME. Based on the negligible role of yttrium with respect to corrosion and oxidation resistance and the similarity of passive protective Al_2O_3 or Cr_2O_3 layers, it is hypothesized that ODS steels will have a similar response mechanism as those seen in other FM steels although based on the mixed results of FM steels, it is not clear whether LME will or will not occur in ODS steels. This research will attempt to determine the LME response of MA956 via two methods: (1) long term exposure of a U-bend specimen in molten lead and (2) *in situ* tensile testing of MA956 in molten lead and LBE. Using the foundations of LME established by Nicholas and Old, experimental conditions will be established that are likely to promote LME. Additionally two control materials including a low alloy steel (1018 steel) and a stainless steel (SS316) will be utilized in an attempt to validate the experimental process.

B. EXPERIMENTAL PROCEDURE

U-bend specimens of MA956 were prepared for extended exposure in molten lead (Figure 5.4). The MA956 used was the same composition as used throughout this research (Table 1.4). The geometry of the U-bend specimens was comparable to examples listed in ASTM G30-97, Standard Practice for Making and Using U-Bend Stress-Corrosion Test Specimens [204]. Using annotation from ASTM G30-97 the geometry of the U-bend specimens was: L=127 mm (total length), M=101 mm (distance between bolt holes), W=19 mm (width), T=1.55 mm (thickness), D=9.59 mm (bolt hole diameter), X=25 mm (length of specimen arms once bent), Y=27.16 mm (distance between specimen arms once bent), R=12 mm (radius once bent), and $\alpha=1.57$ radians (angle of specimen arms once bent). The U-bend specimen was bolt loaded (Figure 5.4b) consistent with recommendations in ASTM G30-97. The compression of the U-bends (Figure 5.4b compared to Figure 5.4a) is elastic, i.e. removing the compressive force of the bolt causes the U-bend to return to its original geometry. Therefore no plastic deformation of the MA956 occurs during this process, and thus, if LME requires plastic deformation as stated by Nicholas and Old, the U-bend exposure alone may be insufficient to determine susceptibility to LME.

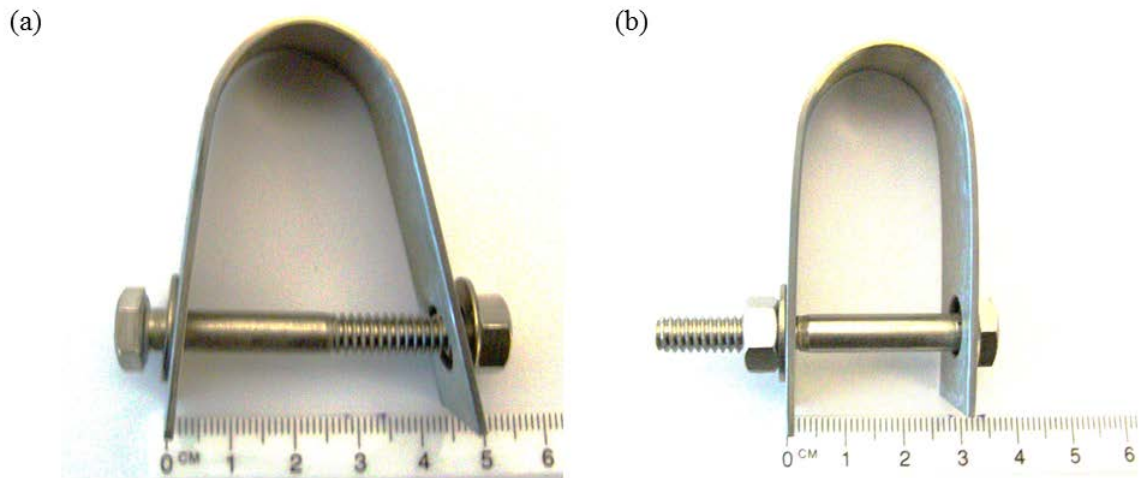


Figure 5.4 MA956 U-bend specimens in (a) unloaded condition and (b) fully loaded condition.

Consistent with ASTM G30-97, exact values of applied stress were not calculated although using similar finite element modeling as done in Chapter IV, the equivalent stress distribution within the U-bend specimen upon loading is shown in Figure 5.5. Finite element modeling of the U-bend specimen was achieved by modeling the U-bend in its relaxed position (Figure 5.4a), applying a restraint on the washer associated with the bolt head (left hand side of Figure 5.4a), and finally applying a normal force on the washer associated with the nut (right hand side of Figure 5.4b). The compression force was increased in the model until horizontal distance between the arms of the U-bend was equal to the measured distance of the actual compressed specimen (Figure 5.4b). This application of restraint and force is shown in Appendix D. The depiction of stress in Figure 5.5 is considered accurate and shows the alloy close to its yield point (88% of yield) when fully loaded. Figure 5.5 also shows the expected distribution of stress: highest stress at the outer edges of the bend and low stress on the flat portions of the specimen.

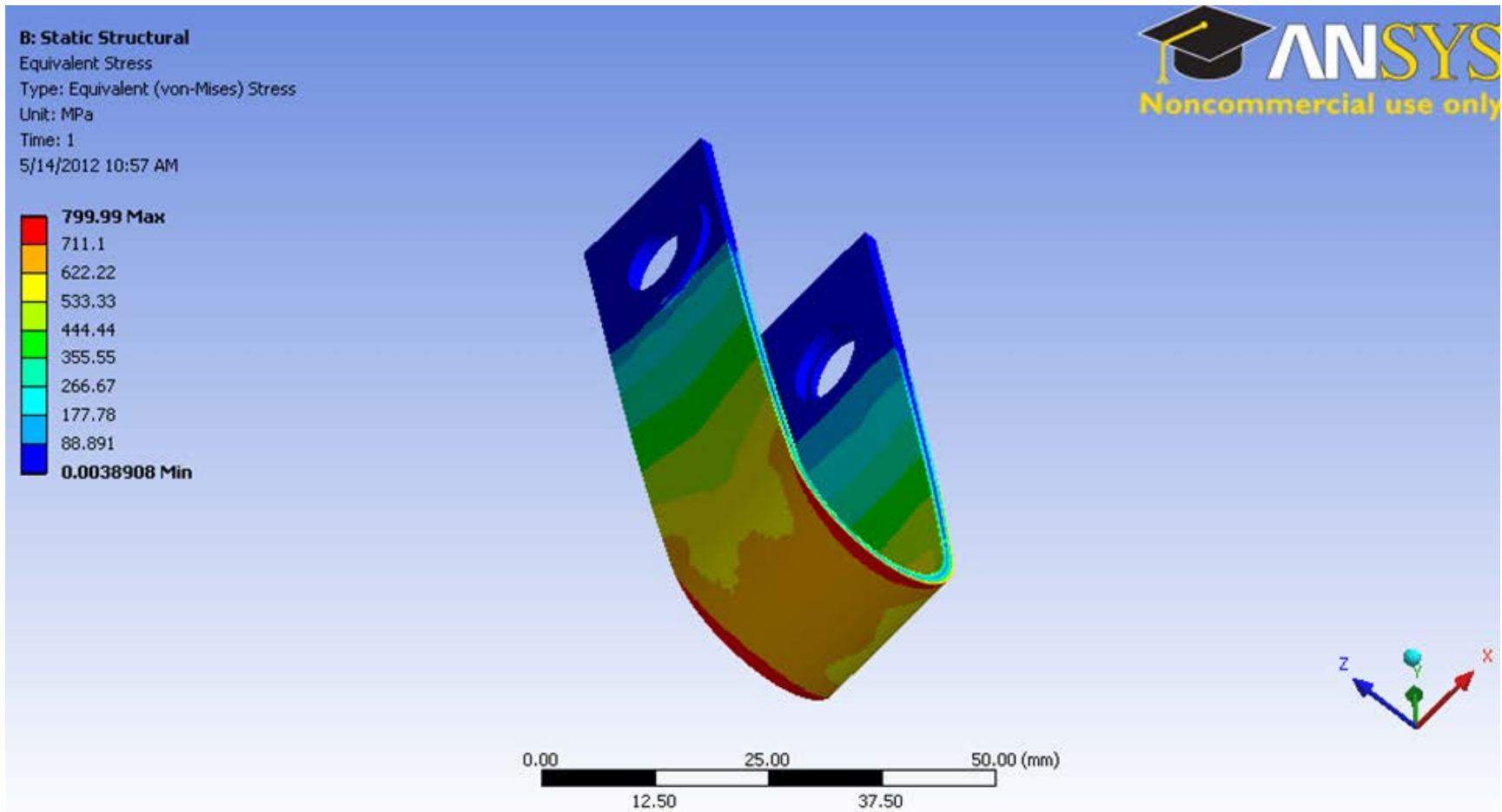


Figure 5.5 Equivalent stress distribution in U-bend specimens.

U-bend specimens were fully submerged in 2.8 kg of 99.9% pure Pb for 300 hours at 350°C (662°F) in a melting pot specifically designed for molten lead (Figure 5.6). The lead used was initially in solid shot form (<2 mm in diameter) prior to melting. The melting pot used had a thermal capacity of 1000 W and contained a ceramic crucible of sufficient capacity to contain two U-bend specimens fully submerged in molten lead. The melting pot was operated in a fume hood and was covered during normal operation. The operating temperature of 350°C was chosen based on the ductility troughs previously discussed for typical embrittler to metal couples (the melting temperature of lead is 327.5°C.) Oxygen was not controlled or measured during the exposure; however, the solubility of oxygen in lead at this temperature is less than 0.1 appm (Figure 5.7). The solubility of oxygen in lead, LBE, and bismuth is shown in Figure 5.7 from Zhang [195].

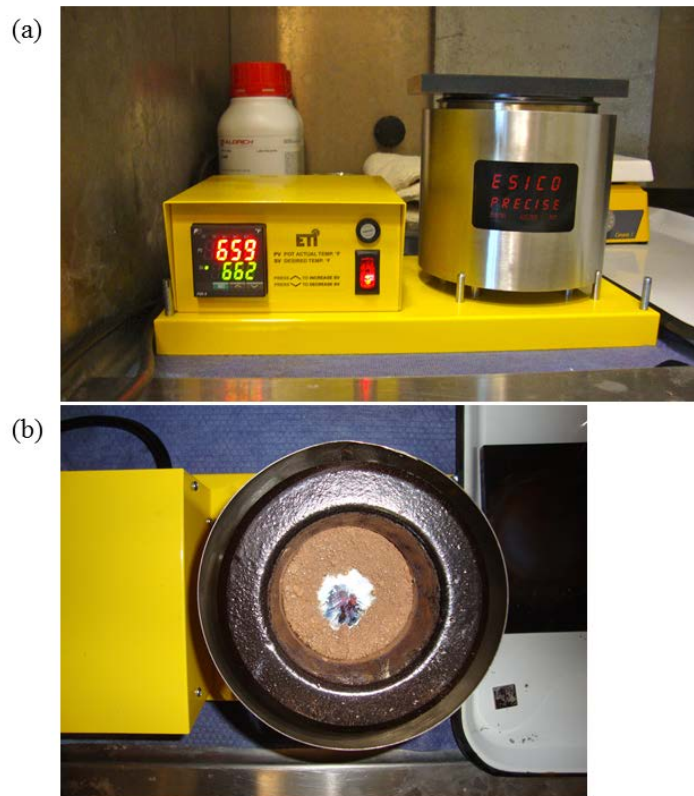


Figure 5.6 (a) Melting pot used for liquid lead exposure of U-bend specimens and (b) top view of melting pot showing thin layer of lead oxide (brown) on top of pure molten lead (silver). In (b) the lead oxide has been manually moved to reveal the pure molten lead layer beneath.

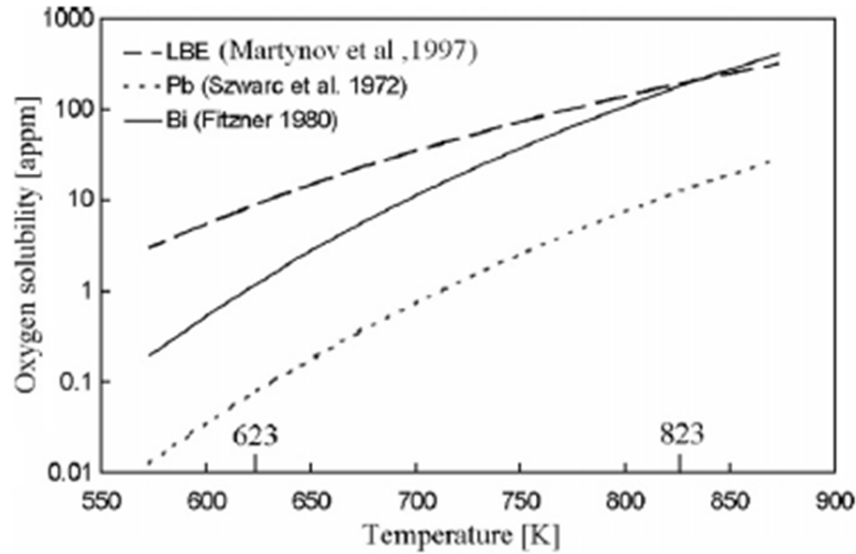


Figure 5.7 Oxygen solubility in lead, LBE, and bismuth from Zhang [from 195].

A thin layer of lead oxide formed on the surface of the lead melt in the melting pot. Beneath this layer pure molten lead was present (Figure 5.6b). The exact nature of the lead oxide was not determined and was not considered significant since the U-bend specimens were submerged below this layer. Two U-bend specimens were exposed in the molten lead. One was a smooth specimen (Figure 5.4b). The second specimen included a 1 mm deep machined notch in the outer edge at the apex of the curve. This notch was selected to help induce a LME response if the alloy was susceptible.

After exposure to molten lead, the MA956 U-bend specimens were cleaned in a nitric acid solution, sectioned, mounted in epoxy, and metallographically prepared with SiC papers for microscopy and EDS analysis. A thin (3 nm) layer of platinum was sputter coated on top of the epoxy mounted sample to allow for SEM analysis. EDS analysis was conducted at 20 keV and was only used for line scans across the metal to embrittler interface of the exposed U-bend specimens. EDS line scans included analysis of energies for Al-K (1.486 keV), Pb-M (2.342), Bi-M (2.419), Cr-K (5.414 keV), Fe-K (6.403 keV), Pb-L (10.550), and Bi-L (10.837). ZAF corrections for atomic number (Z), x-ray absorption (A), and x-ray fluorescence (F) were applied by the EDAX Genesis software package as discussed in Chapter III.

The methods used to evaluate LME by slow strain rate testing (SSRT) are established in ASTM G129-00, Standard Practice for Slow Strain Rate Testing to Evaluate the Susceptibility of Metallic Materials to Environmentally Assisted Cracking, and follow the principles previously discussed by Nicholas and Old [159]. The fundamental principle relies on the evaluation of a change of ductility (measured by strain at failure) from testing in a non-susceptible environment (normally air or an inert gas) and a potentially susceptible environment (the embrittler). ASTM G129-00 assumes the susceptibility is unknown and gives guidelines for the following key experimental variables: (1) strain rate, (2) embrittler volume to exposed specimen surface area, and (3) sample preparation. ASTM G129-00 recommends a constant extension rate test (CERT) with strain rates from 10^{-4} sec^{-1} to 10^{-7} sec^{-1} with a test cell size such that a solution volume to exposed specimen surface area is not less than 30 mL/cm^2 . ASTM G129-00 specifically notes that miniature tensile specimens are normally used and standard specimen machining, degreasing, and cleaning are required. Machine limitations prevented meeting some but not all ASTM G129-00 specifications. Based on initial testing, the minimum cross head speed of the INSTRON 4507 was determined to be 0.1 mm/min which for the long tensile geometry (Figure 4.1c) corresponded to a strain rate of $2.78 \times 10^{-5} \text{ sec}^{-1}$. This value was within the ASTM guidelines, and based on previous research that reported LME response was independent of strain rate, this value of strain rate was considered satisfactory [155, 156]. The embrittler volume to exposed specimen surface area is a function of the specimen and containment vessel geometry. For the experimental setup in this research the limiting component was the diameter of the furnace (assuming a fixed specimen size). Preventing the containment vessel from contacting the inside of the furnace during tensile extension was considered critical and therefore a minimum separation of 1.5 cm between the inner wall of the furnace and the outer wall of containment vessel was established. With these geometric limitations the maximum embrittler volume to exposed specimen surface area was 7.4 mL/cm^2 which was substantially less than the 30 mL/cm^2 recommended by ASTM G129-00. The longer tensile geometry (Figure 4.1c) was selected primarily to achieve a lower strain rate and although this longer geometry allows for a larger volume containment vessel both terms

in the embrittler volume to exposed specimen surface ratio scale with height of the containment vessel, and thus this larger geometry offers no improvement in the embrittler volume to exposed specimen surface ratio. A summary of the conditions recommended by ASTM G129-00 and values used in this research is presented in Table 5.1.

Table 5.1 Summary of conditions used for liquid metal embrittlement experiments.

Parameter	ASTM G129-00 recommendation	Value used in this research	Comment
Cross head speed (mm/min)	0.00015 to 0.15	0.1	ASTM G129-00 gives a nominal cross head speed, but the real consideration is strain rate which is a function of cross head speed and specimen geometry. The 0.1 mm/min value used in this research is the minimum speed of the load frame used.
Strain rate (sec ⁻¹)	10 ⁻⁷ to 10 ⁻⁴	2.78x10 ⁻⁵	With the long tensile geometry (Figure 4.1c) a strain rate within the recommended limits was achieved; however, other research has shown that LME response is independent of strain rate.
Embrittler volume to exposed specimen surface area (ml/cm ²)	30	7.4	The low value used in this research was the maximum amount achievable given the geometry of the available load frame and furnace setup.
Temperature (°C)	-	328 Pb, 150 LBE	ASTM G129-00 does not address temperature since temperature is application specific. Research herein uses temperatures that are close to the melting temperature of the embrittler.

A specific lead containment apparatus was designed and built that could function with the already established specimen geometry and tensile setup discussed in Chapter IV and was capable of meeting most of the requirements in ASTM G129-00. Two different version of this apparatus were designed and built to match the two different lengths of tensile specimens (Figure 5.8 with comparable tensile specimens from Figure 4.1b and c). The two setups are identical with the only difference being the height of the containment device corresponding to the different tensile lengths. The lead containment apparatus was made from SS316 due to its known compatibility with molten lead and was specifically designed to fit with the tensile grips and furnace discussed in Chapter IV. The lead containment apparatus did not interfere with the conduct of the tensile test and did fully contain the embrittler during melting and during operation at temperatures above the melting temperature of the embrittler. The lead containment apparatus contains a machined slot through which the sample was inserted as well as a thin SS316 gasket that helps prevent leakage from the apparatus. An example drawing showing assembly of the lead containment apparatus is shown in Figure 5.9. Full SolidWorks drawings used to manufacture the components of the lead containment apparatus are contained in Appendix E.

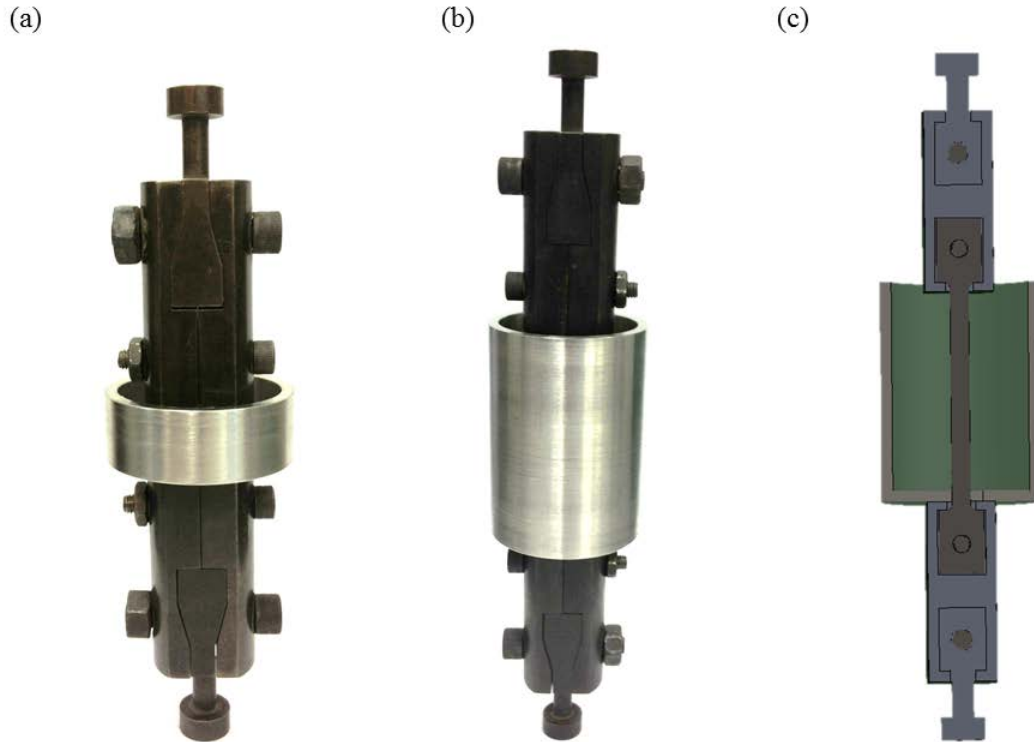


Figure 5.8 (a) Photograph of lead containment apparatus for standard miniature geometry (Figure 4.1b), (b) Photograph of lead containment apparatus for long miniature geometry (Figure 4.1c), and (c) cutaway SolidWorks model of the lead containment apparatus.

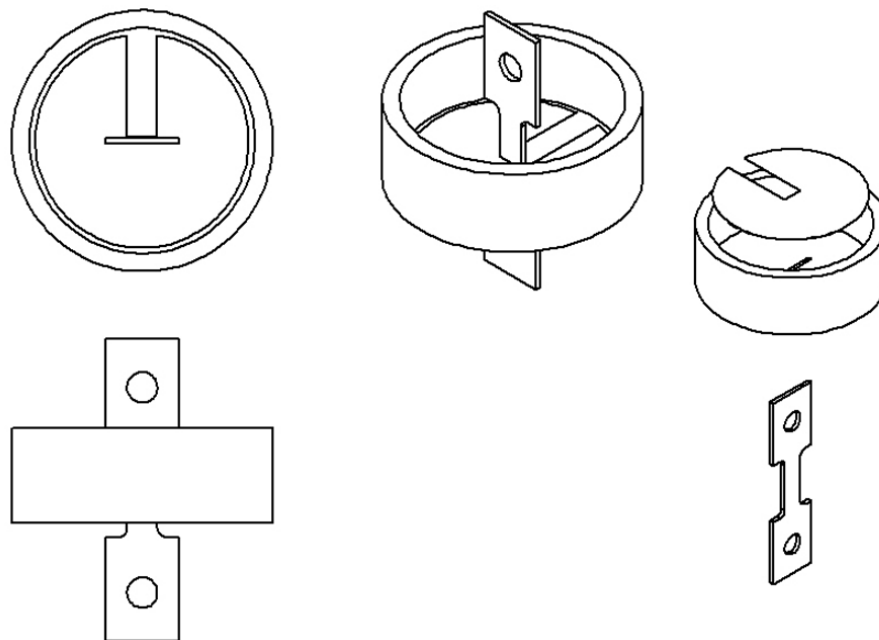


Figure 5.9 SolidWorks images showing assembly of the lead containment apparatus.

The lead containment apparatus when combined with the specimen and tensile grips functions identically to the tensile arrangement discussed in detail in Chapter IV and thus only differences in this setup will be summarized in this chapter. The lead containment apparatus was filled with embrittler in solid form prior to insertion within the INSTRON load frame (Figure 5.10a) and subsequently raised to operating temperature in a similar manner as discussed in Chapter IV causing the embrittler to melt (Figure 5.10b). The fine particle size of the solid embrittler (<2 mm shot for 99.9% pure lead and 1–12 mm for 99.999% pure bismuth) and melting that occurred during heat-up to operating temperature was considered satisfactory to establish the intimate contact deemed necessary for a LME response. Similar to the U-bend exposure experimental setup, oxygen concentration was not controlled or measured; however, using Figure 5.7, the solubility of oxygen in lead at the temperature used ($328^{\circ}\text{C}/601^{\circ}\text{K}$) is less than 0.1 appm and the solubility of oxygen in LBE at the temperature used ($150^{\circ}\text{C}/423^{\circ}\text{K}$) is less than 5 appm. During initial trial runs a lead oxide layer was noted to form on the surface of the lead melt (Figure 5.10b). To minimize the oxidation of the embrittler, final experiments included a layer of graphite powder on top of the solid embrittler. This process was effective at minimizing the visible oxidation of the embrittler although an oxygen saturated environment must still be assumed since no other active oxygen mitigation mechanism or measurement process was in place.

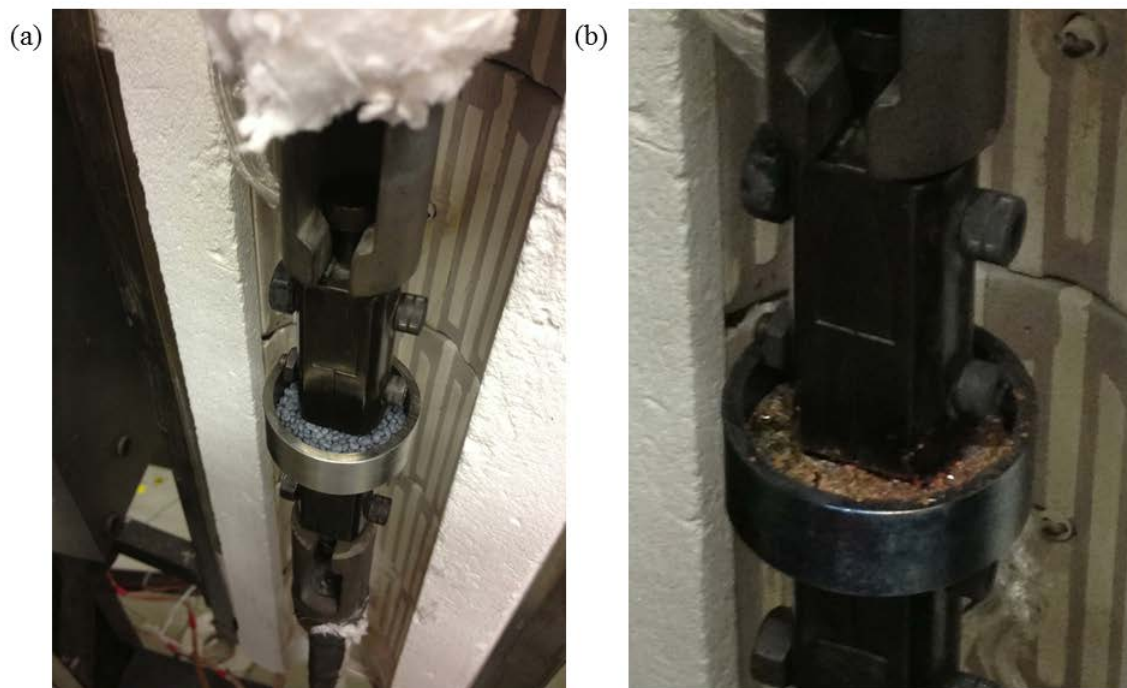


Figure 5.10 Liquid metal embrittlement tensile testing setup (a) at room temperature with solid form embrittler (lead as shown) and (b) at operating temperature (328°C) with molten embrittler (lead with lead oxide layer as shown).

Tensile testing with conditions as stated in Table 5.1 was conducted on three different alloys, 1018 steel, SS316, and MA956, in a potentially embrittling environment (lead and LBE) as well as air. The only experimental variables changed for each test were the alloy and the environment. The LME susceptibility of each these alloys was not known although the compositional variety between the alloys was intentionally selected with the intent to establish experimental controls for a material thought to be susceptible (1018 steel) and a material thought to be immune (SS316) to LME. The basis for the hypothesized susceptibility of 1018 steel and immunity of SS316 came from research by Shunk that showed that pure lead was an embrittler to commercially pure (vice laboratory pure) iron as well as some other selected metals but was not an embrittler to alloyed steels [157]. The additional technique of removing machine compliance, as discussed in Chapter IV was not applied to data in this chapter since the environmentally established conditions could potentially change the machine compliance determined previously.

Since the only desired experimentally determined variable was strain at failure, yield and ultimate tensile strengths were not calculated.

Fractography of specimens was conducted identically to that done in Chapter IV and is restated here. Fractography of specimens was conducted using a Zeiss Neon 40 field emission SEM operating at 20 keV. High magnification imaging was conducted with no specimen tilt and at a low working distance (5 mm) to allow for improved focus. High magnification imaging was taken in representative areas of the fracture surface near the center of the specimen. Low magnification imaging was conducted with specimens tilted at 10 degrees and at a larger working distance (approximately 15 mm) to allow for full visualization of the fractured sample.

C. RESULTS

1. U-bend Results

Neither the normal nor the notched U-bend specimens fractured after exposure to molten lead at 350°C for 300 hours (Figure 5.11). After removal from the lead melting pot, the lead (and lead oxide) quickly solidified on the MA956 specimen (Figure 5.11b and c). This lead layer readily spalled off the sample and no visible cracking or damage was visible on any exterior surface of the U-bend specimens. Based on this initial observation, lead was hypothesized to not have penetrated into the specimen. This hypothesis was reinforced by EDS analysis that confirmed an outer layer of aluminum (Al_2O_3) and inner layer of chromium (Cr_2O_3) on the edges of the specimen (Figure 5.12). EDS analysis also showed no discernible lead penetration past these protective oxide layers into the metal microstructure. No visible cracking was found during SEM analysis of cross sections of the U-bend specimens.

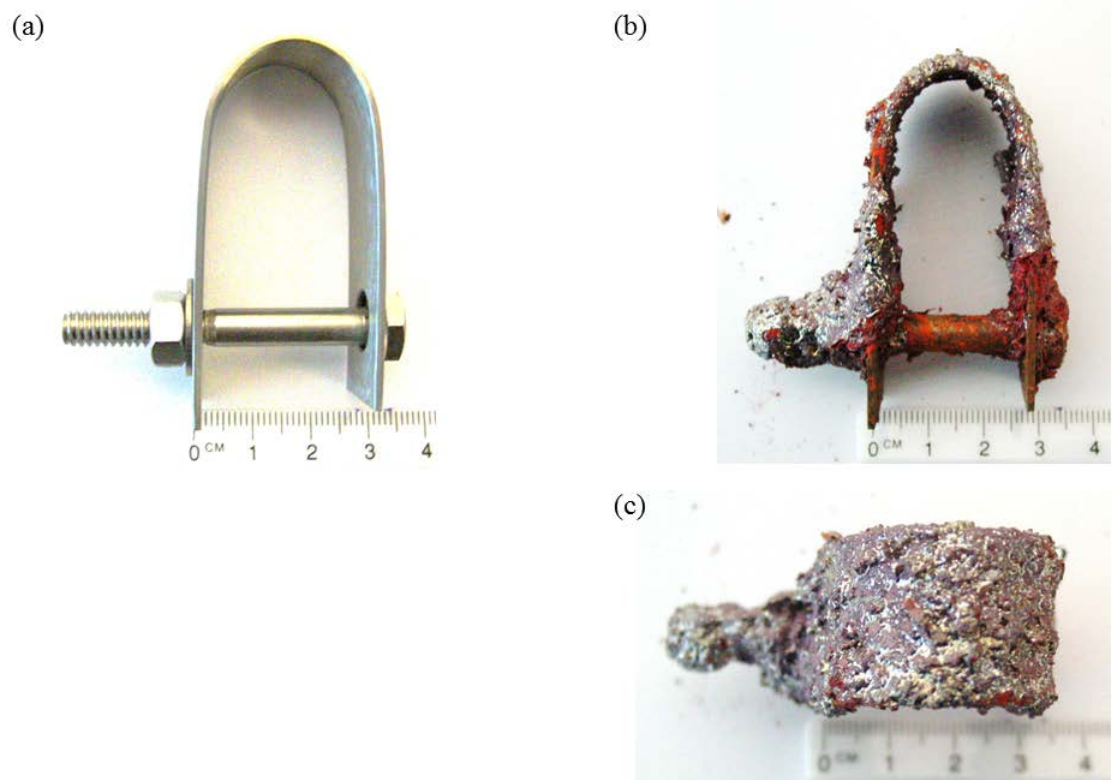


Figure 5.11 Photographs of MA956 U-bend specimens (a) loaded prior to lead exposure, and (b), (c) after exposure to lead at 350°C for 300 hours. The lead (silver) and lead oxide (red) was allowed to solidify on the specimen after exposure but readily spalled off the sample.

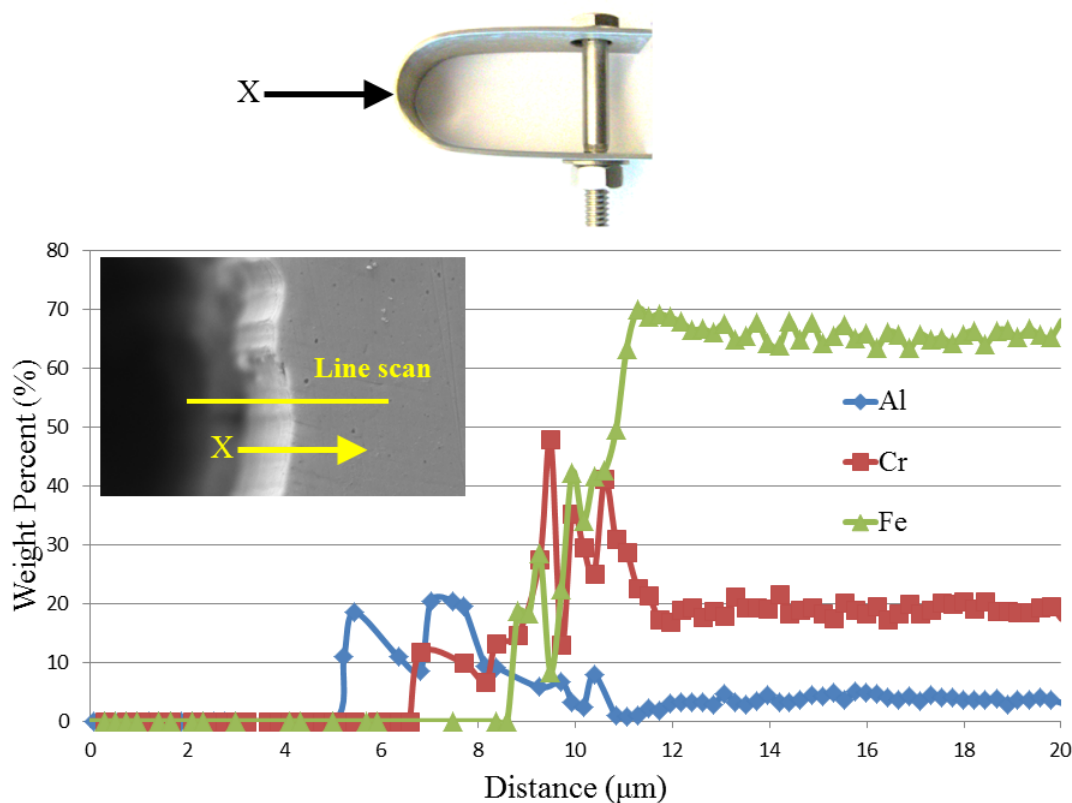


Figure 5.12 Energy dispersive spectroscopy analysis of oxide layers on the outer surface of the MA956 U-bend specimens after exposure to molten lead. The line scan correlates to measurement across the cross section of the specimen at the apex of curvature of the specimen as shown.

2. Slow Strain Rate Testing Results

SSRT of all alloys tested (1018 steel, SS316, and MA956) showed no significant change in tensile behavior from testing in air to the different molten metal environments. In each case, the stress strain curve of the control environment (air) was similar in characteristics to the test environment (lead at 328°C and LBE at 150°C). Specifically the response in the elastic region was similar in each case, the specimen reached an ultimate tensile point in both environments, and the total elongation in each case was comparable between the control environment and the molten metal environment. Several tensile results showed load drops that could be interpreted as serrated flow or upper and lower yield points. While these are possible interpretations, the load frame was observed

to occasionally experience load drops that were believed to be due to operation at the minimum cross head speed for the load frame rather than indicative of a true specimen response. Because of this, small load drops in individual stress strain curves were not utilized as experimental indicators of LME. The determination of LME susceptibility was based on changes in strain at failure and the general characteristics of the stress strain curves as discussed in ASTM G129-00. Fractography showed consistent failure for each alloy in the test environment as compared to the control environment.

Carbon steels heated in the range of 230°C to 370°C are known to show a notable reduction in failure strain due to blue brittleness (in reference to the coloration of the steel due to oxide layer formation in this range of temperature). Blue brittleness is discussed in detail in textbooks [168], and, although the onset or occurrence of blue brittleness is not an area of emphasis for this research, the reduction in ductility from blue brittleness is a concern since the techniques in this research rely on a reduction in ductility as a key indicator for LME. Even steels with low carbon concentrations such as the SS316 and MA956 used in this research may be susceptible to blue brittleness and thus measuring a reduction in ductility due to LME is problematic for an alloy that may already be low in ductility due to other phenomena. The occurrence of blue brittleness, including the reduction in total elongation and namesake coloration, are shown in Figure 5.13 for SS316 and the geometry used in this chapter.



Figure 5.13 Blue brittleness of SS316 for the geometries used in this chapter. Both samples were fractured under identical conditions in air except: (a) 328°C and (b) room temperature.

a. 1018 Steel Results

Tensile results for 1018 steel, both in air and lead at 328°C, showed a consistent response in the elastic and plastic regions, achievement of an ultimate tensile point, and a similar strain at failure (Figure 5.14). The variance in strain to failure was attributed to normal variance in measurements of strain at failure as discussed in Chapter IV and other references [187, 189, 190]. Fractography of 1018 steel specimens was consistent with tensile results and show comparable reduction in cross sectional area and failure across the specimen (Figure 5.15). Based on these results, 1018 steel was determined to not be susceptible to LME in lead under the conditions tested.

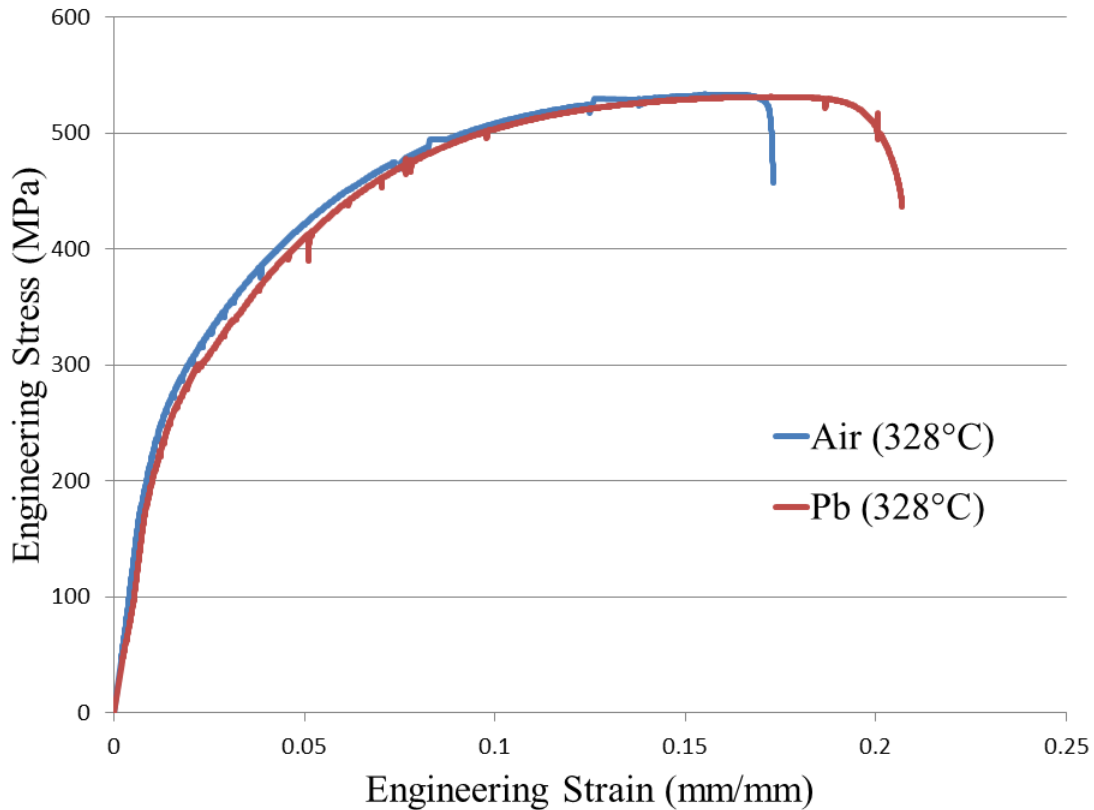


Figure 5.14 Engineering stress-strain curves for 1018 steel in air and molten lead both at 328°C showing similar tensile behavior.

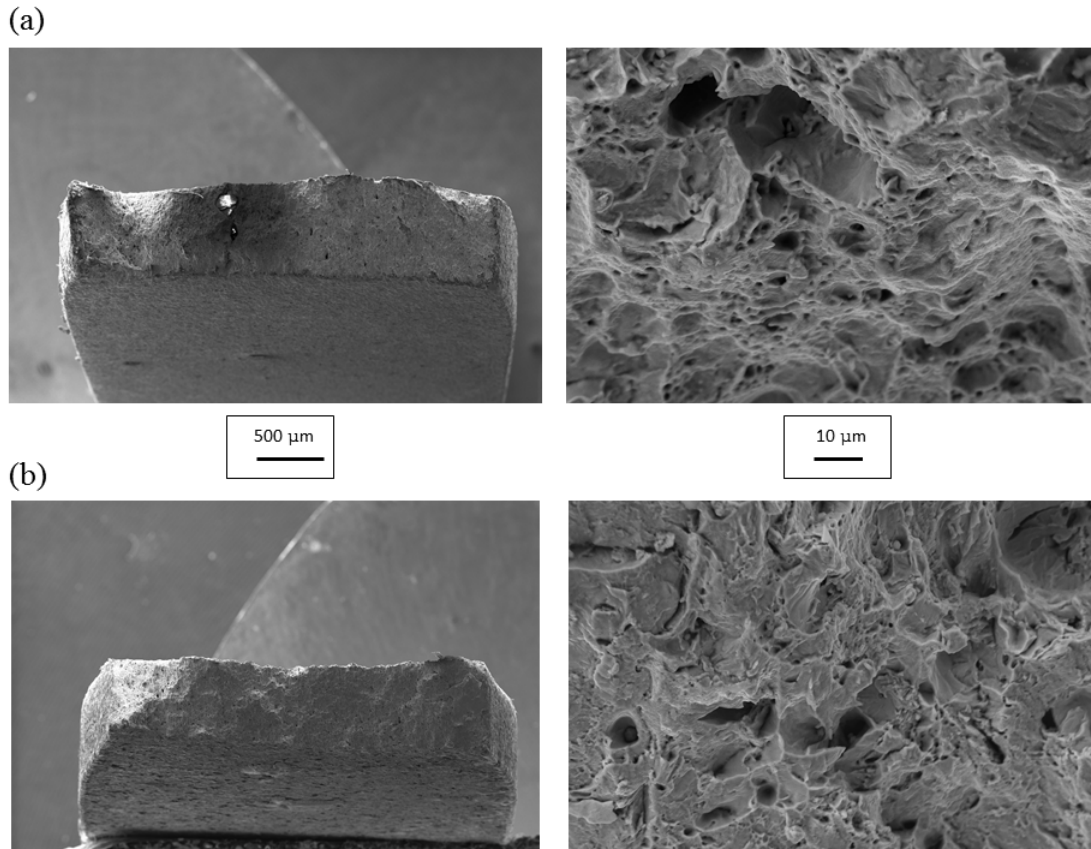


Figure 5.15 Fractography of 1018 steel fractured in (a) air at 328°C and (b) molten lead at 328°C showing similar failure.

Similar to the results in lead, 1018 steel was determined to not be susceptible to LME in LBE for the conditions tested. Tensile results for 1018 steel both in air and LBE at 150°C showed a consistent response in the elastic and plastic regions, achievement of an ultimate tensile point, and a similar strain at failure (Figure 5.16). Fractography of 1018 steel specimens was consistent with tensile results and show comparable reduction in cross sectional area and a ductile failure surface with microvoid coalescence across the specimen (Figure 5.17). No direct comparison is intended between 1018 steel tensile results (Figures 5.14 and 5.16) and the related fractography results (Figures 5.15 and 5.17) across the different environments since testing temperature was also changed, but comparison of the control environments alone (air at varying temperature) in the respective Figures does show the expected increase in ductility as temperature alone is increased. For this reason, the results of Figure 5.14 and

5.16 are intentionally left on two separate plots vice plotting them all on a single plot. This approach highlights the importance of strain at failure for a given metal to embrittle couple without including a varying effect of temperature. This same approach is used for subsequent alloys SS316 and MA956.

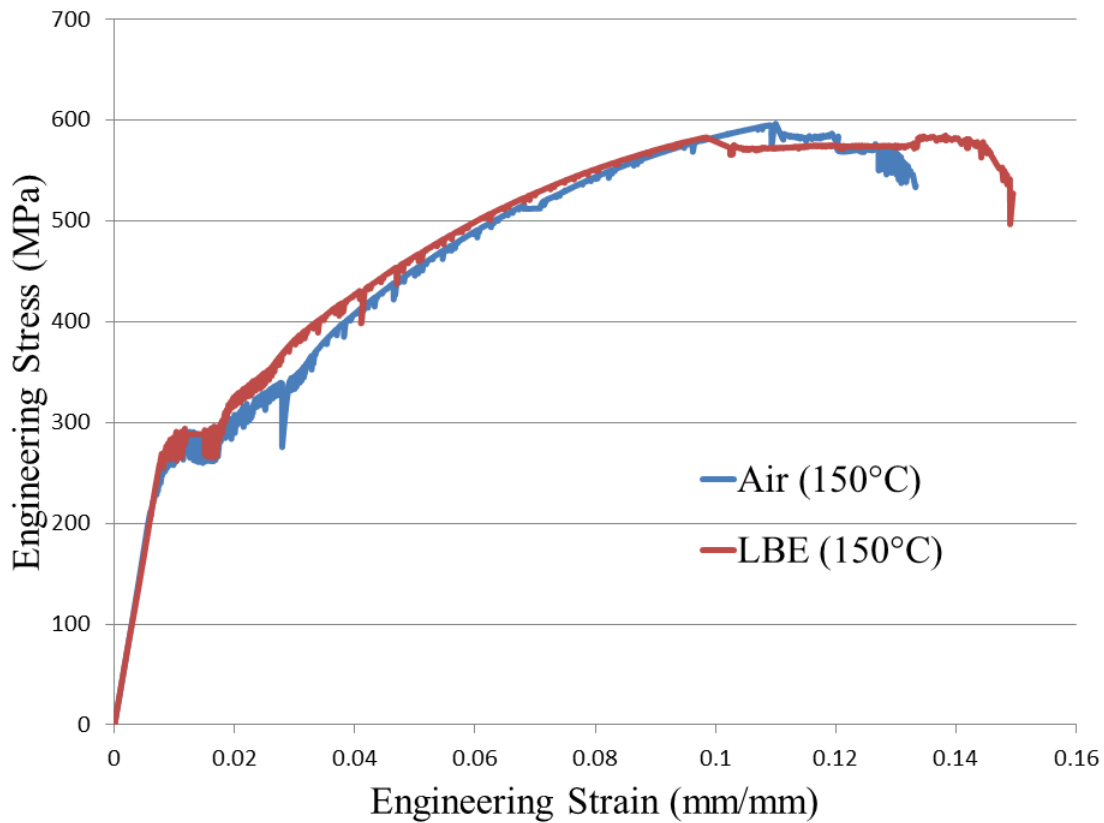


Figure 5.16 Engineering stress-strain curves for 1018 steel in air and molten LBE both at 150°C showing similar tensile behavior.

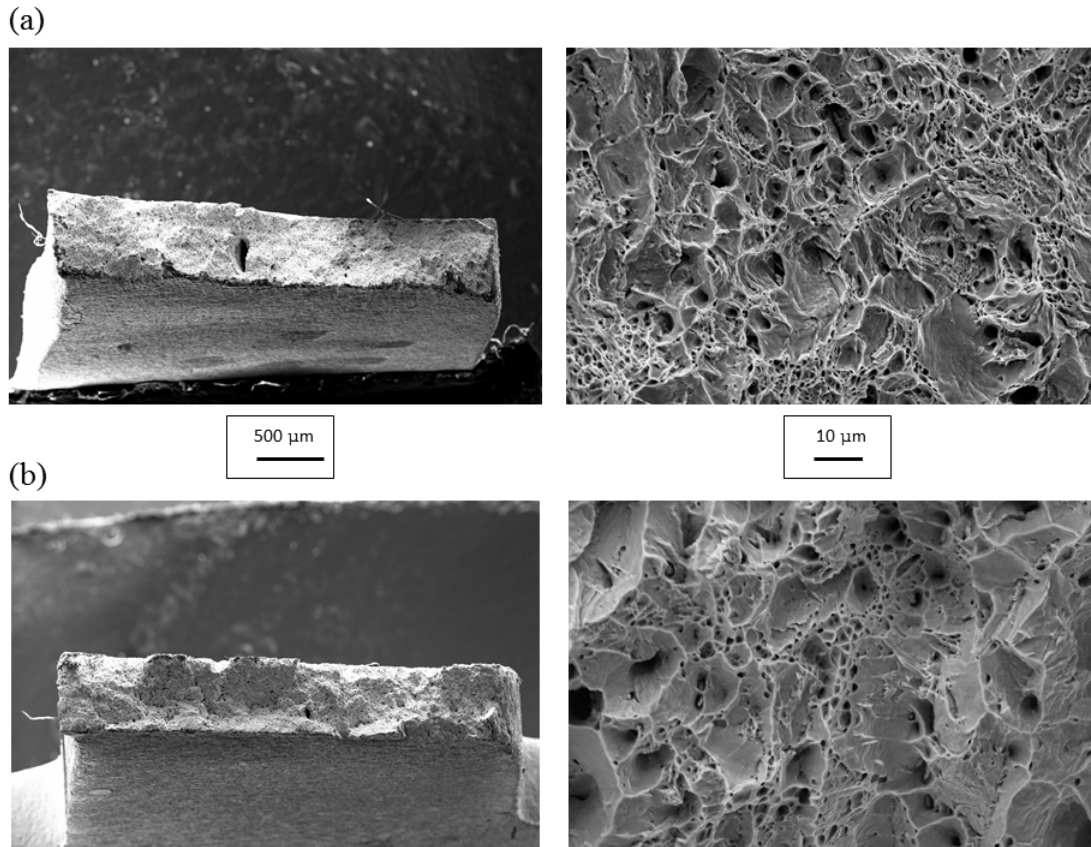


Figure 5.17 Fractography of 1018 steel fractured in (a) air at 150°C and (b) molten lead-bismuth eutectic at 150°C showing similar failure.

b. SS316 Results

Tensile results for SS316 in air and lead both at 328°C showed a consistent response in the elastic and plastic regions, achievement of an ultimate tensile point, and a similar strain at failure (Figure 5.18). Fractography of SS316 specimens was consistent with tensile results and show comparable reduction in cross sectional area and ductile failure across the specimen (Figure 5.19). Based on these results, SS316 was determined to not be susceptible to LME in lead under the tested conditions.

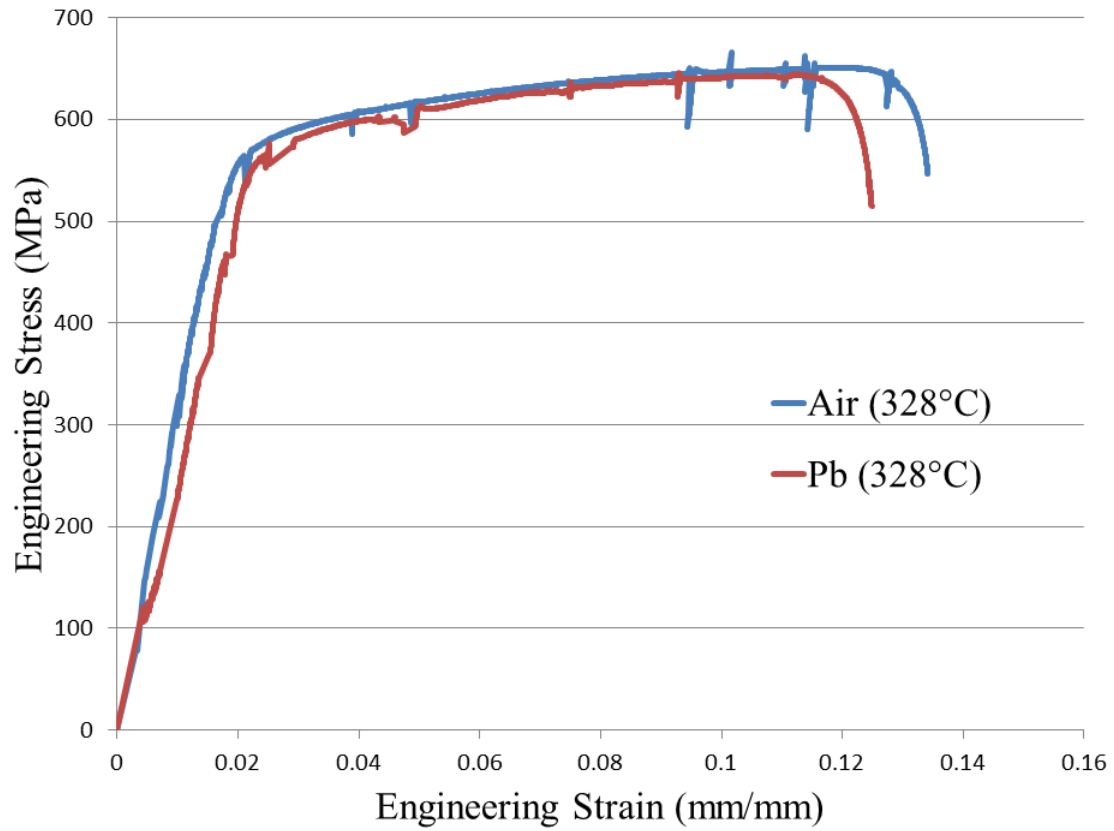


Figure 5.18 Engineering stress-strain curves for SS316 in air and molten lead both at 328°C showing similar tensile behavior.

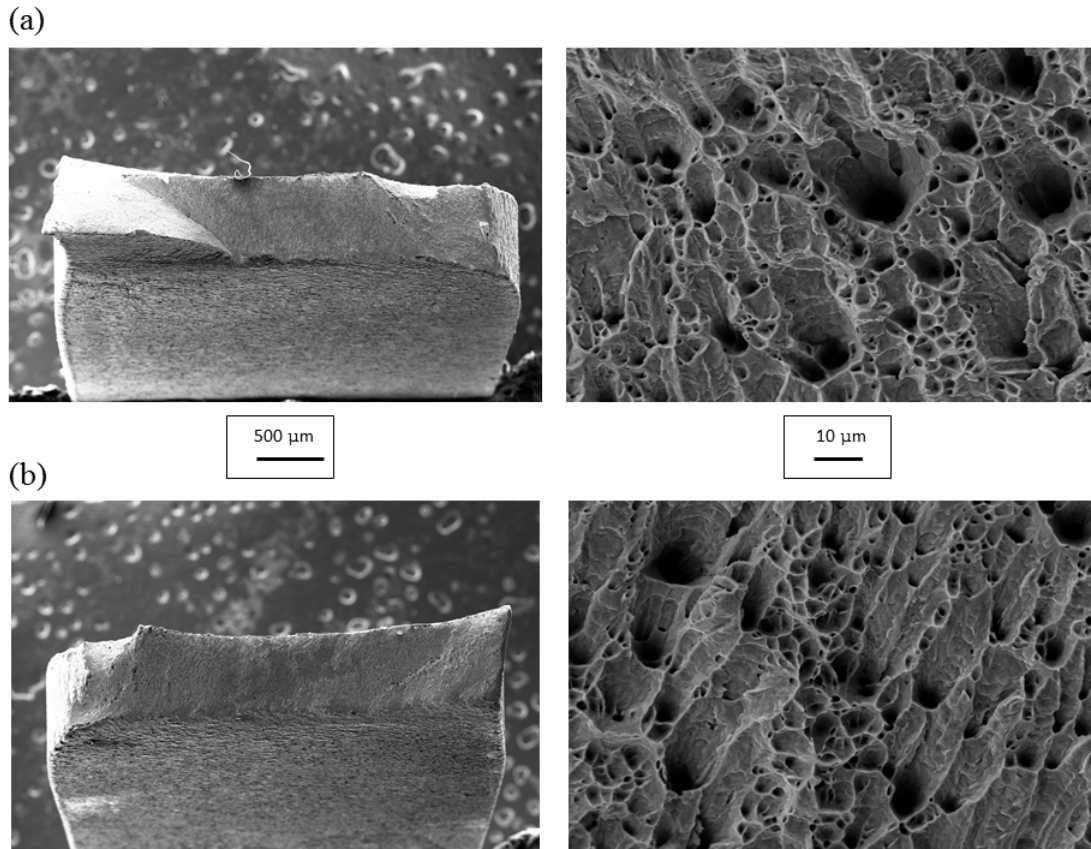


Figure 5.19 Fractography of SS316 fractured in (a) air at 328°C and (b) molten lead at 328°C showing similar failure.

Similar to the results in lead, SS316 was determined to not be susceptible to LME in LBE for the conditions tested. Tensile results for SS316 in air and LBE both at 150°C showed a consistent response in the elastic and plastic regions, achievement of an ultimate tensile point, and a similar strain at failure (Figure 5.20). Fractography of SS316 specimens was consistent with tensile results and show comparable reduction in cross sectional area and a ductile failure surface with microvoid coalescence across the specimen (Figure 5.21).

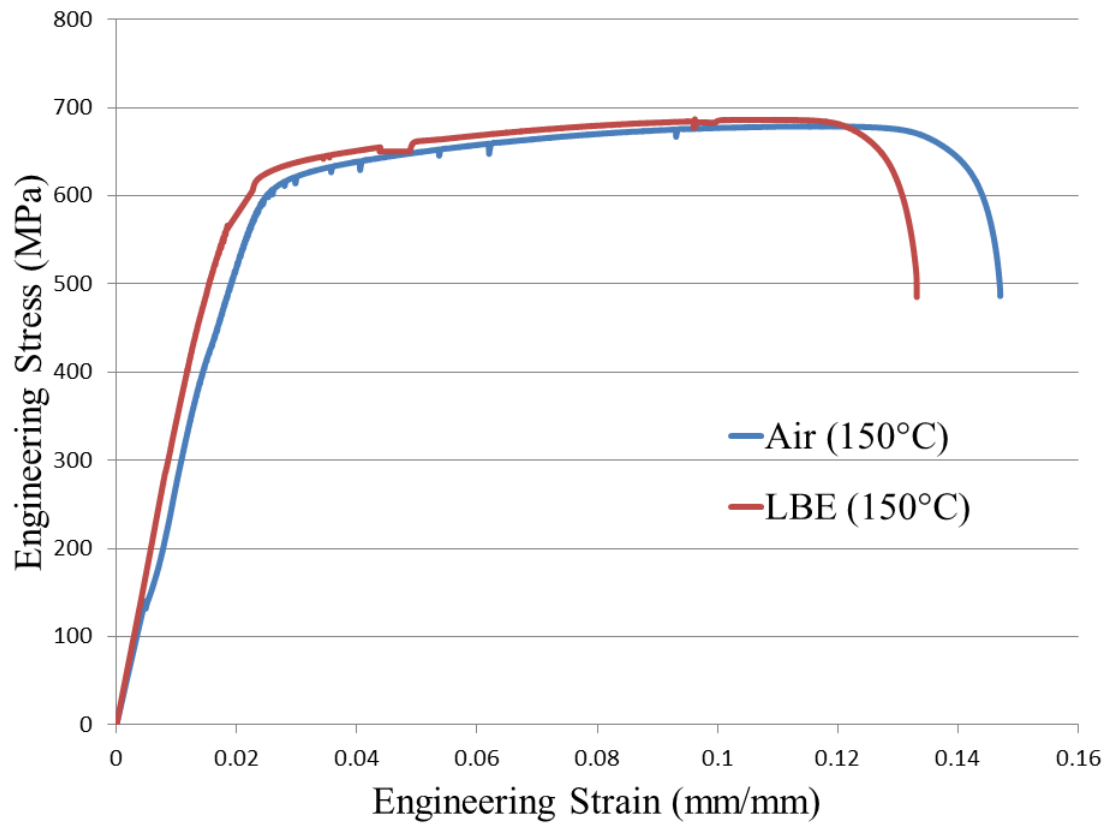


Figure 5.20 Engineering stress-strain curves for SS316 in air and molten LBE both at 150°C showing similar tensile behavior.

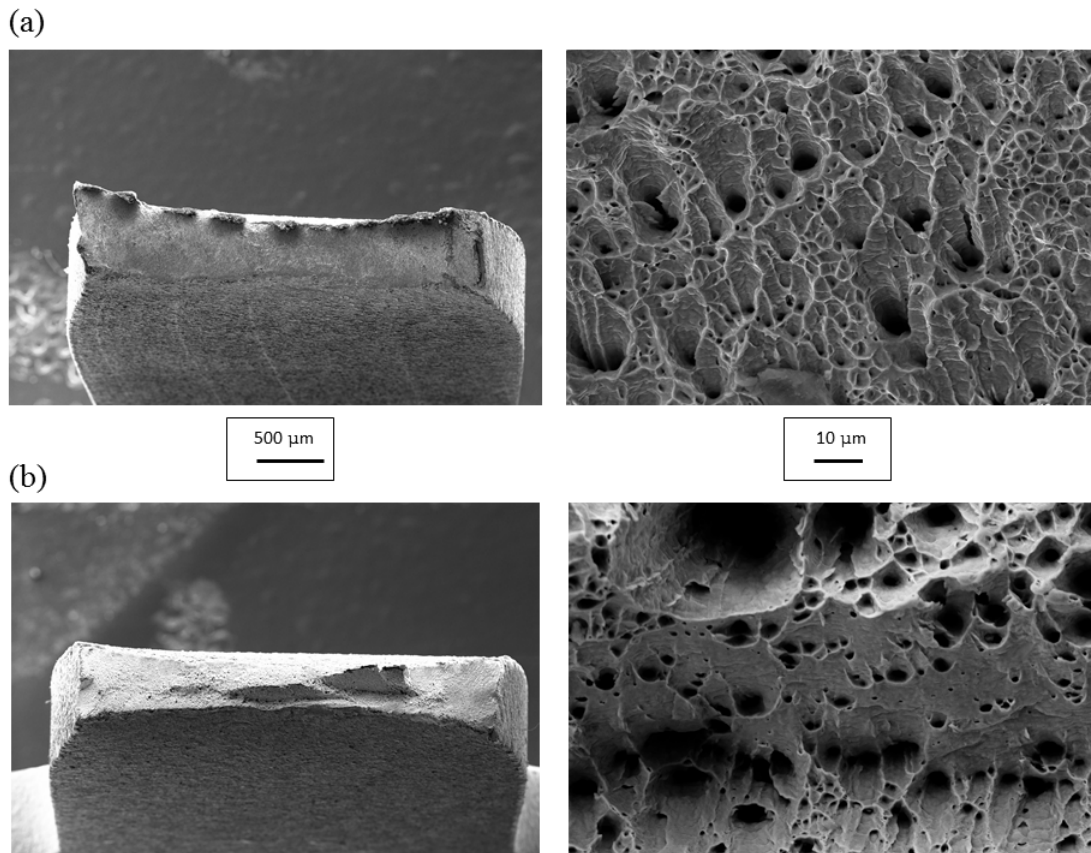


Figure 5.21 Fractography of SS316 fractured in (a) air at 150°C and (b) molten LBE at 150°C showing similar failure.

c. MA956 Results

Tensile results for MA956 in air and lead both at 328°C showed a consistent response in the elastic and plastic regions, achievement of an ultimate tensile point, and a similar strain at failure (Figure 5.22). Fractography of MA956 specimens was consistent with tensile results and show comparable reduction in cross sectional area and ductile failure across the specimen (Figure 5.23). Based on these results, MA956 was determined to not be susceptible to LME in lead under the tested conditions.

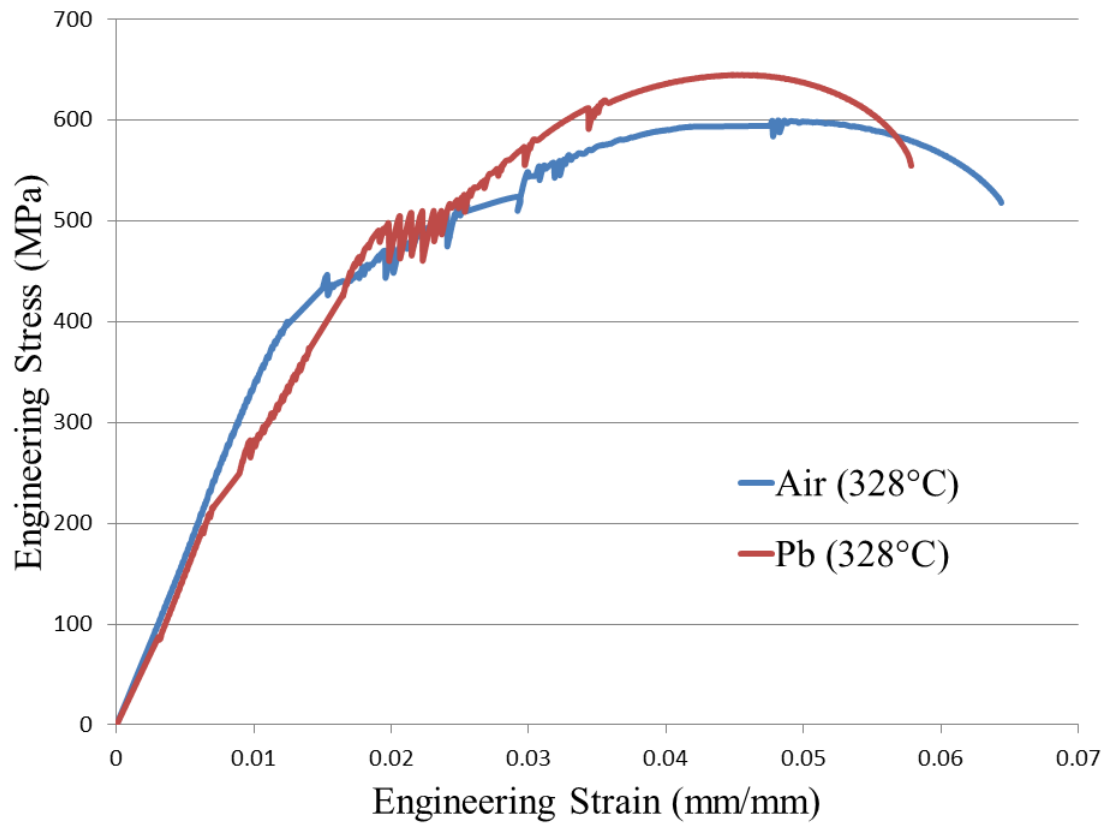


Figure 5.22 Engineering stress-strain curves for MA956 in air and molten lead both at 328°C showing similar tensile behavior.

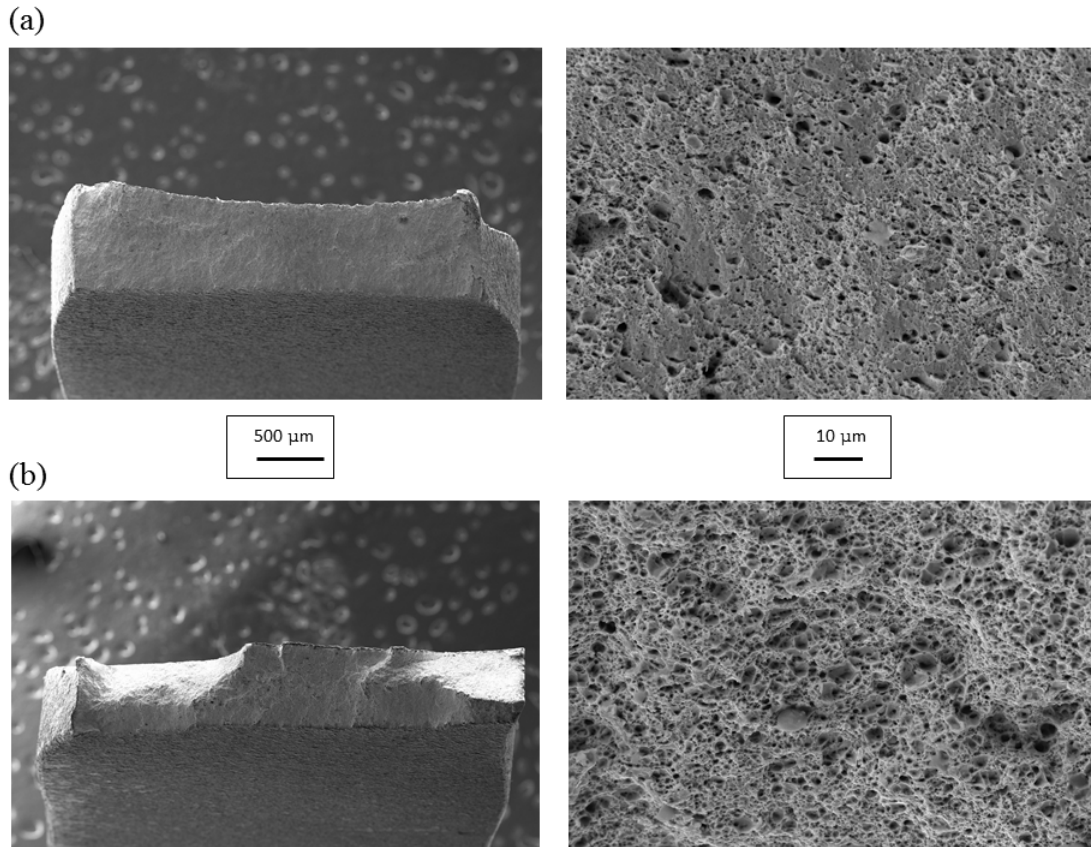


Figure 5.23 Fractography of MA956 fractured in (a) air at 328°C and (b) molten lead at 328°C showing similar failure.

Similar to the results in lead, MA956 was determined to not be susceptible to LME in LBE for the conditions tested. Tensile results for MA956 in air and LBE both at 150°C showed a consistent response in the elastic and plastic regions, achievement of an ultimate tensile point, and a similar strain at failure (Figure 5.24). Fractography of MA956 specimens was consistent with tensile results and show comparable reduction in cross sectional area and a ductile failure surface with microvoid coalescence across the specimen (Figure 5.25).

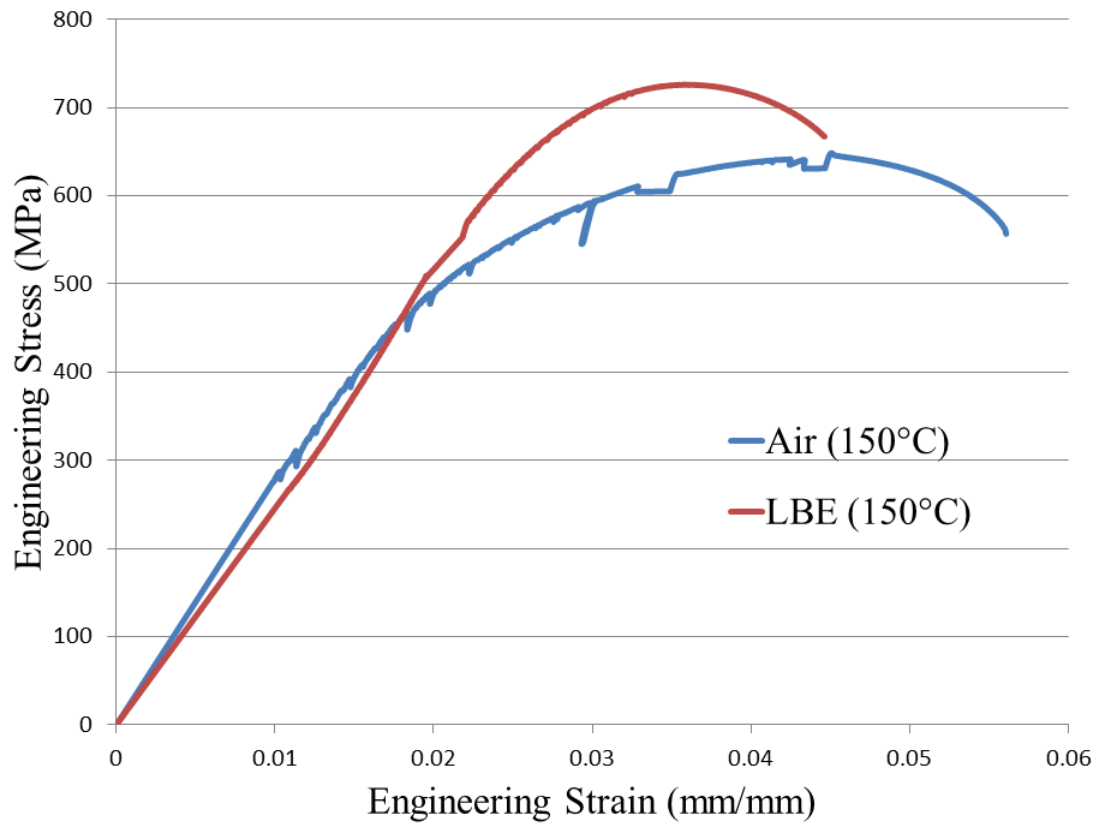


Figure 5.24 Engineering stress-strain curves for MA956 in air and molten LBE both at 150°C showing similar tensile behavior.

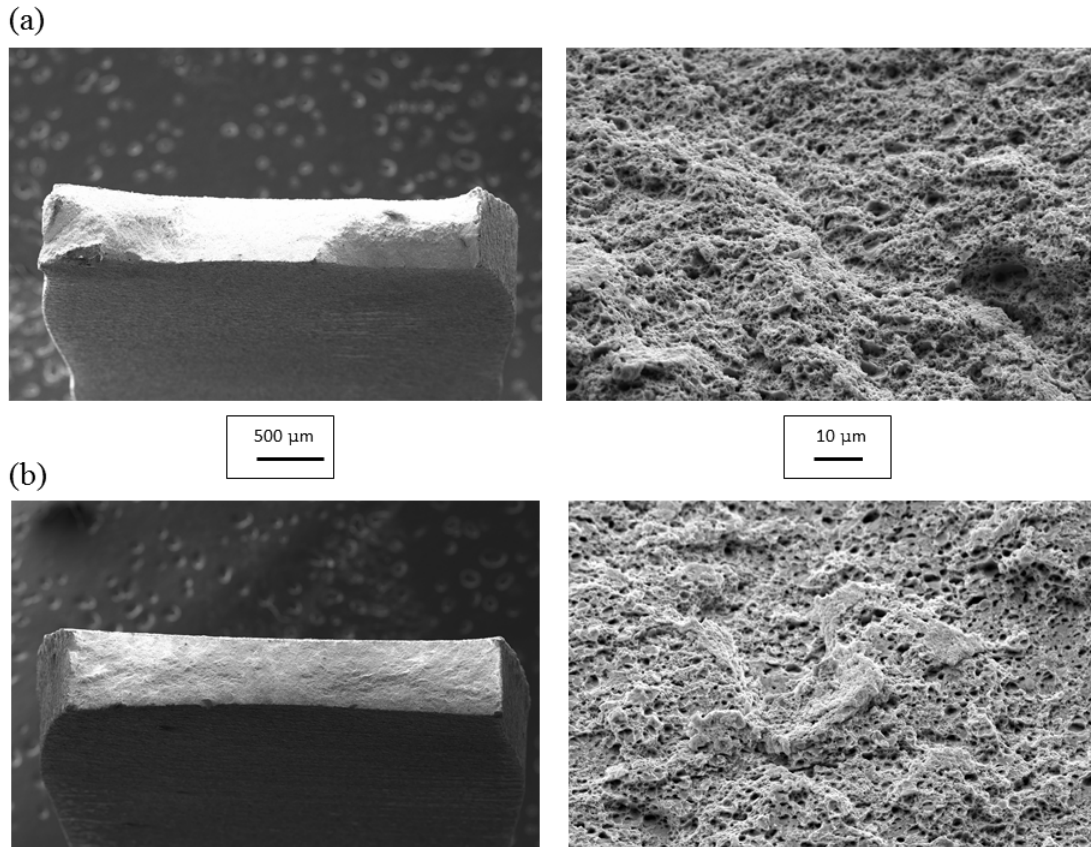


Figure 5.25 Fractography of MA956 fractured in (a) air at 150°C and (b) molten lead-bismuth eutectic at 150°C showing similar failure.

The MA956 tensile response in both lead (Figure 5.22) and LBE (Figure 5.24) showed an increase in ultimate tensile strength and an apparent increase in overall strain hardening above the respective air environments that could not be explained. There was insufficient MA956 material available to make additional specimens to determine if this was a true specimen response, and no basis could be found to hypothesize an increase in strength or strain hardening in either molten environment; however, since in both environments an ultimate tensile point was reached and comparable strain at failures were measured, MA956 was concluded to not be susceptible to LME under the conditions measured.

D. DISCUSSION

The MA956 U-bend exposure experiment suggests immunity to LME and overall resistance to attack from both molten lead and LBE. In this experiment prolonged exposure of MA956 under tension equal to approximately 88% of the alloy's yield point (Figure 5.5) resulted in no failure or cracking of the specimen (Figure 5.11). Although only qualitatively in nature, this approach is consistent with ASTM guidance for SCC determination of U-bend specimens [204]. This immunity is attributed to the protective oxide layers confirmed to exist on MA956 (Figure 5.12). The aluminum and chromium oxide layers found on MA956 in this research are consistent with oxide layers found on MA956 in other general corrosion research in a variety of environments including air [111] and LBE [52, 53, 90]. As proposed by Nicholas [155] and Old [156], these oxide layers are equally effective at preventing LME as long as they remain intact.

In order to test the effectiveness of the oxide layers through failure, MA956 was tested in tension in both molten lead and LBE consistent with guidance in ASTM G129-00 [159]. Guidance on SSRT to determine EAC as well as previous research on LME suggests that LME will cause a reduction in strain at failure, change in failure mode observable by change in the fracture surface, and, in some cases, failure to reach an ultimate tensile point during extension. Results from tensile elongation experiments on MA956 in both molten lead and LBE showed a negligible reduction in strain at failure (Figures 5.22 and 5.24) and overall similar tensile behavior suggesting immunity to LME at the conditions tested. Fracture surfaces were consistent in both environments compared to the control environment (Figure 5.23 and 5.25), suggesting no change in failure mode. These results suggest that the protective oxide layers remained long enough to prevent LME.

In order to attempt to validate the experimental process used in this research, testing was accomplished on two additional alloys, a low alloy steel (1018 steel) and a stainless steel (SS316) in addition to MA956. It was hypothesized that 1018 steel would be susceptible to LME while SS316 would not; however, neither of these alloys demonstrated a LME response in either environment. While not negating the results on MA956, the inability to positively demonstrate an LME response raises questions

regarding the validity of the experimental setup allowing several possible conclusions. Table 5.2 lists a summary of potential conclusions with regard to the LME susceptibility of alloys tested in this research.

Table 5.2 Summary of conclusions with regard to liquid metal embrittlement susceptibility of alloys tested in this research.

Conclusion	Comment	Recommendation
Alloy is not susceptible to LME.	Other research suggests that LME will result in: (1) reduction in strain at failure, (2) observable change in fracture surface, and (3) failure to reach an ultimate tensile point during extension.	With none of these conditions occurring, the alloy is considered immune to LME. The specific reason is the alloy and embrittler do not form an LME couple.
Test temperature does not support an LME response.	Research on LME strongly suggests a “ductility trough” that encompasses the melting temperature of the embrittler. The test temperature used was close to the melting temperature of the embrittler.	A wider range of temperatures would have to be tested, but is not likely to cause a change.
Test strain rate does not support an LME response.	Research on LME suggests that LME response is independent of strain rate. The strain rate used is within ASTM guidelines and was at the lower limit of the load frame and geometry used.	A lower strain rate will require a different experimental setup (a different load frame and/or larger specimen).
Metal and embrittler are not in intimate contact.	Melting of small solid embrittler (<12 mm diameter) was used as the mechanism to achieve intimate contact.	A more complex experimental setup would be required to achieve more intimate contact.
Insufficient embrittler exists to cause an LME response.	The embrittler to metal ratio used is below ASTM guidelines. The amount achieved was at the limit of the load frame setup for the given specimen size.	A different containment vessel to specimen would be required to increase this ratio (larger diameter containment vessel or thinner/narrower sample).
Oxygen concentration is affecting the susceptibility of LME.	The exact role of oxygen during LME is not known although other corrosion related phenomena are known to be heavily dependent on oxygen concentration. Since the concentration of oxygen was not actively controlled or measured during this experiment, the role of oxygen can neither be confirmed nor excluded.	Oxidation of Pb and LBE was limited by applying a thin layer of graphite over the embrittler, but the exact concentration of oxygen in the melt is unknown. Establishing an inert environment in the furnace or active measurement of oxygen within the furnace would be required to control oxygen as a variable.

E. CONCLUSIONS

MA956 is not susceptible to LME in oxygen-saturated molten lead or LBE for the tested conditions, most notably temperatures near the melting temperature of the potential embrittler, and, although the tested conditions are limited in range, they were selected as the most likely conditions to cause LME. When combined with previous research on general LME conditions, the following general conclusions can be drawn:

(1) Maintaining MA956 at less than its yield point will help ensure LME does not occur. No observable changes in the elastic region of any alloy tested occurred in molten lead or LBE and other research has established that dislocation motion is required for LME to occur.

(2) This research has shown negligible LME response near the melting temperature of lead and LBE. Operation above those temperatures, as would be expected in the majority potential applications for MA956 should only lessen the potential for LME.

THIS PAGE INTENTIONALLY LEFT BLANK

VI. CONCLUSIONS AND RELEVANCE OF THIS RESEARCH

The overall objective of this research was to evaluate friction stir welded MA956 as a suitable high temperature welded alloy for use in a variety of extreme coolant conditions. This was accomplished by completing three primary tasks: (1) determining the base metal microstructure and material properties of MA956 at various temperatures, (2) determining the friction stir welded microstructure and material properties at various temperatures, and (3) determining the susceptibility of MA956 to LME. From the results gathered from this research some overall conclusions can be drawn on the use of MA956 and ODS steels in general and the utility of FSW on ODS alloys. When applied to practical applications the relevance of these conclusions becomes evident. Additionally, the research herein has identified some areas that require additional research or consideration with regard to structural materials and joining mechanisms for high temperature applications.

A. CONCLUSIONS

The following conclusions were drawn with regard to MA956 and ODS steels in general:

- FG MA956 has significantly higher yield and ultimate tensile strength than CG MA956 that may make it a suitable alloy as a structural material in highly loaded applications. Grain boundary strengthening and oxide particle dispersion strengthening are the dominant strengthening mechanisms in ODS alloys and give these alloys superior strength compared to traditional FM steels (Chapter IV).

- Several previously undocumented material properties of MA956 were determined including values for Hall-Petch constants and strain hardening coefficients and exponents. Although initially undesirable for room temperature application due its low DBTT, MA956 has improved ductility at high temperature and may be better suited

for high temperature applications than room temperature applications. The low DBTT of MA956 and other ODS steels may require more defined operating parameter selections when transitioning between low and elevated temperatures (Chapter IV).

- MA956 is not susceptible to LME at the conditions tested which included operating temperatures at the melting point of the embrittler and moderate strain rates. The general conditions used were determined to previously cause LME in other metal to embrittler couples (Chapter V).

The following conclusions were drawn with regard to FSW of MA956 and ODS steels in general:

- FSW is capable of producing consolidated defect-free welds in MA956 and other ODS steels without the typical agglomeration of oxide particles and depletion areas seen in other fusion joining techniques. The parameter ratio of tool rotational speed to tool traverse speed defined here as HI is a simplistic but practical method to predict weld consolidation. The heat input during FSW might be roughly described by this ratio, but it cannot be used as an accurate measure of true heat input. Although higher heat input conditions will also form consolidated welds, the detrimental effects of high heat conditions suggest that welding conditions close to the minimum heat input required to consolidate welds will be more beneficial. Successful welding with lower tool rotational speeds is expected to require overall less manufacturing power and may lengthen tool life. Welding with higher traverse speeds will achieve welding in a shorter time period. The range of welding parameters analyzed gives manufacturers more flexibility in processing (Chapter II).

- FSW was found to cause the following generally detrimental effects on FG MA956: (1) grain coarsening resulting in reduction in strength and (2) oxide particle coarsening resulting in reduction in strength. FSW on MA956 also caused large gradients in grain size and hardness on the AS of the weld and although this was not found to be a specific failure location in tensile loading, other failure mechanisms (such

as potentially fatigue) that depend on or are exacerbated by grain boundaries may fail at this location; however all of these detrimental effects were determined to be a function of welding parameters, and thus each can be minimized by selection of welding conditions with lower heat input (Chapter II, III, and IV).

- FSW increased the ductility of FG MA956 and although the reduction in strength of MA956 was dramatic at low temperature (~60% retention of strength) the performance of FSW MA956 at high temperatures was improved over the low temperature conditions (~80% retention of strength at high temperature).

- Titanium nitride particles within MA956 were qualitatively unaffected by FSW. Although this had negligible effect and relevance in MA956, it may be important in other ODS steels that do not contain aluminum and thus form Y-Ti-O particles vice Y-Al-O particles. Such alloys already exist and initial evidence suggests that these alloys may not experience the same degree of particle coarsening as seen in this research; however, other research has shown that ODS alloys that do not contain aluminum have inferior corrosion and oxidation resistance, and thus this reduced corrosion resistance must be balanced against their potentially improved coarsening response.

B. RELEVANCE

The current literature on structural alloys for use in fusion or advanced fission reactors clearly indicates three classes of materials as leading contenders for structural materials within these reactors: (1) vanadium or other refractory metals, (2) SiC composites, and (3) ODS steels. There is currently insufficient manufacturing and operating experience with both vanadium alloys and SiC composites for them to be useful in near term applications; however, there is sufficient manufacturing capability and research on ODS steels for them to be of immediate consideration with the primary limitation being joining of ODS alloys. The work herein has expanded significantly on the knowledge base of FSW on ODS steels by establishing the processing, microstructure, and material property relationships following FSW on ODS steels. This research has shown that judicious selection of welding parameters can produce consolidate welds without sacrificing beneficial microstructure and material properties.

This research also gives a series of “knobs” most notably tool rotation rate and tool traverse rate that may be adjusted to produce desired microstructural properties. Taken with options already available during PM manufacture and post manufacture processing welded alloys may be created with specific end state grain structure and material property performance already in mind. A cartoon summary of the microstructural effects of FSW with varying input conditions on FG MA956 is shown in Figure 6.1. Similarly a cartoon summary of the material properties of a composite weld structure is shown in Figure 6.2.

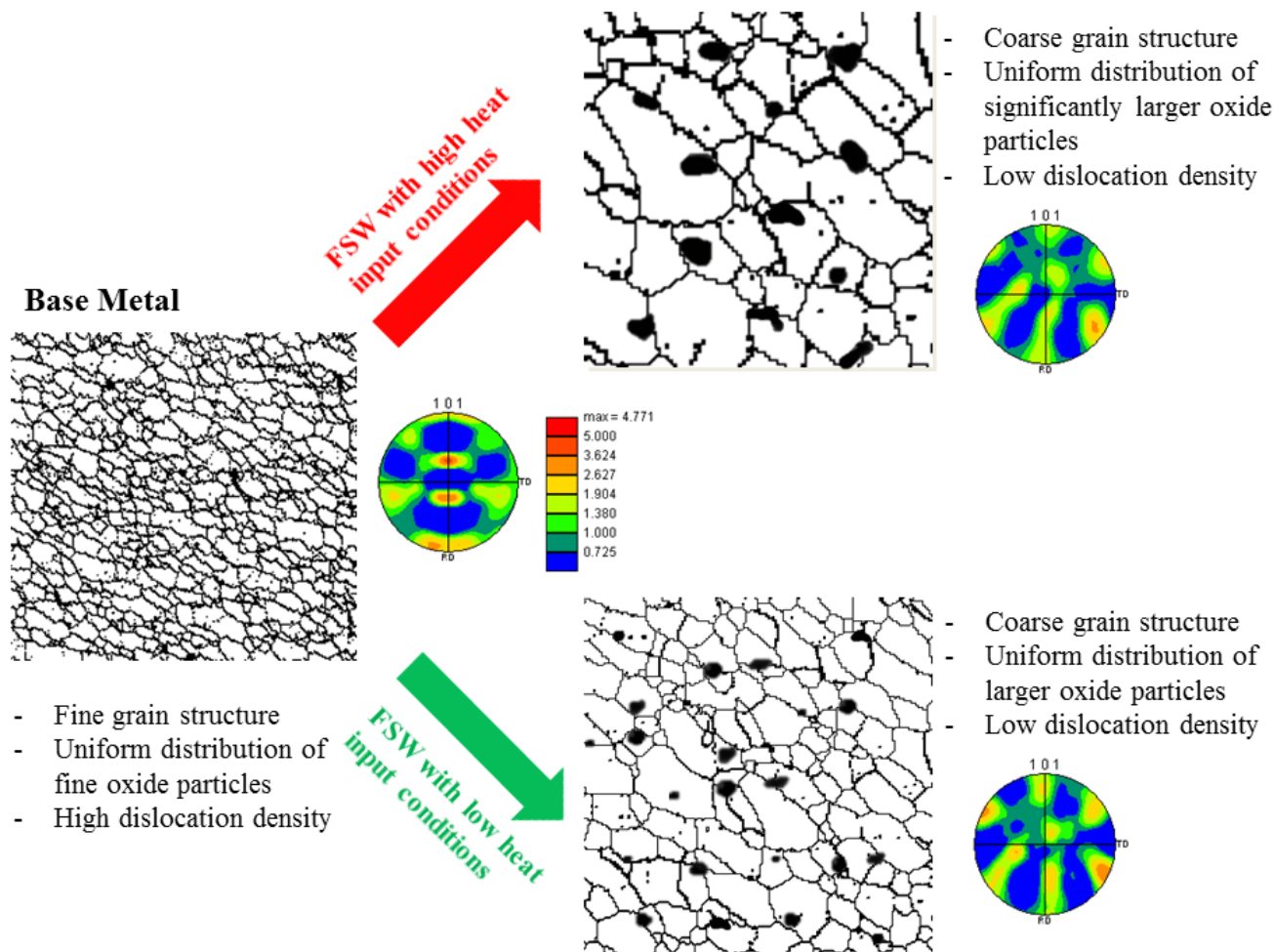


Figure 6.1 Simplified summary of microstructural effects of FSW on MA956 with a fine grain starting microstructure.

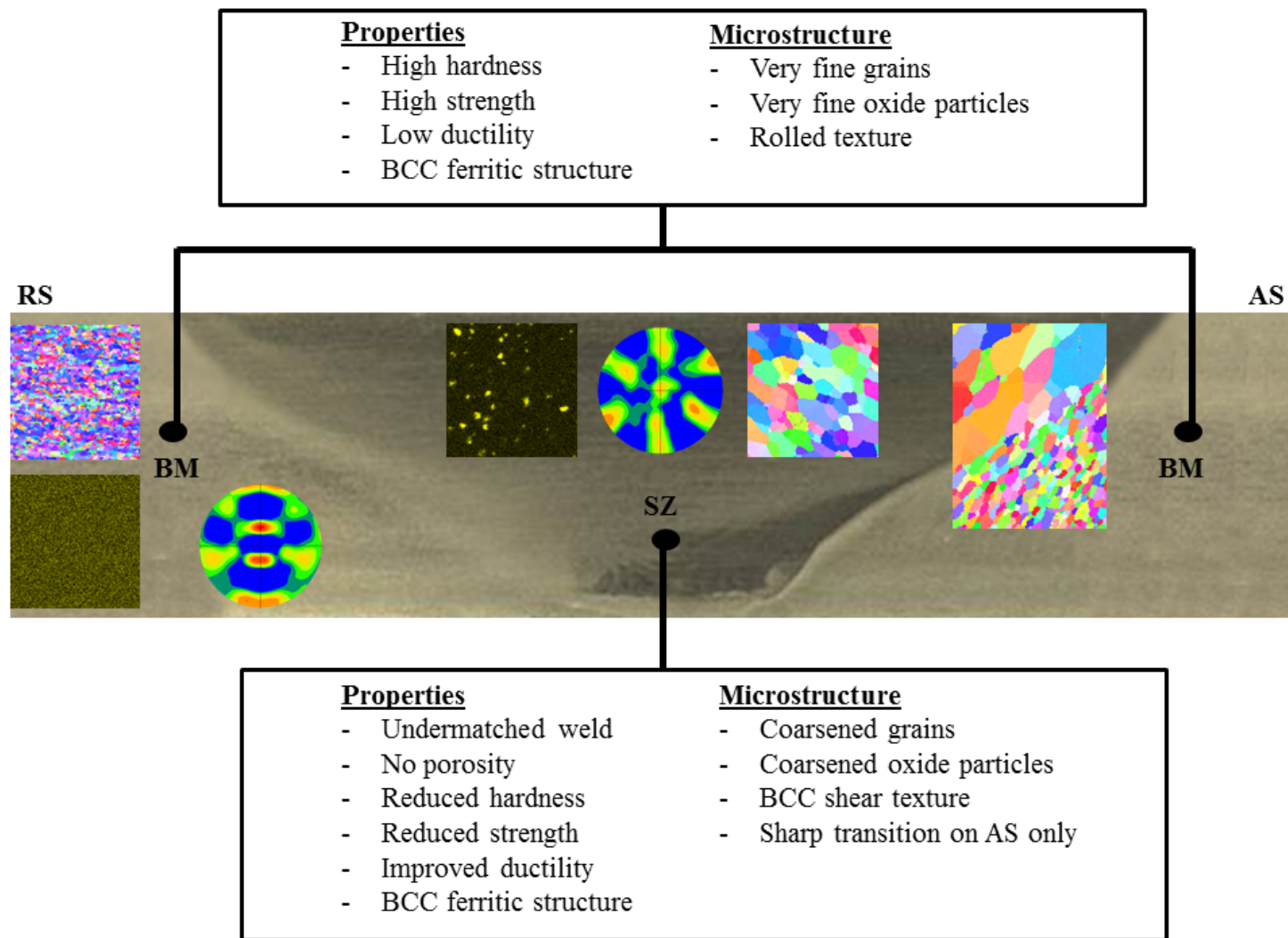


Figure 6.2 Simplified summary of material properties and microstructure for a composite MA956 weld structure.

C. RECOMMENDATIONS FOR FUTURE WORK

In addition to the conclusions that can be drawn from this work, the following additional research questions or recommendations for future work are presented:

- The observed coarsening of the oxides is based on the $\text{Al}_2\text{O}_3\text{-Y}_2\text{O}_3$ system that exists within MA956 (and other aluminum-containing ODS alloys such as PM2000). A separate class of ODS steels exists that does not contain aluminum (most notably MA957, 12/14YWT, and 9/12 Cr-ODS) may not be susceptible to the same coarsening. Research similar to that presented herein on one of these alloys would help establish if the coarsening seen is dependent on $\text{Al}_2\text{O}_3\text{-Y}_2\text{O}_3$ system or was more generically dependent on the FSW process. It is worth noting, however, that aluminum was not arbitrarily chosen as an element within these alloys, but rather serves a critical role in corrosion and oxidation resistance. Use of non aluminum-containing alloys would have to address this issue.

- One of the most insightful aspects of this research has been the oxide particle coarsening following FSW. The degree of oxide particle coarsening was directly correlated to the loss of particle strengthening; however, in addition to providing a dispersion strengthening contribution, the oxide particles within ODS steels also serve as sites for the accumulation of hydrogen and helium atoms to mitigate radiation swelling and thereby giving the alloy improved radiation damage resistance. Whether these oxide particles are as effective in this role upon coarsening is not known. It is hypothesized that the increased size of the particles after FSW would make them less effective as sinks and would thus cause the aggregate alloy to undergo more swelling in areas that were friction stir welded. An experimental regime that includes irradiation of FSW specimens would be needed to prove this hypothesis.

- One of the inherent advantages of ODS steels has been the high temperature stability of the oxide particles. This research has shown that these particles are not stable during the FSW process and coarsen to the degree where they no longer serve as a strengthening contribution. Separate elevated temperature exposure experiments of both BM and FSW MA956 may help establish if the oxide particles remain stable at high

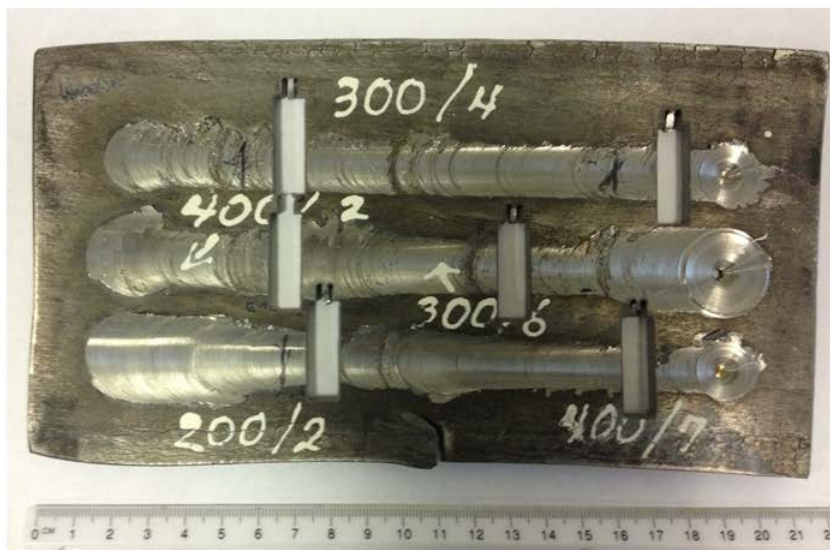
temperature following FSW. If it is found that the oxides in the BM remain stable at high temperature (i.e. do not coarsen), then more in depth analysis of why the FSW process causes the phase transformations and coarsening seen would be required. The enhanced mobility and relatively abundance of aluminum is hypothesized as the primary catalyst for continued phase transformations during FSW.

- The vast majority of research herein analyzed only defect-free weld conditions consistent with the overall task; however, now with a better understanding of the processing to microstructure relationships, analysis similar to that done in this research on defective welds may give additional insight. For example, for defective very low heat input conditions, will the same particle coarsening be observed or is there a minimum heat input required to cause this coarsening?

- One of the foundations of this research has been that heat input (and essentially all microstructural and material property relationships) can be quantified by the term HI. Although still quite useful, this relationship is clearly an oversimplification. Without having to separately establish an entirely new experimental regime, there are two different situations that already exist in this research where only one welding parameter was changed. These situations are a systematic increase in tool traverse speed for two different rotational speeds: 400 RPM/50 MPM, 400 RPM/100 MPM, 400 RPM/175 MPM and 300 RPM/50 MPM, 300 RPM/100 MPM, and 300 RPM/150 MPM. Analysis of these conditions could give far greater insight on the response of MA956 following MA956. This obvious experimental path was not overlooked in this research, and in fact, initial research help determined the final welding conditions used. To accomplish this research the initial experimental plate of MA956 (MA956 plate-1) will have to be utilized. This research would require careful sample preparation and would be proposed to only be viable for the SZ of each section due to the proximity of the weld paths; however, based on the extensive microstructure analysis done in this research, it is hypothesized that the SZs in each of the five conditions of MA956 plate-1 would still be homogenous and respective of each individual condition. Due to the proximity of the weld passes any analysis outside of the SZ would be affected by both the condition in that pass as well as adjacent passes.

APPENDIX A

MA956 Plate – 1



Dimensions:

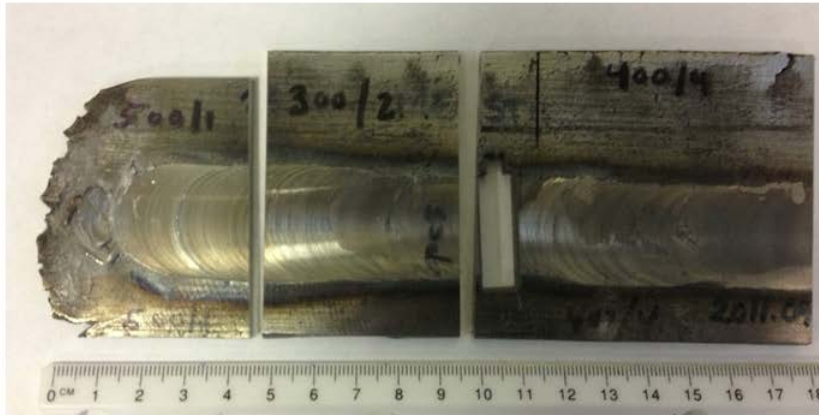
Length = 216 mm
Width = 120 mm
Thickness = 4 mm
Mass = 697 g

Comments:

- Used by MegaStir for 5 FSW conditions as shown (none of these conditions are now considered primary conditions).
- This plate is only used for optical macrographs of weld consolidation.

Figure A.1 MA956 Plate-1.

MA956 Plate – 2



Dimensions:

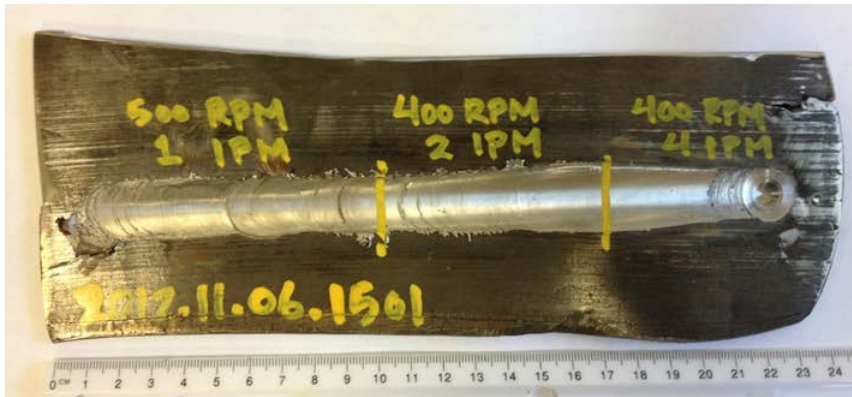
Length = 220 mm
Width = 70 mm
Thickness = 4 mm
Mass = ~200 g

Comments:

- The most utilized piece of all samples. Has the primary FSW conditions of 500/1, 300/2, and 400/4.
- Used for optical macrographs, EBSD, microhardness, SEM, TEM, SAXS.
- Used for FSW tensile specimens.

Figure A.2 MA956 Plate-2.

MA956 Plate – 3



Dimensions:

Length = 250 mm
Width = 88 mm
Thickness = 4 mm
Mass = 627 g

Comments:

- Plate was friction stir welded by MegaStir with conditions as shown.
- Plate used for residual stress measurement in related research at NPS.

Figure A.3 MA956 Plate-3.

MA956 Plate – 4



Dimensions:

Length = 182 mm
Width = 127 mm
Thickness = 4 mm
Mass = 626 g

Comments on use:

- Plate was friction stir welded by MegaStir with conditions as shown.
- Plate used to make longer tensile specimens.

Figure A.4 MA956 Plate-4.

MA956 Plate – 5



Dimensions:

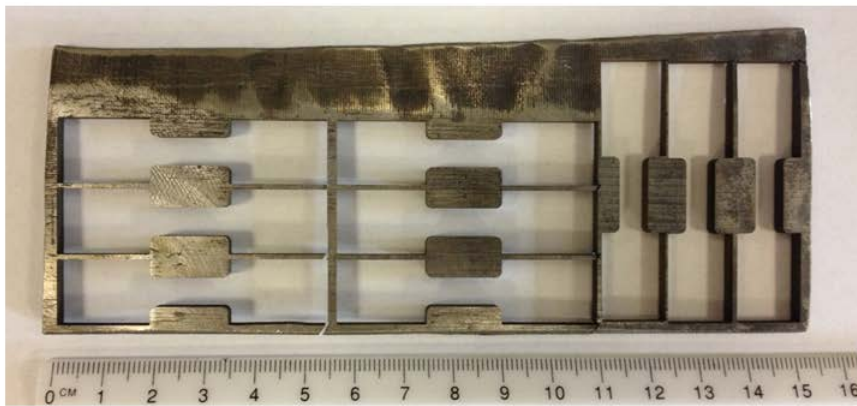
Length = 117 mm
Width = 49 mm
Thickness = 11.4 mm
Mass = 464 g

Comments:

- FSW was accomplished by MegaStir with condition of 275/4.
- Very little supporting data available, but piece is useful comparison for low heat input.
- Plate only used for grain size analysis via EBSD.

Figure A.5 MA956 Plate-5.

MA956 Plate – 6



Dimensions:

Length = 153 mm

Width = 60 mm

Thickness = 3.5 mm

Mass = ~100 g

Comments:

- Plate was used to create 18 tensile specimens for BM analysis as shown (2 specimens from each section shown through the thickness of the plate).

Figure A.6 MA956 Plate-6.

MA956 Plate – 7



Dimensions:

Length = 110 mm
Width = 64 mm
Thickness = 4 mm
Mass = 176 g

Comments:

- Plate used to create new mini-tensile specimens (thinner gage section).

Figure A.7 MA956 Plate-7.

THIS PAGE INTENTIONALLY LEFT BLANK

APPENDIX B

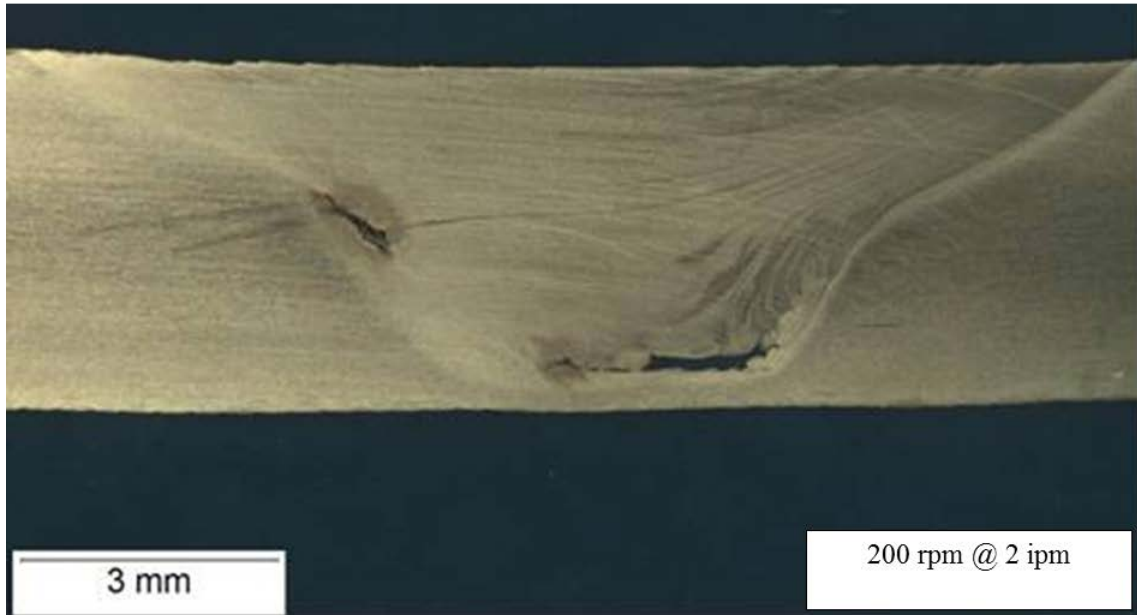


Figure B.1 Optical macrograph for 200 RPM/50 MMPM.

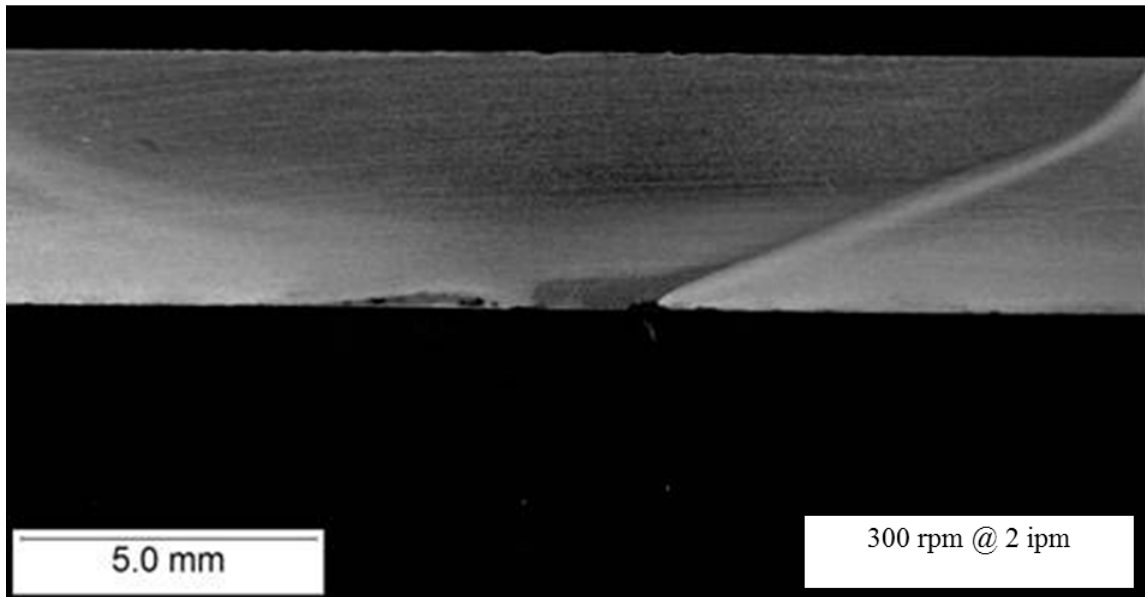


Figure B.2 Optical macrograph for 300 RPM/50 MMPM.

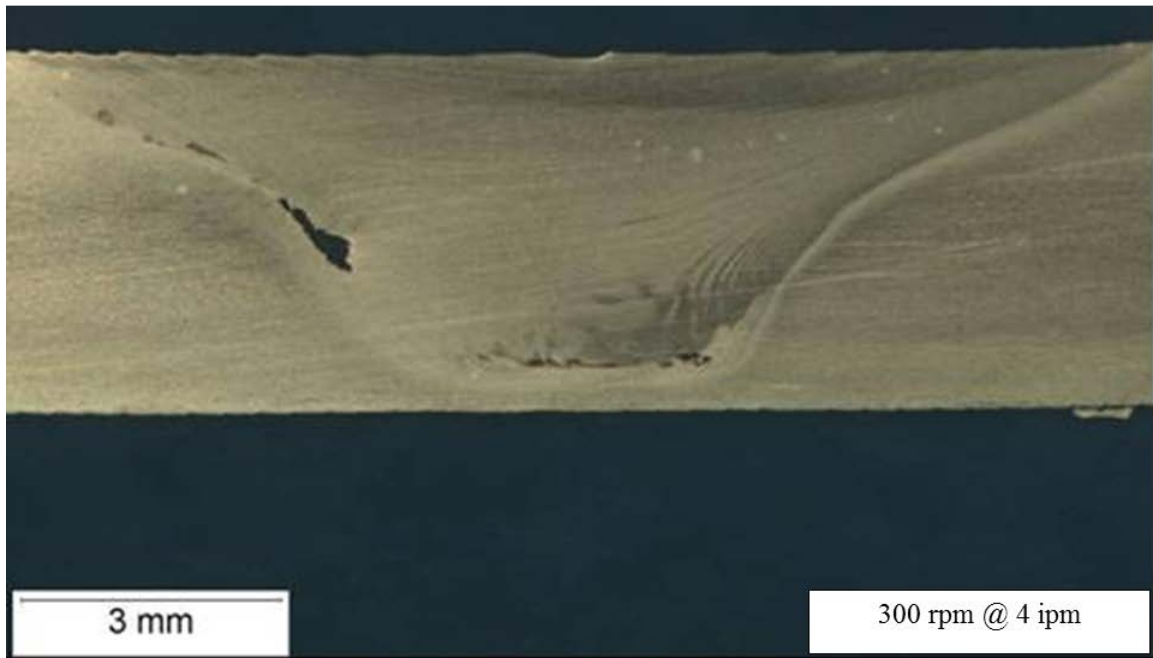


Figure B.3 Optical macrograph for 300 RPM/100 MPM.

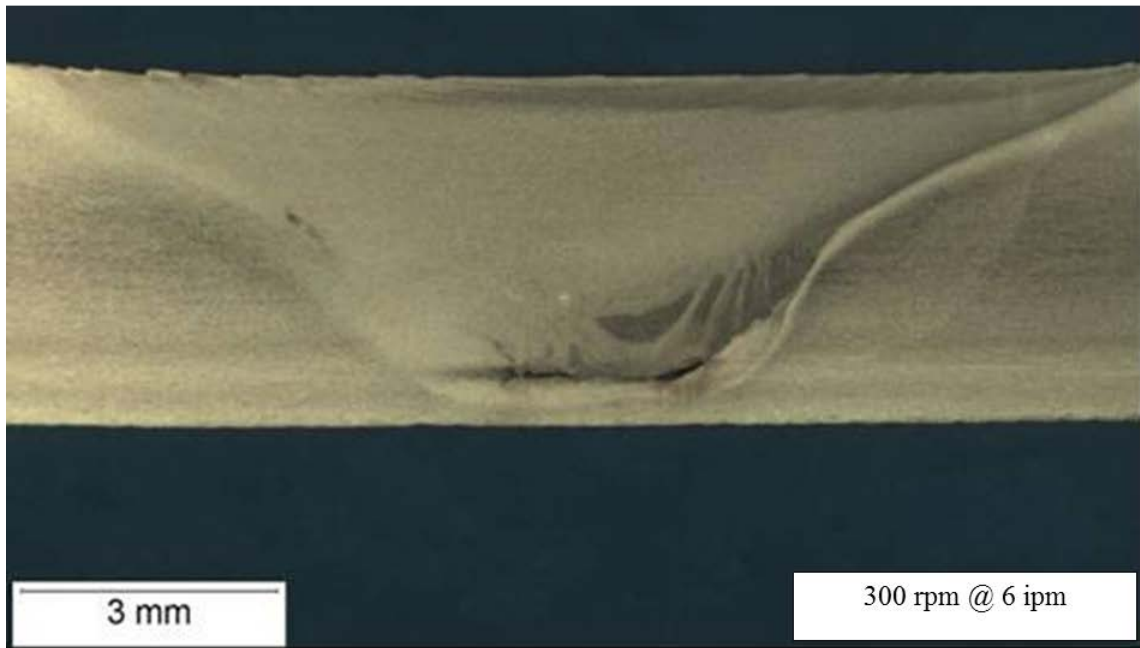


Figure B.4 Optical macrograph for 300 RPM/150 MPM.

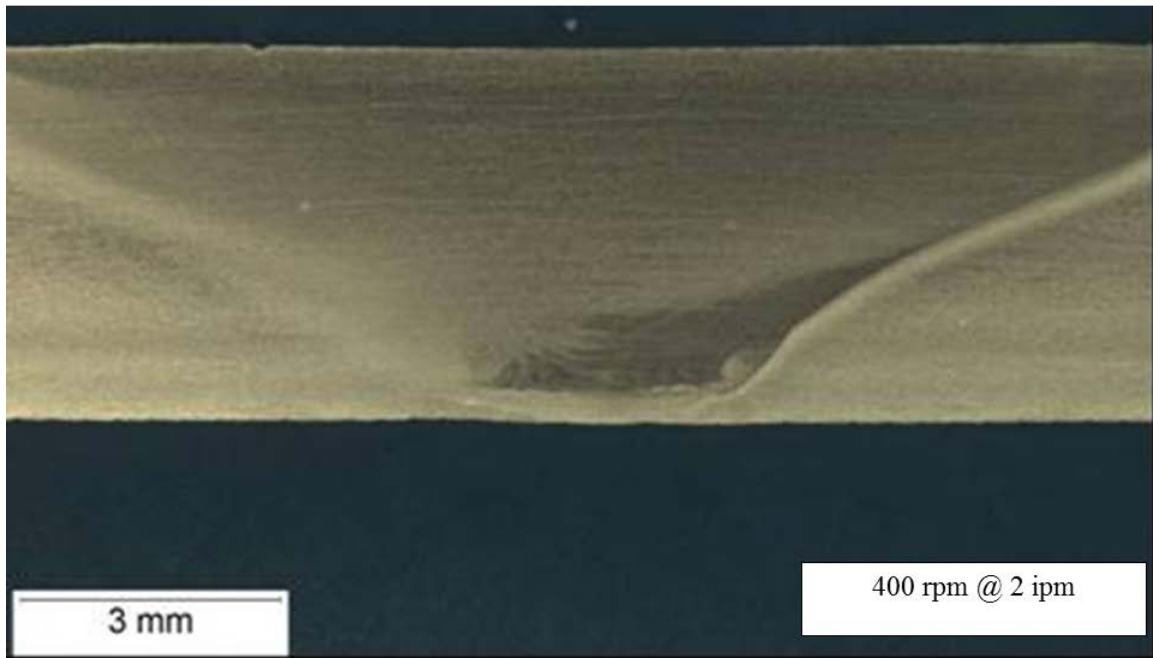


Figure B.5 Optical macrograph for 400 RPM/50 MPM.

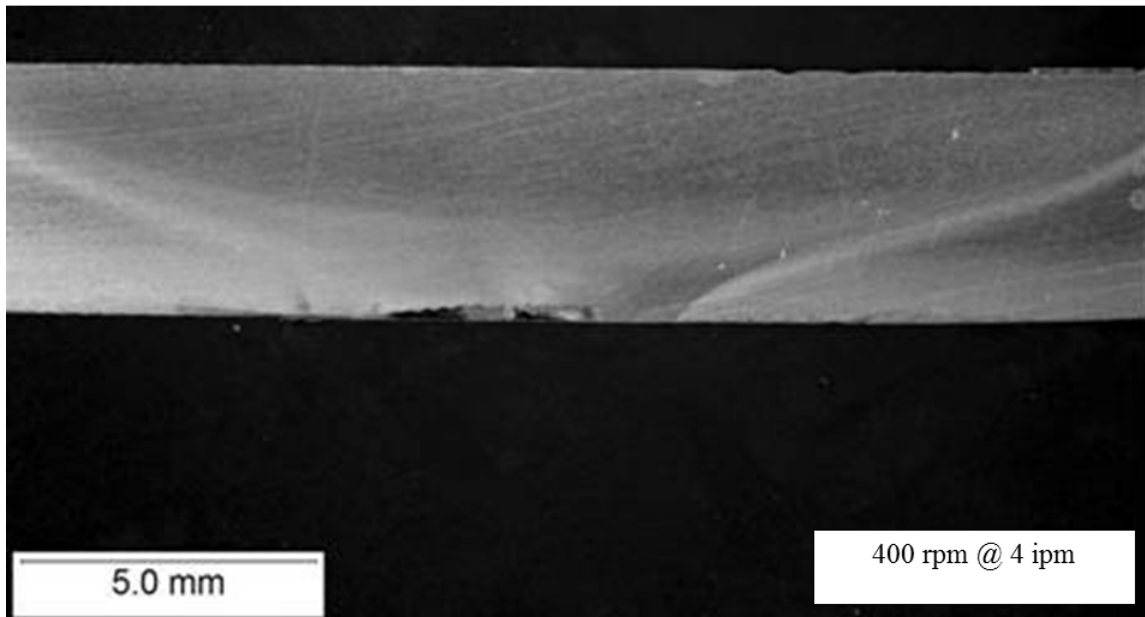


Figure B.6 Optical macrograph for 400 RPM/100 MPM.

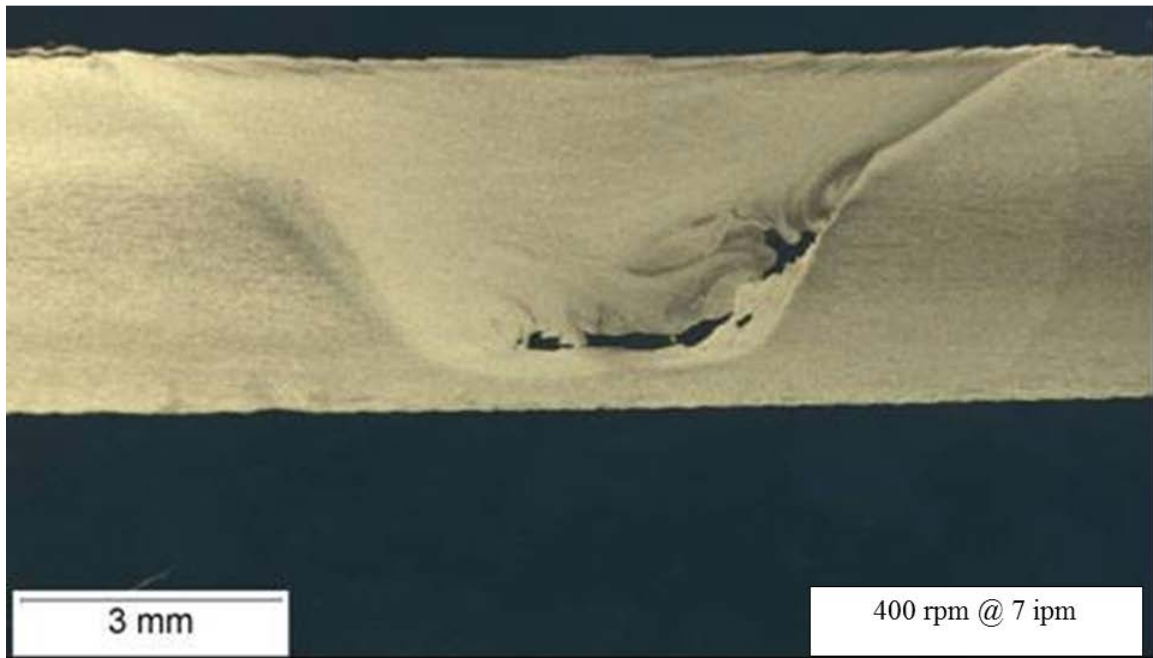


Figure B.7 Optical macrograph for 400 RPM/175 MPM.

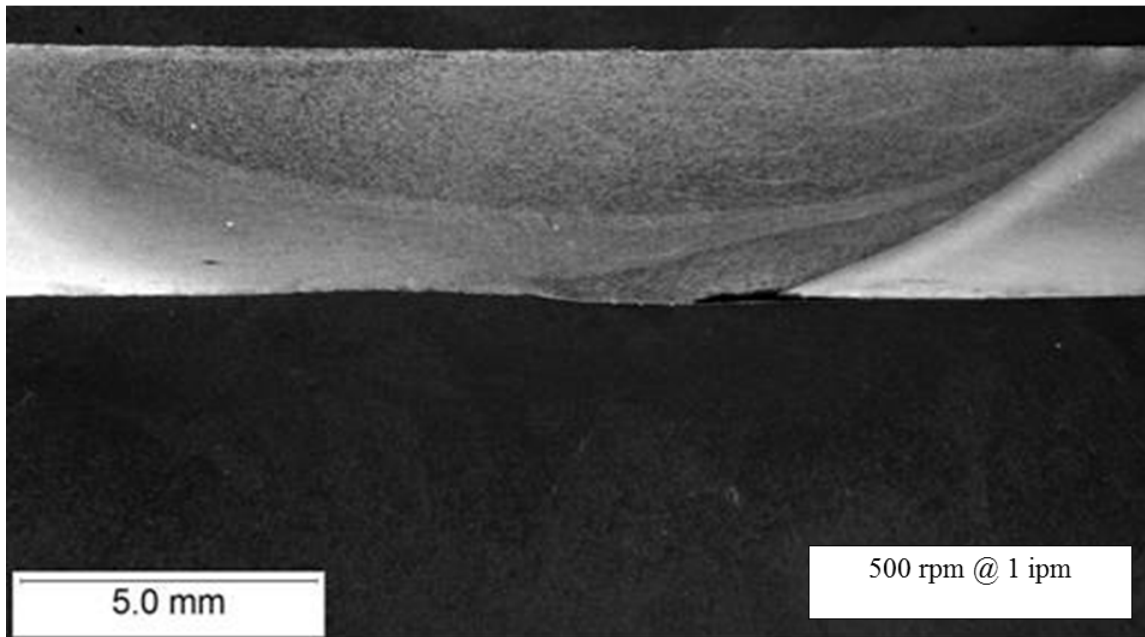


Figure B.8 Optical macrograph for 500 RPM/25 MPPM.

APPENDIX C

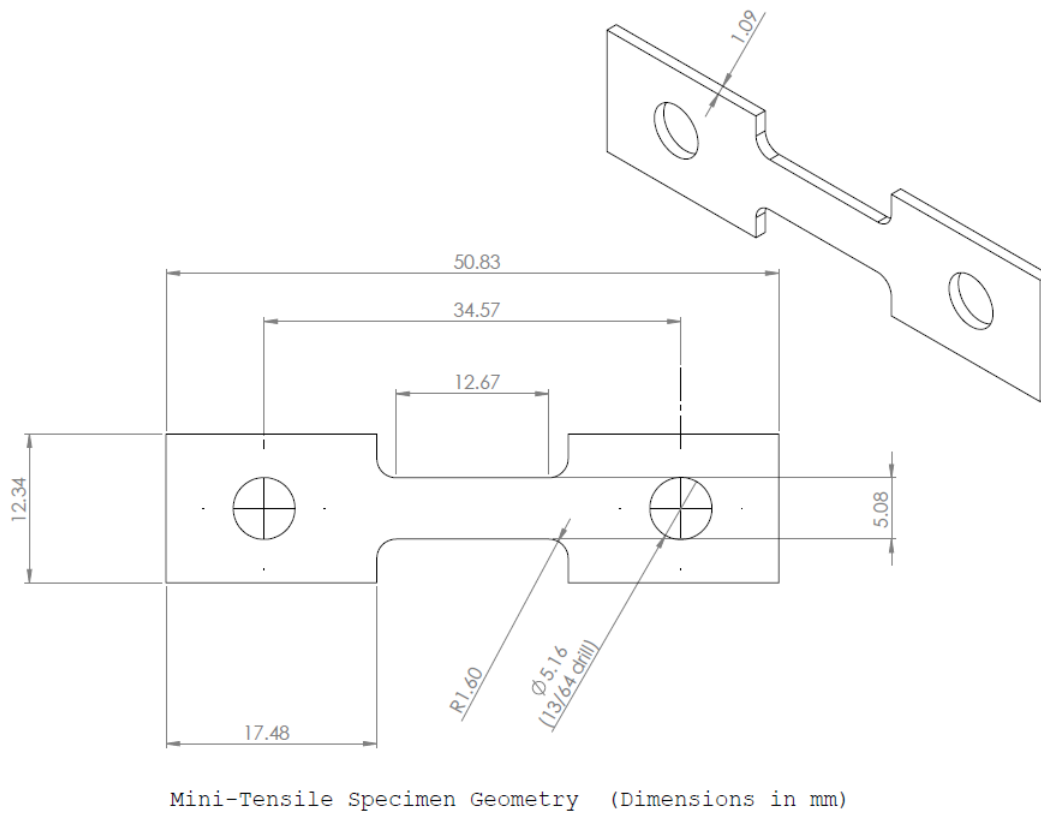
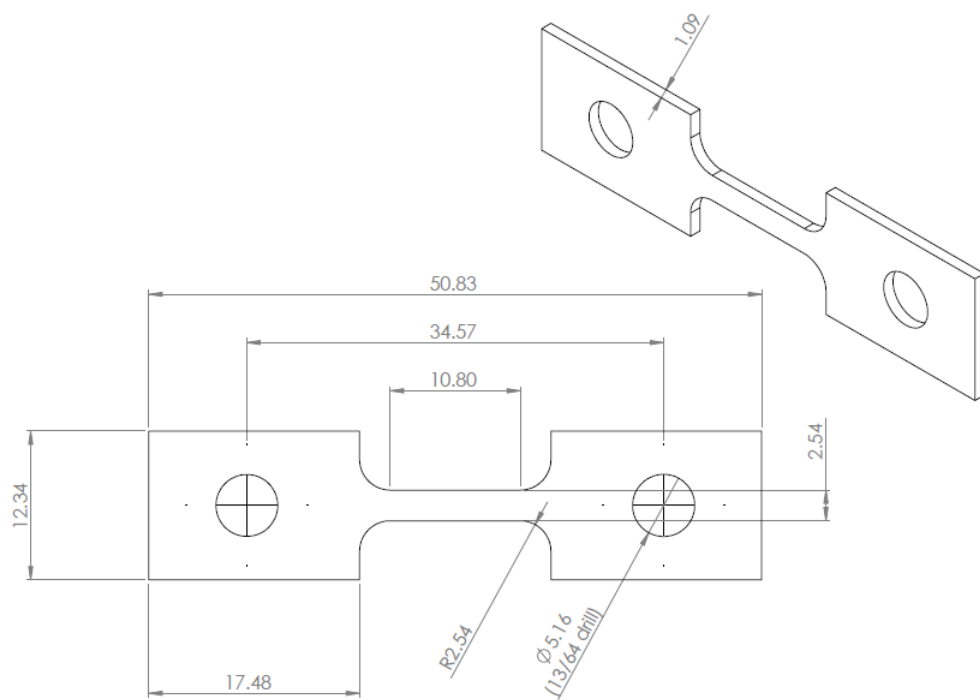
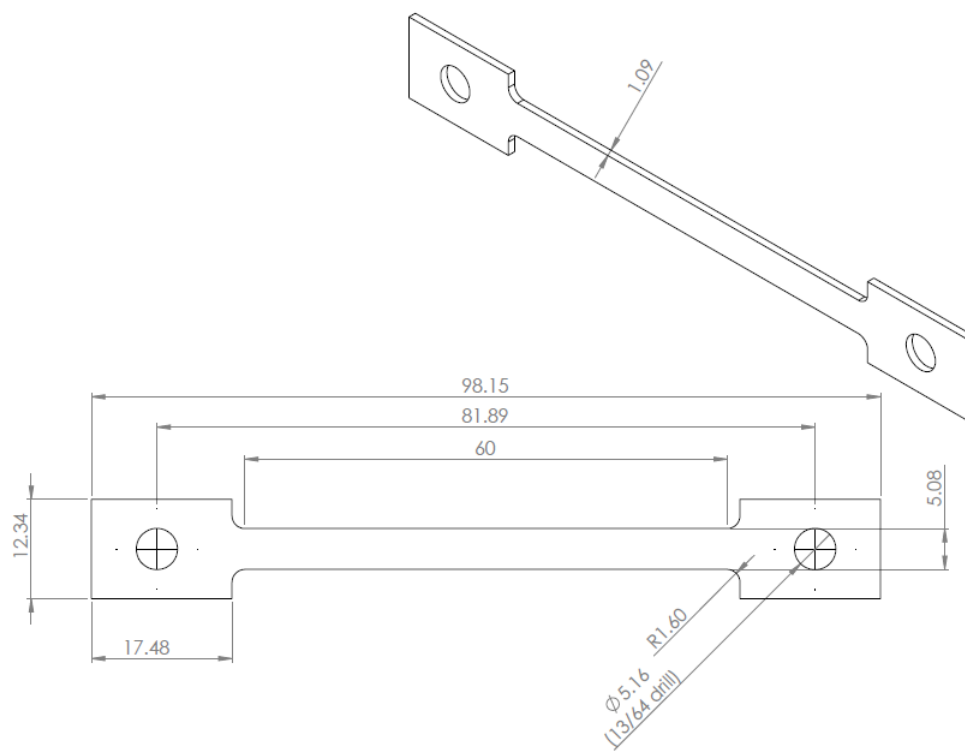


Figure C.1 Engineering drawing for miniature tensile specimen (standard).



New Mini-Tensile Specimen Geometry (Dimensions in mm)

Figure C.2 Engineering drawing for miniature tensile specimen (narrow).



Long-Tensile Specimen Geometry (Dimensions in mm)

Figure C.3 Engineering drawing for miniature tensile specimen (long).

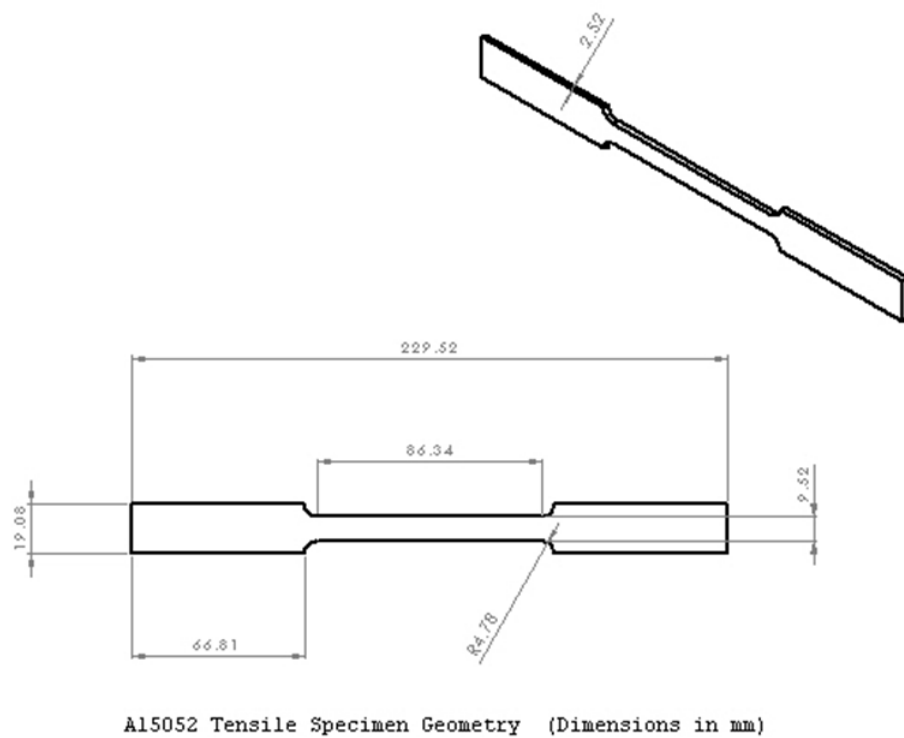


Figure C.4 Engineering drawing for AA5052 specimen.

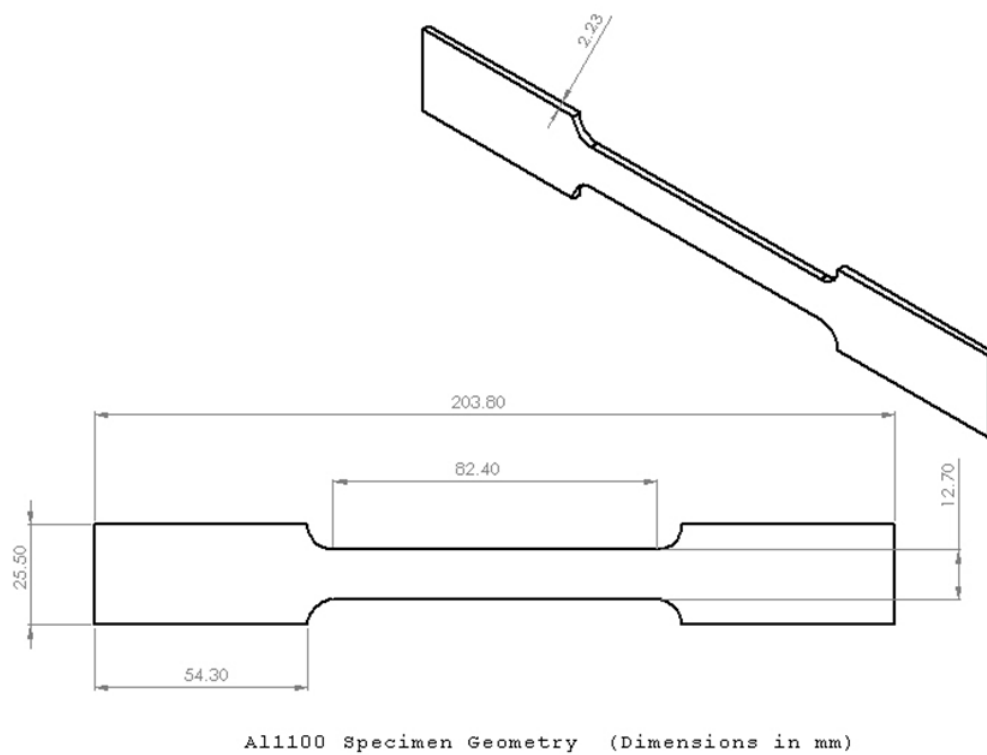


Figure C.5 Engineering drawing for AA1100 specimen.

THIS PAGE INTENTIONALLY LEFT BLANK

APPENDIX D

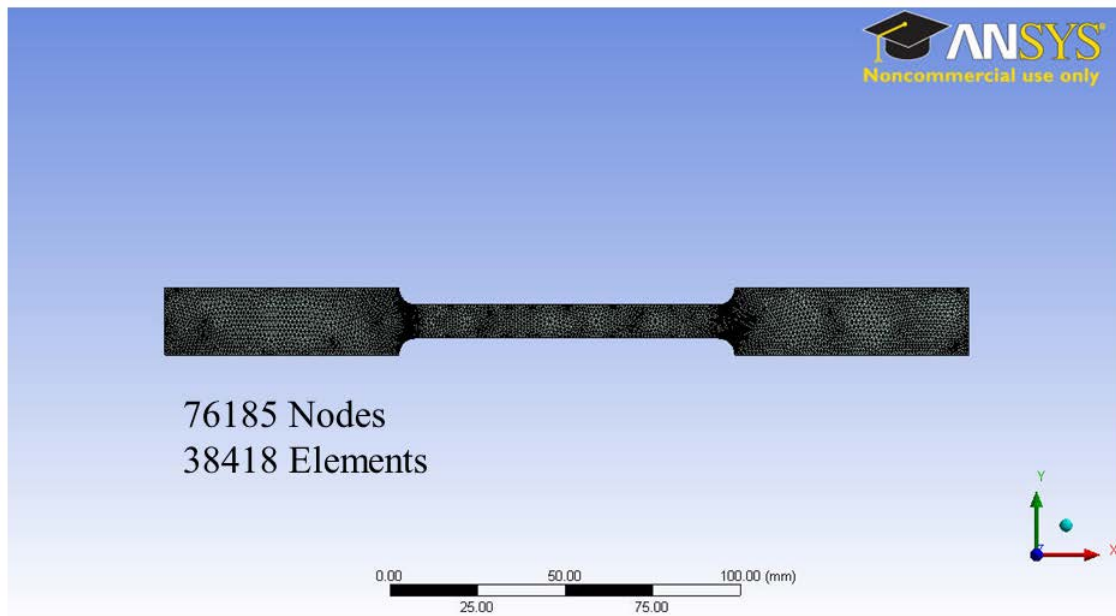


Figure D.1 ANSYS meshing used for AA5052 specimen.

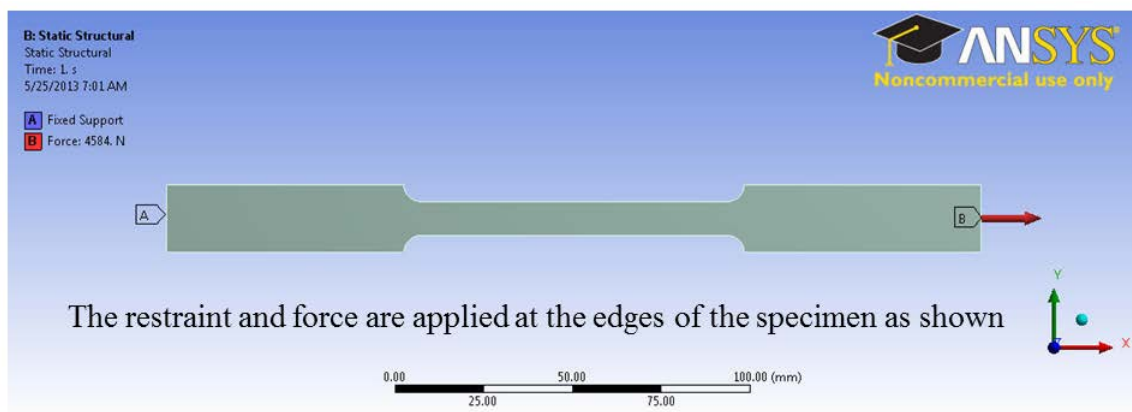


Figure D.2 ANSYS application of restraints and forces for AA5052 specimen.

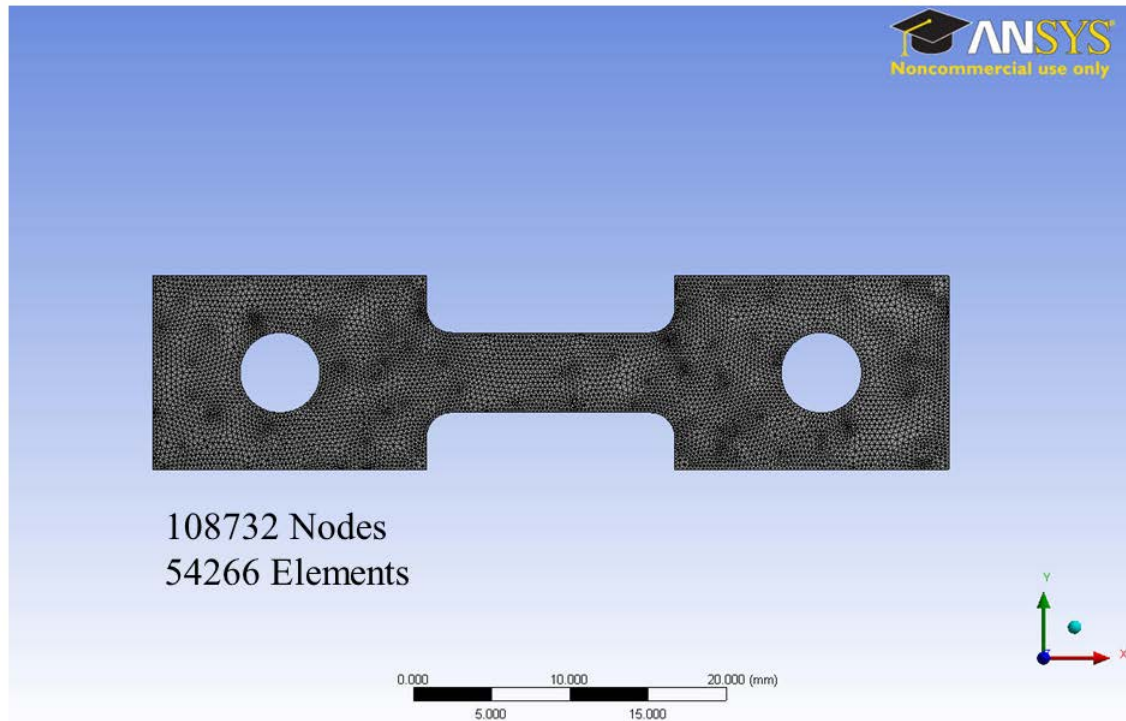


Figure D.3 ANSYS meshing used for miniature tensile specimen geometry (standard).

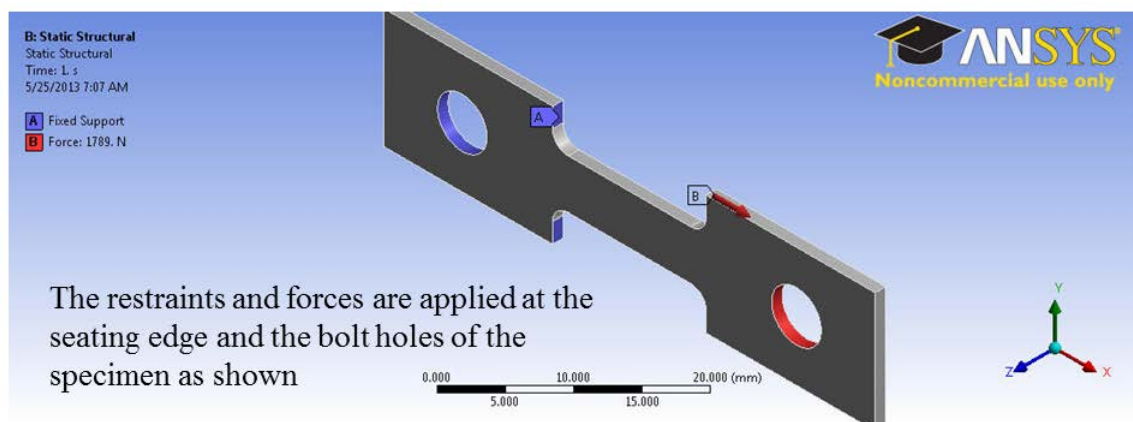


Figure D.4 ANSYS application of restraints and forces for miniature tensile specimen geometry (standard).



Figure D.5 ANSYS meshing used for miniature tensile specimen geometry (narrow).

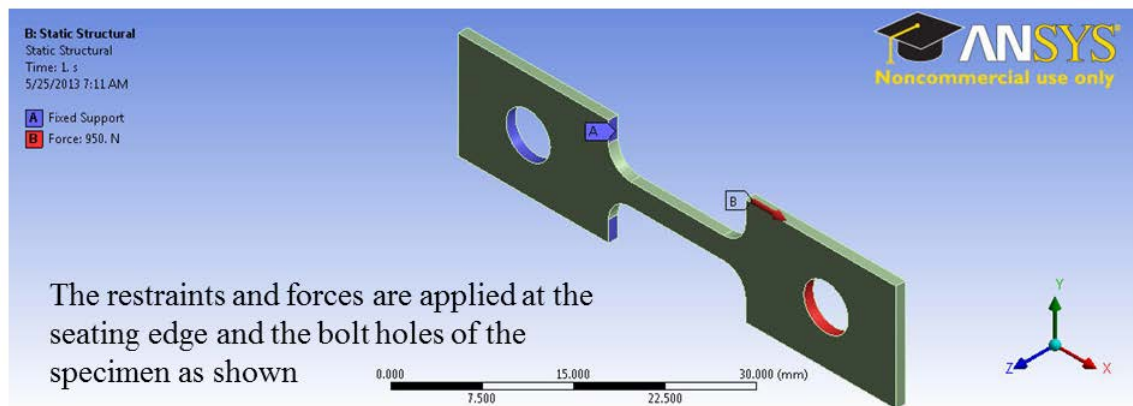


Figure D.6 ANSYS application of restraints and forces for miniature tensile specimen geometry (narrow).

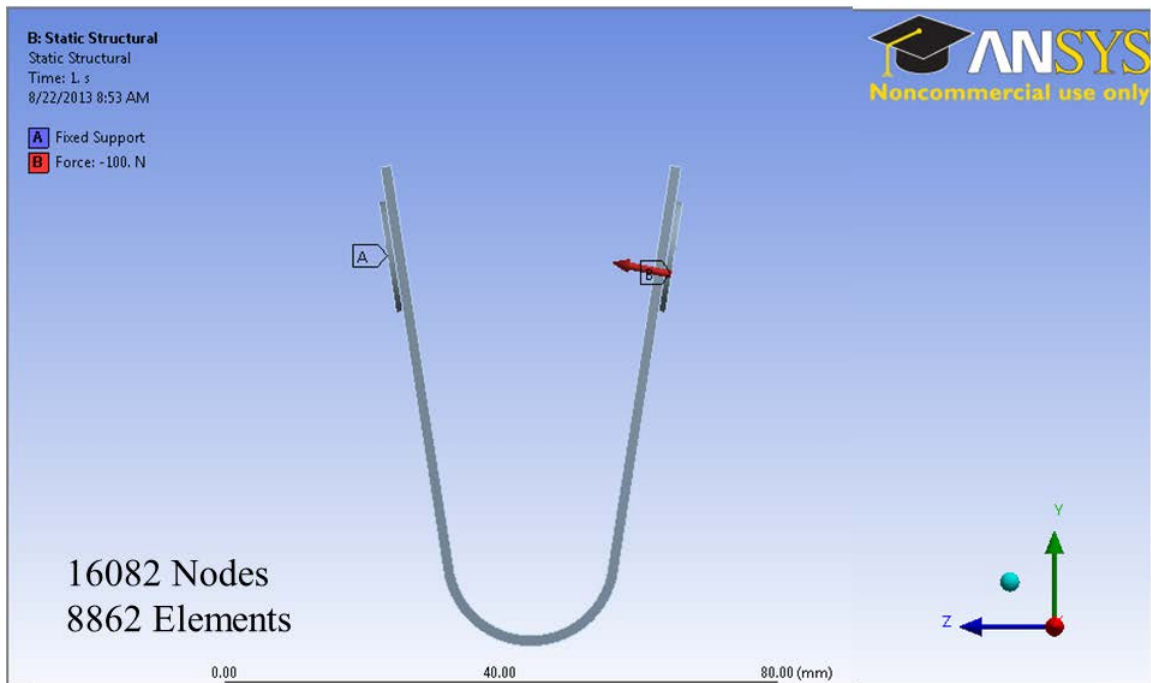


Figure D.7 ANSYS application of restraints and forces for U-bend specimen.

APPENDIX E

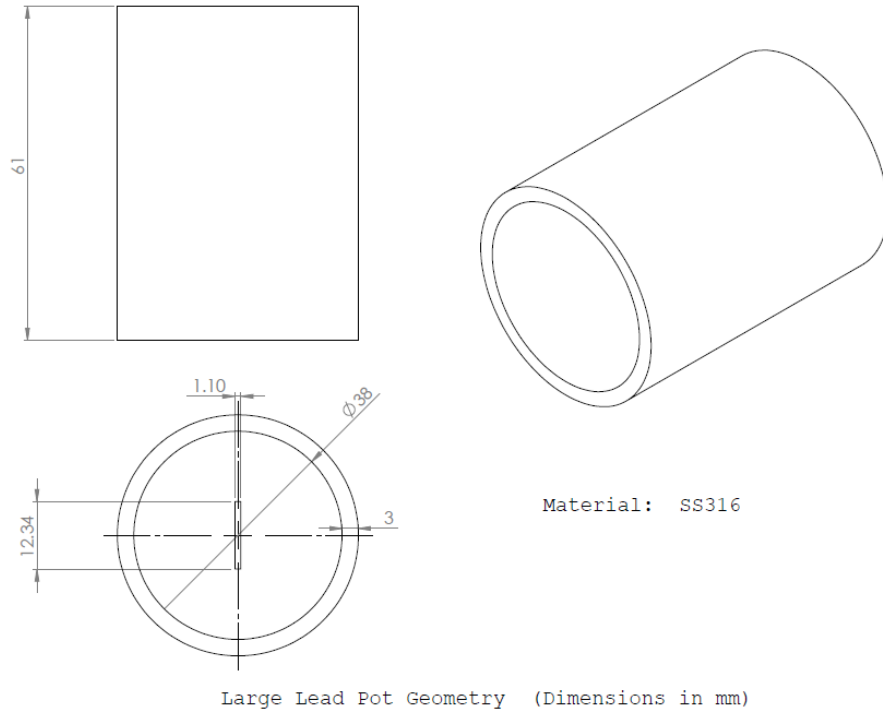
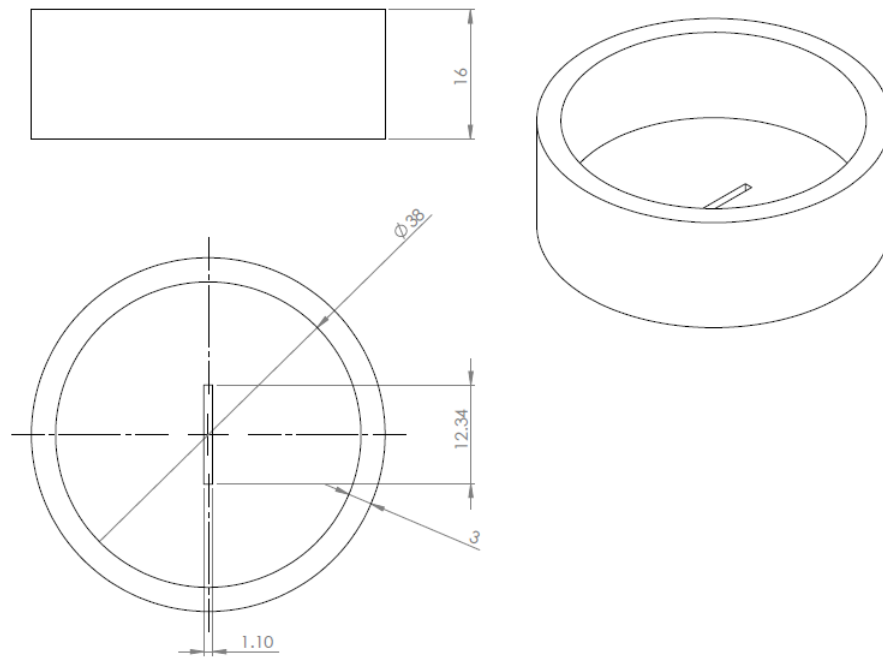
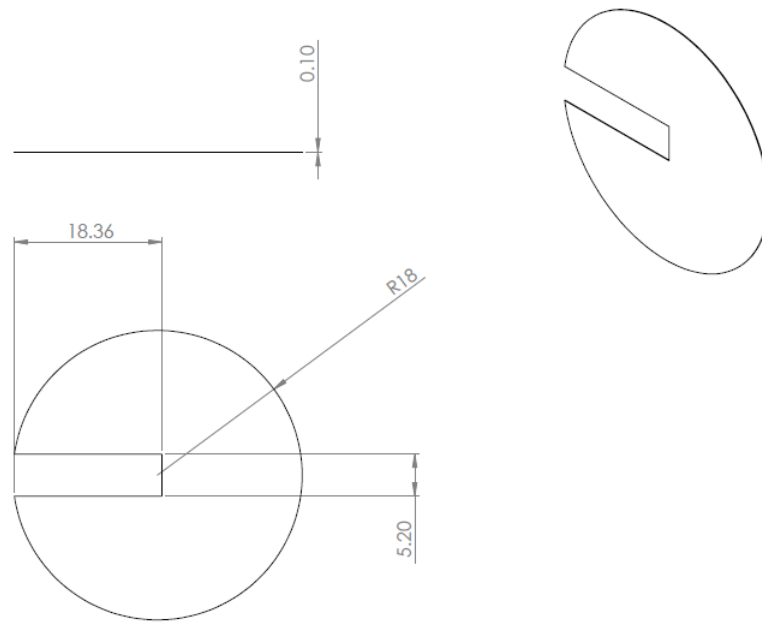


Figure E.1 Engineering drawing for large containment apparatus.



Lead Holder Specimen Geometry (Dimensions in mm)

Figure E.2 Engineering drawing for small containment apparatus.



Shim Disc Specimen Geometry (Dimensions in mm)

Figure E.3 Engineering drawing for gasket used in containment apparatus.

THIS PAGE INTENTIONALLY LEFT BLANK

LIST OF REFERENCES

- [1] S. J. Zinkle and J. T. Busby, "Structural materials for fission & fusion energy," *Materials Today*, vol. 12, pp. 12–19, Nov 2009.
- [2] S. J. Zinkle, "Advanced materials for fusion technology," *Fusion Engineering and Design*, vol. 74, pp. 31–40, Nov 2005.
- [3] E. E. Bloom, "The challenge of developing structural materials for fusion power systems," *Journal of Nuclear Materials*, vol. 258, pp. 7–17, Oct 1998.
- [4] E. E. Bloom, S. J. Zinkle, and F. W. Wiffen, "Materials to deliver the promise of fusion power - progress and challenges," *Journal of Nuclear Materials*, vol. 329, pp. 12–19, Aug 1 2004.
- [5] A. Kimura, "Current status of reduced-activation ferritic/martensitic steels R&D for fusion energy," *Materials Transactions*, vol. 46, pp. 394–404, Mar 2005.
- [6] S. Ukai, S. Mizuta, M. Fujiwara, T. Okuda, and T. Kobayashi, "Development of 9Cr-ODS martensitic steel claddings for fuel pins by means of ferrite to austenite phase transformation," *Journal of Nuclear Science and Technology*, vol. 39, pp. 778–788, Jul 2002.
- [7] R. J. Kurtz, A. Alamo, E. Lucon, Q. Huang, S. Jitsukawa, A. Kimura, *et al.*, "Recent progress toward development of reduced activation ferritic/martensitic steels for fusion structural applications," *Journal of Nuclear Materials*, vol. 386, pp. 411–417, Apr 2009.
- [8] H. Tanigawa, K. Shiba, A. Moeslang, R. E. Stoller, R. Lindau, M. A. Sokolov, *et al.*, "Status and key issues of reduced activation ferritic/martensitic steels as the structural material for a DEMO blanket," *Journal of Nuclear Materials*, vol. 417, pp. 9–15, Oct 1 2011.
- [9] B. van der Schaaf, D. S. Gelles, S. Jitsukawa, A. Kimura, R. L. Klueh, A. Moslang, *et al.*, "Progress and critical issues of reduced activation ferritic/martensitic steel development," *Journal of Nuclear Materials*, vol. 283, pp. 52–59, Dec 2000.
- [10] M. S. El-Genk and J. M. Tournier, "A review of refractory metal alloys and mechanically alloyed-oxide dispersion strengthened steels for space nuclear power systems," *Journal of Nuclear Materials*, vol. 340, pp. 93–112, Apr 2005.
- [11] S. J. Zinkle and N. M. Ghoniem, "Operating temperature windows for fusion reactor structural materials," *Fusion Engineering and Design*, vol. 51–52, pp. 55–71, Nov 2000.

- [12] Nuclear News. (2012) World List of Nuclear Power Plants.
- [13] S. J. Zinkle and G. S. Was, “Materials challenges in nuclear energy,” *Acta Materialia*, vol. 61, pp. 735–758, Feb 2013.
- [14] United States Naval Nuclear Propulsion Program, *100,000,000 Miles Safely Steamed On Nuclear Power*, 1994.
- [15] Lawrence Livermore National Laboratory, “On the Path to Ignition,” *Science and Technology Review*, March 2013.
- [16] A. F. Rowcliffe, L. K. Mansur, D. T. Hoelzer, and R. K. Nanstad, “Perspectives on radiation effects in nickel-base alloys for applications in advanced reactors,” *Journal of Nuclear Materials*, vol. 392, pp. 341–352, Jul 2009.
- [17] G. R. Odette, M. J. Alinger, and B. D. Wirth, “Recent developments in irradiation-resistant steels,” *Annual Review of Materials Research*, vol. 38, pp. 471–503, 2008.
- [18] J. Farmer, “LIFE Material Issues,” *Lawrence Livermore National Laboratory*, 2010.
- [19] D. R. Olander, *Fundamental Aspects of Nuclear Reactor Fuel Elements*: Technical Information Center Energy Research and Development Administration, 1976.
- [20] G. S. Was, *Fundamentals of Radiation Materials Science*. New York, NY: Springer, 2007.
- [21] P. Miao, G. R. Odette, T. Yamamoto, M. Alinger, D. Hoelzer, and D. Gragg, “Effects of consolidation temperature, strength and microstructure on fracture toughness of nanostructured ferritic alloys,” *Journal of Nuclear Materials*, vol. 367, pp. 208–212, Aug 2007.
- [22] T. S. Byun, J. H. Kim, J. H. Yoon, and D. T. Hoelzer, “High temperature fracture characteristics of a nanostructured ferritic alloy (NFA),” *Journal of Nuclear Materials*, vol. 407, pp. 78–82, Dec 15 2010.
- [23] K. Splichal, J. Berka, J. Burda, and M. Zmitko, “Fracture toughness of the hydrogen charged EUROFER 97 RAFM steel at room temperature and 120 degrees C,” *Journal of Nuclear Materials*, vol. 392, pp. 125–132, Jul 1 2009.
- [24] S. Khericha and E. Loewen, “Lead Coolant Test Facility-Design concept and requirements,” *Nuclear Engineering and Design*, vol. 241, pp. 3008–3016, Aug 2011.

- [25] K. Noda, K. Ehrlich, S. Jitsukawa, A. Moslang, and S. Zinkle, “Users’ requirements for IFMIF,” *Journal of Nuclear Materials*, vol. 258, Oct 1998.
- [26] M. B. Lewis, W. R. Allen, R. A. Buhl, N. H. Packan, S. W. Cook, and L. K. Mansur, “Triple Ion-Beam Irradiation Facility,” *Nuclear Instruments & Methods in Physics Research Section B-Beam Interactions with Materials and Atoms*, vol. 43, pp. 243–253, Sep 1989.
- [27] S. Pellegrino, P. Trocellier, S. Miro, Y. Serruys, E. Bordas, H. Martin, *et al.*, “The JANNUS Saclay facility: A new platform for materials irradiation, implantation and ion beam analysis,” *Nuclear Instruments & Methods in Physics Research Section B-Beam Interactions with Materials and Atoms*, vol. 273, pp. 213–217, Feb 15 2012.
- [28] Y. Serruys, P. Trocellier, S. Miro, E. Bordas, M. O. Ruault, O. Kaitasov, *et al.*, “JANNUS: A multi-irradiation platform for experimental validation at the scale of the atomistic modelling,” *Journal of Nuclear Materials*, vol. 386–88, pp. 967–970, Apr 30 2009.
- [29] A. Kimura, R. Kasada, A. Kohyama, H. Tanigawa, T. Hirose, K. Shiba, *et al.*, “Recent progress in U.S.-Japan collaborative research on ferritic steels R&D,” *Journal of Nuclear Materials*, vol. 367, pp. 60–67, Aug 2007.
- [30] S. Jitsukawa, A. Kimura, A. Kohyama, R. L. Klueh, A. A. Tavassoli, B. van der Schaaf, *et al.*, “Recent results of the reduced activation ferritic/martensitic steel development,” *Journal of Nuclear Materials*, vol. 329, pp. 39–46, Aug 1 2004.
- [31] B. van der Schaaf, F. Tavassoli, C. Fazio, E. Rigal, E. Diegele, R. Lindau, *et al.*, “The development of EUROFER reduced activation steel,” *Fusion Engineering and Design*, vol. 69, pp. 197–203, Sep 2003.
- [32] S. Ukai and M. Fujiwara, “Perspective of ODS alloys application in nuclear environments,” *Journal of Nuclear Materials*, vol. 307, pp. 749–757, Dec 2002.
- [33] G. R. Odette and D. T. Hoelzer, “Irradiation-tolerant Nanostructured Ferritic Alloys: Transforming Helium from a Liability to an Asset,” *Journal of the Minerals, Metals, and Materials Society*, vol. 62, pp. 84–92, Sep 2010.
- [34] B. El-Dasher, J. Farmer, J. Ferreira, M. S. de Caro, A. Rubenchik, and A. Kimura, “Corrosion of oxide dispersion strengthened iron-chromium steels and tantalum in fluoride salt coolant: An in situ compatibility study for fusion and fusion-fission hybrid reactor concepts,” *Journal of Nuclear Materials*, vol. 419, pp. 15–23, Dec 2011.

- [35] J. Farmer, B. El-dasher, M. S. de Caro, and J. Ferreira, "Corrosion of Ferritic Steels in High Temperature Molten Salt Coolants for Nuclear Applications," in *Symposium on Materials for Future Fusion and Fission Technologies held at the 2008 MRS Fall Meeting*, Boston, MA, 2009, pp. 41–48.
- [36] J. Farmer, B. El-dasher, J. Ferreira, M. Serrano de Car, and A. Kimura, "Coolant Compatability Studies for Fusion and Fusion-Fission Hybrid Reactor Concepts: Corrosion of Oxide Dispersion Strengthened Iron-Chromium Steels and Tantalum in High Temperature Molten Flouride Salts," 2010.
- [37] L. L. Hsiung, M. J. Fluss, S. J. Tumey, B. W. Choi, Y. Serruys, F. Willaime, *et al.*, "Formation mechanism and the role of nanoparticles in Fe-Cr ODS steels developed for radiation tolerance," *Physical Review B*, vol. 82, Nov 9 2010.
- [38] P. Hosemann, M. Hawley, D. Koury, J. G. Swadener, J. Welch, A. L. Johnson, *et al.*, "Characterization of oxide layers grown on D9 austenitic stainless steel in lead bismuth eutectic," *Journal of Nuclear Materials*, vol. 375, pp. 323–330, Apr 2008.
- [39] P. Miao, G. R. Odette, J. Gould, J. Bernath, R. Miller, M. Alinger, *et al.*, "The microstructure and strength properties of MA957 nanostructured ferritic alloy joints produced by friction stir and electro-spark deposition welding," *Journal of Nuclear Materials*, vol. 367, pp. 1197–1202, Aug 2007.
- [40] M. J. Alinger, G. R. Odette, and D. T. Hoelzer, "On the role of alloy composition and processing parameters in nanocluster formation and dispersion strengthening in nanostuctured ferritic alloys," *Acta Materialia*, vol. 57, pp. 392–406, Jan 2009.
- [41] S. Noh, R. Kasada, A. Kimura, S. H. C. Park, and S. Hirano, "Microstructure and mechanical properties of friction stir processed ODS ferritic steels," *Journal of Nuclear Materials*, vol. 417, pp. 245–248, Oct 1 2011.
- [42] T. Muroga, D. K. Sze, and K. Okuno, "Overview of the TITAN project," *Fusion Engineering and Design*, vol. 87, pp. 613–619, Aug 2012.
- [43] D. J. Lloyd, "Particle-Reinforced Aluminum and Magnesium Matrix Composites," *International Materials Reviews*, vol. 39, pp. 1–23, 1994 1994.
- [44] J. W. Kaczmar, K. Pietrzak, and W. Wlosinski, "The production and application of metal matrix composite materials," *Journal of Materials Processing Technology*, vol. 106, pp. 58–67, Oct 31 2000.
- [45] S. Ukai, T. Nishida, H. Okada, T. Okuda, M. Fujiwara, and K. Asabe, "Development of oxide dispersion strengthened ferritic steels for FBR core application, (I) - Improvement of mechanical properties by recrystallization processing," *Journal of Nuclear Science and Technology*, vol. 34, Mar 1997.

- [46] S. Ukai, T. Nishida, T. Okuda, and T. Yoshitake, "Development of oxide dispersion strengthened steels for FBR core application, (II) - Morphology improvement by martensite transformation," *Journal of Nuclear Science and Technology*, vol. 35, pp. 294–300, Apr 1998.
- [47] C. Balazsi, F. Gillemot, M. Horvath, F. Weber, K. Balazsi, F. C. Sahin, *et al.*, "Preparation and structural investigation of nanostructured oxide dispersed strengthened steels," *Journal of Materials Science*, vol. 46, pp. 4598–4605, 2011.
- [48] C. L. Chen and Y. M. Dong, "Effect of mechanical alloying and consolidation process on microstructure and hardness of nanostructured Fe-Cr-Al ODS alloys," *Materials Science and Engineering a-Structural Materials Properties Microstructure and Processing*, vol. 528, pp. 8374–8380, Nov 2011.
- [49] J. S. Benjamin, "Dispersion Strengthened Superalloys by Mechanical Alloying," *Metallurgical Transactions*, vol. 1, pp. 2943–2951, 1970.
- [50] C. Suryanarayana, E. Ivanov, and V. V. Boldyrev, "The science and technology of mechanical alloying," *Materials Science and Engineering a-Structural Materials Properties Microstructure and Processing*, vol. 304, pp. 151–158, May 2001.
- [51] Z. J. Zhou, S. Yang, W. H. Chen, L. Liao, and Y. G. Xu, "Processing and characterization of a hipped oxide dispersion strengthened austenitic steel," *Journal of Nuclear Materials*, vol. 428, pp. 31–34, Sep 2012.
- [52] J. Lim, H. O. Nam, I. S. Hwang, and J. H. Kim, "A study of early corrosion behaviors of FeCrAl alloys in liquid lead-bismuth eutectic environments," *Journal of Nuclear Materials*, vol. 407, pp. 205–210, Dec 2010.
- [53] P. Hosemann, H. T. Thau, A. L. Johnson, S. A. Maloy, and N. Li, "Corrosion of ODS steels in lead-bismuth eutectic," *Journal of Nuclear Materials*, vol. 373, pp. 246–253, 2008.
- [54] S. S. Hwan, B. H. Lee, J. G. Kim, and J. Jang, "SCC and corrosion evaluations of the F/M steels for a supercritical water reactor," *Journal of Nuclear Materials*, vol. 372, pp. 177–181, Jan 2008.
- [55] R. L. Klueh, J. P. Shingledecker, R. W. Swindeman, and D. T. Hoelzer, "Oxide dispersion-strengthened steels: A comparison of some commercial and experimental alloys," *Journal of Nuclear Materials*, vol. 341, pp. 103–114, May 2005.
- [56] J. Wang, W. Yuan, R. S. Mishra, and I. Charit, "Microstructure and mechanical properties of friction stir welded oxide dispersion strengthened alloy," *Journal of Nuclear Materials*, vol. 432, pp. 274–280, 2013.

- [57] J.-A. J. Wang, I. G. Wright, M. J. Lance, and K. C. Liu, *Interface Fracture Toughness Evaluation for MA956 Oxide Film*, 2006.
- [58] Y. Wu, E. M. Haney, N. J. Cunningham, and G. R. Odette, "Transmission electron microscopy characterization of the nanofeatures in nanostructured ferritic alloy MA957," *Acta Materialia*, vol. 60, pp. 3456–3468, May 2012.
- [59] J. Chao, J. L. Gonzalez-Carrasco, and C. Capdevila, "Influence of annealing at 1100 degrees C and 475 degrees C on the mechanical properties at room temperature of an iron base ODS alloy," *Isij International*, vol. 47, pp. 1214–1220, 2007.
- [60] C. L. Chen, P. Wang, and G. J. Tatlock, "Phase transformations in yttrium-aluminium oxides in friction stir welded and recrystallised PM2000 alloys," *Materials at High Temperatures*, vol. 26, pp. 299–303, Sep 2009.
- [61] X. Chen, R. Haasch, and J. F. Stubbins, "Impedance spectroscopy and microstructural characterization of the corrosion behavior of FeCrAl alloy in lead-bismuth eutectic," *Journal of Nuclear Materials*, vol. 431, pp. 125–132, Dec 2012.
- [62] H. J. K. Lemmen, K. J. Sudmeijer, I. M. Richardson, and S. van der Zwaag, "Laser beam welding of an Oxide Dispersion Strengthened super alloy," *Journal of Materials Science*, vol. 42, pp. 5286–5295, Jul 2007.
- [63] R. L. Klueh, P. J. Maziasz, I. S. Kim, L. Heatherly, D. T. Hoelzer, N. Hashimoto, *et al.*, "Tensile and creep properties of an oxide dispersion- strengthened ferritic steel," *Journal of Nuclear Materials*, vol. 307, pp. 773–777, Dec 2002.
- [64] J. H. Kim, T. S. Byun, D. T. Hoelzer, S. W. Kim, and B. H. Lee, "Temperature dependence of strengthening mechanisms in the nanostructured ferritic alloy 14YWT: Part I-Mechanical and microstructural observations," *Materials Science and Engineering a-Structural Materials Properties Microstructure and Processing*, vol. 559, pp. 101–110, Jan 2013.
- [65] J. H. Kim, T. S. Byun, D. T. Hoelzer, C. H. Park, J. T. Yeom, and J. K. Hong, "Temperature dependence of strengthening mechanisms in the nanostructured ferritic alloy 14YWT: Part II-Mechanistic models and predictions," *Materials Science and Engineering a-Structural Materials Properties Microstructure and Processing*, vol. 559, pp. 111–118, Jan 2013.
- [66] D. T. Hoelzer, J. Bentley, M. A. Sokolov, M. K. Miller, G. R. Odette, and M. J. Alinger, "Influence of particle dispersions on the high-temperature strength of ferritic alloys," *Journal of Nuclear Materials*, vol. 367, pp. 166–172, Aug 2007.

- [67] A. Hirata, T. Fujita, Y. R. Wen, J. H. Schneibel, C. T. Liu, and M. W. Chen, "Atomic structure of nanoclusters in oxide-dispersion-strengthened steels," *Nature Materials*, vol. 10, pp. 922–926, Dec 2011.
- [68] P. D. Edmondson, C. M. Parish, Y. Zhang, A. Hallen, and M. K. Miller, "Helium bubble distributions in a nanostructured ferritic alloy," *Journal of Nuclear Materials*, vol. 434, pp. 210–216, Mar 2013.
- [69] Y. Chen, K. Sridharan, T. R. Allen, and S. Ukai, "Microstructural examination of oxide layers formed on an oxide dispersion strengthened ferritic steel exposed to supercritical water," *Journal of Nuclear Materials*, vol. 359, pp. 50–58, Dec 2006.
- [70] T. Kaito, T. Narita, S. Ukai, and Y. Matsuda, "High temperature oxidation behavior of ODS steels," *Journal of Nuclear Materials*, vol. 329, pp. 1388–1392, Aug 2004.
- [71] T. Narita, S. Ukai, T. Kaito, S. Ohtsuka, and Y. Matsuda, "Water corrosion resistance of ODS ferritic-martensitic steel tubes," *Journal of Nuclear Science and Technology*, vol. 45, pp. 99–102, 2008.
- [72] S. Ukai, S. Ohtsuka, T. Kaito, H. Sakasegawa, N. Chikata, S. Hayashi, *et al.*, "High-temperature strength characterization of advanced 9Cr-ODS ferritic steels," *Materials Science and Engineering a-Structural Materials Properties Microstructure and Processing*, vol. 510–11, pp. 115–120, Jun 2009.
- [73] S. Ohtsuka, S. Ukai, M. Fujiwara, T. Kaito, and T. Narita, "Improvement of creep strength of 9CrODS martensitic steel by controlling excess oxygen and titanium concentrations," *Materials Transactions*, vol. 46, pp. 487–492, Mar 2005.
- [74] Y. Yano, R. Ogawa, S. Yamashita, S. Ohtsuka, T. Kaito, N. Akasaka, *et al.*, "Effects of neutron irradiation on tensile properties of oxide dispersion strengthened (ODS) steel claddings," *Journal of Nuclear Materials*, vol. 419, pp. 305–309, Dec 2011.
- [75] H. S. Cho, A. Kimura, S. Ukai, and M. Fujiwara, "Corrosion properties of oxide dispersion strengthened steels in super-critical water environment," *Journal of Nuclear Materials*, vol. 329, pp. 387–391, Aug 2004.
- [76] V. L. Arbuzov, B. N. Goshchitskii, V. V. Sagaradze, S. E. Danilov, and A. E. Kar'kin, "Accumulation and Annealing of Radiation Defects under Low-Temperature Electron and Neutron Irradiation of ODS Steel and Fe-Cr Alloys," *Physics of Metals and Metallography*, vol. 110, pp. 366–377, 2010.
- [77] R. Schaublin, A. Ramar, N. Baluc, V. de Castro, M. A. Monge, T. Leguey, *et al.*, "Microstructural development under irradiation in European ODS ferritic/martensitic steels," *Journal of Nuclear Materials*, vol. 351, pp. 247–260, Jun 2006.

- [78] S. Y. Zhong, J. Ribis, V. Klosek, Y. de Carlan, N. Lochet, V. Ji, *et al.*, “Study of the thermal stability of nanoparticle distributions in an oxide dispersion strengthened (ODS) ferritic alloys,” *Journal of Nuclear Materials*, vol. 428, pp. 154–159, Sep 2012.
- [79] C. A. Williams, P. Unifantowicz, N. Baluc, G. D. W. Smith, and E. A. Marquis, “The formation and evolution of oxide particles in oxide-dispersion-strengthened ferritic steels during processing,” *Acta Materialia*, vol. 61, pp. 2219–2235, Apr 2013.
- [80] T. K. Kim, C. S. Bae, D. H. Kim, J. Jang, S. H. Kim, C. B. Lee, *et al.*, “Microstructural observation and tensile isotropy of an austenitic ODS steel,” *Nuclear Engineering and Technology*, vol. 40, pp. 305–310, Jun 2008.
- [81] M. F. Maday, “Comparison of the low cycle fatigue behaviour of F82H mod. and Eurofer 97 in water coolant,” *Fusion Engineering and Design*, vol. 61–62, pp. 665–670, Nov 2002.
- [82] H. Li, A. Nishimura, T. Muroga, and T. Nagasaka, “Fatigue life and strain hardening behavior of JLF-1 steel,” *Journal of Nuclear Materials*, vol. 386, pp. 433–436, Apr 30 2009.
- [83] H. Li, A. Nishimura, T. Nagasaka, and T. Muroga, “Fatigue life and cyclic softening behavior of JLF-1 steel,” *Fusion Engineering and Design*, vol. 82, pp. 2595–2600, Oct 2007.
- [84] H. L. Li, A. Nishimura, Z. X. Li, T. Nagasaka, and T. Muroga, “Low cycle fatigue behavior of JLF-1 steel at elevated temperatures,” *Fusion Engineering and Design*, vol. 81, pp. 241–245, Feb 2006.
- [85] G. Gupta, P. Ampornrat, X. Ren, K. Sridharan, T. R. Allen, and G. S. Was, “Role of grain boundary engineering in the SCC behavior of ferritic-martensitic alloy HT-9,” *Journal of Nuclear Materials*, vol. 361, pp. 160–173, Apr 15 2007.
- [86] P. Ampornrat, G. Gupta, and G. S. Was, “Tensile and stress corrosion cracking behavior of ferritic-martensitic steels in supercritical water,” *Journal of Nuclear Materials*, vol. 395, pp. 30–36, Dec 2009.
- [87] P. Hosemann, Y. Dai, E. Stergar, H. Leitner, E. Olivas, A. T. Nelson, *et al.*, “Large and Small Scale Materials Testing of HT-9 Irradiated in the STIP Irradiation Program,” *Experimental Mechanics*, vol. 51, pp. 1095–1102, Sep 2011.

- [88] S. Qvist, A. M. Bolind, P. Hosemann, Y. Q. Wang, J. Tesmer, M. S. De Caro, *et al.*, “Capability demonstration of simultaneous proton beam irradiation during exposure to molten lead-bismuth eutectic for HT9 steel,” *Nuclear Instruments & Methods in Physics Research Section a-Accelerators Spectrometers Detectors and Associated Equipment*, vol. 698, pp. 98–105, Jan 2013.
- [89] A. K. Roy, M. K. Hossain, R. Prabhakaran, and S. Sama, “Environment-assisted cracking of structural materials under different loading conditions,” *Corrosion*, vol. 61, pp. 364–370, Apr 2005.
- [90] S. Takaya, T. Furukawa, K. Aoto, G. Muller, A. Weisenburger, A. Heinzl, *et al.*, “Corrosion behavior of Al-alloying high Cr-ODS steels in lead-bismuth eutectic,” *Journal of Nuclear Materials*, vol. 386, pp. 507–510, Apr 2009.
- [91] S. Takaya, T. Furukawa, M. Inoue, T. Fujisawa, T. Okuda, F. Abe, *et al.*, “Corrosion resistance of Al-alloying high Cr-ODS steels in stagnant lead-bismuth,” *Journal of Nuclear Materials*, vol. 398, pp. 132–138, Mar 2010.
- [92] Special Metals Corporation and B. W. Baker, Private Communication, 2013.
- [93] Special Metals Corporation, “Engineering Data Sheet for Incoloy MA956 SMC-008,” 2004.
- [94] B. Wilshire, “Creep processes in dispersion-strengthened alloys,” in *Deformation, Processing, and Properties of Structural Materials: Symposium Honoring Professor Oleg D Sherby*, E. M. Taleff, C. K. Syn, and D. R. Lesuer, Eds., 2000.
- [95] B. Wilshire, “Creep mechanisms in oxide-dispersion-strengthened alloys,” *Creep and Fracture of Engineering Materials and Structures*, pp. 19–28, 1996.
- [96] B. Dubiel, W. Osuch, M. Wrobel, P. J. Ennis, and A. Czyrskafimonowicz, “Correlation of the Microstructure and the Tensile Deformation Of Incoloy MA956,” *Journal of Materials Processing Technology*, vol. 53, pp. 121–130, Aug 1995.
- [97] M. Bartsch, A. Wasilkowska, A. Czyrska-Filemonowicz, and U. Messerschmidt, “Dislocation dynamics in the oxide dispersion strengthened alloy INCOLOY MA956,” *Materials Science and Engineering a-Structural Materials Properties Microstructure and Processing*, vol. 272, pp. 152–162, Nov 15 1999.
- [98] J. Chao, J. L. Gonzalez-Carrasco, J. Ibanez, M. L. Escudero, and G. Gonzalez-Doncel, “Effects of the alumina scale on the room-temperature tensile behavior of preoxidized MA 956,” *Metallurgical and Materials Transactions a-Physical Metallurgy and Materials Science*, vol. 27, pp. 3809–3816, Dec 1996.

- [99] J. D. Whittenberger, "Elevated-Temperature Mechanical-Properties of the Iron Base Oxide Dispersion Strengthened Alloy MA-956 Bar," *Metallurgical Transactions a-Physical Metallurgy and Materials Science*, vol. 12, pp. 845–851, 1981.
- [100] A. Y. Badmos, H. Bhadeshia, and D. J. C. MacKay, "Tensile properties of mechanically alloyed oxide dispersion strengthened iron alloys - Part 1 - Neural network models," *Materials Science and Technology*, vol. 14, pp. 793–809, Aug 1998.
- [101] A. Y. Badmos and H. Bhadeshia, "Tensile properties of mechanically alloyed oxide dispersion strengthened iron alloys - Part 2 - Physical interpretation of yield strength," *Materials Science and Technology*, vol. 14, pp. 1221–1226, Dec 1998.
- [102] R. J. Salomon, "Incoloy Alloy MA956 - Strain-Rate and Temperature Effects on the Microstructure and Ductility," *Journal De Physique IV*, vol. 3, Nov 1993.
- [103] C. H. Zhang, A. Kimura, R. Kasada, J. Jang, H. Kishimoto, and Y. T. Yang, "Characterization of the oxide particles in Al-added high-Cr ODS ferritic steels," *Journal of Nuclear Materials*, vol. 417, pp. 221–224, Oct 1 2011.
- [104] A. Alamo, H. Regle, and J. L. Bechade, "Effects Of Processing On Textures And Tensile Properties Of Oxide Dispersion Strengthened Ferritic Alloys Obtained By Mechanical Alloying," in *Advances in Powder Metallurgy & Particulate Materials - 1992, Vol 7: Novel Powder Processing*, J. M. Capus and R. M. German, Eds., 1992, pp. 169–182.
- [105] A. Alamo, H. Regle, G. Pons, and J. L. Bechade, "Microstructure and Textures of ODS Ferritic Alloys Obtained by Mechanical Alloying," in *Mechanical Alloying*, vol. 88, P. H. Shingu, Ed., 1992, pp. 183–190.
- [106] H. Regle and A. Alamo, "Secondary Recrystallization of Oxide Dispersion-Strengthened Ferritic Alloys," *Journal De Physique Iv*, vol. 3, pp. 727–730, Nov 1993.
- [107] J. P. Hurley, C. Kelley, N. Bornstein, and I. G. Wright, "Corrosion of MA754 and MA956 in a Commercial Aluminum Melter," in *High Temperature Corrosion and Protection of Materials 7, Pts 1 and 2*, vol. 595–598, P. Steinmetz, I. G. Wright, A. Galerie, D. Monceau, and S. Mathieu, Eds., 2008, pp. 611–619.
- [108] M. Rees, R. C. Hurst, J. C. Healy, J. D. Parker, and L. Inst Mech Engineers, "Creep behaviour of candidate tubular ferritic oxide-dispersion-strengthened heat exchanger components," in *Sixth International Conference on Creep and Fatigue: Design and Life Assessment at High Temperature*, 1996.

- [109] J. C. Healy, M. Rees, J. D. Parker, and R. C. Hurst, "The multiaxial creep behaviour of ferritic ODS alloys as candidate materials for high temperature heat exchangers," *Creep and Fracture of Engineering Materials and Structures*, 1996.
- [110] C. Capdevila, I. Toda, J. Chao, and C. Garcia de Andres, "Influence of Plastic Deformation on Recrystallized Microstructure of Fe-Base ODS Alloy," in *Thermec 2009, Pts 1–4*, vol. 638–642, T. Chandra, N. Wanderka, W. Reimers, and M. Ionescu, Eds., 2010, pp. 2209–2214.
- [111] M. C. Garcia-Alonso, M. L. Escudero, and J. L. Gonzalez-Carrasco, "Evaluation of the scale integrity in the Al₂O₃/MA956 system at different polarisation by using EIS," *Materials and Corrosion-Werkstoffe Und Korrosion*, vol. 52, pp. 524–530, Jul 2001.
- [112] J. Ruiz, M. L. Escudero, H. Canahua, and M. C. Garcia-Alonso, "Optimal conditions for alumina coating formation on the MA956 superalloy for prosthetic bearing applications," *Journal of Biomedical Materials Research*, vol. 46, pp. 179–185, Aug 1999.
- [113] P. Seiler, M. Baeker, and J. Roesler, "Influence of creep and cyclic oxidation in thermal barrier coatings," *International Journal of Materials Research*, vol. 103, pp. 50–56, Jan 2012.
- [114] M. G. McKimpson and D. Odonnell, "Joining ODS Materials for High-Temperature Applications," *Jom-Journal of the Minerals Metals & Materials Society*, vol. 46, pp. 49–51, Jul 1994.
- [115] R. Lindau, M. Klimenkov, U. Jaentsch, A. Moeslang, and L. Commin, "Mechanical and microstructural characterization of electron beam welded reduced activation oxide dispersion strengthened - Eurofer steel," *Journal of Nuclear Materials*, vol. 416, pp. 22–29, Sep 1 2011.
- [116] V. G. Krishnardula, N. I. Sofyan, W. F. Gale, and J. W. Fergus, "Joining of ferritic oxide dispersion strengthened alloys," *Transactions of the Indian Institute of Metals*, vol. 59, pp. 199–203, Apr 2006.
- [117] V. G. Krishnardula, R. Aluru, N. I. Sofyan, J. W. Fergus, and W. F. Gale, *Solid-State Diffusion Bonding of MA956 and PM2000*, 2006.
- [118] A. Ambroziak, "Investigations of the friction welding of Incoloy MA 956 alloy," *Archives of Civil and Mechanical Engineering*, vol. 10, pp. 5–13, 2010 2010.
- [119] K. Shinozaki, C. Y. Kang, Y. C. Kim, M. Aritoshi, T. H. North, and Y. Nakao, "The metallurgical and mechanical properties of ODS alloy MA 956 friction welds," *Welding Journal*, vol. 76, pp. S289-S299, Aug 1997.

- [120] W. M. Thomas, E. D. Nicholas, J. C. Needham, M. G. Murch, P. Templesmith, and C. J. Dawes, G.B. Patent Application No. 9125978.8, 1991.
- [121] R. S. Mishra and Z. Y. Ma, "Friction stir welding and processing," *Materials Science & Engineering R-Reports*, vol. 50, pp. 1–78, Aug 31 2005.
- [122] R. Nandan, T. DebRoy, and H. K. D. H. Bhadeshia, "Recent advances in friction-stir welding - Process, weldment structure and properties," *Progress in Materials Science*, vol. 53, pp. 980–1023, Aug 2008.
- [123] A. Steuwer, S. J. Barnes, J. Altenkirch, R. Johnson, and P. J. Withers, "Friction Stir Welding of HSLA-65 Steel: Part II. The Influence of Weld Speed and Tool Material on the Residual Stress Distribution and Tool Wear," *Metallurgical and Materials Transactions a-Physical Metallurgy and Materials Science*, vol. 43A, pp. 2356–2365, Jul 2012.
- [124] S. J. Barnes, A. R. Bhatti, A. Steuwer, R. Johnson, J. Altenkirch, and P. J. Withers, "Friction Stir Welding in HSLA-65 Steel: Part I. Influence of Weld Speed and Tool Material on Microstructural Development," *Metallurgical and Materials Transactions a-Physical Metallurgy and Materials Science*, vol. 43A, pp. 2342–2355, Jul 2012.
- [125] Y. S. Sato, P. Arkom, H. Kokawa, T. W. Nelson, and R. J. Steel, "Effect of microstructure on properties of friction stir welded Inconel Alloy 600," *Materials Science and Engineering a-Structural Materials Properties Microstructure and Processing*, vol. 477, pp. 250–258, Mar 25 2008.
- [126] H.-H. Cho, H. N. Han, S.-T. Hong, J.-H. Park, Y.-J. Kwon, S.-H. Kim, *et al.*, "Microstructural analysis of friction stir welded ferritic stainless steel," *Materials Science and Engineering a-Structural Materials Properties Microstructure and Processing*, vol. 528, pp. 2889–2894, Mar 15 2011.
- [127] A. K. Lakshminarayanan and V. Balasubramanian, "Understanding the Parameters Controlling Friction Stir Welding of AISI 409M Ferritic Stainless Steel," *Metals and Materials International*, vol. 17, pp. 969–981, Dec 2011.
- [128] M. B. Bilgin and C. Meran, "The effect of tool rotational and traverse speed on friction stir weldability of AISI 430 ferritic stainless steels," *Materials & Design*, vol. 33, pp. 376–383, Jan 2012.
- [129] M. W. Mahoney, C. G. Rhodes, J. G. Flintoff, R. A. Spurling, and W. H. Bingel, "Properties of friction-stir-welded 7075 T651 aluminum," *Metallurgical and Materials Transactions a-Physical Metallurgy and Materials Science*, vol. 29, pp. 1955–1964, Jul 1998.

- [130] R. Nandan, G. G. Roy, T. J. Lienert, and T. DebRoy, "Numerical modelling of 3D plastic flow and heat transfer during friction stir welding of stainless steel," *Science and Technology of Welding and Joining*, vol. 11, pp. 526–537, Sep 2006.
- [131] J. W. Qian, J. L. Li, F. Sun, J. T. Xiong, F. S. Zhang, and X. Lin, "An analytical model to optimize rotation speed and travel speed of friction stir welding for defect-free joints," *Scripta Materialia*, vol. 68, pp. 175–178, Feb 2013.
- [132] S. K. Chimbli, D. J. Medlin, and W. J. Arbegast, *Minimizing lack of consolidation defects in friction stir welds*, 2007.
- [133] P. Biswas, D. A. Kumar, and N. R. Mandal, "Friction stir welding of aluminum alloy with varying tool geometry and process parameters," *Proceedings of the Institution of Mechanical Engineers Part B-Journal of Engineering Manufacture*, vol. 226, pp. 641–648, Apr 2012.
- [134] Q. Zhang, M. Mahfouf, G. Panoutsos, K. Beamish, and I. Norris, "Knowledge discovery for friction stir welding via data driven approaches Part 1-correlation analyses of internal process variables and weld quality," *Science and Technology of Welding and Joining*, vol. 17, pp. 672–680, Nov 2012.
- [135] Q. Zhang, M. Mahfouf, G. Panoutsos, K. Beamish, and I. Norris, "Knowledge discovery for friction stir welding via data driven approaches Part 2-multiobjective modelling using fuzzy rule based systems," *Science and Technology of Welding and Joining*, vol. 17, pp. 681–693, Nov 2012.
- [136] S. Rajakumar, C. Muralidharan, and V. Balasubramanian, "Developing Empirical Relationships to Predict Grain Size and Hardness of the Weld Nugget of Friction Stir Welded AA7075-T6 Aluminium Alloy Joints," *Experimental Techniques*, vol. 36, pp. 6–17, Jul-Aug 2012.
- [137] L. Y. Wei and T. W. Nelson, "Correlation of Microstructures and Process Variables in FSW HSLA-65 Steel," *Welding Journal*, vol. 90, pp. 95S-101S, May 2011.
- [138] A. Heidarzadeh, T. Saeid, H. Khodaverdizadeh, A. Mahmoudi, and E. Nazari, "Establishing a Mathematical Model to Predict the Tensile Strength of Friction Stir Welded Pure Copper Joints," *Metallurgical and Materials Transactions B-Process Metallurgy and Materials Processing Science*, vol. 44, pp. 175–183, Feb 2013.
- [139] W. J. Arbegast and P. Hartley, in *Proceedings of the Fifth International Conference on Trends in Welding Research*, Pine Mountain, GA, 1998.
- [140] T. Hashimoto, S. Jyogan, K. Nakata, Y. Kim, and M. Ushio, in *Proceedings of the First International Symposium on Friction Stir Welding*, Thousand Oaks, CA, 1999.

- [141] M. West, B. Jahsthi, P. Hosemann, and V. Sodesetti, "Friction stir welding of oxide dispersion strengthened alloy MA956," in *Friction Stir Welding and Processing VI*, TMS, Warrendale, PA, 2011, pp. 33–40.
- [142] F. Legendre, S. Poissonnet, P. Bonnaillie, L. Boulanger, and L. Forest, "Some microstructural characterisations in a friction stir welded oxide dispersion strengthened ferritic steel alloy," *Journal of Nuclear Materials*, vol. 386–88, pp. 537–539, Apr 30 2009.
- [143] M. H. Mathon, V. Klosek, Y. de Carlan, and L. Forest, "Study of PM2000 microstructure evolution following FSW process," *Journal of Nuclear Materials*, vol. 386, pp. 475–478, Apr 30 2009.
- [144] B. K. Jasthi, S. M. Howard, W. J. Arbegast, G. J. Grant, S. Koduri, and D. R. Herling, "Friction stir welding of MA 957 oxide dispersion strengthened ferritic steel," in *Friction Stir Welding Processing III*, San Francisco, CA, 2005, pp. 75–79.
- [145] W. Han, S. Ukai, F. Wan, Y. Sato, B. Leng, H. Numata, *et al.*, "Hardness and Micro-Texture in Friction Stir Welds of a Nanostructured Oxide Dispersion Strengthened Ferritic Steel," *Materials Transactions*, vol. 53, pp. 390–394, Feb 2012.
- [146] W. T. Han, F. R. Wan, B. Leng, S. Ukai, Q. X. Tang, S. Hayashi, *et al.*, "Grain characteristic and texture evolution in friction stir welds of nanostructured oxide dispersion strengthened ferritic steel," *Science and Technology of Welding and Joining*, vol. 16, pp. 690–696, Nov 2011.
- [147] A. Etienne, N. J. Cunningham, Y. Wu, and G. R. Odette, "Effects of friction stir welding and post-weld annealing on nanostructured ferritic alloy," *Materials Science and Technology*, vol. 27, pp. 724–728, Apr 2011.
- [148] M. J. Peel, A. Steuwer, P. J. Withers, T. Dickerson, Q. Shi, and H. Shercliff, "Dissimilar friction stir welds in AA5083-AA6082. Part I: Process parameter effects on thermal history and weld properties," *Metallurgical and Materials Transactions a-Physical Metallurgy and Materials Science*, vol. 37A, pp. 2183–2193, Jul 2006.
- [149] S. Swaminathan, K. Oh-Ishi, A. P. Zhilyaev, C. B. Fuller, B. London, M. W. Mahoney, *et al.*, "Peak Stir Zone Temperatures during Friction Stir Processing," *Metallurgical and Materials Transactions a-Physical Metallurgy and Materials Science*, vol. 41A, pp. 631–640, Mar 2010.
- [150] D. Rosenthal, "The Theory of Moving Sources of Heat and Its Application to Metal Treatments," *Transactions of the ASME*, pp. 849–866, 1946.
- [151] S. Kou, *Welding Metallurgy*, 2nd ed. Hoboken, NJ: John Wiley and Sons, 2003.

- [152] R. W. Messler, *Principles of Welding*. Troy, NY: Wiley-VCH, 2004.
- [153] Z. Feng and W. Ren, "Initial investigation on joining ODS alloy using friction stir welding for Gen IV nuclear reactor heat exchanger applications," in *Proceedings of the Asme Pressure Vessels and Piping Conference 2007, Vol 6: Materials and Fabrication*, 2007, pp. 431–438.
- [154] C. L. Chen, G. J. Tatlock, and A. R. Jones, "Microstructural evolution in friction stir welding of nanostructured ODS alloys," *Journal of Alloys and Compounds*, vol. 504, pp. S460-S466, Aug 2010.
- [155] M. G. Nicholas and C. F. Old, "Liquid-Metal Embrittlement," *Journal of Materials Science*, vol. 14, pp. 1–18, 1979.
- [156] C. F. Old, "Liquid-Metal Embrittlement of Nuclear-Materials," *Journal of Nuclear Materials*, vol. 92, pp. 2–25, 1980.
- [157] F. A. Shunk and W. R. Warke, "Specificity as an Aspect of Liquid-Metal Embrittlement," *Scripta Metallurgica*, vol. 8, pp. 519–526, 1974.
- [158] R. C. Asher, D. Davies, and S. A. Beetham, "Some Observations In Compatibility Of Structural-Materials With Molten Lead," *Corrosion Science*, vol. 17, pp. 545–557, 1977.
- [159] ASTM G129–00, "Standard Practice for Slow Strain Rate Testing to Evaluate the Susceptibility of Metallic Materials to Environmentally Assisted Cracking," 2006.
- [160] A. D. Rollett and S. I. Wright, "Typical Texture in Metals," in *Texture and Anisotropy*, New York, NY: Cambridge University Press, 1998.
- [161] U. F. Kocks, C. N. Tome, and H. R. Wenk, *Texture and Anisotropy: Preferred Orientation in Polycrystals and their Effect on Materials Properties*: Cambridge University press, 1998.
- [162] B. Dubiel, A. Czyrska-Filemonowicz, and P. J. Ennis, "Dislocation-particle interactions during deformation of the FeCrAl-oxide dispersion strengthened INCOLOY MA956 at RT-1050 degrees C," in *Microstructural Stability of Creep Resistant Alloys for High Temperature Plant Applications*, A. Strang, J. Cawley, and G. W. Greenwood, Eds., ed, 1998, pp. 215–221.
- [163] R. D. Doherty, D. A. Hughes, F. J. Humphreys, J. J. Jonas, D. J. Jensen, M. E. Kassner, *et al.*, "Current issues in recrystallization: a review," *Materials Science and Engineering a-Structural Materials Properties Microstructure and Processing*, vol. 238, pp. 219–274, Nov 15 1997.

- [164] F. J. Humphreys, "A unified theory of recovery, recrystallization and grain growth, based on the stability and growth of cellular microstructures .1. The basic model," *Acta Materialia*, vol. 45, pp. 4231–4240, Oct 1997.
- [165] J. Baczynski and J. J. Jonas, "Texture development during the torsion testing of alpha-iron and two IF steels," *Acta Materialia*, vol. 44, pp. 4273–4288, Nov 1996.
- [166] S. Li, I. J. Beyerlein, and M. A. M. Bourke, "Texture formation during equal channel angular extrusion of fcc and bcc materials: comparison with simple shear," *Materials Science and Engineering a-Structural Materials Properties Microstructure and Processing*, vol. 394, pp. 66–77, Mar 2005.
- [167] R. W. Fonda and K. E. Knipling, "Texture development in friction stir welds," *Science and Technology of Welding and Joining*, vol. 16, pp. 288–294, May 2011.
- [168] M. Meyers and K. Chawla, *Mechanical Behavior of Materials*, 2nd ed.: Cambridge University Press, 2009.
- [169] H. Cama and T. A. Hughes, "The Stability of Dispersoids In Mechanically Alloyed Ferritic ODS Alloys," in *Conference of the Electron-Microscopy-and-Analysis-Group of the Institute-of-Physics: Electron Microscopy and Analysis 1993 (EMAG93)*, Liverpool, England, 1993, pp. 361–364.
- [170] H. Cama and T. A. Hughes, "The Role of Dispersoids in Maintaining The Corrosion-Resistance of Mechanically Alloyed Oxide Dispersion-Strengthened Alloys," *Scripta Metallurgica Et Materialia*, vol. 32, May 15 1995.
- [171] A. Kruk, B. Dubiel, and A. Czyrska-Filemonowicz, "3D imaging and metrology of yttria dispersoids in INCOLOY MA956 by electron tomography," in *Electron Microscopy Xiv*, vol. 186, D. Stroz and K. Prusik, Eds., ed, 2012.
- [172] M. F. Hupalo, M. Terada, A. M. Kliauga, and A. F. Padilha, "Microstructural characterization of INCOLOY alloy MA 956," *Materialwissenschaft Und Werkstofftechnik*, vol. 34, pp. 505–508, May 2003.
- [173] Y. Z. Shen, T. T. Zou, S. Zhang, and L. Z. Sheng, "Identification of Oxide Phases in Oxide Dispersion Strengthened PM2000 Steel," *Isij International*, vol. 53, pp. 304–310, 2013.
- [174] P. Unifantowicz, R. Schaeublin, C. Hebert, T. Plocinski, G. Lucas, and N. Baluc, "Statistical analysis of oxides particles in ODS ferritic steel using advanced electron microscopy," *Journal of Nuclear Materials*, vol. 422, pp. 131–136, Mar 2012.
- [175] T. J. Collins, "ImageJ for microscopy," *Biotechniques*, vol. 43, Jul 2007.

- [176] J. Woertz, "Redistribution Mechanisms and Quantification of Homogeneity in Friction Stir Welding and Processing of an Aluminum Silicon Alloy," PhD Dissertation, Mechanical and Aerospace Engineering Department, Naval Postgraduate School, Monterey, CA, 2013.
- [177] J. Ilavsky and P. R. Jemian, "Irena: tool suite for modeling and analysis of small-angle scattering," *Journal of Applied Crystallography*, vol. 42, pp. 347–353, Apr 2009.
- [178] N. W. M. Ritchie, "Spectrum Simulation in DTSA-II," *Microscopy and Microanalysis*, vol. 15, pp. 454–468, Oct 2009.
- [179] J. L. Caslavsky and D. Viechnicki, "Phase-Equilibria Studies In The Ternary-System $\text{Al}_2\text{O}_3/\text{Y}_2\text{O}_3/\text{Nd}_2\text{O}_3$ Using ODTA," *American Ceramic Society Bulletin*, vol. 61, pp. 808–808, 1982 1982.
- [180] M. Medraj, R. Hammond, M. A. Parvez, R. A. L. Drew, and W. T. Thompson, "High temperature neutron diffraction study of the $\text{Al}_2\text{O}_3\text{-Y}_2\text{O}_3$ system," *Journal of the European Ceramic Society*, vol. 26, pp. 3515–3524, 2006 2006.
- [181] J. I. Goldstein, D. E. Newbury, P. Echlin, and D. C. Joy, *Scanning Electron Microscopy and X-ray Microanalysis: A Text for Biologists, Material Scientists, and Geologists*, 2nd ed. New York, NY: Kluwer Academic Plenum Publishers, 1992.
- [182] O. Fabrichnaya, H. J. Seifert, R. Weiland, T. Ludwig, F. Aldinger, and A. Navrotsky, "Phase equilibria and thermodynamics in the $\text{Y}_2\text{O}_3\text{-Al}_2\text{O}_3\text{-SO}_2$ -system," *Zeitschrift Fur Metallkunde*, vol. 92, pp. 1083–1097, Sep 2001.
- [183] J. S. Abell, I. R. Harris, B. Cockayne, and B. Lent, "INVESTIGATION OF PHASE-STABILITY IN $\text{Y}_2\text{O}_3\text{-AL}_2\text{O}_3$ SYSTEM," *Journal of Materials Science*, vol. 9, pp. 527–537, 1974.
- [184] P. W. Voorhees, "The Theory of Ostwald Ripening," *Journal of Statistical Physics*, vol. 38, pp. 231–252, 1985.
- [185] K. H. Ho and S. T. Newman, "State of the art electrical discharge machining (EDM)," *International Journal of Machine Tools & Manufacture*, vol. 43, pp. 1287–1300, Oct 2003.
- [186] W. N. Sharpe, D. Danley, and D. A. LaVan, "Microspecimen tensile tests of A533-B steel," *Small Specimen Test Techniques*, vol. 1329, pp. 497–512, 1998.
- [187] M. L. Hamilton, M. A. Blotter, and D. J. Edwards, "Evaluation of Miniature Tension Specimen Fabrication Techniques and Performance," *Small Specimen Test Techniques Applied to Nuclear Receptor Vessel Thermal Annealing and Plant Life Extension*, vol. 1204, 1993.

- [188] R. W. Hertzberg, *Deformation and Fracture Mechanics of Engineering Materials*, 4th ed. Hoboken, NJ: John Wiley & Sons, Inc., 1996.
- [189] Y. H. Zhao, Y. Z. Guo, Q. Wei, T. D. Topping, A. M. Dangelewicz, Y. T. Zhu, *et al.*, “Influence of specimen dimensions and strain measurement methods on tensile stress-strain curves,” *Materials Science and Engineering a-Structural Materials Properties Microstructure and Processing*, vol. 525, pp. 68–77, Nov 2009.
- [190] P. Han, *Tensile testing*. Materials Park, Ohio: ASM International, 1992.
- [191] P. Jung, A. Hishinuma, G. E. Lucas, and H. Ullmaier, “Recommendation of miniaturized techniques for mechanical testing of fusion materials in an intense neutron source,” *Journal of Nuclear Materials*, vol. 232, pp. 186–205, Sep 1996.
- [192] U. F. Kocks, A. S. Argon, and M. F. Ashby, “Thermodynamics and Kinetics of Slip,” *Progress in Materials Science*, vol. 19, pp. 1–281, 1975.
- [193] J. S. Zhang, “A review of steel corrosion by liquid lead and lead-bismuth,” *Corrosion Science*, vol. 51, pp. 1207–1227, Jun 2009.
- [194] J. Zhang, P. Hosemann, and S. Maloy, “Models of liquid metal corrosion,” *Journal of Nuclear Materials*, vol. 404, pp. 82–96, Sep 1 2010.
- [195] J. S. Zhang and N. Li, “Review of the studies on fundamental issues in LBE corrosion,” *Journal of Nuclear Materials*, vol. 373, pp. 351–377, Feb 2008.
- [196] NACE ASTM G193–11a, “Standard Terminology and Acronyms Relating to Corrosion,” 2011.
- [197] J. C. Lynn, W. R. Warke, and P. Gordon, “Solid Metal-Induced Embrittlement of Steel,” *Materials Science and Engineering*, vol. 18, pp. 51–62, 1975.
- [198] Y. Miwa, S. Jitsukawa, and T. Tsukada, “Stress corrosion cracking susceptibility of a reduced-activation martensitic steel F82H,” *Journal of Nuclear Materials*, vol. 386, pp. 703–707, Apr 30 2009.
- [199] A. Legris, G. Nicaise, J. B. Vogt, J. Foct, D. Gorse, and D. Vancon, “Embrittlement of a martensitic steel by liquid lead,” *Scripta Materialia*, vol. 43, pp. 997–1001, Nov 13 2000.
- [200] J. Van den Bosch, R. W. Bosch, D. Sapundjiev, and A. Almazouzi, “Liquid metal embrittlement susceptibility of ferritic-martensitic steel in liquid lead alloys,” *Journal of Nuclear Materials*, vol. 376, pp. 322–329, Jun 15 2008.

- [201] J. Van den Bosch, G. Coen, R. W. Bosch, and A. Almazouzi, “TWIN ASTIR: First tensile results of T91 and 316L steel after neutron irradiation in contact with liquid lead-bismuth eutectic,” *Journal of Nuclear Materials*, vol. 398, pp. 68–72, Mar 2010.
- [202] J. Van den Bosch, P. Hosemann, A. Almazouzi, and S. A. Maloy, “Liquid metal embrittlement of silicon enriched steel for nuclear applications,” *Journal of Nuclear Materials*, vol. 398, pp. 116–121, Mar 2010.
- [203] T. Auger and G. Lorang, “Liquid metal embrittlement susceptibility of T91 steel by lead-bismuth,” *Scripta Materialia*, vol. 52, pp. 1323–1328, Jun 2005.
- [204] ASTM G30–97, “Standard Practice for Making and Using U-Bend Stress-Corrosion Test Specimens,” 2009.

THIS PAGE INTENTIONALLY LEFT BLANK

INITIAL DISTRIBUTION LIST

1. Defense Technical Information Center
Ft. Belvoir, Virginia
2. Dudley Knox Library
Naval Postgraduate School
Monterey, California